UNIVERSITY OF SOUTHAMPTON
FACULTY OF ENGINEERING AND THE ENVIRONMENT
INSTITUTE OF SOUND AND VIBRATION RESEARCH

AIRCRAFT TURBINE COMBUSTION NOISE PROCESSING

by

Paúl Rodríguez García

Thesis for the degree of Doctor of Philosophy

October 2016

UNIVERSITY OF SOUTHAMPTON
Faculty of Engineering and the Environment
Institute of Sound and Vibration Research

Abstract

Doctor of Philosophy

AIRCRAFT TURBINE COMBUSTION NOISE PROCESSING

by Paúl Rodríguez García

Appraisal of the noise produced at the combustion stage in a jet engine is becoming more important, as fan and jet noise have been significantly reduced over many years. Therefore, combustion noise is contributing more to overall noise, especially at low jet velocities. Environmental regulations stipulate that gas emissions from a jet engine should be reduced. Thus, new techniques have been introduced in their operation, especially concerning the combustion process. Accordingly, there is a need for improved processing methods in order to extract combustion noise from other sources in new build engines.

A novel processing technique to extract turbofan engine combustion noise called 3S-Array is presented. It has been developed using a multiple coherence technique with data acquired in the in-duct and external sound fields of a jet engine. In-duct sensors are located in the combustion chamber and in the nozzle of the engine, and external data is acquired using an array of microphones. A beamformed signal focused on the nozzle of the engine is generated with the data from the external array. Jet noise and influences of the room on the array output are reduced using this focusing technique, which is referred to as Focused Beamformed Output (FBO).

Results show that using this new 3S-Array technique with two of the in-duct sensors and the focused beamformed signal as the third one, provides a better estimator of combustion noise than the 3-signal coherence technique alone, or the Coherence-Output Power Spectra (COP), both of which are reported in the literature as methods for the extraction of combustion noise from the radiated noise spectrum.

Contents

List of Figures

List of Tables

Declaration of Authorship

I, Paúl Rodríguez García, declare that this thesis titled, 'Aircraft Turbine Combustion Noise Processing' and the work presented in it are my own. I confirm that:

- This work was done wholly or mainly while in candidature for a research degree at this University.
- Where any part of this thesis has previously been submitted for a degree or any other qualification at this University or any other institution, this has been clearly stated.
- Where I have consulted the published work of others, this is always clearly attributed.
- Where I have quoted from the work of others, the source is always given. With the exception of such quotations, this thesis is entirely my own work.
- I have acknowledged all main sources of help.
- Where the thesis is based on work done by myself jointly with others, I have made clear exactly what was done by others and what I have contributed myself.
- Parts of this work have been published, as listed in Section 1.4.

Signed:

Date: March 22nd, 2016

Acknowledgements

I would like to thank all of the people who have helped me during the last three years (and a bit more) of adventures.

First of all, my parents and family for supporting me in all of my decisions and always being there to help and care for me, even from such a distance.

I'd like to acknowledge Rolls-Royce for the financial support provided for the studying of my PhD, Dr Ajith Appukuttan for his support, and Chris Knighton for his help with the synchronisation of data.

I am very grateful to my supervisors, Dr Keith Holland and Dr Brian Tester, for their patience, guidance, and the opportunity to work with them.

Thanks to the UTC officemates for the great days we've had together. It has been a pleasure to have passed this time with all of you.

I also have to say thank you to Dani. Together we entered into the unknown, and without him this adventure would never have been possible.

Thank you, Camille for always being there through the good and bad moments, and for pushing me when I've needed it.

Thanks to all of my Spanish friends who have supported me, those who have visited (Adolfo, Piru, Manu, Mario) and also to those who could not.

I want to give special thanks to Hessam Alavi for all of his help and for always finding the time. I appreciate it a lot. Also, thanks to Takashi Takeuchi, for his friendship, advice, and all of the great moments we had together working in Opsodis.

I cannot forget all the people I've met during these years, especially those at Pansy Road, Halil, Kuti, Edu, and everyone else who passed by.

And last but not least, I would like to thank my Spanish advisers Antonio Pena, Marisol Torres, Manuel Sobreira, and Philip Newell for their help and support to start all of this.

Abbreviations

ACARE	**A**dvisory **C**ouncil for **A**eronautics **R**esearch in **E**urope
AFR	**A**ir to **F**uel **R**atio
AGARD	**A**dvisory **G**roup for **A**eronautical **R**esearch and **D**evelopment
ANOPP	**A**ircraft **NO**ise **P**rediction **P**rogram
ANTLE	**A**ffordable **N**ear-**T**erm **L**ow **E**missions
BPF	**B**lade **P**assing **F**requency
BSS	**B**lind **S**ource **S**eparation
CO2	**C**arbon di**O**xide
CSD	**C**ross- **S**pectral **D**density
COP	**C**oherent **O**utput **P**ower (spectra)
DAMAS	**D**econvolution **A**pproach for the **M**apping of **A**coustic **S**ources
DAS	**D**elay **A**nd **S**um
DLR	**D**eutsches Zentrum fr **L**uft- und **R**aumfahrt e.V.
FBO	**F**ocussed **B**eamforming **O**utput
FFT	**F**ast **F**ourier **T**ransform
HPF	**H**igh **P**ass **F**ilter
ICA	**I**ndependent **C**ontent **A**nalisys
ICSV	**I**nternational **C**ongress on **S**ound and **V**ibration
IDG	**I**ntegrated **D**rive **G**enerator
INTA	**I**nstituto **N**acional de **T**ecnica **A**eroespacial
ISCA	**I**terative **S**idelobe **C**leaner **A**lgorithm
ISVR	**I**nstitute **S**ound and **V**ibration **R**esearch
NNLS	**N**on-**N**egative **L**east **S**quares
LPF	**L**ow **P**ass **F**ilter

LTI	**L**inear **T**ime **I**nvariant
NOx	**N**itrogen **O**xide
PSD	**P**ower **S**pectral **D**ensity
PSF	**P**oint **S**pread **F**unction
RP	**R**umble **P**robe
RR	**R**olls-**R**oyce
RRD	**R**olls-**R**oyce **D**eutschland
RRUK	**R**olls-**R**oyce **U**united **K**ingdom
SVD	**S**ingular**V**alue **D**ecomposition

Symbols

Greek symbols

Δ_t	time delay
δ_ω	bandwidth
δ_θ	angle difference
γ^2_{xy}	coherence function between x and y
Λ_{mn}	normalisation constant
ψ_x, ψ_z, ψ_z	simplification terms
τ	time constant
ω	radial frequency
$\overline{r}, \overline{\varphi}, \overline{z}$	direction cosines, used in reference to the axes x, y, z
μ	hub-tip ratio
ξ	threshold

Roman symbols

C_{12}	cross correlation between the points 1 and 2
F	constant
G	constant
c_0	speed of sound in air at ambient conditions
c	speed of sound in air
f	frequency
f_{mn}	cut-on mode frequency
f_s	sampling frequency
G_{comb}	one-side Cross-Spectral Density of the radiated combustion noise
G_{xx}	one-side Auto-Spectral Density Function of x

G_{xy}	one-side Cross-Spectral Density Function between x and y
G_{yy}	one-side Auto-Spectral Density Function of y
H	constant
H_{xy}	Transfer function between x and y
I	constant
J_m	Bessel function of order m
j	imaginary unit
k	wavenumber
L	Number of microphones of an array
M	Mach number
m	number of modal diameters
N_m	Neumann function of order m
N_s	number of data segments to obtain a coherence
n	number of modal circles
n_d	process averages
P_I	confidence interval for zero coherence
p	sound pressure
R	cross correlation normalised amplitude
R_{xy}	cross correlation function between x and y
R_{xx}	auto correlation function of x
R_d	mean radius of an annular duct
r_0	outer radius of an annular duct
r_1	inner radius of an annular duct
r_l	distance from the lˆth sensor to a focusing point in meters
r_ref	reference distance
SMP	number of samples
S_{xy}	cross-power spectral density between x and y
S_{xx}	auto-power spectral density of the signal x
t	time variable
$x(t)$	time varying signals
X_T	finite Fourier Transform of $x(t)$

Operators

$E[.]$	expectancy
$s.d.[.]$	standard deviation
$(.)^*$	conjugate transpose
$(.)^H$	Hermitian of a matrix
$< . >_t$	time-average

Dedicated to my family

Chapter 1

Introduction

1.1 Noise from a Jet Engine

A jet engine is a complex acoustic source which is mainly composed by three sections: the fan and compressor, the combustion chamber, and the turbine. Then, we can study the noise produced by a turbofan by analysing the noise produced by its components.

Some of these noises are more dominant in the overall noise emission, like fan, compressor, and jet noise as is shown in Figure 1.1. However, combustion noise is becoming more important in the overall picture as other noise sources are reduced considerably [1], especially due to the increase of the ratio between the bypass duct and the core of the engine (bypass ratio).

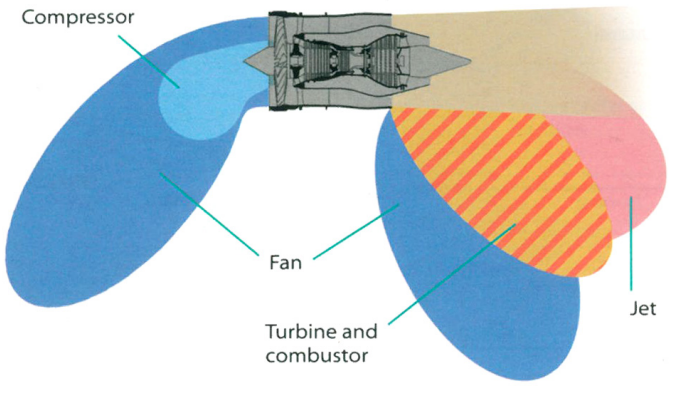

FIGURE 1.1: Different noises produced from a Jet Engine [2]

Fan noise can be easily identified on approach because it has a high frequency tonal characteristic which depends of the number of blades and rotation speed of the engine, and it is mainly emitted from the inlet but also through the bypass duct or the nozzle of the jet engine. The compressor noise is also tonal and emitted from the inlet but it is less dominant than the fan noise although it is generated close to it. On the other hand, the mix in the rear part of the engine between the high velocity jet exhaust and the external air creates a turbulence which produces broadband jet noise and which is mostly heard at take-off [3].

The noise generated in the core of the turbofan engine has been denominated core noise, and it includes combustion noise produced by the combustion process, turbine noise, compressor noise, and all the noises related with the gas processes of the turbofan. Core noise was considered unimportant versus fan and jet noise from static-engine tests [3], but fan and especially jet noise are reduced during flight conditions, making core noise a principal contributor to overall turbofan noise [4, 5].

1.2 The Combustion Process

Combustion is a stage of the working cycle of a jet engine where the fuel is burned and converted into thermal energy. Combustion chambers are situated after compression and before the turbines in a turbofan as it is shown in Figure 1.2.

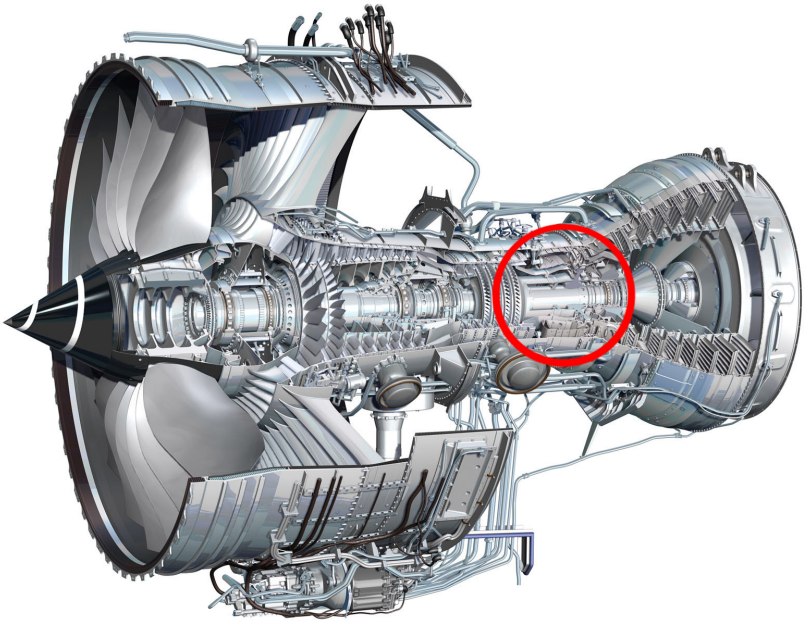

FIGURE 1.2: Combustion Chamber in a Trent 1000 - Cutaway View

They also are called combustor, burner, or flame holder, and there are principally three different types of combustion chambers used for gas turbine engines [2]: the multiple chamber, the tubo-annular chamber, and the annular chamber.

All types of combustion chambers are composed of two parts. A first zone where the fuel is injected and burned, and a second zone where the very high temperatures are reduced using cold air.

The combustion chamber most used nowadays is the annular chamber, such as the one shown in Figure 1.3, which is composed of only one flame tube and one air casting, and it has the fuel injectors and the igniters spaced circumferentially.

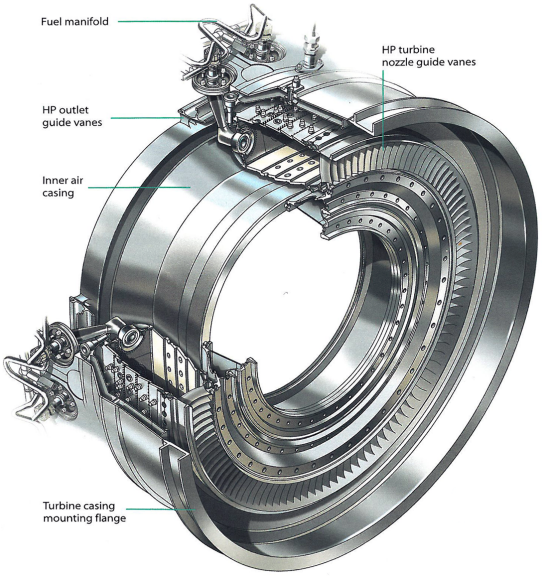

FIGURE 1.3: Annular combustion chamber (From [2])

The main benefit of this kind of combustion system is that it can be 75% shorter than the tubo-annular combustor to produce the same power output. Moreover, control emissions and combustion efficiency are also better since it has a smaller wall area than the tubo-annular combustor and more air can be used for the combustion process instead of cooling. On the other hand, the weakness of this design lies in its complex structure. The construction of an annular combustion chamber becomes very complex, and development testing can only be carried out mainly at the end stage when it is manufactured [2].

A closer look at the annular combustor is shown in Figure 1.4.

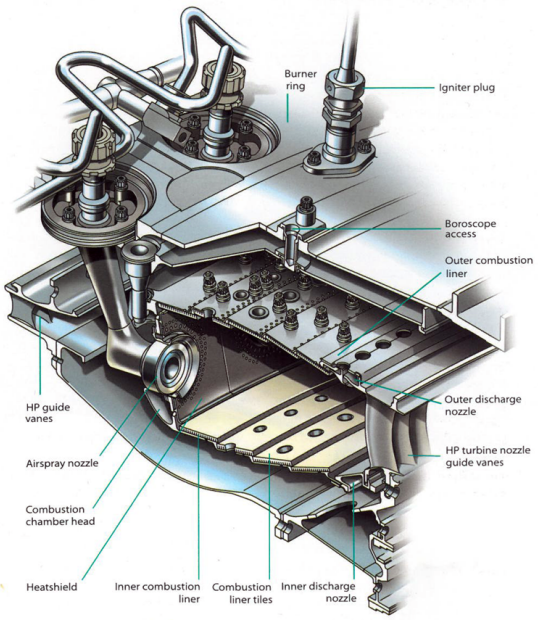

FIGURE 1.4: Section of an annular combustion chamber (From [2])

1.2.1 Combustion Noise Acquisition

Rumble probes are dynamic pressure transducers installed in the combustion chamber during the measurement rigs through the boroscope access or the igniter plug. Normally, they are mounted in a 50 mm tube which introduces a resonance in the output signal at around 2.5 kHz (quarter wavelength resonance). However, this resonance is not important in the analysis of combustion noise as it is not in the frequency range of interest, which is below 1 kHz.

All the combustion processes are very turbulent in order to achieve a good mixture between fuel and air. A broadband noise would be expected from that turbulence, but it is filtered in its way out through the turbine and it comes out through the nozzle.

Jet noise is reduced during flight conditions due to minor jet velocity. Therefore, jet noise levels are higher during normal rig measurements than during flight conditions [1]. This makes it more difficult to perceive combustion noise in a static rig because it becomes smaller in comparison with jet noise than it would be during flight conditions, where it is not expected that combustion noise would change.

1.2.2 Combustion Noise Types

It is common to define combustion noise at least as two different problems due to how is it generated. One from the turbulences and the combustion process carried out in

the combustion chamber (direct combustion noise) and another produced while the gas leaves the combustion chamber (indirect combustion noise).

New combustion systems were introduced to reduce emissions and also meet future requirements. New lean combustion systems [6] such as lean-burn combustion, which reduces smoke and NO_x by removing fuel-rich pockets in the combustion; or staged fuel injection [7], rich-quench-lean combustors [8], or lean premixed prevaporised combustion [9]. The main problem with these systems is that the noise can be amplified since they generate turbulence fluctuations and inhomogeneous heat is released [10, 11].

In the case of lean-burn combustion, that problem is improved by supplying the fuel in two different stages. One "pilot" fuel supply for the low power operation and one "main" supplier for the higher operation levels [2]. Nevertheless, this approach introduces even more complexity in the system.

Generally, the hotter the combustion process is, the less CO_2 and smoke emissions are, but the NO_x levels are increased. However, reducing the temperature in the combustion process by changing the AFRs[1] introduces aeroacoustic instabilities in form of rumbling noise.

1.3 Research Objective

The main aim of this project is to develop novel processing techniques to study how the combustion noise propagates from the combustion chamber of the jet engine through the nozzle into the far field in order to try to reduce jet engine noise and produce less annoyance to the population, but also to meet environmental regulations such as ACARE 2020 [12]. It is formed by specific objectives which are:

- extract the contribution of combustion noise from other sources
- process and appraise noise measurement data and attempt to extract combustion noise from it
- appraise existing combustion noise separation techniques
- develop novel methods for processing in-duct measured data to distinguish the contribution of different combustion noise sources to far-field noise data
- make informed recommendations for future studies

[1] Air to Fuel Ratio

1.4 Original Contribution

The main original contributions of this thesis are listed below:

1. This project provides to Rolls-Royce (which provides 100% of the funding) a new processing technique for a better knowledge of combustion noise which will help to implement the combustion strategy plan.
2. It adds valuable recommendations for the next noise measurement campaigns because the processing is directly related to how the data is acquired.
3. An extensive overview of combustion noise processing techniques in the literature is reviewed.
4. A novel method for the extraction of combustion noise is presented, validated with simulations, and applied to actual measured data.
5. A cross-comparison between different processing techniques for the identification of indirect combustion noise was accomplished.
6. An approach of the modal behaviour of the combustion chamber has been appraised.
7. A better understanding of the generated noise in the combustion chamber which reaches the far field is provided.

Parts of this work have been published (or internally published) as:

- P. Rodríguez García and K. R. Holland, "Exploring and developing processing techniques for the extraction of aircraft combustion noise," *20th International Congress in Sound and Vibration*, 2013.
- K. R. Holland, P. Rodríguez García, and B. J. Tester, "ISVR Combustion Noise Instrumentation Requirements" *Rolls-Royce internal contract report*, 2013.
- P. Rodríguez García, K. R. Holland, and B. J. Tester, "Extraction of Turbofan Combustion Noise Spectra Using a combined Coherence-Beamforming Technique," *Rolls-Royce internal contract report CR 13/05*, 2014.
- P. Rodríguez García, K. R. Holland, and B. J. Tester, "Extraction of Turbofan Combustion Noise Spectra Using a combined Coherence-Beamforming Technique," *20th AIAA/CEAS Aeroacoustics Conference Atlanta, GA.*, 2014.

1.5 Project Plan

The initial 12 months of the project were mainly spent performing experiments. They were characterised by two big measurement campaigns in Rolls-Royce UK and Germany. Moreover, data was extracted, and a first appraisal was calculated. Current combustion noise extraction techniques were analysed and applied. Furthermore, a literature review of combustion noise was carried out.

- A large-scale noise measurement campaign of the Trent 1000 was carried out at Rolls-Royce Derby. Besides, another large-scale noise measurement campaign of a BR700 type engine was carried out at Rolls-Royce Dahlewitz in Germany. They were preceded by the set up and preparation of all the equipment and special design of new rigs. Data was acquired in the combustor chamber and different positions in the engine in order that combustion noise can be extracted and analysed. The rig used for the measurements are explained in Chapter 8 and Appendix A.
- The combustion noise extraction technique proposed by Harper-Bourne [13] was replicated using data from ANTLE measurements at INTA in 2005 in order to be compared and as a first approximation of a combustion noise extraction technique. It is shown in Section 7.3.1.
- The author was inducted and familiarised with the LMS software X-Cada and TestLab by Christopher Knighton at Rolls-Royce Derby. Data from the measurement campaigns were transferred and most of the data has been pre-processed. Knowledge in the use of this system is very useful for future work together in the near future. A short user guide is presented in Appendix D.

The second part of the project (months 12^{th} to 24^{th}) was based in the study of the in-duct propagation and cross-comparison of known combustion noise extraction techniques presented in the literature (and the comparison between their conclusions).

- Study of the correlations between data from different azimuthal positions in the combustion chamber was carried out and explained.
- Modal behaviour of the combustion chamber was appraised.
- Pre-Filtering techniques proposed by Miles from NASA [14–19] were applied to ANTLE data in order to cross compare pre-filtered correlation techniques and the conclusions. A delay extraction technique using the phase of the cross spectra was

introduced (in order to avoid the use of filters), and published in the 20^{th} ICSV[2] [20]

In the third part of the project (months 25^{th} to 30^{th}) the new processing technique for the extraction of combustion noise was developed and defined.

- A new technique to extract combustion noise was presented. It has been developed using a multiple coherence technique with data acquired in the in-duct and far-field of the jet engine. In-duct sensors are located in the combustion chamber and in the nozzle of the engine, and far-field data is acquired using an external array of microphones. A beamformed signal focused in the nozzle of the engine is generated with the data from the array. Jet noise and influences of the room in the far-field are rejected using this focusing technique, which is being denominated Focused Beamformed Output (FBO). Results show that using a three signal coherence technique with two of the in-duct sensors and the focused beamformed signal provides a better estimator of combustion noise than the traditional three signal coherence techniques and the coherent output power spectra (COP), which are the coherence methods most commonly found in the literature for the extraction of combustion noise.
- The 3S-Array technique was published in the 20^{th} AIAA/CEAS Aeroacoustics Conference [21].

The last part of the project (months 31^{th} to 36^{th}) were reserved for the realisation of improvements in the technique, and a more exhaustive explanation of its benefits and limitations.

1.6 Thesis Organisation

The main subject of the project is introduced in this first chapter. Moreover, brief descriptions of each chapter are enumerated, a summary of main tasks of the project, and novel contributions are also presented.

An extended literature review is presented in Chapter 2. Combustion noise problem is defined and its characteristics are enumerated. Different techniques used to separate

[2]International Congress in Sound and Vibration

combustion noise are presented. Processing done by RRUK and NASA from different measurement campaigns were presented and compared.

In Chapter 3 a study of the propagation between the combustion chamber, the nozzle, and microphones in the external field has been introduced and explained by the use of cross correlations and phase studies between the data acquired in the different parts of the in-duct of the ANTLE engine. Different processing techniques from the literature are cross-compared. The delay between the different acquisition points is calculated by the use of cross correlations for different frequency ranges, and also by the study of the phase response of the cross spectra between the studied points.

In Chapter 4 a modal behaviour of the combustion chamber is presented and appraised. A physical and mathematical approximation of the calculation of the modes in an annular duct are presented. First cut-on modes of the combustion chamber of the ANTLE engine are estimated. They have been studied in comparison with the phase response of the cross spectra between the data acquired in different positions of the combustion chamber, the nozzle, and the far field of the ANTLE engine.

In Chapter 5 a novel method for the extraction of combustion noise called "3S-Array" is presented and explained.

The validation of the 3S-Array technique is presented in Chapter 6 with simulations of the combustion noise estimator and description of the source image calculation. A study of the bias and random error in the coherence calculation is also carried out.

The application of the 3S-Array technique is shown in Chapter 7 and Chapter 8 using data from the ANTLE and BR700 engines respectively. Both Chapters start with the description of the test set-up and the instrumentation used, followed by the data appraisal in time and frequency domain, and the source image. The combustion noise estimators are shown and compared at one power speed.

Finally, the summary of key results are enumerated in Chapter 9 and the conclusions and recommended work in Chapter 10.

The applications of the 3S-Array in the Rolls-Royce T1000 data are presented in Appendix A, the description of the response of the external arrays in Appendix B, and extended results of Chapter 7 and Chapter 8 are shown in Appendix C. The process to extract the acquired data from the Sony tapes is explained in Appendix D, and extended results of the phase study in Chapter 4 are shown in Appendix E.

Chapter 2

Literature Review

A literature review of the study of combustion noise is presented in this Chapter. The problem of combustion noise is introduced and research studies about combustion noise are presented. Early definitions of the combustion process are enumerated and acquisition methods for the analysis of combustion noise are catalogued depending of the type of measurement.

2.1 Introduction

The noise generated in the combustion chamber started many investigations with a common objective: to extract and quantify the noise produced by the combustion process. The first combustion process created by the humans was the creation of fire, but its main study appeared in the 20^{th} century with the transportation combustion engines. Before going into detail on various combustion noise extraction techniques, it is worth summarasing the study of the combustion process over time to explain its complicated nature.

2.2 What is combustion?

The combustion noise problem involves the study of acoustics, turbulence, and various combustion phenomena, composed of non-trivial chemical and physical processes. Analytical models exist for simple laminar flame combustion situations. This is the starting point for a mathematical representation of combustion noise. The combustion noise problematic is relatively new, compared to duct or jet noise, for example. It has

certainly become more prominent with the appearance of turbo-propulsion systems. A list of the most important scientific combustion terms and definitions were defined by the AGARD[1] as a result of the first combustion meetings in the early 1950s [22, 23].

2.2.1 Early definitions of combustion

The early research on combustion noise was based on the study of the open flame [24] and the effects of the pressure on the fundamental parameters of the flames: the burning velocity, the spectra, and the temperature. Two types of gaseous flames are defined in the literature: premixed flames and non-premixed flames, which are also called diffusion flames [25, 26]. In the first case, the fuel and oxidizer are premixed before entering the reaction zone. In the second case, the reactants are mixed at the same time as the combustion, like in a candle.

These studies were fundamental first for the development of the rocket motor, and then for more complex combustion systems later, using higher pressures and performance propellants. The need for a flame propagation thermal mechanism was ended when it was discovered that the premixed flame burning velocity changed with the pressure and the fuel used [23].

Flame-spreading characteristics in combustion were described by Maccallum in 1957 [27]. Flame spreading is important for developing high-intensity combustion systems for aircraft applications. When a fuel is mixed with an oxidizer, its flame must be stabilised. The flame can be stabilised with the use of a bluff body, a can, or independent pilots such as the system shown in Figure 2.1 [28, 29]. There are different flame-spreadings for different types of flow (laminar flow, turbulent flow, etc.) each of which need to be stabilised. This can be achieved by controlling the relationship between local flow and burning velocity. Some examples of bluff bodies are rods, gutters and discs [22]. The study of stabilisation with bluff bodies was followed by a study of flame stabilisation in cans and the effects of flame spreaders in overall combustion efficiency.

Macallum concluded that the combustion extinguishes depending on the characteristics of the spreader and especially on the ratio of the mix. Several different studies and theory about the stabilisation of the flame for different flows are found in the literature, which explains the difficulty in defining the theoretical behaviour of the combustion process.

[1] **A**dvisory **G**roup for **A**eronautical **R**esearch and **D**evelopment

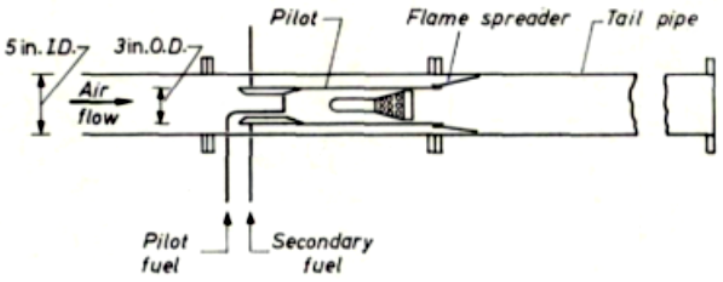

FIGURE 2.1: Early combustion system with flame spreaders (from [27])

2.2.1.1 Theoretical studies

In 1980, O'Brien [30] presented an approach to define enclosed turbulent flames using probability density functions. This was later improved by Pope in 1985 [31, 32] for more cases. Other approaches were presented to reduce the computational cost of the solution of turbulent flames, such as the flamelet theories by Williams [33, 34] and by Peters [35].

Strahle [36] surmised the theoretical studies of the combustion process only provide minor help to the understanding of combustion noise. The theory cannot fully explain exact scaling rules, frequency content, or detailed directivity effects.

2.3 Combustion noise data acquistion methods

2.3.1 Single far field measurement

One of the first and simplest methods to identify core noise from other turbofan noise is to acquire data with a single transducer in the far field of the engine and then to separate the different noise sources from frequencies within the spectrum [37]. Tonal noises produced by rotational parts of the engine, such as the fan and the compressor, can be separated in the spectra from the core noise and from the jet noise. Some jet noise behaviour can be predicted by models [38, 39] and the eighth power law, the remaining part of the spectrum could then be attributed to internal sources. This technique is approximate and does not provide a complete view of each noise source. It simply provides an overview of the noise propagated to the far field from the whole turbofan.

2.3.2 Multiple far field measurement

A multiple set of transducers can be installed in the far field of a jet engine to improve the quality of the acquired data by using spatial filtering operations, known as beamforming [40]. The idea of using a phased microphone array was first conceived in the 1970's [41, 42], based on a military antenna source location technique, and was adapted to aeroacoustics and many other fields [43, 44].

Fisher et al. introduced, in 1977, a "polar correlation" source location method [38, 45] for the study of turbofan noise. This uses a polar arc array of far field microphones centred on the jet nozzle, which was further developed by Tester and Fisher [39]. Tester introduced the AFINDS source breakdown technique [46, 47], capable of separating core noise from the other noise sources of the engine using models of the sources.

Also, in 1980, Parthasarathy et al. presented a technique to separate core noise and jet noise from the external field [48] and, recently, Funke introduced a new source distribution technique called SODIX which also uses data acquired only from an external array [49] to separate the different turbofan noise sources.

Core noise results from AFINDS calculations are compared with those from the method presented in this thesis. AFINDS (from "AARC-Funded ISVR Non-linear least squares Directional Source") is capable of separating the contribution of each source to the far field by using known models of the sources and their approximate positions. It is based on a phased array method that uses non-linear least squares analysis, and it requires a model of far-field cross-spectral matrix for each source type that is going to extract. Each of those models has a few parameters, such as relative intensity of the source, axial origin, directivity characteristics, etc. where the position of the source is one of the key parameters, learnt by experience. The non-linear least squares process (for example the Matlab function 'nlinfit') converges to the global minimum in a few iterations from the relatively small number of unknowns.

Beamforming techniques provide an approximate source strength at a focussed point. The lowest frequency resolution depends on the size of the array while the highest frequency that can be measured without aliasing depends on the separation between the microphones. Beamforming techniques can also be limited by the wave propagation model used.

Holland [50] used a wall-mounted spiral array to determine the sound power output of the ANTLE engine and in addition, he used the same array as a scanning focused

beamformer to obtain diagnostic information about source location at different parts of the engine.

The post-processing beamforming algorithms however can improve the signal to noise ratio between the desired signal and the unwanted signals away from the focal point. Various methods exist, including: Conventional beamforming[2] (which maximizes the energy of the source by adjusting the propagation time from the source to the microphones of the array), or conventional deconvolution methods such as DAMAS [51, 52] or NNLS [53]. Deconvolution methods use an iterative algorithm to recover the position and the strength of acoustic sources, they can increase the dynamic range but they can also introduce misleading spots instead of continuous distributions, and in addition, they require a heavy computational effort. The novel iterative sidelobe cancellation process ISCA [54] is also a deconvolution method that combines a localization algorithm with an iterative approach to enhance the dynamic range of the beamformer output.

Other beamforming procedures such as time-reversal [55, 56] (which uses propagation equations to reconstruct the sound field), or functional beamforming [57, 58] (that uses the mathematics of functions of matrix applied after conventional beamforming in the frequency domain) are also computationally expensive.

The conventional beamforming method was used in this thesis because it is a very fast and robust method. In addition, it can be used in the time domain, which is a fundamental point of the technique presented by the author.

2.3.3 Combination of in-duct and far field measurements

Pressure transducers can be installed inside the duct of the jet engine in different positions like the combustion chamber or the nozzle, for example. Intuitively, the best way to know how much combustion noise propagates from the combustion chamber to the external field is by acquiring as much information as possible along the propagation path.

Siller (DLR), Arnold (RRD), and Michel (DLR) used a beamformed signal focused on the nozzle to calculate the coherence with a transducer installed inside the combustion chamber of a Rolls-Royce BR700 engine [59], at the Hucknall site of Rolls-Royce within the European funded research project RESOUND (done simultaneously with the RANNTAC liner test). They showed that internal noise formed in the combustion chamber

[2] in the Frequency domain: CBF, also called Delay And Sum: DAS

can be detected at the nozzle of the engine. Harper-Bourne [13] carried out a combustion noise study of the ANTLE engine by using a similar two signal coherence technique between data acquired by an in-duct sensor and one external microphone.

Krejsa [4, 60, 61] presented a far field combustion noise estimator using a three signal coherence technique which agrees with the three signal coherence technique for flow noise rejection presented previously by Chung [62, 63]. This technique requires three output measurements for the identification of a single unmeasured source. It is explained in detail in Section 5.4.

These types of measurements are the basis of the novel method presented in this thesis, which applies the three signal coherence technique to the data acquired by two in-duct sensors and a focused beamformed signal from an external array of microphones as the third. It enhances the benefit of using the three signal coherence technique by including an array of microphones in the external field of the engine. This technique, called here the "3S-Array" technique, improves on the noise rejection of unwanted sources in the external field by replacing the single external signal with the focused signal from all the microphones in the array, termed here the Focused Beamformed Output (FBO). The FBO in combination with the data acquired in the combustion chamber and the nozzle of the engine provides a more reliable combustion noise estimator.

The 3S-Array is based in a combination of the 3-signal (3-S) coherence procedure presented by Chung [63] and Krejsa [60], and the time shift focusing beamforming approached by Siller and Michel [59], who studied the core noise of an aero-engine with the aid of a phased line array of microphones. Siller and Michel applied the COP method using the beamformed output of an external line array and a signal from a single in-duct sensor. The 3S-Array Technique combines the benefits of the 3-signal coherence versus the COP, and the use of a beamformed signal in the external field, where unwanted sources can contaminate data acquired by a single sensor.

The benefits of using the new 3S-Array method versus the three signal coherence technique alone, or the two signal technique, are explained in Chapter 5, where these methods are compared.

2.3.3.1 Time domain analysis

In the 1970's, Matthews [64], Burdsall [65], and Karchmer [66] started to carry out studies of the time domain correlation between turbofan internal and external pressure measurements. They proved that some of the far field acoustic energy is generated in

the core of the engine, however, despite the fact that the cross correlation results only prove a linear relation between the pressure measured within the core and the far field of the engine, it was shown that the correlation peak provides an estimate of the acoustic propagation time [3]. The delay obtained by the cross correlation of, for example, two in-duct pressure measurements would indicate the direction of the propagation.

In 2006, Miles used data from a Pratt and Whitney PW4098 engine to improve the three signal coherence technique by correcting the time delay between the combustor and the far field pressure signals, and, therefore, maximising their coherence [14–16]. He also studied the propagation time between pressure measurements at different positions to estimate direct and indirect combustion noise spectra [17, 19]. His conclusions were contrary to the ones of Harper-Bourne in [13], as explained in Section 2.4.

2.3.3.2 Frequency domain analysis

Generally, noise estimators are given in the frequency domain. Spectral density functions provide a power distribution in the frequency domain, which can be calculated by applying Finite Fourier Transforms to the time domain acquired data [67–70]. The auto-power and cross-power spectral density functions are needed to obtain the transfer function between two pressure measurements [3].

In 1976, Karchmer and Reshotko [66] calculated the transfer function between the nozzle and the far field pressure data, and between the combustion chamber and the far field pressure data after correcting the propagation time delay obtained from the cross correlations. They found a non frequency-dependant delay (linear propagation) from the amplitude and phase results between the nozzle and the far field pressure data. On the other hand, the transfer function between the combustor and far field measured pressures showed a phase shift in the frequency region of interest as well as a variation in amplitude proportional to the square of the frequency. This suggested that turbulent hot spots acted as noise sources, and served to be one of the first indirect combustion noise references [71].

Hultgren [72], in 2011, carried out an extension of the previous work of Miles and Hultgren [18] attempting to determine the turbine transfer of combustion noise of a Honeywell TECH977 turbofan engine. He concluded that selecting the correct turbine-attenuation function improves both combustion and total noise predictions. “The indirect noise occurs over the same basic frequency range as the direct noise, but their spectral-distribution shapes could be quite different” [72].

In 2008, Mendoza [73] analysed data from the same engine using a three signal far field method and processing technique from Hsu and Ahuja [74], which uses only data from external microphones. His method, however, did not work well for frequencies for which internal sources had a similar amplitude.

2.3.3.3 Extensions of the three signal technique and modal techniques

The three signal (3-S) technique is useful when a noise-free source signal can't be measured, and when the unwanted noises at each measurement point are uncorrelated between them. Minami and Ahuja [75] argued the possible errors of the 3-S when two sources are measured in addition to noise instead of only one source. They used a five-microphone method from Hsu and Ahuja [74] that is able to separate two different correlated noise sources contaminated by extraneous noise from far field measurements.

The method from Hsu and Ahuja [74], called 5-S CSA here, is a five microphone conditional spectral analysis technique that combines the COP and the 3-S with Conditional Spectral Analysis (CSA). It is applicable when one of the two existing sources, which are correlated, is obtainable, to determine both sources and the unwanted noise. A measure of one of the two sources and three output measurements are needed for this technique.

The 5-S CSA first uses the COP to separate the signal that is correlated with the source, to obtain the contribution of the part that can be measured. Secondly, it uses the 3-S to remove the unwanted noise. It would need four measurements instead of five if a clean version of the source can be obtained (which is normally not the case), if not, two measurements are needed at the source position. In addition, two noise sources are allowed to contribute at a measurement point to the overall noise by the 5-S CSA technique, even if they are correlated with three of the five-output measurements [76–79].

The 5-S CSA technique was not applied in this thesis because it doesn't fit with the studied scenarios. It needs two correlated sources, which is not always possible when measuring at different locations in a combustion chamber (as explained in Section 3.1.1, data acquired by the probes installed in the inner case of the combustion chamber can't be treated as the same acoustic event, and then, it can't be analysed with same statistical processes) or there are simply not enough inputs to apply it in the collected data. The 5-S CSA technique would work with 4 measurements if one pure-clean measure of one of the sources is known, which is not true for the studied cases in this thesis either.

Bennett [80] presented an implementation to calculate the complex modal amplitude of an acoustic mode of interest based on methods of Yardley [81] and Åbom [82]. Davis and

Bennett used that implementation to present a novel CSA-modal technique [77, 79, 83] that enhances the 5-S (5-S modal). They replaced one of the microphone measurement outputs with one of the calculated acoustic modes of interest. They also applied this modal technique to improve the 3-S method[77] (called here 3-S modal) which permits the isolation and removal of unwanted noise. The benefit of this technique is that the contribution of each source at different mode orders, in an axial position, and over a desired frequency range, can be known.

Those techniques are not applied in this thesis because this level of modal decomposition needs data from a set of sensor rings that were not available.

Examples of the applications of the 3-S, 5-S CSA, 3-S modal, 5-S modal, and modal decomposition techniques can be found from Davis and Bennett [77, 79, 83, 84], Pardowitz et Al. [78], and Blacodon and Lewy [85] under the EU-FP7 European project TEENI (Turboshaft Engine Exhaust Noise Identification).

Other good examples of coherence based techniques' comparisons in the literature can be found from Hultgren [86], where he compares Combustor-Noise models. The summary of coherence based techniques by Bennett and Fitzpatrick [76], where they did a comparison of the COP, 3-S, and CSA techniques, and their performance was examined experimentally with an acoustics set-up of three loudspeakers and four microphones. And the investigation of classic and novel coherence basic techniques by Davis and Bennett [79].

2.4 Study of direct and indirect combustion noise

Different kinds of combustion noise were classified by Strahle [36, 87] depending on their source. He proposed that noise can be produced by at least three different combustion mechanisms.

Firstly, direct combustion noise was defined as the turbulence interacting with the reactions. Secondly, indirect combustion noise was caused by an alteration of flow velocity caused in the combustor. Thirdly, the concept of entropy noise was introduced as an example of indirect noise. It was defined as the creation of noise by the convection of hot spots generated in the combustion process.

In recent studies, indirect noise is generally considered to be entirely entropy noise, or entropy fluctuations converted to noise at the turbine stage [15, 17].

There are other factors that further complicate the system. For example, in a ducted design, wall reflections can alter direct combustion noise [88]. Entropy inhomogeneities in nozzles also generate indirect combustion noise, as described by Ffowcs Williams, and by Marble and Candel [89, 90]. But there has been much discussion about how much indirect combustion noise affects overall combustion noise. Recent studies by Leyko [91] show the need to study indirect noise generation further. He showed that indirect combustion noise is a relevant source in combustion noise, but that it depends on the operation conditions of the engine, the geometry of the combustion chamber, and the frequency range.

The group of Engine Acoustics at the DLR lead by Prof Lars Enghardt set-up a dedicated test facility to generate entropy waves in a controlled way which they called Entropy Wave Generator (EWG). The entropy waves were electrically generated and accelerated through a convergent divergent nozzle. Experimental results from Bake, Kings, and Röhle [92] agreed well with numerical simulations described by Mühlbauer et al. [93] and with theoretical predictions from Marble and Candle [90].

Bake et al. expanded the studies at the EWG with more experimental results but also with CFD simulations and CAA analysis, using clearer definitions of flow and boundary conditions [94]. They concluded in the importance of the reflections from up and downstream components, that are mixed with the direct and indirect noise. They also identify strong indirect sources at the throat of the nozzle using source location methods, which their source strength increases with Mach number, and the indirect sources were found larger than the direct ones due to the heating.

This thesis is concerned with the processing of combustion noise data from a number of whole-engine and rig tests and involves the development of novel signal processing and analysis techniques. In short, signals are acquired from three measurement positions : 1) in the combustion chamber of the engine, 2) in the hot nozzle, and 3) in the near field away from the engine. Combustion noise can then be extracted by studying the relationship between the signals acquired in the combustion chamber, those in the other positions of the engine and in the near field by the application of autocorrelation and coherence techniques. There are few full-scale measurement campaigns in the literature, where a study attempts to subtract direct and indirect noise from overall combustion noise.

Two recent studies were used as principal reference for this thesis: 1) the study of the ANTLE engine, by Harper-Bourne, using a two signal coherence technique and 2) the study of the Honeywell TECH977 research engine, principally by Miles and Hultgren,

who used a three signal coherence technique. In the former study, Harper-Bourne concluded that direct combustion noise is present up to 100 Hz while indirect combustion noise is dominant at higher frequencies. However, Hultgren and Miles [18] concluded that direct combustion noise is situated between 200 Hz and 400 Hz and that indirect combustion noise is situated below 200 Hz, with a peak around 100 Hz [15].

2.4.1 M. Harper-Bourne: 2008

Harper-Bourne [13] presented an Impulse Response method assuming that the combustion noise, which radiates to the external microphones, is linearly-related to and spatially coherent with that in the nozzle. Combustion components are extracted by calculating the acoustic coherence between the probes and the microphones. The spectrum of the radiated combustion noise can then be determined from Equation 2.1, where $\gamma^2_{xy}(\omega)$ is the coherence between the signals from a jet-pipe probe and a microphone and where $G_{yy}(\omega)$ is the autopower spectra of the sound received at one microphone,

$$G_{comb}(\omega) = \gamma^2_{xy}(\omega) G_{yy}(\omega) \tag{2.1}$$

Cross correlations between the signals from the external microphones and the probes in the combustion chamber and the jet-pipe were calculated. Broadband characteristics were found within the cross correlations between the signals from the probes in the jet-pipe and the microphones but not from the probes in the combustion chamber.

Equation 2.1 was applied to the signal from the probes in the combustion chamber using the assumption that direct combustion noise could be extracted from the signal acquired directly in the combustor. Equation 2.1 was then applied to the signal from the probes in the nozzle assuming that the combination of both direct and indirect combustion noise could be extracted from the data. Thus, direct and indirect combustion noise could then be extracted from their comparison.

Harper-Bourne concluded that direct combustion noise was dominant at low frequencies below 100 Hz. Indirect, or entropy noise, was found at higher frequencies, with the peak at 200 Hz.

It has not been proven that a coherence comparison between the combustion chamber and the nozzle can be used, especially since the transducers in the combustion chamber are very different from the transducers used in the nozzle. In the author's opinion, probes installed in the combustion chamber may be affected by a proximity effect due to the

fact that they are in an enclosure. They would, therefore, also acquire evanescent waves (or near-field standing waves). Thus, there would be a bias error difference between 1) the coherence results from the signals acquired by the external microphones and the nozzle probes, and 2) the coherence using the signals from the microphones and the probes in the combustion chamber, especially at low frequencies. While this bias error is not removed by the two signal coherence technique, used by Harper-Bourne, it is by the three signal coherence technique, which will be discussed in the next section.

2.4.2 H. Miles: 2006-2010

Miles [15] presented a contrary set of conclusions. He defined a source location technique [14] based on adjusting the time delay between the combustor pressure sensor signal and the near field microphone signal to maximize the coherence and remove as much variation of the phase angle with frequency as possible. He found that the noise in the 200-400 Hz frequency band is related to direct noise while the noise below 100 Hz is related to coherent indirect combustion noise from "hot spots" travelling (slower) at the flow velocity through the turbine.

He described a diagnostic technique based on the three-signal technique by Krejsa and Chung that uses an adjustable time delay to try to maximize that coherence. A three-signal method (called here 3-S technique) with a new additional "phase-angle-based discriminator" was then introduced [16, 18, 19].

Miles' conclusions are based on the assumption that indirect combustion noise propagates at the local flow velocity, while direct combustion noise propagates faster at the speed of sound. He found that the 0-200 Hz band signal took more time to travel the same distance as the 200-400 Hz band.

Time delays were found using cross correlation functions. He compared cross correlation functions between filtered and unfiltered signals acquired in the combustion chamber with the external microphone signals. It was concluded that using a low-pass filter at frequencies below 400 Hz eliminated direct combustion noise signals. The delay calculated from the cross correlations becamed bigger when the cut-off frequency of the filter was reduced. This was because, in his opinion, the unfiltered data includes the indirect combustion noise signal, which travels more slowly due to the entropy velocity in the combustion chamber. Entropy noise becomes acoustic, and starts travelling at the speed of sound, when it reaches the turbine blades and vorticity waves are generated [95].

Coherence analysis can be adversely affected in a multiple source measurement if there is a delay between separated signals recorded at the same time but if the delay is long compared with the duration of the acquisition [69]. A time-delay bias error can occur if there is a physical propagation between the recorded signals. Coherence can also be reduced if calculated using FFT operations, which are based on averaging small data samples. This error, however, can be avoided by introducing a pre-computational delay.

It has to be noted that all of these techniques make the assumption of a one dimensional acoustic wave propagation. This may be valid at low frequencies but will less valid at higher frequencies due to complicated geometry. This assumption needs to be investigated further.

In the author's opinion, the analysis presented by Hultgren and Miles cannot be directly compared with Harper-Bourne's. Results from both analyses are based on single experiments with different engines and different testing conditions. Comparisons cannot be made unless both methods are applied to the same data from the same engine. This comparison was published by the author [20] and is detailed in Chapter 3, where both techniques are applied to the same data from the ANTLE engine test campaign.

2.5 Summary

In this chapter, investigations into the study of the combustion noise generated by a turbofan have been introduced, from which it is clear the need to develop novel processing techniques to separate combustion noise from other jet engine sources. An extended literature review was presented including references to existing combustion noise studies and the definition of direct and indirect combustion noise concepts.

The techniques presented serve as a basis for the novel "3S-Array" processing technique for the extraction of combustion noise, which will be presented in this thesis.

Two main techniques can be classified in terms of the number of sensors used. A two-signal technique uses data acquired in two positions either in the combustion chamber and the external field, or in the nozzle and the external field. The processing applied in this case is known as Coherence Output Power (COP) spectrum. A three-signal technique, called here "3-S", uses data acquired in the combustion chamber, the nozzle, and the external field.

The main difference between the COP and the 3-S techniques is the validity of their assumptions. The former is sensitive to unwanted sources, which can contaminate the required combustion noise signal.

Many tests of full-scale aircraft engines are also carried out indoors in order to reduce costs. This introduces room-environmental noise into the external field measurement, such as reflections and reverberation, which degrade both the COP and 3-S estimators.

Chapter 3

Study of in-duct propagation as an approach to indirect combustion noise

In this chapter, the sound propagation delay between the positions where in-duct probes are installed within a jet engine is estimated using various techniques, and a cross comparison between previous studies is carried out. A pre-filtering technique utilised by Miles is applied to the acquired data from the ANTLE engine which was studied by Harper-Bourne in order to cross compare their results and conclusions about indirect combustion noise. Moreover, the delay between the installed probes is estimated by cross correlating the acquired data at different positions. A study in the frequency domain of the phase response of the cross spectra between that data shows a possible modal behaviour, which is analysed in the next chapter.

The instrumentation of the ANTLE engine experiment is shown in Figure 3.1. Four rumble probes were installed in the combustion chamber (RP1, RP2, RP3 and RP4), two further probes in the hot-nozzle (RPA and RPB), and six microphones in the near field of the engine (M1 to M6). The rumble probes are dynamic pressure transducers with high specifications. The ones used in this test are from the CP models of Vibro-Meter, providing a flat response up to 10 kHz with an extreme high temperature capability (up to 780C) however, the dependence of the sensitivity at high temperatures is only provided at 120 Hz.

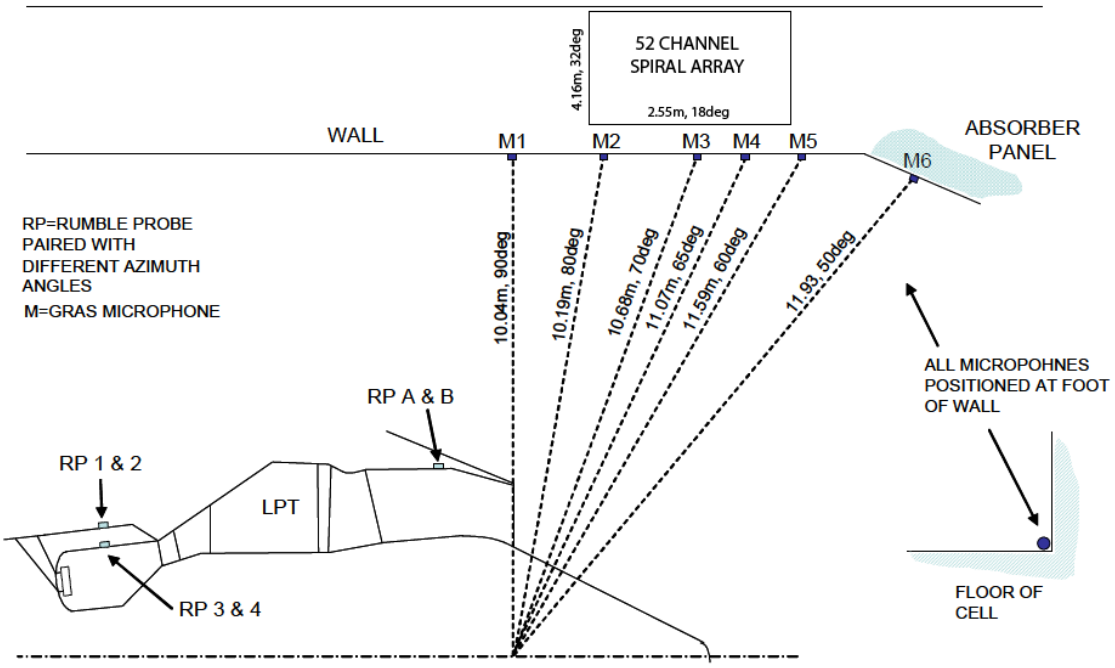

FIGURE 3.1: ANTLE instrumentation layout updated from [13]. The spiral array is placed in the wall at 7.2 m from the axis of the engine

3.1 Delay Estimation

A study of the propagation between the data acquired in the different positions of an aircraft engine during the measurement rigs is presented in this section. Data acquired using the different located probes is analysed and compared between them in order to calculate the time that it takes for the produced signal to propagate from where the probes are installed (from the combustion chamber to the nozzle and to far field).

The estimated physical delay between probes is compared with the real distance between them in order to get more information about the in-duct propagation.

3.1.1 Use of Cross Correlation

As it was explained in Chapter 2, the study of the cross correlation between two signals is useful to know how similar they are. It is an operation which can be calculated in the time domain or in a faster way by applying the Inverse Fourier Transform to the cross spectrum of those signals.

Firstly, a comparison of the distances between the probes and microphones is carried out in order to check that the delay is larger for further distances. The main aim behind the

calculation of these delays is to ascertain if there is any variation in the time propagation between different positions for different frequencies or after applying different processing techniques.

Correlations are calculated by applying the inverse FFT to the calculated cross spectra, which was obtained using 32 s of each signal, and by applying a windowing of 8192 samples with a frequency sample of 32768 Hz (quarter of a second). The number of averages utilised are 251. The correlations are represented normalised (with amplitude $\boldsymbol{R}$) following Equation 7.2.

From Figure 3.2 can be extracted the physical delays between the three measurement positions for the ANTLE engine: the combustion chamber, the nozzle, and the external microphones. The position of each probe is detailed in Figure 3.3, being RP1 and RP1 the probes installed in the outer case of the combustion chamber, RP3 and RP4 the probes installed in the inner case of the combustion chamber, and RPA and RPB the probes installed in the nozzle.

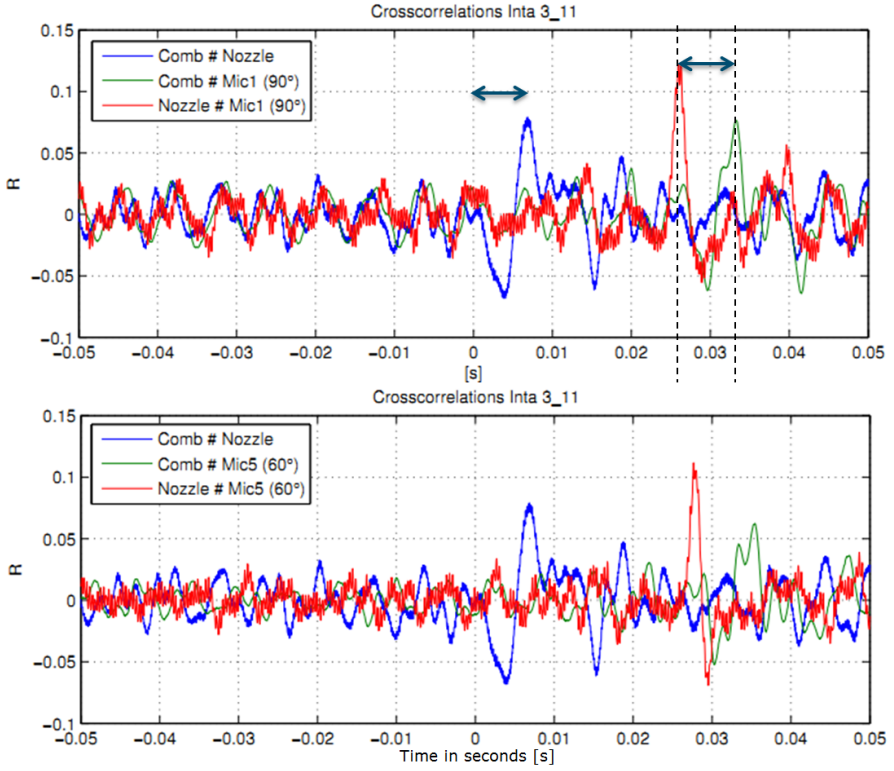

FIGURE 3.2: Cross Correlation for different Microphone Angles at a low power setting

In the upper side graph of Figure 3.2 are shown the cross correlations of the data acquired in the three measurement positions using the microphone situated at 90° of the nozzle. On the other hand, the microphone situated at 60° (further) is utilised for the lower side graph results.

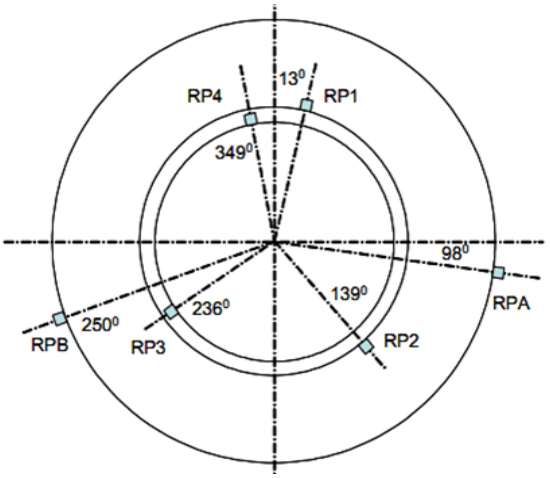

FIGURE 3.3: Position of the probes installed in the combustion chamber (RP1 to RP4) and the nozzle (RPA and RPB)

A delay of 7 ms can be extracted from the correlation of the data acquired in the combustion chamber and in the nozzle, which is represented by a blue line in the graphs. The green line represents the correlation between the data acquired in the combustion chamber and by the external microphone, and the red line represents the correlation between the data acquired in the nozzle and by the external microphone. Then, the delay between the 90° microphone and the nozzle (red line) is 26 ms. The delay between the combustion chamber and the external microphone (green line) is larger, as expected, and of 33 ms, which corresponds of the addition of the delay between the combustion chamber and the nozzle plus the delay between the nozzle and the external microphone.

Same conclusions were extracted from the correlations using the further microphone situated at 60° from the nozzle, but the only difference is that there is 1 ms more of delay than expected.

A comparison between internal probes is carried out in Figure 3.4 and Figure 3.5. In the first one, the correlations between the data acquired by the four probes in the combustion chamber and the data acquired in the nozzle are represented. From the graph, it can be extracted that there is any relation only between the data acquired in the nozzle and in the probes RP1 and RP2 installed in the outer case (lines blue and green respectively). This correlation may be done due to both probes being affected by the same spurious signal (which would be dominating the acquired signal), like an external tone. It also shows that there is not any clear relation between the data acquired in the inner case of the combustion chamber and in the nozzle.

There are tones which are affecting the results of the correlation between the signals.

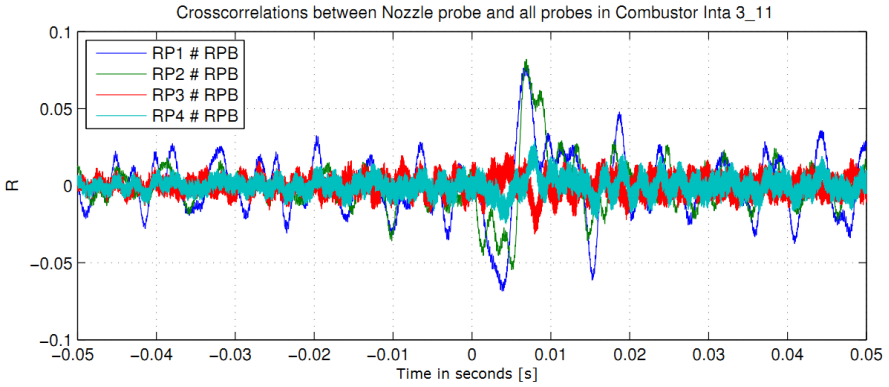

FIGURE 3.4: Cross correlations between data acquired by the Nozle probes and the ones in the Combustion Chamber

Then, if the signals are dominated by those BPF[1] tones, then the cross correlation between them will show the similarities between them but in terms of those undesired tones. It is therefore necessary to previously remove those tones prior to carry out the cross correlation calculations.

A further study of the data acquired in the combustion chamber is presented in Figure 3.5. The cross correlations between the data acquired by the probes installed in the inner case of the combustion chamber (probes RP3 and RP4) and in the outer case of the combustion chamber (probes RP1 and RP2) are represented.

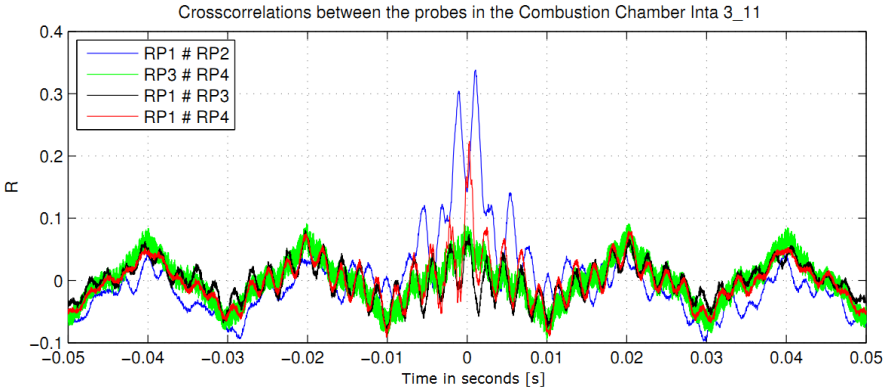

FIGURE 3.5: Cross xorrelations between data acquired by all the probes in the Combustion Chamber

It is shown that there is correlation between the data acquired by the probes in the outer case (blue line), but not between the data acquired by the internal probes. Furthermore, there is correlation between RP1 with RP4, but this is only because of their proximity.

This fact shows that the data acquired in the different positions of the inner case of the combustion chamber have no relation between them. This may be due to the combustion

[1]Blade Passing Frequency

process not being the same along all the combustion chamber. In the combustor, fuel is mixed with air and ignited, creating different acoustic events in different positions of the chamber. Accordingly, data acquired by the probes installed in the inner case of the combustion chamber can't be treated as the same acoustic event, and then, it can't be analysed with same statistical processes.

3.1.2 Application of pre-filtering

A study of how much time it takes a signal to travel from the combustion chamber to the far-field of a jet engine by applying frequency filtering and cross correlation techniques was carried out in comparison with the analysis presented in [14] by Miles.

That comparison was based on checking if the delay between the data acquired in the different positions of the jet engine becomes bigger when the signals are pre-filtered with different LPF[2] applying progressively lower cut off frequencies before cross correlating them. The main aim of this particular study is to check if it is possible that the signals propagate slower for a certain frequency band because they are propagated as entropy noise (indirect combustion noise).

This process involves studying the influence of filtering the data acquired in the combustion chamber and external microphones before calculate their cross correlation.

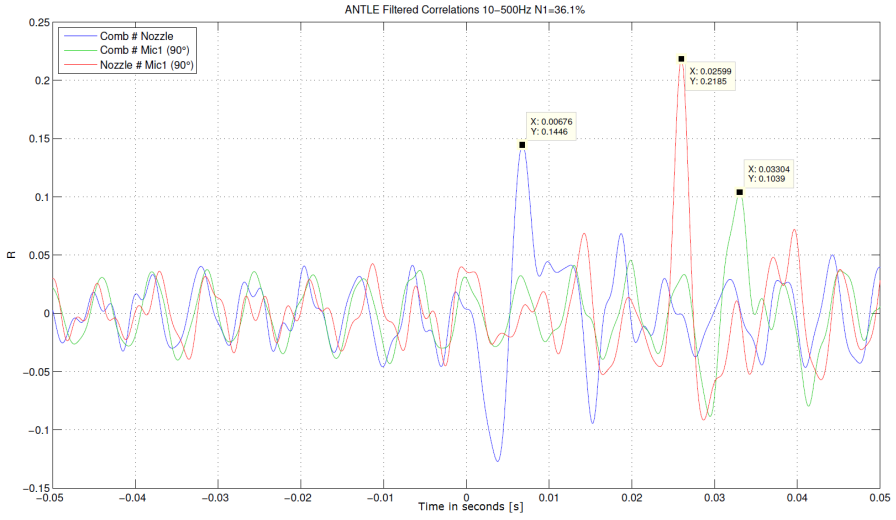

FIGURE 3.6: Filtered Cross Correlation for different Microphone Angles at a low power setting

Miles finally concluded in [15] that the 0 to 200 Hz band signal took more time than the 200 to 400 Hz band signal to travel the same distance. Then, it was concluded

[2]Low (frequencies) Pass Filters

that indirect combustion noise is situated in the frequency band between 0 and 200 Hz as it is explained in Chapter 7. He tried to minimise the phase angle variation of the cross spectrum with the frequency by applying a "source location technique based on adjusting the time delay between the combustor pressure sensor signal and the far-field microphone signal to maximize the coherence and remove as much variation of the phase angle with frequency".

The purpose of the present study is to cross-analyse those conclusions presented by Miles but utilising data acquired in a different experiment instead. Then, several things can be checked, such as the influence in the result of the following factors:

- Difference between experiments setup
- Difference between the position of the sensors
- Differences in the processing

The first cross-analysis presented was implemented by applying frequency filtering before calculating the cross correlation between the signals acquired in the combustion chamber and in an external microphone as a first appraisal.

The data employed was recorded at INTA during the ANTLE engine measurement campaign, funded by the EU and the SILENCE(R) programmes. The data utilised was acquired by the sensor which was installed in the outer ring of the combustion chamber (RP1), and by an external microphone which was situated at 10 m of the nozzle of the engine (MIC1). One big difference between both experiments is the distance of the external microphones in the measurements (10 m for ANTLE Vs 30 m for Miles)

The cross correlations between the data acquired in the external case of the combustion chamber (RP1) and the external microphone situated at 90° are represented in Figure 3.7. Low pass filters of different cut-off frequencies are applied to the data previous to the calculations.

The aim of this process is to prove if there is any difference in the downstream propagation from the combustion chamber between frequency bands.

It can be seen that only the cross correlation of the signals which are filtered with the cut-off at 100 Hz (red line in the graph) has a noticeable larger delay than the other cross correlations, for which the delays are quite similar to the un-filtered cross correlation. Moreover, a tonal presence at 150 Hz can be estimated from the sinusoidal response

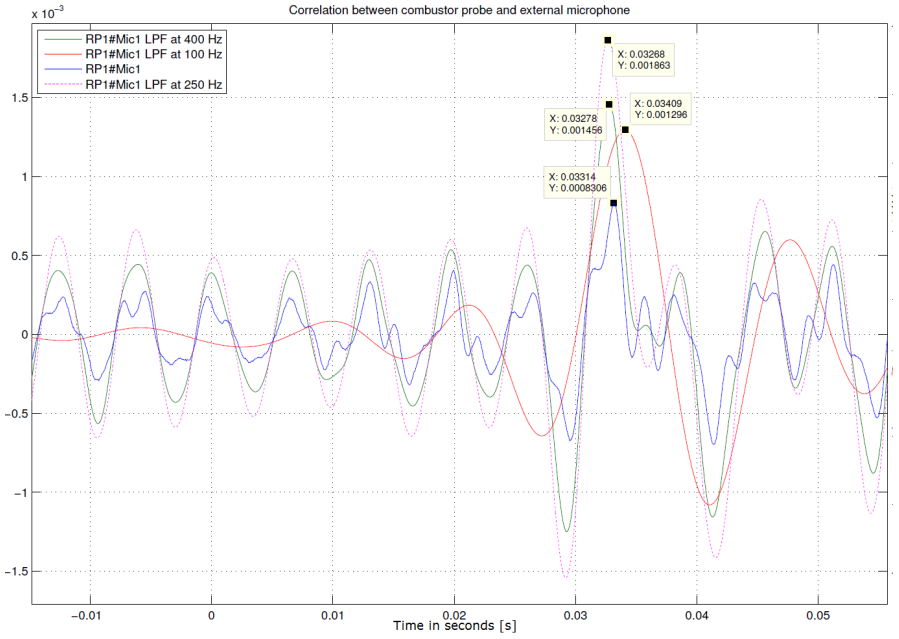

FIGURE 3.7: Filtered cross correlations between the combustion chamber and a external microphone

away from the main peaks of correlation. It has a periodicity of 6.6 ms approximately, which corresponds to a tone of 150 Hz, an harmonic of the mains power frequency.

A zoomed version of Figure 3.7 is presented in Figure 3.8 to show fine detail.

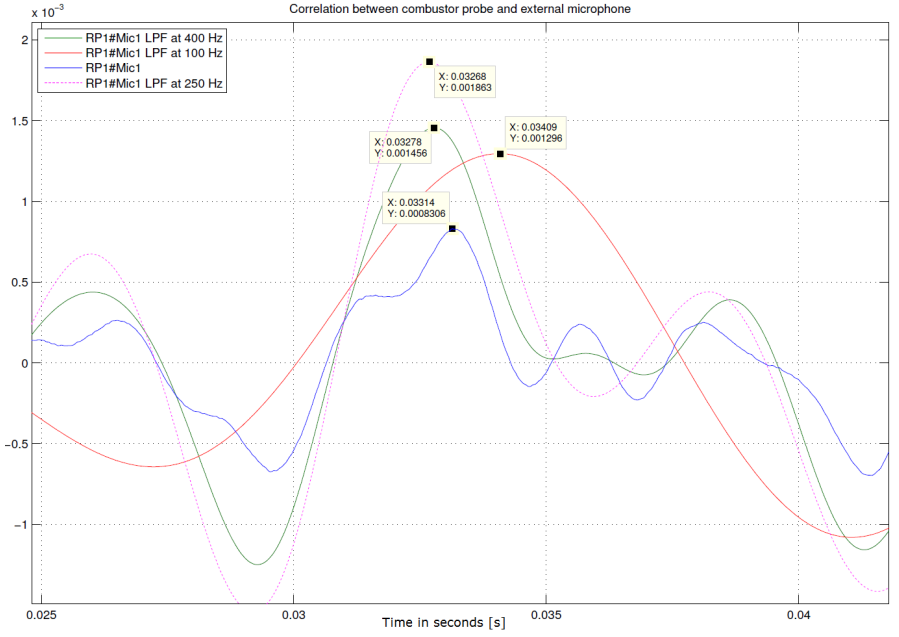

FIGURE 3.8: Zoomed Filtered Cross Correlations

Only a small delay close to 1 ms can be noticed from the cross correlation calculated with the data which was filtered with a cut-off of 100 Hz (represented by a red line in the graphs). For the other results, variations with respect to the non-filtered data cross correlation are almost not noticed.

In Table 3.1 are represented those estimated delays after applying the LPF and calculating the cross correlations.

Filtering	**Delay in ms**
No Filtering	33.14
LPF 100 Hz	34.09
LPF 250 Hz	32.62
LPF 400 Hz	32.78

TABLE 3.1: Estimated delays for different cut-off frequencies of the Low Pass Filters applied to the data before the calculation of the cross correlation to extract them

The filter used was a Butterworth with order 2 as the one shown in Figure 3.9

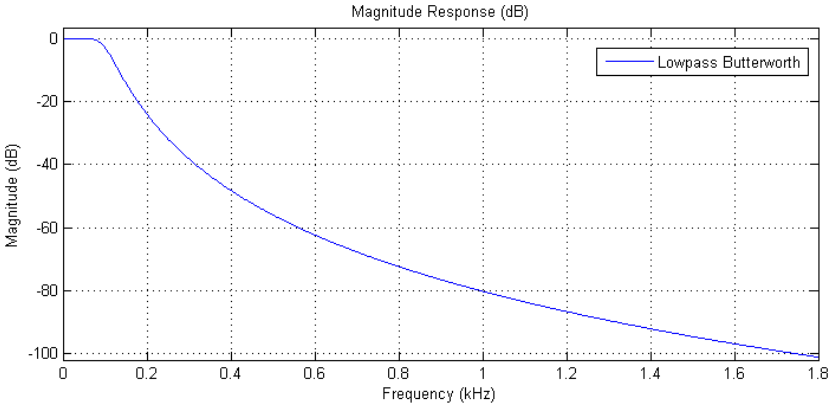

FIGURE 3.9: Butterworth lowpass filter at 100 Hz with order 2.

Results are clearly dominated by a tonal component. In the opinion of the author, the estimated delay it is too much dependent of the sinusoidal behaviour of the cross correlation, and that affects its value, inasmuch as it is extracted from its maximum. However, the presence of the peaks does indicate that there is some delay in the propagation at frequencies below 100 Hz

On the other hand, it was proben that there is some delay in the propagation at those frequencies (below 100 Hz), because in fact, even if the maximum of correlation corresponds with the mains frequency or its harmonic, mains cannot be delayed.

3.1.2.1 Pre-filtering to avoid mains interference

Different filtering is applied in order to avoid completely the possible influence of the mains. In this case a lower cut-off frequency of 60 Hz is also utilised to set up Band Pass Filters. The filters employed are again Butterworth with order 2. The resultant cross correlations are shown in Figure 3.10 and the estimated delays are enumerated in Table 3.2

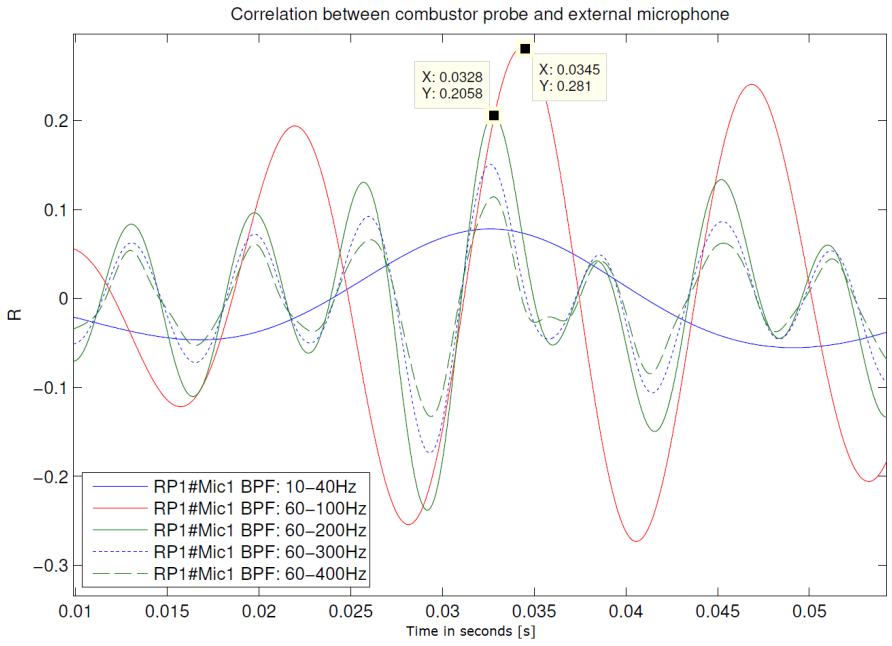

FIGURE 3.10: Band Pass Filtered Cross Correlations (avoiding mains) for data acquired between the external case of combustion chamber and the microphone situated at 90° of the nozzle

Filtering	Delay in ms
No Filtering	33.14
BPF 10-40 Hz	32.60
BPF 60-100 Hz	34.50
BPF 60-200 Hz	32.80
BPF 60-300 Hz	32.60
BPF 60-400 Hz	32.80

TABLE 3.2: Estimated delays for different cut-off frequencies of the Low Pass Filters applied to the data before the calculation of the cross correlation to extract them avoiding mains (50 Hz)

Again, only a larger delay can be noticed for a range of frequencies below 100 Hz. The estimated delay for the bands between 60 Hz and 200, 300 and 400 Hz are quite the same.

3.1.2.2 Pre-filtering in octave bands

In another study of filtering, the delays were estimated after applying band pass filtering in octave bands. Estimated values are shown in Table 3.3.

Filtering	**Delay in ms**
No Filtering	33.14
BPF 62.5 Hz Band	33.89
BPF 125 Hz Band	25.81
BPF 250 Hz Band	32.28
BPF 500 Hz Band	35.66
BPF 1000 Hz Band	20.01
BPF 2000 Hz Band	1.60
BPF 4000 Hz Band	13.84
BPF 8000 Hz Band	22.63

TABLE 3.3: Estimated delays in octave bands applied to the data before the calculation of the cross correlation to extract them

It can be seen that when applying band filtering in narrower bands, cross correlations are clearly dominated by sinusoidal components. Results over 1 kHz band can be discarded due to it seems that the correlation between the signals at those frequency bands are dominated by external tones. Moreover, they are out of the frequency range of interest for combustion noise. On the other hand, at lower frequencies there is a noticeable lower value for the estimated delay for the band centered at 125 Hz. This may indicate that the harmonic of the mains frequency (situated at 150 Hz) is acquired at both studied positions at the same time as it would be expected, and the larger delay estimated around that frequencies in previously estimations is really obtained due to slower propagation at low frequencies. Regardless, the estimation of the delay in octave bands is not too much more conclusive.

On the other hand, no large improvements are appreciated in the coherence after applying the delay extracted from those cross correlations to the time signal data before calculating the coherence, as it was presented by Miles in his research. That is because the external microphones for the ANTLE engine measurement were situated at 10 m of the nozzle of the engine, whilst in the experiment by NASA they were at 30 m. Then, the delays estimated by Miles were three times larger than the delays estimated in the ANTLE engine measurements. In the studied case, the longest delay is 33 ms, and the windowing used for the analysis is a raised cosine of 8192 samples for a sample rate of 32768 Hz, that is a 250 ms window. Then, one signal and its delayed version acquired

in a different position are not going to be processed by totally separated windows in the coherence calculation process. Hence, the coherence is not being affected much by the different delays.

The estimated coherence between the signals acquired in the combustion chamber and in the far field (that is the largest distance between sources, where the delay would be more influent) is compared with a un-delayed version of that coherence in Figure 3.11.

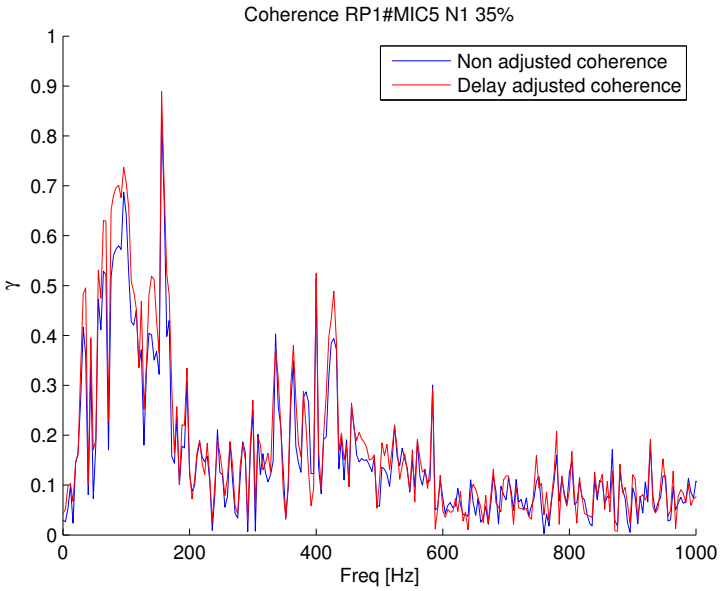

FIGURE 3.11: Comparison between coherence and un-delayed coherence

The two signals were aligned prior to the calculation of the coherence.

3.1.2.3 Study between the combustion chamber and the nozzle

The same delay estimation technique is carried out between the combustion chamber and the nozzle. In Table 3.4 and Figure 3.12 are represented the estimated delays between the external case of the combustion chamber and the nozzle.

From the results, it can be seen that a delay of 1.8 ms is estimated again for the frequency range between 60 and 100 Hz, meanwhile there is almost no difference in the time propagation for other frequencies. This may suggest that the delay estimated between the combustion chamber and the external microphone would be dominated by the delay between the combustion chamber and the nozzle.

The exact distance between the probes in the combustion chamber and nozzle is unknown, but it can be estimated from the plan of the engine. In the following, these data

Filtering	**Delay in ms**
No Filtering	6.8
BPF 60-100 Hz	8.6
BPF 60-200 Hz	7.0
BPF 60-300 Hz	6.8
BPF 60-400 Hz	6.8

TABLE 3.4: Estimated delays for different frequency bands. The filtering is applied to the data before the calculation of the cross correlation to extract the delays. The signals utilised were acquired in the external case of the combustion chamber (RP1)and in the nozzle (RPB)

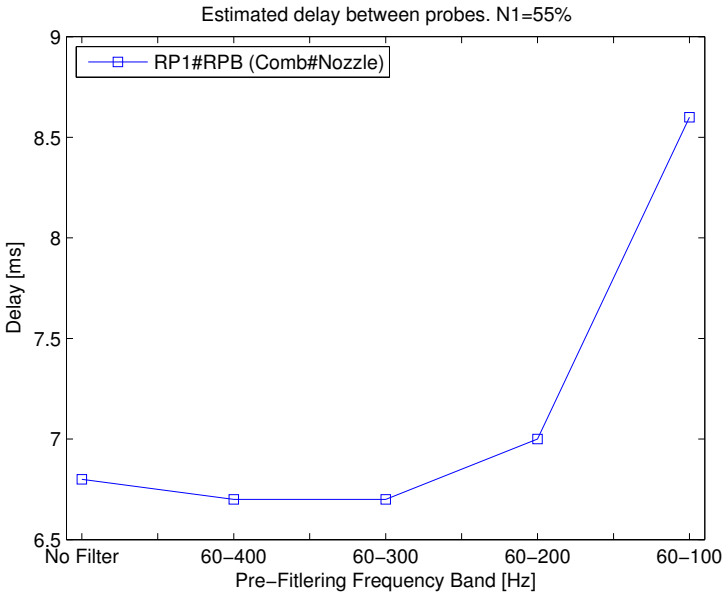

FIGURE 3.12: Estimated delay between the outer case of the combustion chamber and the nozzle

are used to calculate the velocity of the propagation using the time shift and distance between them.

No flow and ambient temperature was assumed for the appraisal of the in-duct propagation (speeds significant flow in the propagation direction will increase the speed by $c_o(1+M)$, where M is Mach number). Considering a delay of 7 ms, then, for a distance of 3 m the speed of propagation would be $v = 3m/0.007s = 285m/s$. For a 2.4 m separation it would be $344m/s$. The exact separation in plan between the probe installed in the combustion chamber and the probe situated in the nozzle is 1.7 m, that would suggest a propagation speed of $v = 1.7m/0.007s = 242m/s$. But the reality is that the path is larger than that, because it is not a straight line. At least, the curve of the duct should be considered, and also all the path through the turbines.

In conclusion, for the ANTLE engine, it was not found that the signal from the combustion chamber propagates at different speeds depending the frequency, as seen in [14]. However, a slightly larger delay was found with the lowest frequency filtering, which agrees with Miles results. This analysis probes the difference in the generation of combustion noise between engines, and the need of the individual study of each engine.

3.1.3 Phase Analysis to Avoid Filtering

A study of the phase of the cross spectra is carried out in order to extract the delay between the data acquired in the different positions of the in-duct. Then, a comparison of the estimated delay with the cross correlation and filtering techniques is done. The benefit of the phase study is that the time delay (strictly group delay) between two positions for any frequency range can be estimated without distorting the data by the application of any filtering.

Then, delay in a frequency band can be extracted from its slope by

$$\Delta t = \frac{d\theta}{d\omega}[s] \tag{3.1}$$

where $d\theta$ is the angle difference in radians, and $d\omega$ the bandwidth studied in radians per second ($2\pi Hz$).

In Figure 3.13 are represented two gradients extrapolated from the phase response of a cross spectra. It belongs to the cross spectra between the data acquired by the probes RP1 (external case of combustion chamber) and RPB (nozzle).

The red line represents a gradient between 60 Hz and 100 Hz and it is calculated by

$$\Delta t_1 = \frac{(2.738 - 0.9474)rad}{(2\pi(100 - 60))Hz} = 7.1ms$$

The green line represents a gradient between 60 Hz and 200 Hz and it is calculated by

$$\Delta t_2 = \frac{(2.738 - (-2.99))rad}{(2\pi(192 - 60))Hz} = 6.9ms$$

Those gradients were extrapolated from the phase response. Further work is required in order to obtain more accurate gradients, as for example, the use of LSFM (least squares fit method). The delay can be also estimated from the gradient of the unwrapped phase response as it is shown in Figure 3.14.

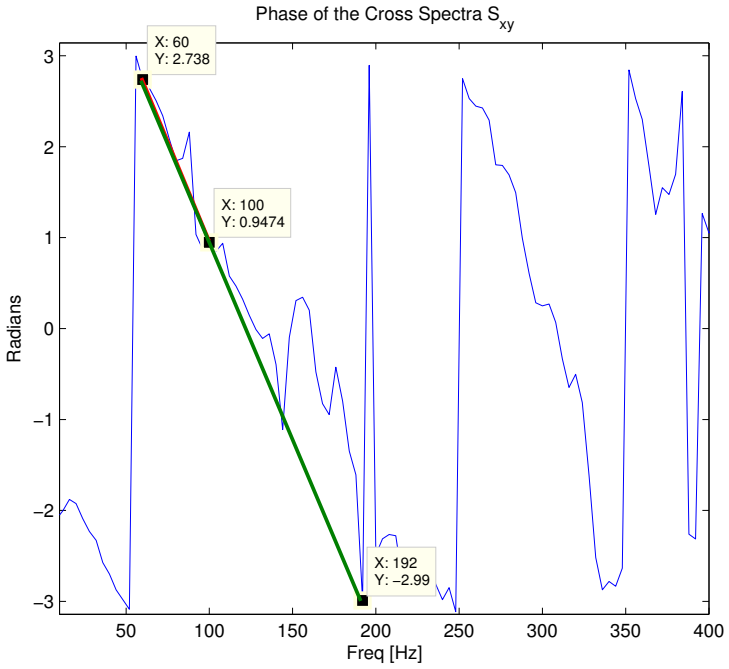

FIGURE 3.13: Calculation of the delay from the gradient of the phase of the cross spectra between data acquired by the probes installed in the outer case of the combustion chamber (RP1) and the nozzle (RPB)

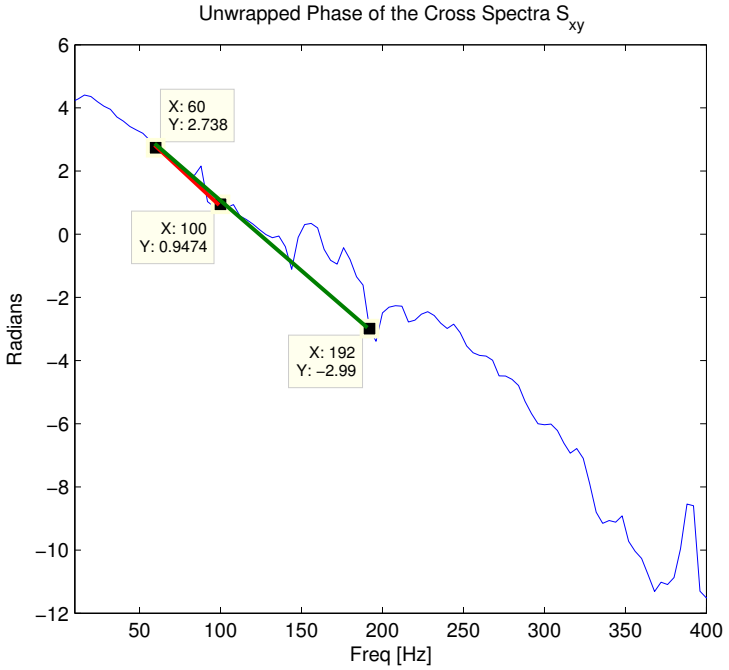

FIGURE 3.14: Calculation of the delay from the gradient of the unwrapped phase of the cross spectra between data acquired by the probes installed in the outer case of the combustion chamber (RP1) and the nozzle (RPB)

The advantage of the unwrapped phase is that a regression line can be set in a desired bandwidth avoiding the phase jumps. Then, the gradient can be estimated at any desired range of frequencies.

3.1.3.1 Un-delayed phase

There is also more ways to analyse the delay from the phase of the cross spectra.

Following the idea that a positive time delay (waveform shift to the right) adds a negatively sloped linear phase to the original spectral phase, and that a negative time delay (waveform shift to the left) adds a positively sloped linear phase to the original spectral phase, the phase of the cross spectra calculated between two of the acquiring data points can be "un-delayed" to verify how the estimated delay behaves in the frequency domain, and in order to obtain more information from it.

That idea is applied by multiplying the cross spectra Sxy by $e^{-j\omega\delta t}$ in order to "un-delay" the phase in the frequency domain.

An "un-delayed" phase is represented in Figure 3.15 in comparison with the coherence, the phase, and the unwrapped phase, at a low power setting.

This method helps to check the behaviour of the phase in the frequency domain, and also to set the ranges of interest. The same phase analysis is represented in Figure 3.16 and Figure 3.17 at a mid and high power setting respectively.

These common variations starting at 100 Hz and 200 Hz suggest a modal behaviour of the combustion chamber, specially at low engine speeds, where better results of coherence are shown. A modal study of the combustion chamber is presented in Chapter 4, where this suggestion is probed. More examples for different power settings and locations are presented and analysed.

3.2 Conclusions

Larger delays are estimated when data was filtered below 100 Hz from the study of the cross correlations between the data acquired in different points of the in-duct of the ANTLE engine. The aim of that study was to try to locate and differentiate direct and indirect combustion noise, following the processing suggested by Miles in [19]. Nevertheless, the delays and differences are not so conclusive to set any statement about that. Moreover, it was found that the filtering technique proposed by Miles was not

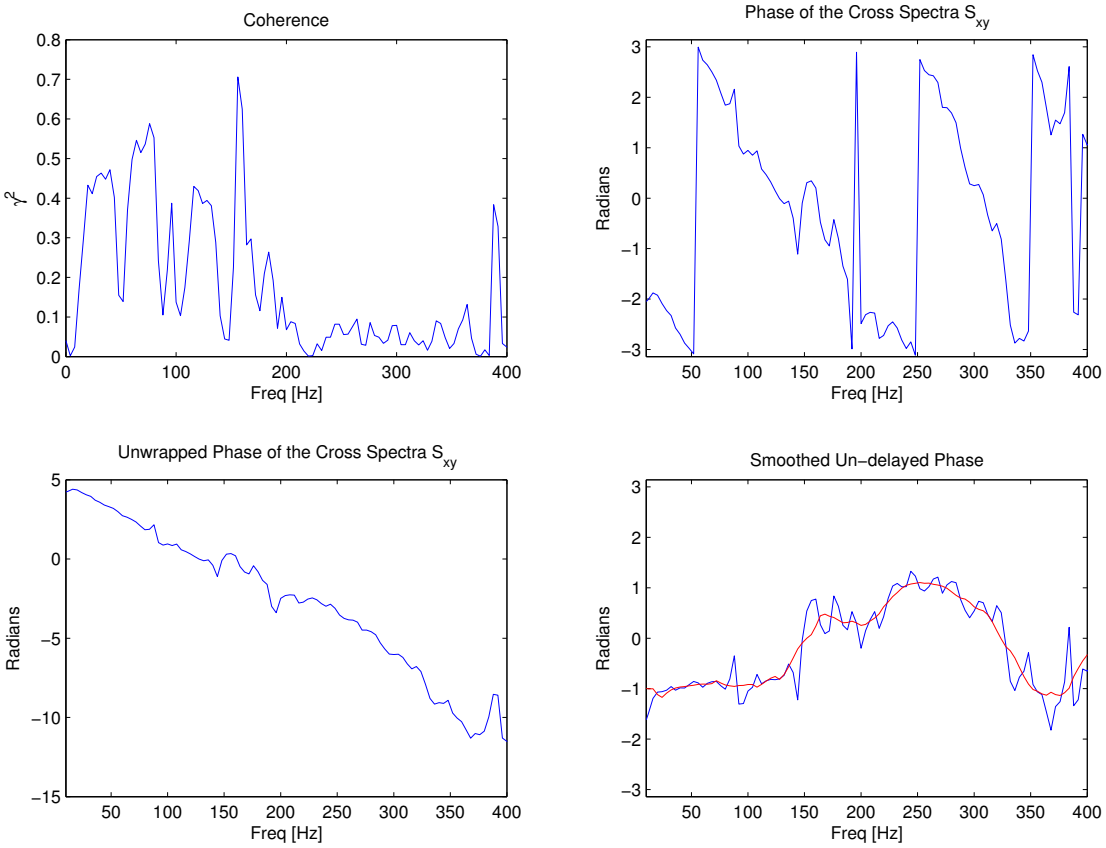

FIGURE 3.15: Phase study between RP1 (outer combustor) and RPB (nozzle) at a low power setting, with a delay from the cross correlation of 6.8 ms

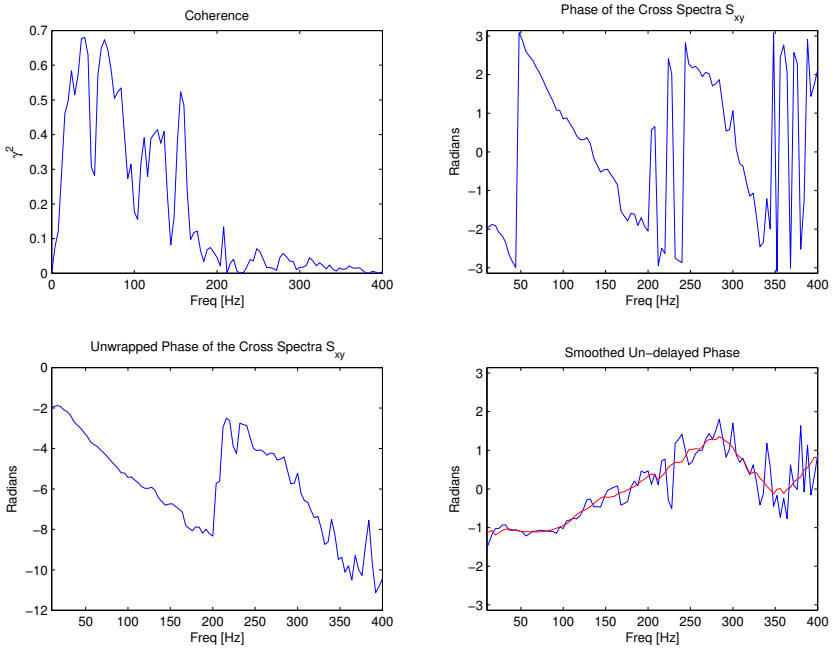

FIGURE 3.16: Phase study between RP1 (outer combustor) and RPB (nozzle) at a mid power setting, with a delay from the cross correlation of 7.0 ms

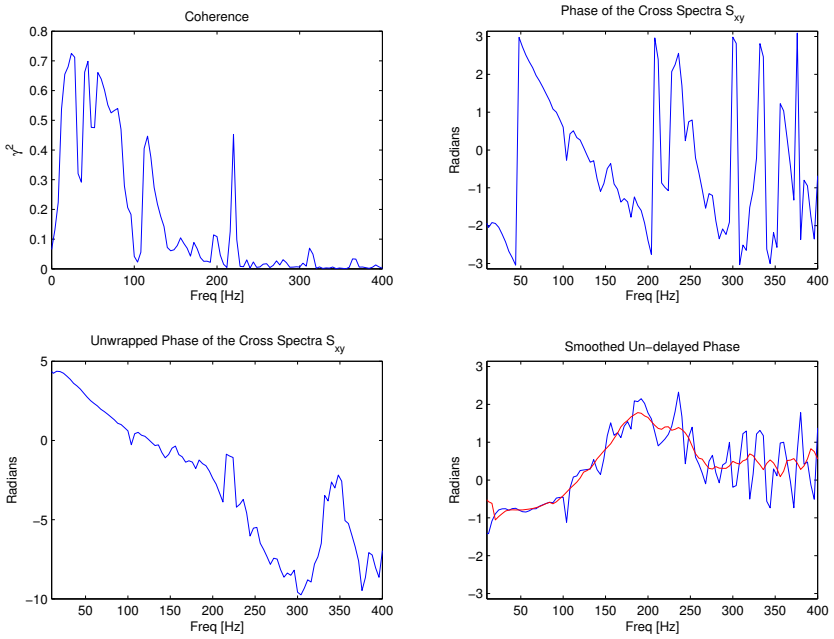

FIGURE 3.17: Phase study between RP1 (outer combustor) and RPB (nozzle) at a high power setting, with a delay from the cross correlation of 8.3 ms

so conclusive probably due to the difference in the experiments. Finally, it seems that direct and indirect combustion noise might be situated in the same frequency range, and to keep trying to separate them need more research, which would deviate the main aim of this thesis. This analysis probes the difference in the generation of combustion noise between engines, and the need of the individual study of each engine.

The advantage of using the cross-spectral phase data was also demonstrated. An estimated delay of 1 ms is found to be added to the propagation between the combustion chamber and the nozzle, meanwhile no delay is added between the nozzle and external microphones (at least it was not found using the cross correlation techniques).

A possible modal behaviour of the combustion chamber is related to the study of the phase of the cross spectra. Further research is presented in Chapter 4.

Combustion noise estimated from correlation may be only a part of the total combustion noise in the external field because it is dependant of the linearity of the process itself (that is, non-linearity is not considered), and also of the response of the probes (actually expected to be flat at the range of frequencies of interest but might include differences at certain conditions that will bias the correlation results).

Chapter 4

Modal Study of the Combustion Chamber

Propagation from the combustion chamber to the nozzle, and to the far field of the engine, may be biased by transmission effects in the in-duct of the engine. A possible modal behaviour of the combustion chamber was found in Chapter 3 related to the study of the phase of the cross spectra. A study of the modal behaviour of the combustion chamber of the ANTLE engine is carried out in this chapter.

4.1 Modes of an annular duct

Spinning modes were defined in [96] in comparison with plane wave propagation. Considering a uniform rigid duct with no steady flow inside, spinning modes have a cut-off property which sets a critical value where there is no propagation below it. Moreover, the amplitude of the pressure wave travelling along the duct can be related with the sound power transmitted towards the opening [97].

A plane wave can be transmitted along a uniform straight duct in the axial direction. This is the simplest mode of sound transmission. Other modes of transmission will depend of the shape of the duct, but the average of the pressure over any cross section of the duct always will be instantaneously zero.

Two kind of modes were defined in the literature [97]. A steady pressure which is spinning around the duct axis [97], and a stationary pressure pattern which fluctuates in time [99].

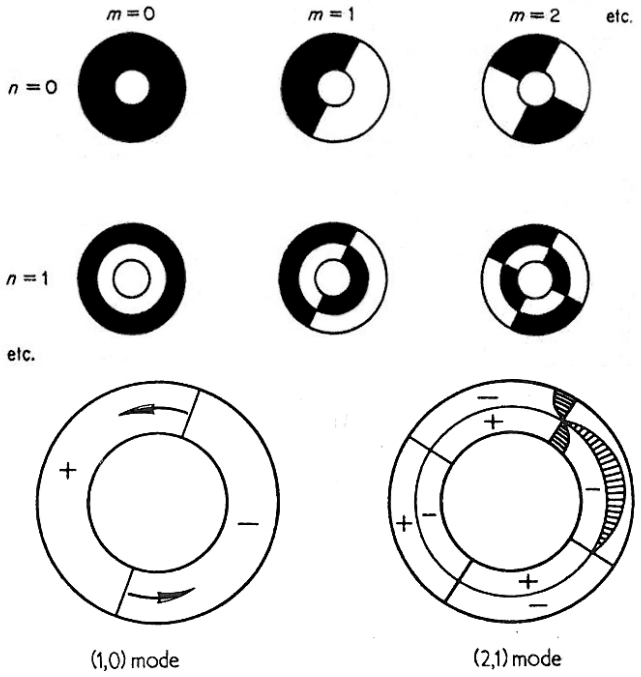

FIGURE 4.1: Patterns of sound pressure across an annular duct from [97] and [98]

In the case of an annular duct, the modes can be sorted by circles and nodal diameters, where there is no pressure at the nodal lines. The number of nodal diameters is usually defined as m, meanwhile the number of nodal circles is defined by n.

Patterns of sound pressure across an annular duct for different values of m and n are shown in Figure 4.1.

4.1.1 Physical Approximation

Higher order modes can be described in terms of plane waves. The annular cavity can be approximated as a rectangular cavity if the annulus is straightened out, therefore, the walls will be plane instead of cylindrical. Then, propagation of plane waves can be assumed between infinite rigid walls as the transmission of duct modes in one direction for an annular cavity [97].

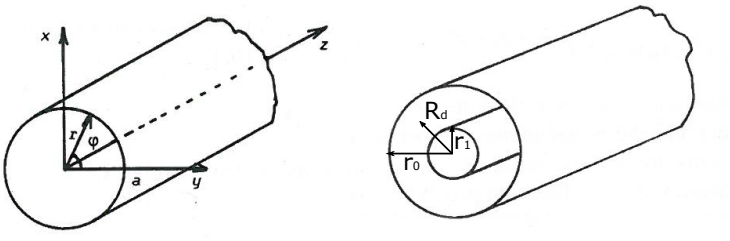

FIGURE 4.2: Cylindrical and annular duct from [100]

Two conditions have to be set. Firstly, the pattern has to be repeated along the propagation axis (each time as the same distance of the mean perimeter of the annulus), as it would be in an annular cavity. Direction cosines $(\overline{r}, \overline{\varphi}, \overline{z})$ can be used in reference to the axes (x, y, z) presented in Figure 4.2. Considering plane waves, with wave-number k ($\lambda = 2\pi/k$), travelling between the walls in the direction of $(\overline{r}, \overline{\varphi}, \overline{z})$, continuity along the annular duct can be expressed as a phase condition in the φ direction, where

$$\overline{\varphi} k 2\pi R_d = 2\pi m \tag{4.1}$$

being m any integer, and R_d the mean radius of the annular duct.

Secondly, the other condition should be set for the propagation of the plane waves between the rigid walls. At the walls, phase is changing, and it follows

$$\overline{r} k (r_0 - r_1) = n\pi \tag{4.2}$$

being n any integer, and $r_0 - r_1$ the difference between the external and internal radius of the annular duct respectively.

The transmission direction in the annulus of the annular duct are defined by the mode numbers (m,n) for any wave number k, where the direction cosines $\overline{\varphi}$ and $\overline{r}$ are settled by Equation 4.1 and Equation 4.2.

The squared value of the defined direction cosines $(\overline{r}, \overline{\varphi}, \overline{z})$ should lie between 0 and 1, and they are related by

$$\overline{r}^2 = (1 - \overline{\varphi}^2 - \overline{z}^2) > 0 \tag{4.3}$$

where in terms of the wave number, and using Equation 4.1 and Equation 4.2, can be concluded that

$$k > k_{mn} \tag{4.4}$$

where k_{mn} is the transverse modal wave number

$$k_{mn} R_d = \left(m^2 + \frac{n^2 \pi^2 R_d^2}{(r_0 - r_1)^2} \right)^{1/2} \tag{4.5}$$

which can be also finally presented as

$$k_{mn}^2 = \left(\frac{m}{R_d}\right)^2 + \left(\frac{n\pi}{r_0 - r_1}\right)^2 \tag{4.6}$$

The transverse wave number can be used to calculate the axial modal wave number k_{zm}

$$k_{zm} = \left(k^2 - k_{mn}^2\right)^{1/2} \tag{4.7}$$

It can be observed that if $k > k_{mn}$ (above cut-off), then k_{zm} is real and the mode propagates in the z direction. But if $k < k_{mn}$ (below cut-off), then k_{zm} will be imaginary and the mode perturbation decays exponentially.

That is, there is a minimum frequency (or wave number) where a (m, n) mode can be represented by a plane wave in an annular duct [97].

4.2 Modal appraisal of the combustion chamber of the ANTLE engine

An appraisal of annular modes in the outer case of the combustion chamber is presented.

An annular combustion chamber can be modelled as a uniform annular duct. Sound propagation inside it can be visualised as plane waves travelling along the axis but also by waves propagating in a spiral way round the duct. Cut-off frequencies can be calculated.

From [98], for axisymmetric ducts with large hub-tip ratios

$$\mu = \frac{r_1}{r_0} > 0.5 \tag{4.8}$$

modal behaviour in an annular duct can be approximated by Equation 4.6

The hub-tip ratio of the annular combustion chamber of the ANTLE engine is larger than 0.5, then, the approximation presented in Equation 4.6 can be applied in order to estimate the cut-off frequencies of the modes into it.

$$\mu_{ANTLE} = \frac{r_1}{r_0} = \frac{0.40\ m}{0.45\ m} = 0.89 > 0.5 \tag{4.9}$$

where $r_1 = 0.40$ m is the inside radius, and $r_0 = 0.45$ m the outside radius of the annular combustion chamber for the ANTLE engine.

First modes of the ANTLE combustion chamber are then calculated as a first approximation by

$$f_{mn} = \frac{ck}{2\pi} \tag{4.10}$$

for the different temperatures measured at the combustor inlet plane for speeds of N1 at low, mid, and high power settings. No flow was assumed.

First cut-on modes of the external case of the combustion chamber of the ANTLE engine are enumerated in Table 4.1.

m	n	k_{mn}	f_{mn} (Low, 645.8K)	f (Mid, 700.1K)	f (High, 754.9K)
1	0	2.3529	191 Hz	199 Hz	206 Hz
2	0	4.7059	382 Hz	397 Hz	413 Hz
3	0	7.0588	572 Hz	596 Hz	619 Hz
4	0	9.4118	763 Hz	795 Hz	825 Hz
0	1	62.8319	5094 Hz	5304 Hz	5508 Hz

TABLE 4.1: Estimated first cut-on modes in the outer case Combustion Chamber for the different temperatures in the combustor inlet plane (T30) for the speeds of N1 at low, mid, and high power settings respectively. No flow is assumed

First cut-on modes in the inner case of the combustion chamber of the ANTLE engine were estimated. They are shown in Table 4.2, where $r_1 = 0.24$ m is the inside radius, and $r_0 = 0.40$ m the outside radius of the inner case of the combustion chamber.

m	n	k_{mn}	f_{mn} (Low, 1371.9K)	f (Mid, 1507.0K)	f (High, 1683.6K)
1	0	3.1250	369 Hz	387 Hz	409 Hz
2	0	6.2500	739 Hz	774 Hz	818 Hz
3	0	9.3750	1108 Hz	1161 Hz	1227 Hz
4	0	12.5000	1477 Hz	1548 Hz	1636 Hz
0	1	19.6350	2320 Hz	2432 Hz	2570 Hz

TABLE 4.2: Estimated first cut-on modes in the inner case of the Combustion Chamber for the different temperatures in the combustor exit plane (T40) for the speeds of N1 at low, mid, and high power settings respectively. No flow is assumed

In addition, first cut-on modes in the nozzle of the ANTLE engine were estimated. They are shown in Table 4.3, where $r_1 = 0.450$ m is the inside radius, and $r_0 = 0.544$ m the outside radius of the nozzle of the ANTLE engine.

As it can be seen from Figure 4.3, the temperature of the air flow in the outlet of the compressor (HP), and in the liner inlet of the combustion chamber is close to 650 K.

m	n	k_{mn}	f_{mn} (Low, 800.7K)	f (Mid, 836.9K)	f (High, 901.1K)
1	0	2.0121	182 Hz	186 Hz	193 Hz
2	0	4.0241	363 Hz	371 Hz	385 Hz
3	0	6.0362	545 Hz	557 Hz	578 Hz
4	0	8.0483	727 Hz	743 Hz	771 Hz
0	1	33.4212	3017 Hz	3085 Hz	3200 Hz

TABLE 4.3: Estimated first cut-on modes in the Nozzle for the different temperatures in the LP turbine outlet guide vane plane (T50) for the speeds of N1 at low, mid, and high power settings respectively. No flow is assumed

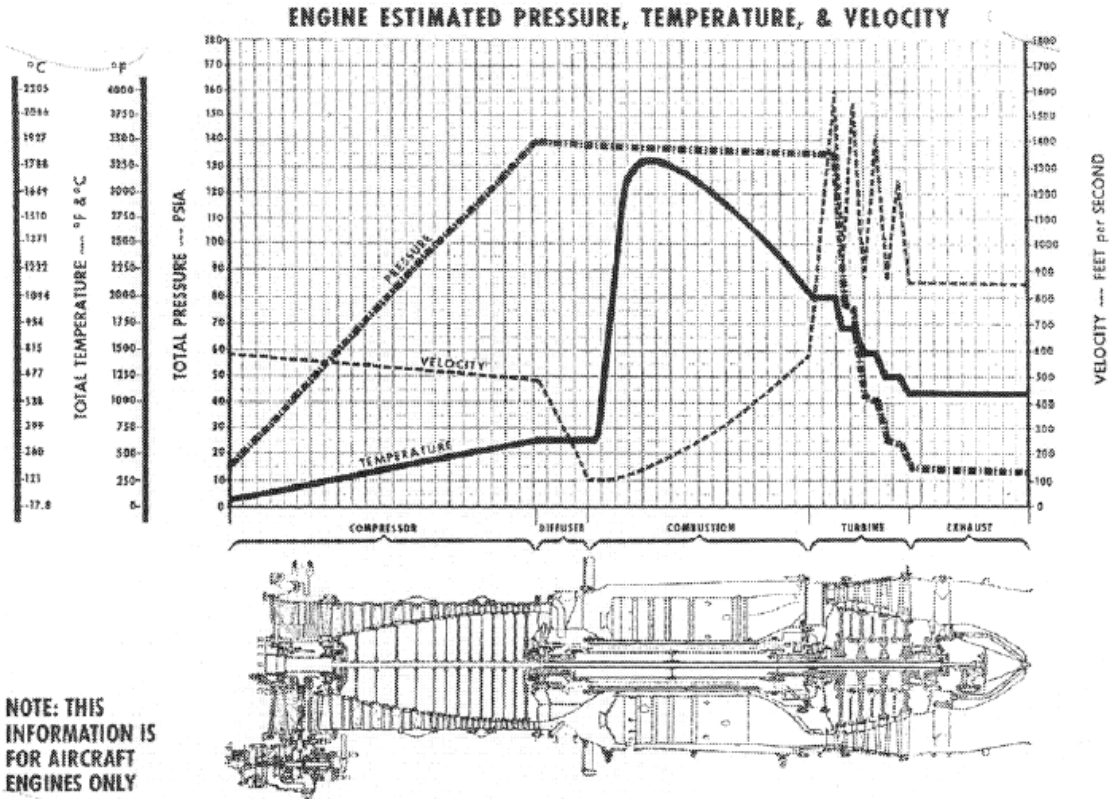

FIGURE 4.3: Sample Engine Pressure, Temperature, and Velocity of air flow from [101]

Temperature affects the speed of sound. Temperature in the combustion chamber can reach $1900°C$. Moreover, air reaches the combustor after the compressor stage, reaching a pressure of 140 PSI (965 kPa), meanwhile pressure in ambient conditions is 101 kPa. Air pressure and humidity barely affect the speed of sound, however, small changes in humidity can bias the response and behaviour of the probes. Air pressure and velocity along the jet engine process are also shown in Figure 4.3.

A temperature of $600°C$ was assumed in the outer case of the combustion chamber due to possible heat transfers from the inner case of the combustion chamber to the outer case. The outer case is where probes RP1 and RP2 are situated. Speed of sound c for

$321°C$ is 489 m/s, meanwhile the speed of sound c for $600°C$ is 592 m/s. For ambient conditions speed of sound c_0 is 343 m/s.

4.2.1 Modal estimation from the phase study

Modal response in the ANTLE combustion chamber has been cross-compared with the theoretical estimated values. Changes in the behaviour of the propagation inside the combustor can be detected by analysing the phase of the cross spectra between different points inside it. Multiple results of phase response for data acquired in different positions of the engine are shown in Appendix E.

From the set of results in Appendix E, it can be seen that the phase response of the cross spectra between the data acquired by the probes RP1 and RP2 in the outer case of the combustion chamber has a flat response for frequencies below 200 Hz. This flat response in that frequency range is present for all the analysed power settings.

This variation in the phase may be produced due cut on to the first mode, which was estimated at 191 Hz. A flat response in the phase indicates that a plane wave is propagating.

Coherence and phase response of the cross spectra from data acquired in the outer case of the combustion chamber of the ANTLE engine and estimated cut-on of first circumferential modes in the combustion chamber are shown in comparison with the phase response in Figure 4.4. More examples for multiple different positions and power settings are shown in Appendix E.

A second alteration in the phase response of the cross spectra can be found between 350 and 400 Hz. This variation may be related with the estimated second circumferential mode, the cut-on for which was estimated at 360 Hz.

Suggested patterns of sound pressure across the combustion chamber of the ANTLE engine derived from the presented study of the phase response of the cross spectra are shown in Figure 4.5.

For the different relations between the data acquired by the different probes, it can be concluded that the estimated patterns of sound pressure can slightly rotate their position for the different modes.

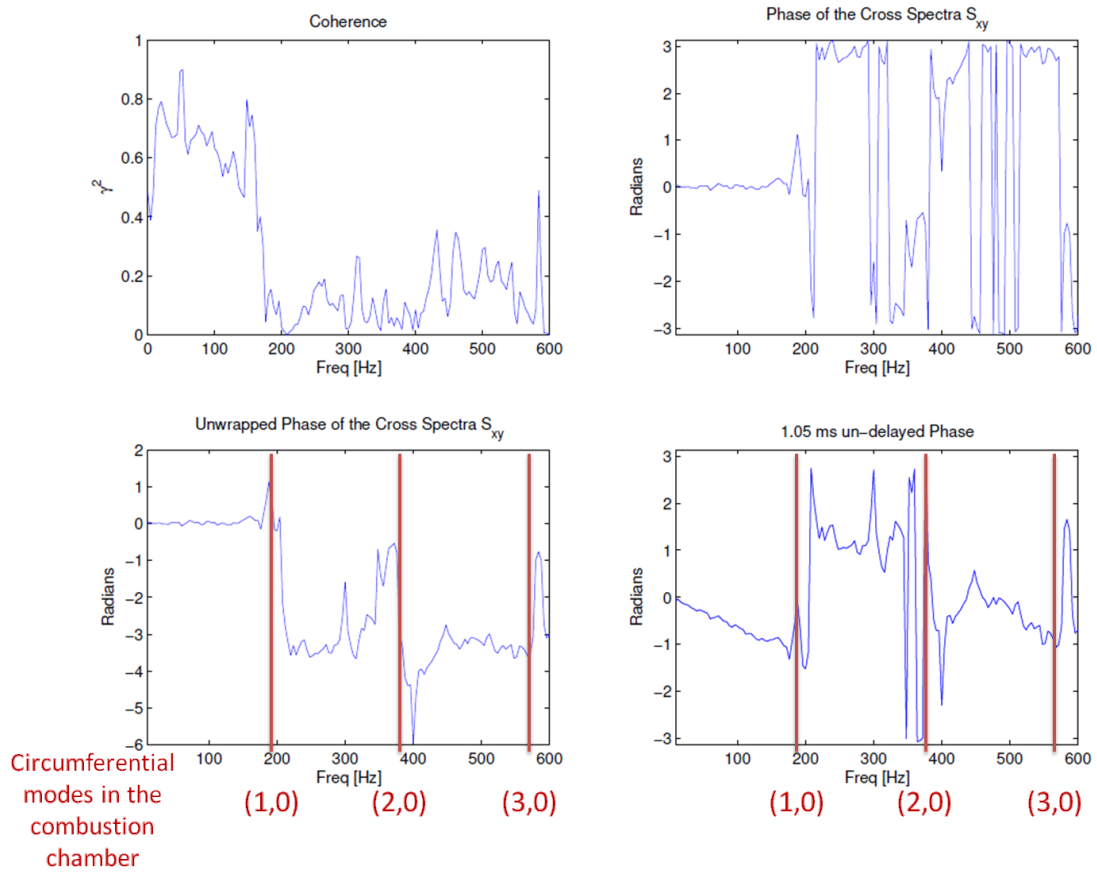

FIGURE 4.4: Coherence and phase response of the cross spectra from data acquired in the outer case of the combustion chamber of the ANTLE engine. Estimated cut-on of first circumferential modes in the combustion chamber are shown in comparison with the phase response

4.2.2 Final considerations

Finally, it has to be noted that the analysed decay in the phase over 200 Hz shown in Section 3.1.3.1 could be produced by the decay in the value of the coherence over exactly the same frequency. On the other hand, that decay in the coherence could be established due to the first cut-on mode, which is situated around 200 Hz.

The values of the coherence between the data acquired in the combustion chamber and the data acquired by the external microphones are larger for the 60° microphone (MIC5) than the 90° (MIC1) as it was expected considering the jet engines noise radiation patterns.

A possible combustion noise tone was identified around 450 Hz. It is dependent of the power settings because it goes up to 500 Hz for the High N1 speed, and it is probably

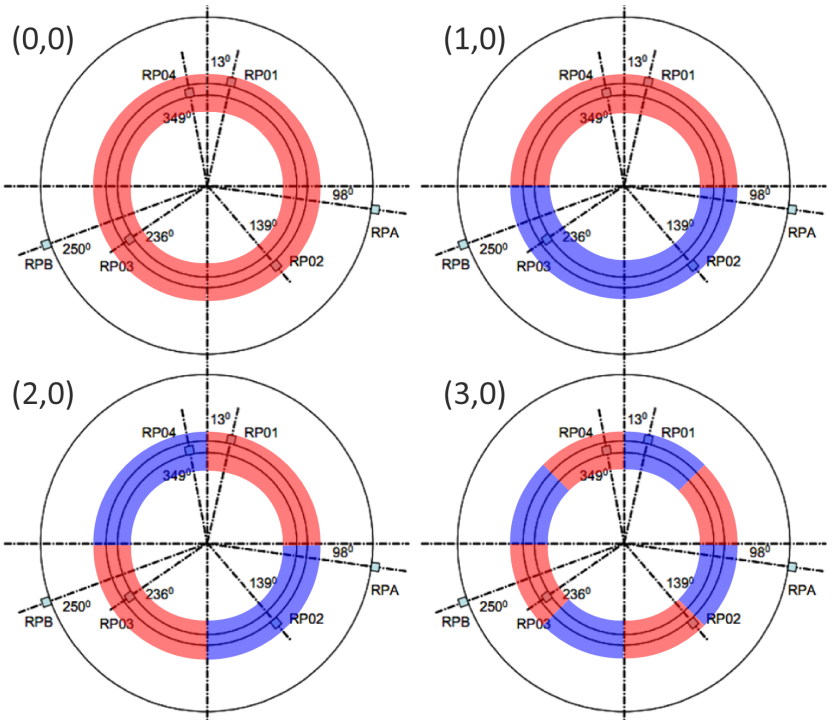

FIGURE 4.5: Suggested patterns of sound pressure across the combustion chamber of the ANTLE engine derived from the study of the phase response of the cross spectra of the data acquired by the shown probes

related with the HP turbine and the speed of N3 too. However, is not clearly related with any BPF. First BPF related to N1 is situated over 600 Hz.

The possible modal behaviour at low frequencies is also noticed in the data acquired in the nozzle, but it is not so dominant. However, it is barely noticed in the external microphones, where the maximum of coherence is still between 0 and 200 Hz, but with smaller amplitudes.

In conclusion, it is shown that the modal response in the ANTLE combustion chamber agrees with the theoretical estimated values obtained from its size and combustion process characteristics. This shows the dependence on the size of the combustion chamber and the temperature of the combustion process into the first cut-on modes that will affect the propagated combustion noise. Moreover, it is shown again the need of more sensors in the combustion chamber, which will allow applying multiple coherence-modal techniques such as those descried in Section 2.3.3.3.

4.3 Summary

A physical approximation of the modal behaviour of an annular duct has been introduced and explained in this chapter. Moreover, the first cut-on modes for the annular combustion chamber of the ANTLE engine were estimated.

Estimated cut-on modes of the combustion chamber of the ANTLE engine have been cross-compared with the behaviour of the phase of the cross spectra, calculated from the measured data.

It was concluded that plane wave is propagating along the outer case of the combustion chamber up to 200 Hz. But it is not totally clear if that plane wave is reaching the nozzle where the probe RPB is situated. Further research in this topic is needed in order to investigate if that behaviour from the combustion chamber can be noticed in the far field (external microphones) with noticeable levels over jet and fan noise.

Chapter 5

New Combustion Noise Estimator: The 3S-Array

A new processing technique to extract turbofan engine combustion noise called 3S-Array is presented. It has been developed using a multiple coherence technique with data acquired in the in-duct and external sound fields of a jet engine. In-duct sensors are located in the combustion chamber and in the nozzle of the engine, and external data is acquired using an array of microphones. A beamformed signal focused in the nozzle of the engine is generated with the data from the external array. Jet noise and influences of the room on the array output are reduced using this focusing technique, which is referred to as Focused Beamformed Output (FBO).

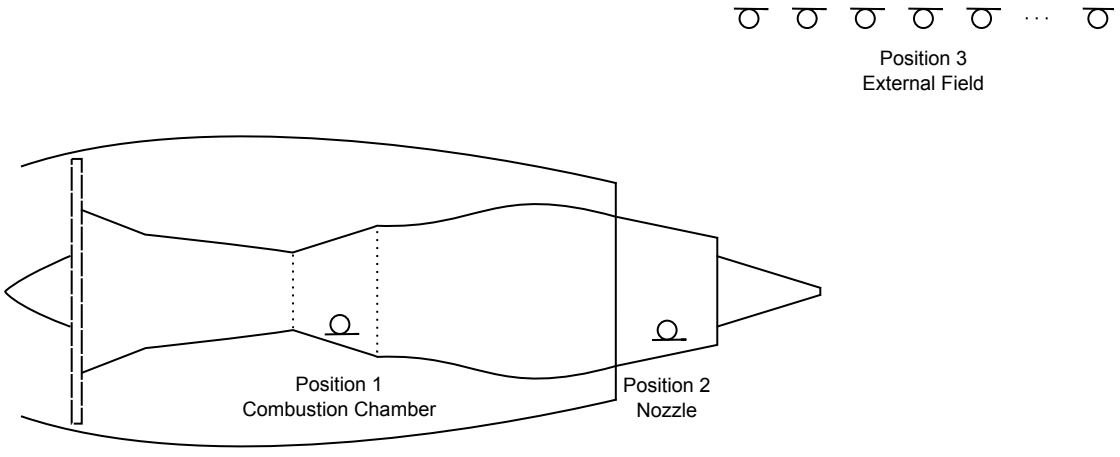

FIGURE 5.1: Illustration of a data acquisition test set up and the measurement points

Results show that using this new 3-S Array technique with two of the in-duct sensors and the focused beamformed signal as the third one, provides a better estimator of combustion noise than the 3-signal coherence technique alone, or the Coherence-Output

Power Spectra (COP), both of which are reported in the literature as methods for the extraction of combustion noise from the radiated noise spectrum.

5.1 Introduction

A new processing technique to extract combustion noise is presented here. It enhances the benefit of using the 3-S processing technique by including an array of microphones in the external field of the engine. This technique, called here the 3S-Array technique, improves on the noise rejection of unwanted sources in the external field by replacing the single external signal with the focused signal from all the microphones in the array, termed here the Focused Beamformed Output (FBO). The FBO in combination with the data acquired in the combustion chamber and the nozzle of the engine provides a more reliable combustion noise estimator.

The main objective of the current work is to develop and evaluate this 3S-Array processing technique in order to improve our understanding of how the combustion noise propagates from the combustion chamber through the nozzle and into the far field.

A summary of the relevant signal processing definitions is given in Section 5.2, the COP technique is described in Section 5.3, and the 3-S coherence technique in Section 5.4. The 3S-Array method is described in Section 5.5 supported by simulations of the technique and application to full-scale engine data in the following chapters, including comparisons with the COP and 3-S techniques.

5.2 Signal processing definitions

The processing systems defined here are linear and time-invariant(LTI), which can be characterized entirely by an impulse response function. The output of the system in the time domain is the convolution of the input with its impulse response. Moreover, the same LTI system can be characterised in the frequency domain by its transfer function [102]. The output of the system in the frequency domain is the product of its transfer function and the input of the system, both transformed into the frequency domain.

Different ways to represent the definition of the Cross-Spectral Density Function (CSD) are described [102] as

$$S_{xy}(f) = \int_{-\infty}^{\infty} R_{xy}(\tau) e^{-j2\pi f\tau} d\tau \tag{5.1}$$

$$S_{xy}(f) = H_{xy}(f) S_{xx}(f) \tag{5.2}$$

$$S_{xy}(f) = \lim_{T \to \text{inf}} \frac{E\left[X_T^*(f) Y_T(f)\right]}{T} \tag{5.3}$$

where $X_T(f)$ and $Y_T(f)$ are finite Fourier transforms of the time varying sensor signals $x(t)$ and $y(t)$ with $X_T^*(f)$ the complex conjugate, S_{xy} is their Cross-Spectral Density Function, and R_{xy} their cross correlation function. Equation 5.1 states that the Cross-Spectral Density Function is the Fourier transform of the cross correlation function, which provides a measure of the degree to which the two signals are related in the frequency domain. Any causal time delay relationship between the signals can be evaluated from the phase spectrum, the CSD being a complex quantity. Furthermore, the CSD is defined in Equation 5.3 as the averaged expected value of the signal finite transforms after an infinite number of repetitions.

Here, one-side Cross-Spectra Density functions are used [102], which are defined as

$$\begin{aligned} G_{xy}(f) &= 2S_{xy}(f) && f > 0 \\ &= S_{xy}(f) && f = 0 \\ &= 0 && f < 0 \end{aligned} \tag{5.4}$$

5.3 Two-signal Coherent Output Power (COP) technique

Consider the single-input/single-output system shown in Figure 5.2 [68].

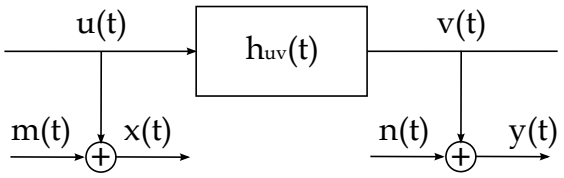

FIGURE 5.2: Single input/output linear system with uncorrelated input and output noise, the basis of the COP technique

Here, $u(t)$ and $v(t)$ are combustion noise signals at two measurement points. They are linearly related by the LTI system h_{uv}. The signals $x(t)$ and $y(t)$ are the actual

measured signals at those positions, where $m(t)$ and $n(t)$ stand for unwanted noise which contaminate the combustion signals $u(t)$ and $v(t)$ such that

$$\left.\begin{aligned} x(t) &= u(t) + m(t) \\ y(t) &= v(t) + n(t) \end{aligned}\right\} \tag{5.5}$$

The system shown in Figure 5.2 has been reconfigured in Figure 5.3 with a parallel block diagram. Both represent the same physical phenomenon.

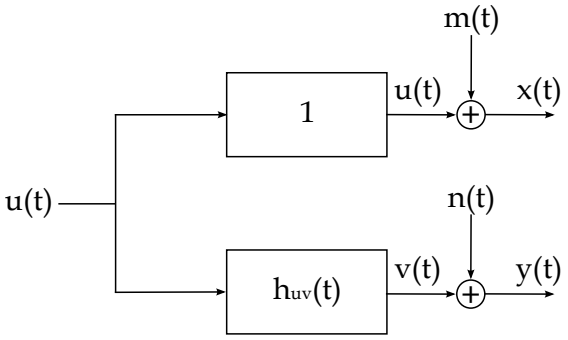

FIGURE 5.3: Linear system equivalent to a single input/output system

The coherence function, which provides a measure of the degree of linearity between the two signals $x(t)$ and $y(t)$, is defined as

$$\gamma_{xy}^2(f) = \frac{|G_{xy}(f)|^2}{G_{xx}(f)G_{yy}(f)} \tag{5.6}$$

and its values are between 0 and 1, however, coherence levels over 0.2 are considered as the minimum acceptable by the author in this thesis. Theoretically, the correlation between two random signals it should be 0 for an infinite time signal through an ideal linear system, but in a real physical scenario it is greater than 0. Simulations carried on with random signals of the same length as the studied ones showed that it is 0.1, and thats why the author chooses 0.2 as a minimum threshold value for coherence. In addition, changes in the coherence level are clearer only over that value for the studied data.

The squared amplitude of the cross-spectral density between $x(t)$ and $y(t)$ is defined [63] as

$$|G_{xy}(f)|^2 = G_{uu}(f)G_{vv}(f) \tag{5.7}$$

Equation 5.7 is valid if the unwanted noises $n(t)$ and $m(t)$ are assumed uncorrelated of each other and with the combustion signals $x(t)$ and $y(t)$, such as

$$\begin{aligned} G_{xy}(f) &= E\left[X^*Y\right] = E\left[(U+M)^*(V+N)\right] = E\left[U^*V + M^*V + U^*N + M^*N\right] \\ &\stackrel{1}{=} E\left[U^*V\right] = G_{uv}(f) \end{aligned} \tag{5.8}$$

where equality 1 is true for a large number of averages and then, the PSD $G_{mv}(f) = G_{un}(f) = G_{mn}(f) = 0$.

Equation 5.6 can be expanded in terms of the input signal $u(t)$ and required output signal $v(t)$. The numerator can be substituted with Equation 5.7, and the denominator with an expanded version of the PSD $G_{xx}(f)$ and the PSD $G_{yy}(f)$ as follows

$$\begin{aligned} G_{xx}(f) &= \int_{-\infty}^{\infty} E\left\{[u(t)+m(t)]\,[u(t+\tau)+m(t+\tau)]\right\} \exp^{-j2\pi f\tau}\, d\tau \\ &= \int_{-\infty}^{\infty} E\left\{u(t)u(t+\tau) + m(t)m(t+\tau) + u(t)m(t+\tau) + m(t)u(t+\tau)\right\} \exp^{-j2\pi f\tau}\, d\tau \\ &\stackrel{1}{=} \int_{-\infty}^{\infty} \left[R_{uu}(\tau)R_{mm}(\tau)\right] \exp^{-j2\pi f\tau}\, d\tau = G_{uu}(f) + G_{mm}(f) \end{aligned} \tag{5.9}$$

with the PSD $G_{yy}(f)$ expanded as Equation 5.9, which results

$$\left.\begin{aligned} G_{xx}(f) &= G_{uu}(f) + G_{mm}(f) \\ G_{yy}(f) &= G_{vv}(f) + G_{nn}(f) \end{aligned}\right\} \tag{5.10}$$

The product of the PSD $G_{xx}(f)$ and $G_{yy}(f)$, which is the denominator of the coherence function shown in Equation 5.6, results

$$G_{xx}(f)G_{yy}(f) = G_{uu}(f)G_{vv}(f) + G_{mm}(f)G_{vv}(f) + G_{nn}(f)G_{uu}(f) + G_{mm}(f)G_{nn}(f) \tag{5.11}$$

Finally, substituting Equations 5.7 and 5.11 in Equation 5.6, the coherence function of the actual measured signals $x(t)$ and $y(t)$ is presented in terms of the combustion signals $u(t)$ and $v(t)$, and the unwanted noise $m(t)$ and $n(t)$ as

$$\begin{aligned}\gamma_{xy}^2(f) &= \frac{|G_{xy}(f)|^2}{G_{xx}(f)G_{yy}(f)} \\ &= \frac{G_{uu}(f)G_{vv}(f)}{G_{uu}(f)G_{vv}(f) + G_{uu}(f)G_{nn}(f) + G_{mm}(f)G_{vv}(f) + G_{mm}(f)G_{nn}(f)} \\ &\stackrel{1}{=} \frac{1}{1 + \frac{G_{nn}(f)}{G_{vv}(f)} + \frac{G_{mm}(f)}{G_{uu}(f)} + \frac{G_{mm}(f)G_{nn}(f)}{G_{uu}(f)G_{vv}(f)}}\end{aligned} \tag{5.12}$$

where the equality number 1 is carried out dividing the numerator and denominator by $G_{uu}(f)G_{vv}(f)$.

The ratios of the auto-spectral density of the unwanted noise for the input and output are stated [63] in Equation 5.12 by the terms

$$\left.\begin{aligned}\frac{G_{mm}(f)}{G_{uu}(f)} &= \psi_x \\ \frac{G_{nn}(f)}{G_{vv}(f)} &= \psi_y\end{aligned}\right\} \tag{5.13}$$

Equation 5.12 can be rewritten in terms of Equation 5.13 such as

$$\frac{(1 - \gamma_{xy}^2(f))}{\gamma_{xy}^2(f)} = \psi_x + \psi_y + \psi_x\psi_y \tag{5.14}$$

The Coherence-Output Power Spectra is an estimator of the desired signal by using the actually measured ones. It is defined in [68] as the product of coherence $\gamma_{xy}^2(f)$ and PSD $G_{yy}(f)$, that is

$$\begin{aligned}\gamma_{xy}^2(f)G_{yy}(f) &= \frac{G_{yy}(f)}{1 + \frac{G_{nn}(f)}{G_{vv}(f)} + \frac{G_{mm}(f)}{G_{uu}(f)} + \frac{G_{mm}(f)G_{nn}(f)}{G_{uu}(f)G_{vv}(f)}} \\ &= \frac{G_{vv}(f) + G_{nn}(f)}{1 + \frac{G_{nn}(f)}{G_{vv}(f)} + \frac{G_{mm}(f)}{G_{uu}(f)} + \frac{G_{mm}(f)G_{nn}(f)}{G_{uu}(f)G_{vv}(f)}} \\ &\stackrel{1}{\approx} G_{vv}(f)\end{aligned} \tag{5.15}$$

where the approximation 1 is only possible if the PSD of unwanted noise signals $m(t)$ and $n(t)$ are much smaller than that of the combustion signal $u(t)$ and $v(t)$ respectively, that is $G_{mm} << G_{uu}$, and $G_{nn} << G_{vv}$. Therefore, it can be concluded that the COP is

underestimating the extraction of G_{uu} and G_{vv} due to their dependence to the unwanted noise signals.

5.4 Three-signal (3-S) Coherence technique

Consider the system shown in Figure 5.4 as it was presented by Krejsa [60].

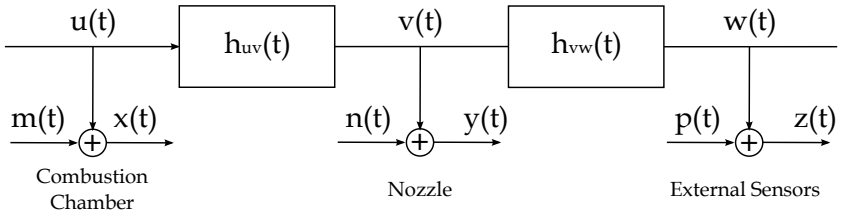

FIGURE 5.4: Representation of the propagation of combustion noise with 3 measurement points. Schematic diagram for coherence-techniques measurements

Here $u(t)$, $v(t)$, and $w(t)$ are the actual combustion signals at the three measurement points, namely at a location near the combustor, at or near the final nozzle, and at a point outside the engine, ideally in the far-field. The signals $x(t)$, $y(t)$, and $z(t)$ are the signals actually measured at those points with $m(t)$, $n(t)$ and $p(t)$ representing the unwanted non-combustion noise signals that contaminate $u(t)$, $v(t)$ and $w(t)$. These measured signals are a combination of the desired combustion noise signals and unwanted random and uncorrelated noises. Therefore,

$$\left.\begin{aligned} x(t) &= u(t) + m(t) \\ y(t) &= v(t) + n(t) \\ z(t) &= w(t) + p(t) \end{aligned}\right\} \tag{5.16}$$

The unwanted noise in the vicinity of the combustion chamber $m(t)$ might be caused by hydrodynamic pressure fluctuations and similarly for $n(t)$ but in addition $n(t)$ and $p(t)$ will contain acoustic signals from other sources such as turbine noise and jet noise. The external signal $z(t)$ will also be contaminated by reflections if measured in an in-door test bed[1].

The layout shown in Figure 5.4 can be replotted with a block diagram with parallel propagation of the combustion noise signal $u(t)$. It is represented in Figure 5.5 as done by Hultgren and Miles [18].

[1]This is an important consideration nowadays with the increase of the use of in-door tests

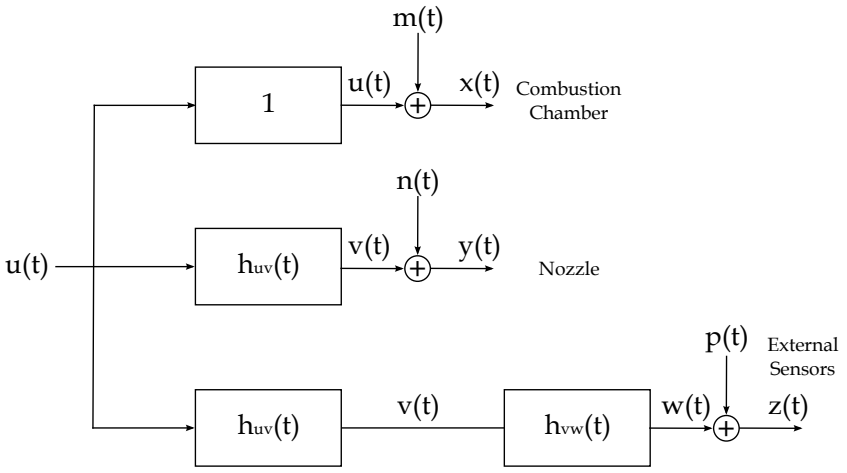

FIGURE 5.5: Representation of the propagation of combustion noise with 3 measurement points. General schematic diagram for three-signal technique

Both layouts represent the same physical system, and the objective is to extract the required combustion noise PSD G_{ww} from the measured signals $x(t)$, $y(t)$, and $z(t)$.

It is assumed that the unwanted noise signals $m(t)$, $n(t)$, and $p(t)$ are mutually uncorrelated between them and with the combustion noise signals $u(t)$, $v(t)$, and $w(t)$ such that

$$\begin{aligned} G_{mn}(f) &= E\left[M^*(f)N(f)\right] = 0 \\ G_{mp}(f) &= E\left[M^*(f)P(f)\right] = 0 \\ G_{np}(f) &= E\left[N^*(f)P(f)\right] = 0 \end{aligned} \tag{5.17}$$

which states that for an infinite number of averages, the in-duct unwanted noises $n(t)$ and $m(t)$ are uncorrelated between them and with the unwanted noise $p(t)$, which is generated between the nozzle and the exterior sound field. This assumption is reasonable because of the different nature of the signals and if they are separated, as it would happen in a real scenario like the one presented.

The following equations are functions of frequency, (f) which is omitted to simplify the notation. They describe the assumptions which have to be made in order to acquire the cross-spectra of the desired signals $u(t)$, $v(t)$, and $w(t)$, from the contaminated measured signals $x(t)$, $y(t)$, and $z(t)$.

$$G_{xz} = E\left[(U+M)^*(W+P)\right] = E\left[U^*W + M^*P + U^*P + M^*W\right]$$
$$\stackrel{1}{=} E\left[U^*W\right] = G_{uw} \tag{5.18}$$
$$G_{yz} = E\left[(V+N)^*(W+P)\right] = E\left[V^*W + N^*W + V^*P + N^*P\right]$$
$$\stackrel{2}{=} E\left[V^*W\right] = G_{vw} \tag{5.19}$$
$$G_{xy} = E\left[(U+M)^*(V+N)\right] = E\left[U^*V + M^*V + U^*N + M^*N\right]$$
$$\stackrel{3}{=} E\left[U^*V\right] = G_{uv} \tag{5.20}$$

where equalities 1, 2 and 3 are true for a large number of averages and then, the cross-spectral densities which include the unwanted noises are zero.

Equation 5.13 can be updated to the three signal system such as

$$\left.\begin{aligned} \frac{G_{mm}}{G_{uu}} &= \psi_x \\ \frac{G_{nn}}{G_{vv}} &= \psi_y \\ \frac{G_{pp}}{G_{ww}} &= \psi_z \end{aligned}\right\} \tag{5.21}$$

then, Equation 5.14 can be updated for the three-signal case such as

$$\left.\begin{aligned} \frac{(1-\gamma_{xy}^2)}{\gamma_{xy}^2} &= \psi_x + \psi_y + \psi_x\psi_y \\ \frac{(1-\gamma_{yz}^2)}{\gamma_{yz}^2} &= \psi_y + \psi_z + \psi_y\psi_z \\ \frac{(1-\gamma_{zx}^2)}{\gamma_{zx}^2} &= \psi_z + \psi_x + \psi_z\psi_x \end{aligned}\right\} \tag{5.22}$$

The PSD of the actually measured signals $x(t)$, $y(t)$, and $z(t)$ can be expressed from Equations 5.10 and 5.21 as follows

$$G_{xx} = G_{uu} + G_{nn} = G_{uu}\left(1 + \frac{G_{mm}}{G_{uu}}\right) = G_{uu}(1+\psi_x)$$
$$G_{yy} = G_{vv} + G_{mm} = G_{vv}\left(1 + \frac{G_{nn}}{G_{vv}}\right) = G_{vv}(1+\psi_y)$$
$$G_{zz} = G_{ww} + G_{pp} = G_{ww}\left(1 + \frac{G_{pp}}{G_{ww}}\right) = G_{ww}(1+\psi_z) \tag{5.23}$$

therefore, the coherence between the signals acquired by the far field sensor and the in-duct ones result from Equations 5.6, 5.7, and 5.23 such as

$$\begin{aligned}
\gamma_{xy}^2 &= \frac{|G_{xy}|^2}{G_{xx}G_{yy}} = \frac{G_{uu}G_{vv}}{G_{uu}(1+\psi_x)G_{vv}(1+\psi_y)} = \frac{1}{(1+\psi_x)(1+\psi_y)} \\
\gamma_{xz}^2 &= \frac{|G_{xz}|^2}{G_{xx}G_{zz}} = \frac{G_{uu}G_{ww}}{G_{uu}(1+\psi_x)G_{ww}(1+\psi_z)} = \frac{1}{(1+\psi_x)(1+\psi_z)} \\
\gamma_{yz}^2 &= \frac{|G_{yz}|^2}{G_{yy}G_{zz}} = \frac{G_{vv}G_{ww}}{G_{vv}(1+\psi_y)G_{ww}(1+\psi_z)} = \frac{1}{(1+\psi_y)(1+\psi_z)}
\end{aligned} \tag{5.24}$$

The system presented in Equation 5.24 can therefore be resolved in order to obtain the PSD of the propagated combustion noise signals $u(t)$, $v(t)$, and $w(t)$. Firstly, the three equations must be re-organised such as

$$\begin{aligned}
\frac{\gamma_{yz}^2}{\gamma_{xy}^2} &= \frac{(1+\psi_x)(1+\psi_y)}{(1+\psi_y)(1+\psi_z)}; (1+\psi_x) = \frac{\gamma_{yz}^2(1+\psi_z)}{\gamma_{xy}^2} = \frac{\gamma_{yz}^2}{\gamma_{xy}^2\gamma_{xz}^2(1+\psi_x)} \\
\frac{\gamma_{xz}^2}{\gamma_{xy}^2} &= \frac{(1+\psi_x)(1+\psi_y)}{(1+\psi_x)(1+\psi_z)}; (1+\psi_y) = \frac{\gamma_{xz}^2(1+\psi_z)}{\gamma_{xy}^2} = \frac{\gamma_{xz}^2}{\gamma_{xy}^2\gamma_{yz}^2(1+\psi_y)} \\
\frac{\gamma_{xy}^2}{\gamma_{xz}^2} &= \frac{(1+\psi_x)(1+\psi_z)}{(1+\psi_x)(1+\psi_y)}; (1+\psi_z) = \frac{\gamma_{xy}^2(1+\psi_y)}{\gamma_{xz}^2} = \frac{\gamma_{xy}^2}{\gamma_{xz}^2\gamma_{yz}^2(1+\psi_z)}
\end{aligned} \tag{5.25}$$

which results

$$\begin{aligned}
(1+\psi_x) &= \frac{|\gamma_{yz}|}{|\gamma_{xy}|\,|\gamma_{xz}|} \\
(1+\psi_y) &= \frac{|\gamma_{xz}|}{|\gamma_{xy}|\,|\gamma_{yz}|} \\
(1+\psi_z) &= \frac{|\gamma_{xy}|}{|\gamma_{xz}|\,|\gamma_{yz}|}
\end{aligned} \tag{5.26}$$

Finally, from Equations 5.23 and 5.26, the auto-power spectra of the combustion noise signal propagated to the exterior sound field can be extracted from the measured signals such as

$$
\begin{aligned}
G_{uu} =& \frac{G_{xx}}{(1+\psi_x)} = \frac{|\gamma_{xy}|\,|\gamma_{xz}|}{|\gamma_{yz}|} G_{xx} = \frac{|G_{xy}|\,|G_{xz}|}{|G_{yz}|} \\
G_{vv} =& \frac{G_{yy}}{(1+\psi_y)} = \frac{|\gamma_{xy}|\,|\gamma_{yz}|}{|\gamma_{xz}|} G_{yy} = \frac{|G_{xy}|\,|G_{yz}|}{|G_{xz}|} \\
G_{ww} =& \frac{G_{zz}}{(1+\psi_z)} = \frac{|\gamma_{xz}|\,|\gamma_{yz}|}{|\gamma_{xy}|} G_{zz} = \frac{|G_{xz}|\,|G_{yz}|}{|G_{xy}|} \;\square
\end{aligned}
\tag{5.27}
$$

This approach was developed by Chung in [63] in 1977 for microphone flow-noise rejection using the general schematic diagram for the three-signal-technique showed in Figure 5.5. On the other hand, Krejsa obtained the same external sound field results as Equation 5.27 from the schematic diagram for coherence-techniques measurements presented in Figure 5.4.

The strength of the 3-signal coherence method versus the COP, which is a 2-signal coherence method, is that the 3-signal method involves only measured cross-spectra, which is affected by the unwanted noise only if this noise correlates in the different measurement positions. This can be avoided, for example, with an optimal separation of the sensors [18]. On the other hand, COP uses measured auto-power spectra, which will always include an unwanted noise component.

It is important to note here that the 3-signal technique yields a reliable estimate of $G_w w$ which is entirely independent of the calibrations of the two internal sensors at x and y. This is very important as these calibrations may be difficult or impossible to estimate.

5.5 3-S Array technique

Data from an external array is used to generate a beamformed signal focused in the nozzle of the engine, which is referred to as Focused Beamformed Output (FBO). Influences of the room on the array output are reduced, as it is the contribution of some unwanted noise sources located away from the nozzle such as jet noise. Results (in the next chapters) show that using a 3-signal coherence technique with two of the in-duct sensors and the focused beamformed signal provides a better estimator of combustion noise than the 3-signal coherence technique alone, or the Coherence-Output Power Spectra (COP).

This technique is based in a combination of the 3-signal coherence procedure presented by Chung [63] and Krejsa [60], and the time shift focusing beamforming approached by Siller and Michel [59], who studied the core noise of an aero-engine with the aid of a

phased line array of microphones. Siller and Michel applied the COP method using the beamformed output of an external line array and a signal from a single in-duct sensor. The 3-S Array Technique combines the benefits of the 3-signal coherence versus the COP, and the use of a beamformed signal in the external field, where unwanted sources can contaminate data acquired by a single sensor.

The 3S-Array combustion noise estimator can be calculated by applying Equation 5.27. Then, the PSD of the combustion noise in the external field G_{ww}, can be calculated from the CSD of the actually measured contaminated signals. These are the CSD of the signals acquired in the combustion chamber and the external field G_{xz}, the CSD of the signals acquired in the nozzle and the external field G_{yz}, and the CSD of the signals acquired in the combustion chamber and the nozzle G_{xy}.

5.5.1 Focused Beamfored Output (FBO)

The Focused Beamformed Output (FBO) is a single time-domain signal created from the signals acquired by the microphones of an array. The FBO signal is calculated by correcting the attenuation and the propagation time from a focusing point to every microphone of the array for all the signals acquired by the array. With this methodology, the external array is behaving like a super-microphone which is pointing to a single point, and produces a single output signal, which is composed of as many signals as microphones in the array.

This classical beamforming technique is known as delay-and-sum beamforming [103], and maximizes the energy of the signals coming from the direction of focus whilst signals from other directions are rejected. It is classically presented in the frequency domain, but here is calculated in the time domain in order to be aligned and processed with the signals from the combustion chamber and the nozzle.

The process to calculate the FBO is as follows:

Firstly, the geometries of the experiment are calculated, that is, the distances from each microphone of the array to the desired focusing point i.e. the centre of the nozzle in the plane of the exit. From those distances, a negative phase shift can be obtained by applying delays to the sensor inputs.

Then, the FBO signal can be obtained as the sum of the time-adjusted and weighted channels as

$$FBO(t) = \frac{1}{L}\sum_{l=1}^{L} z_l(t-\tau_l)\frac{r_l}{r_{ref}} \tag{5.28}$$

where $FBO(t)$ is the Focused Beamformed Output signal in the time domain, L is the number of microphones of the array, z_l is the signal acquired by the l^{th} sensor of the array, τ_l is the time delay which has to be applied to each signal, and r_l/r_{ref} is the amplitude decay factor for each acquired signal, where r_l is the distance from the l^{th} sensor to the focusing point in meters, and r_{ref} a reference distance.

For digital signals, the delay is actually computed by subtracting the number of samples of the signal corresponding to the delay τ_l. The number of samples to subtract is calculated as follows

$$SMP_l = \frac{r_l f_s}{c} \tag{5.29}$$

where f_s is the sampling frequency and c the speed of sound.

The calculated Focused Beamformed Output signal can be used as a single measured signal $z(t)$, which can be processed with the data acquired by the two in-duct sensors $x(t)$ and $y(t)$ in order to obtain the 3S-Array combustion noise estimator as described in Equation 5.27.

The position of the source at the nozzle exit where the FBO is focused is determined empirically by scanning along the jet centre line of the jet, using the same approach as Siller, Arnold, and Michel [59]. This compensates the refraction in the shear layer of the jet due to jet velocity. A simulation of the FBO source image, done by scanning along the jet axis is explained in Section 6.2.1.

5.6 Summary

The theoretical foundations of the combustion noise extraction method "3S-Array" have been presented in this chapter in comparison with the COP and 3-S techniques. The 3S-Array enhances the benefit of using the 3-S processing technique by including an array of microphones in the external field of the engine, then, unwanted sources in the external field can be rejected by calculating the Focused Beamformed Output (FBO) of the signals acquired by the microphones in the external array, pointing to the end of the nozzle of the engine.

A summary of the relevant signal processing definitions needed to understand the different techniques, and the process to calculate the focused beamformed signal in the time domain were also given.

Chapter 6

Validation and applications of the 3S-Array technique

6.1 Simulations of the 3S-Array Combustion Noise Estimator

The validation and characterization of the proposed 3S-Array method has been studied by evaluating different simulated scenarios.

Let us begin by defining the geometry of the experiment. The end of the nozzle was defined in the coordinates (0,0,0), and the combustion chamber was defined at a position equivalent to a delay of 8 ms upstream of the nozzle. Three measurement positions were defined at the combustion chamber, the nozzle, and externally to the engine with an array of microphones.

Computer simulations are carried out in order to evaluate the differences between the COP, the 3-S, and the 3S-Array coherence techniques, and to asses the benefits of the FBO of the external array in the 3S-Array method.

The system presented in Figure 5.4 has been simulated. The COP, the 3-S coherence, and the 3S-Array techniques are compared for diverse states such as different amounts of unwanted noise, which distort the combustion noise signals, or various separation between the sensors. The aim of the simulation is to have a measure of how the 3S-Array method improves the estimation of combustion noise versus the other reported techniques.

6.1.1 Response of the Microphone Array

The FBO depends directly of the ability of the array to locate and discriminate a source. This characteristic of the array is represented by its Point Spread Function (PSF). The PSF determines the characteristics of the beamforming in terms of the shape of the main beam and its side lobes [52]. It is defined as the beamformed response of a point source with unit strength at an arbitrary position of a grid.

Geometries from an actual measurement campaign in Dahlewitz were used for the next PSF representations. A point source was defined in the coordinates (0,0,0), which correspond with the end of the nozzle. The point spread function for the ISVR spiral array focusing into nozzle at 350 Hz is shown in Figure 6.1. The spiral array is situated 4 m away from the nozzle parallel to the engine.

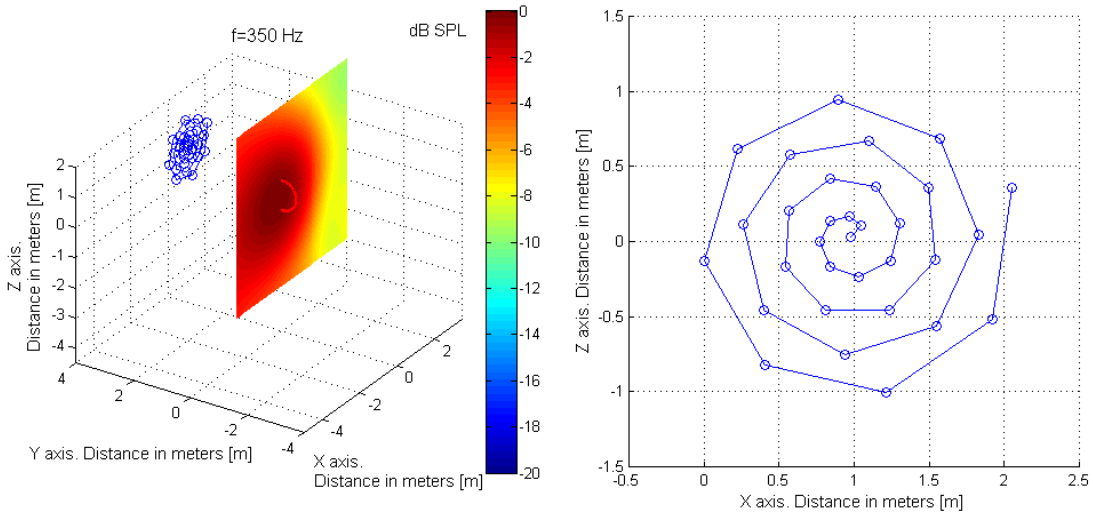

FIGURE 6.1: Point spread function for ISVR spiral array focussed on the nozzle at 350 Hz

From Figure 6.1 it can be seen that the spiral array is starting to locate the point source at 350 Hz. However, a better resolution at this frequency would be desirable for combustion noise measurement, which could be achieved by an improved array design. A full set of its PSF for different array shapes at different frequencies can be found in Appendix B.

The array geometry, 3D response pattern, and directivity elevation cut of the ISVR spiral array is shown in Figure 6.2.

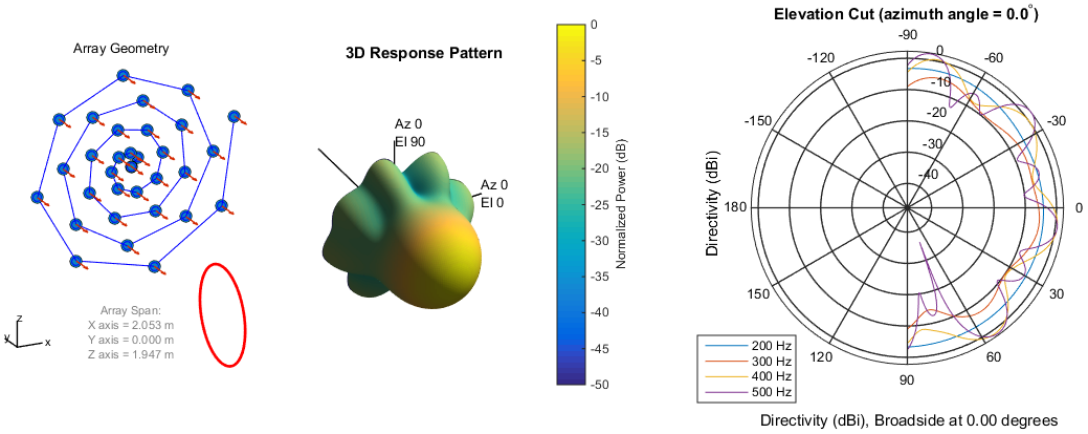

FIGURE 6.2: Array geometry, 3D response pattern and directivity elevation cut of the ISVR spiral array

6.1.2 Generation of the Signals

A random noise signal with a standard normal distribution has been generated as the combustion noise signal $u(t)$. Signals $v(t)$ at the nozzle, and $w(t)$ at the external field have been created from a linearly delayed version of the combustion signal $u(t)$. Signals $w(t)$ corresponding to the external array have been propagated accordingly with the geometries of the spiral arrays.

The presented combustion noise extraction techniques were applied to the simulated data. Two COP estimators were obtained by applying Equation 5.15 to the signals at the combustor and the external field, and the signals at the nozzle and the external field. Moreover, Equation 5.27 was applied to the simulated data of the three single sensors at the combustion chamber, the nozzle, and the external field in order to obtain the three signal coherence method. External field data is simulated from the virtual sensor of the external field array at 90 degrees, which is used by the COP and the three signal techniques. Finally, the 3S-Array combustion noise estimator was obtained by applying Equation 5.27 to the data from the combustor, the nozzle, and the full external array after calculating its Focused Beamformed Output.

Figure 6.3 shows the assessed combustion noise estimators. This is an ideal case, where simulated data was affected only with the effect of propagation, and not with noise.

It can be seen from Figure 6.3 that the estimators resolve almost perfectly the generated combustion noise signal. This is due to the absence of any noise. The desired combustion noise signal was propagated to the nozzle and to the external field without any contamination.

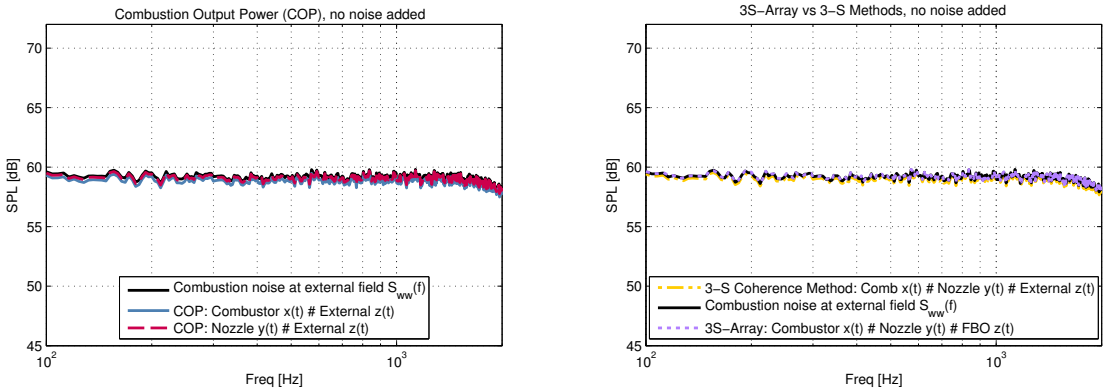

FIGURE 6.3: COP vs 3S vs 3-S Array estimators without noise contaminating the combustion noise signal

6.1.3 Addition of Noise

Random complex error was added to the sound pressure acquired by each virtual sensor with different signal to noise ratios in order to simulate a more realistic scenario and to check how noise affects to the estimators.

Figure 6.4 shows the assessed combustion noise estimators after uncorrelated random noise with a signal to noise ratio (SNR) of -10dB (noise 10dB higher than signal) was added to all the simulated sensors.

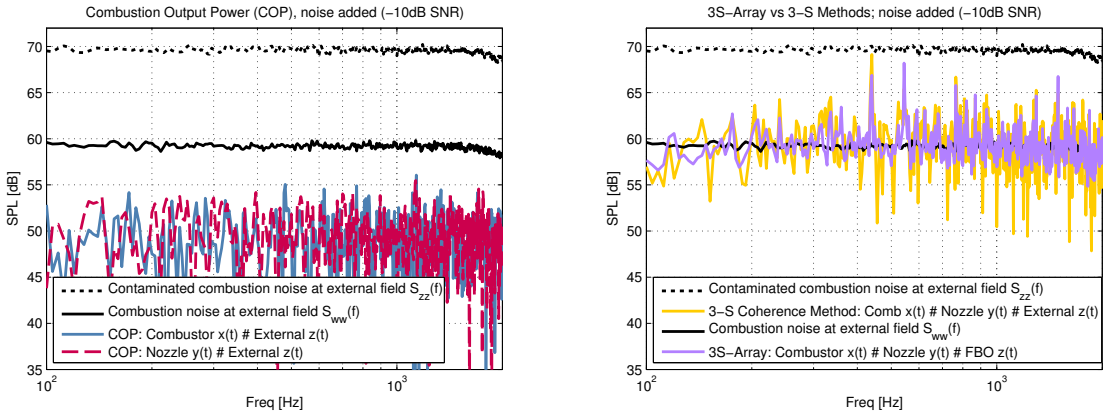

FIGURE 6.4: COP vs 3-S vs 3S-Array estimators. Uncorrelated random noise was added to all the sensors with a SNR of -10dB related to the combustion noise signal.

It can be seen from Figure 6.4 that the COP (left) has been biased by the noise. However, 3-S and 3S-Array (right) results in better estimate. Also, the 3S-Array estimator seems to be less affected by the noise.

As the simulated combustion noise signal and the contaminating noises have a flat spectrum, a statistical comparison of the estimators can be calculated. The mean and

standard deviation (std) of the estimators are shown in Figure 6.5. It can be seen that the COP is clearly biased and also that the 3S-Array has a minor standard deviation, which means that it is less affected by the unwanted noise.

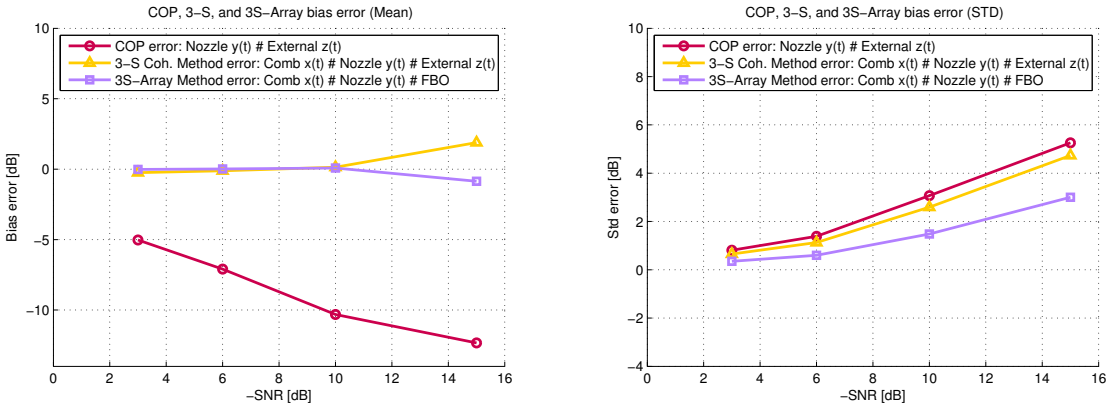

FIGURE 6.5: Bias and standard deviation of error in the spectral estimate of the combustion noise at the external sensor versus signal-to-noise ratio at the sensors for the three processing techniques.

6.1.4 Addition of External Noise Source

The main characteristic of the 3S-Array is its ability to discriminate against sources outside the focusing point. A new external noise source was created 3m downstream of the nozzle in order to probe that. The beamformed signal focused on the nozzle of the engine is generated with the data from the virtual external array. In a real scenario, other sources such as jet noise and reflections within the test cell would be significantly reduced by using this focusing technique.

The results in Figure 6.6 show that the 3S-Array method provides a better estimate of combustion noise than the 3-S technique alone for different levels of SNR. It can be seen that the 3S-Array estimator has a similar response to the 3-S estimator below 275 Hz. This is because of the lack of resolution of the spiral array at low frequencies, which can be corrected with an improved design of the array.

6.2 Application of 3S-Array technique to engina data

6.2.1 Source Image Calculation

The external array can be used to obtain the source image along the jet axis of the engine or in a plane. It can be done by focusing the array in the desired positions and

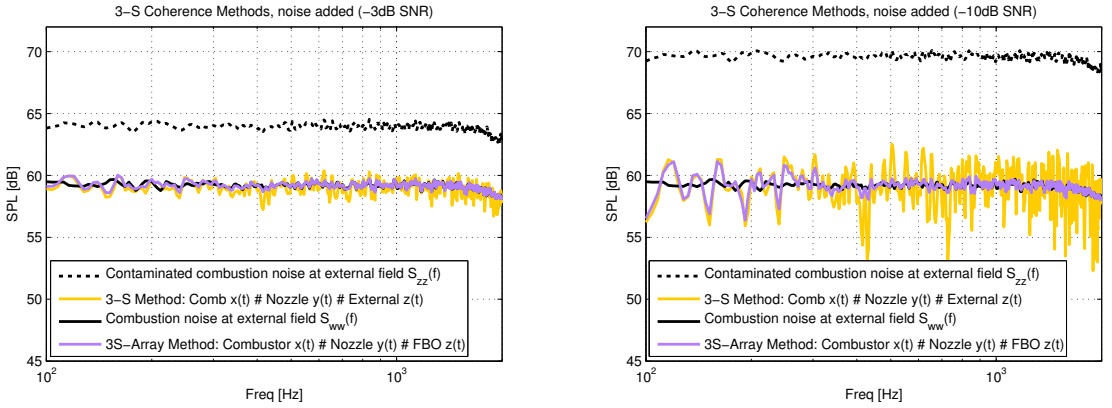

FIGURE 6.6: Spectral estimates of combustion noise at external sensor as a function of frequency for the three techniques with a signal-to-noise ratio of -3dB (left) and -10dB (right) and contaminated by the signal from an additional source, located away from the nozzle position.

calculating its Focused Beamformed Output for every desired position.

The source image of the simulated source is shown in Figure 6.7, where the area scanned goes from 6 meters upstream to 6 meters downstream of the end of the nozzle with a space resolution of 20 cm, and it can be concluded that the source image is capable to locate the position of the simulated source, which is at 0m. Results shows also the lack of resolution of the array at low frequencies especially distances far from its centre.

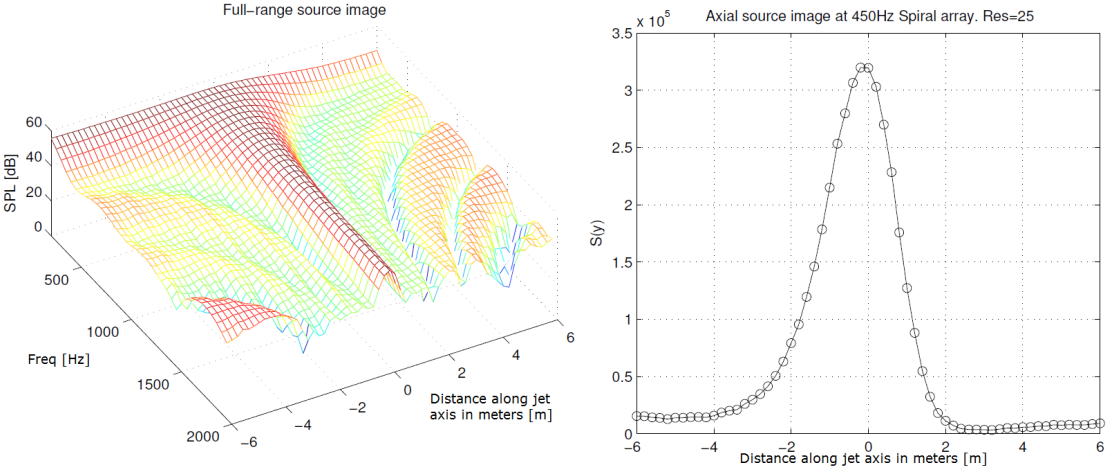

FIGURE 6.7: Full-range source image along the jet axis (left) and detailed result of the source image at 450 Hz (right) for the simulated point source at the nozzle

6.3 Error in Coherence

Error is inherit in all empirical experiments. The amount of error introduced in each calculation must be estimated and shown in comparison with the calculated final results in order to decide if they are useful or not.

Two types of error can be estimated: bias and random error. Bias error is consistent and repeatable, it is a systematic constant offset, meanwhile random error is generated from random fluctuations in the measurements or calculations. Random error can be reduced when the experiment is repeated many times, but bias error will not change.

From [68], an approximation of the bias error introduced in the coherence calculations can be calculated by

$$b\left[\hat{\gamma}_{xy}^2(f)\right] \approx \frac{1}{n_d}(1-\hat{\gamma}_{xy}^2(f))^2 \tag{6.1}$$

which means that the bias error (as a function of the coherence) approaches to zero when the number of process averages n_d is high, or the coherence $\hat{\gamma}_{xy}^2$ is close to 1.

Calculated bias error are shown versus coherence in linear and logarithm scale in Figures 6.8 and 6.9. The coherence represented in the graphs (in blue), and its error (in green added to the coherence, and in red subtracted) were calculated using the data from the ANTLE experiment acquired by the probe situated in the combustion chamber (labelled RP1) and the data acquired by the probe situated in the nozzle (labelled RPB) for a value of N1[1].

From the graphs, it is clearly shown that the difference between the bias error and the coherence becomes clearer for a lower number of averages in the coherence calculation (in this case 25 averages versus 251, which is the maximum number of averages possible for the data used, signals of 32 seconds with a sampling frequency of 32768 Hz. A window of 8192 samples was utilised)

It can be also noticed that the bias error is greater for the lower values of coherence.

The random error can be calculated by

$$\epsilon\left[\hat{\gamma}_{xy}^2(f)\right] = \frac{s.d.[\hat{\gamma}_{xy}^2(f)]}{\gamma_{xy}^2(f)} = \frac{\sqrt{2}(1-\hat{\gamma}_{xy}^2(f))}{|\gamma_{xy}|\sqrt{n_d}} \tag{6.2}$$

[1]First Shaft r.p.m.

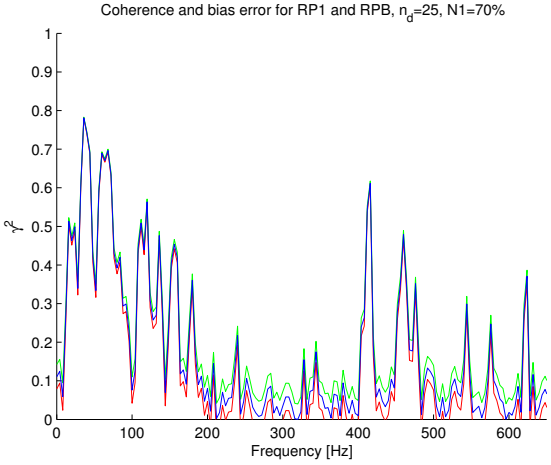

FIGURE 6.8: Coherence and bias error using an average of 25 times and lineal scale

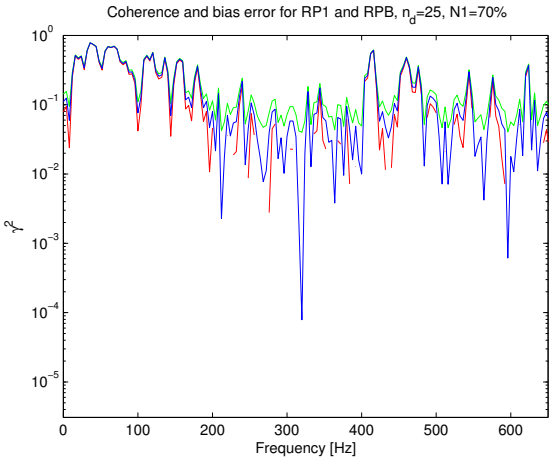

FIGURE 6.9: Coherence and bias error using an average of 25 averages and logarithm scale

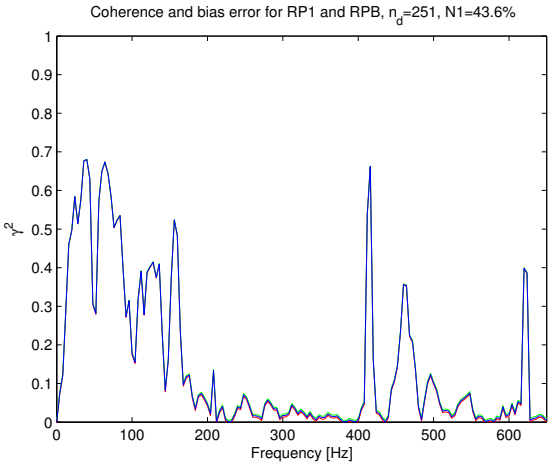

FIGURE 6.10: Coherence and bias error using an average of 251 times and lineal scale

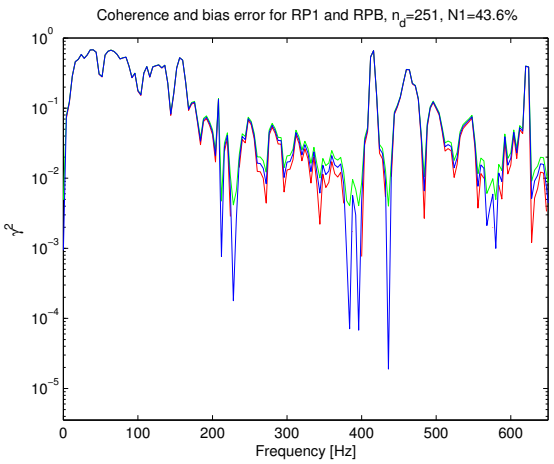

FIGURE 6.11: Coherence and bias error using an average of 251 times and logarithm scale

as it is derived in [68], where the random error is defined as a ratio between the standard deviation of the coherence by the coherence itself.

From 6.2 can be extracted the standard deviation of the coherence and it can be defined as a product of the random error with the coherence

$$s.d.[\hat{\gamma}^2_{xy}(f)] = \epsilon\left[\hat{\gamma}^2_{xy}(f)\right]\gamma^2_{xy}(f) \tag{6.3}$$

The calculated standard deviation is represented in comparison with the coherence in Figure 6.12.

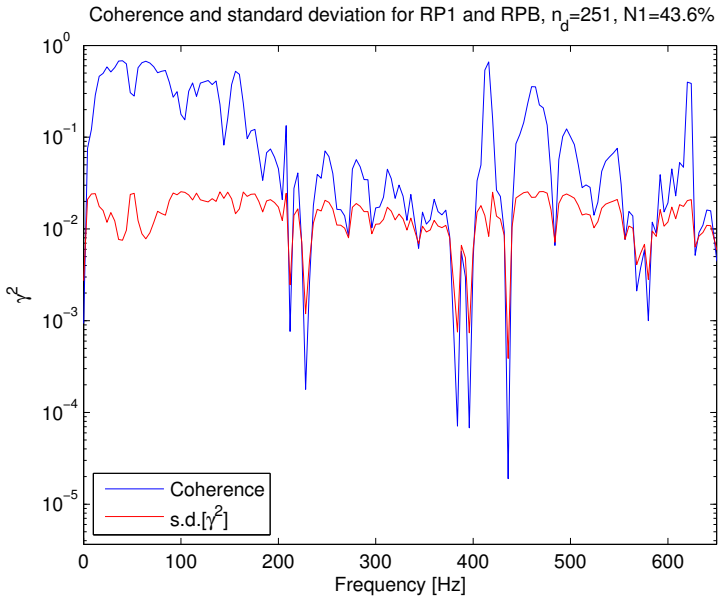

FIGURE 6.12: Coherence and standard deviation using an average of 251 times

It can be seen that the standard deviation value keeps a constant level (unless when the coherence is tending to zero) setting a threshold. It can be concluded that the better values of coherence are those where the difference between the coherence and the standard deviation is bigger.

The threshold in the standard deviation depends also on the number of averages, as it is shown in Figure 6.13. The difference between the coherence and the standard deviation becomes smaller for a fewer number of averages used to calculate the standard deviation. That proves again that better results of coherence are obtained for a larger number of averages used in its calculation.

The range of possible error in the coherence calculation represented by the standard deviation is shown in Figure 6.14 and Figure 6.15 in linear and logarithm scales respectively. A range of the estimated error is shown. The maximum values of that error range have been calculated adding the standard deviation estimated from the coherence to the same coherence (red line). On the other hand, the minimum values of that range have been calculated by subtracting the standard deviation to the coherence.

Finally, it is important to know how much this error affects the overall combustion noise spectra. In Figure 6.16 the Combustion Noise Spectra is shown as it is shown in Figure 7.12, but at this time, with the range of error added into the calculation of the coherence.

The green curve in Figure 6.16 was calculated by adding the error to the coherence before multiplying it with the auto power spectra of the data acquired in the far field,

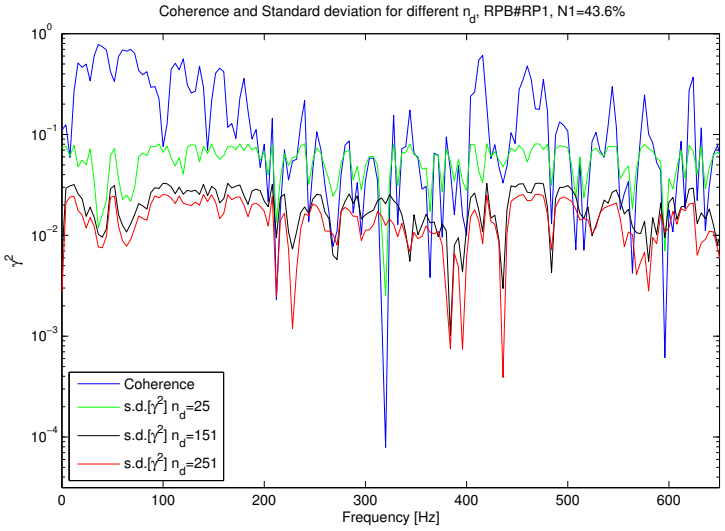

FIGURE 6.13: Coherence and Standard deviation for different averages

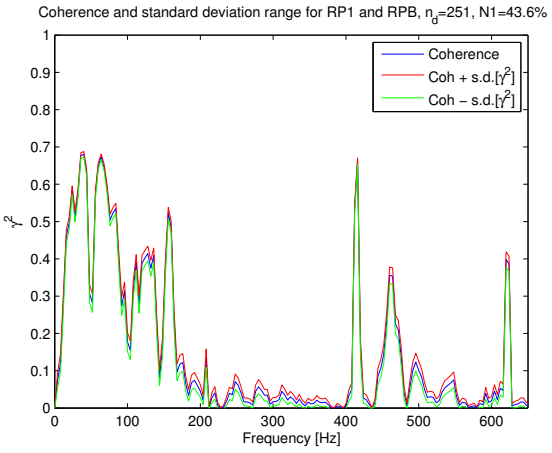

FIGURE 6.14: Coherence standard deviation using an average of 251 times and lineal scale

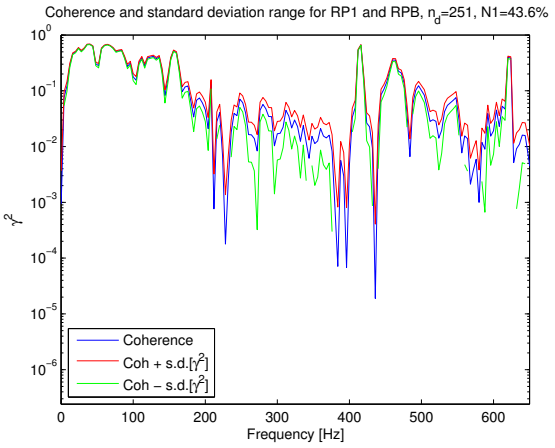

FIGURE 6.15: Coherence standard deviation using an average of 251 times and logarithmic scale

to obtain the final combustion noise spectra (also known as COP) as it is defined in Equation 2.1.

From the graph, it can be seen that the error added by the calculation of the coherence only affects a maximum of 2 dB SPL in the combustion noise spectra. Therefore, it can be concluded that it almost does not affect the combustion noise calculation.

In the same way, the error introduced in the in the 3S-Array spectra by the Coherence calculations is shown in Figure 6.17

It should be noticed that some important assumptions are made for these error calculations. The events are assumed to be stationary and ergodic random processes. That

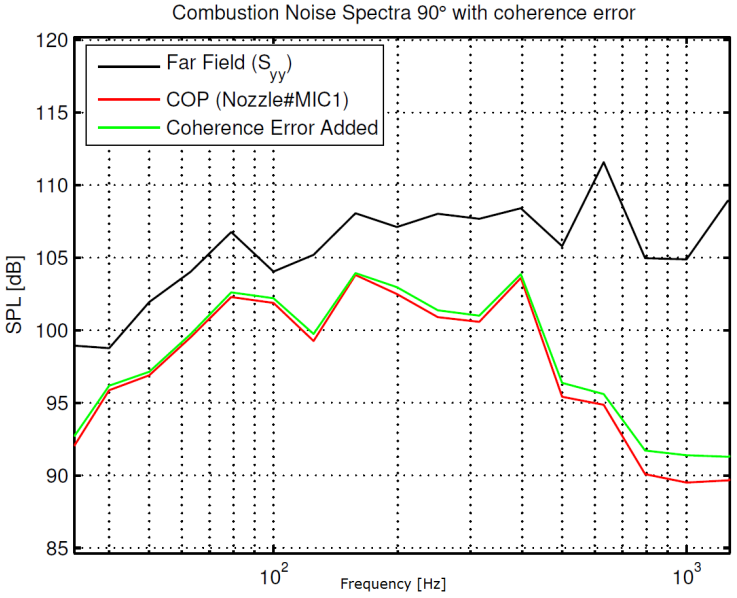

FIGURE 6.16: Error introduced by the Coherence calculations in the Combustor Noise Spectra

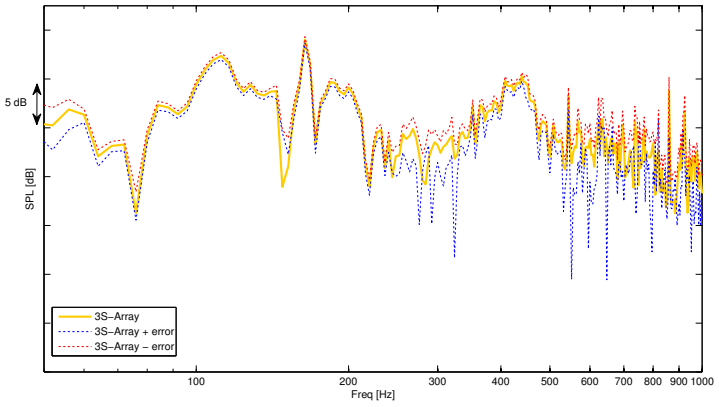

FIGURE 6.17: Error introduced by the Coherence calculations in the 3S-Array

implies processes with statistical properties which will not change over time (stationary), and with statistical properties which can be deducted from a enough sample data (ergodic). Moreover, Gaussianity was assumed too, but most of the acquired signals follow those assumptions.

The statistical error for the 3S coherence is derived from that using two signals [14] and it is expressed as

$$\epsilon[\hat{G}_{ww}(f)] \leq \frac{1}{2}\epsilon\left[\hat{\gamma}^2_{xz}(f)\right] + \frac{1}{2}\epsilon\left[\hat{\gamma}^2_{yz}(f)\right] + \frac{1}{2}\epsilon\left[\hat{\gamma}^2_{xy}(f)\right] + \epsilon[\hat{G}_{zz}(f)] \tag{6.4}$$

6.3.1 Maximum and minimum of coherence

The aligned and unaligned technique from Miles [14, 18] establishes a maximum and a minimum level of coherence for the COP and 3S techniques. It states that the maximum level of coherence is achieved when the time series are aligned, and that a coherence threshold value, or noise floor, can be obtained by deliberately misaligning them (then the signals will be uncorrelated).

This threshold ξ was defined for the COP as

$$\xi < \hat{\gamma}^2_{xy} \leq 1 \tag{6.5}$$

and for the 3S as

$$\xi^2 < \frac{\hat{\gamma}^2_{xz}\hat{\gamma}^2_{yz}}{\hat{\gamma}^2_{xy}} < 1 \tag{6.6}$$

where

$$\xi^2 = 1 - (1 - P_I)^{1/(N_s - 1)} \tag{6.7}$$

where P_I is a confidence interval for zero coherence and N_s the number of data segments to obtain the coherence.

Results of the COP, 3S, and 3S-array techniques are shown the following chapters using data acquired from full-scale engine measurements. The maximisation of the coherence was applied in their calculations (though the changes are minor due to the small distance between the different acquisition positions) but not the noise floor level to show where the signals are poorly correlated.

Chapter 7

Application of 3S-Array: the ANTLE engine

7.1 Test set-up

The Rolls-Royce ANTLE engine, which is shown in Figure 7.1, is a Trent 500 research engine, which has a lean-burn combustor in addition to other modifications [104].

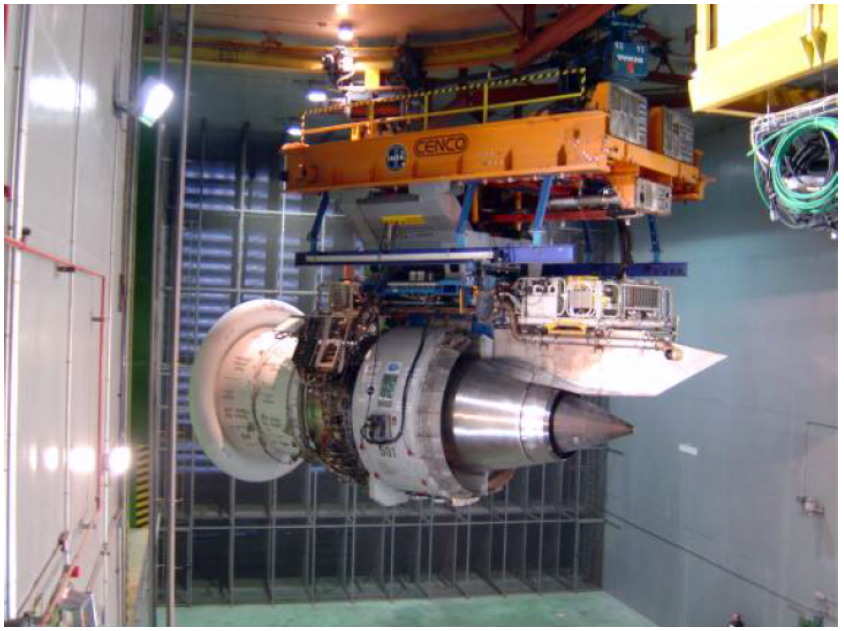

FIGURE 7.1: The large ANTLE 3/4 cowl engine being moved into the INTA test bed. Image extracted from [105]

Noise data measured from the ANTLE engine was acquired at INTA, in Spain in 2005, by DLR and ISVR within the framework of the EU Framework 5 project SILENCE(R). The

data has previously been analysed by Harper-Bourne [13], Bennett and Fitzpatrick [106, 107] and Holland [50, 106], and was used as a first approximation of how to analyse combustion noise. The following new results are presented and compared with those from Harper-Bourne.

The instrumentation of the rig is shown in Figure 7.2. Four rumble probes were installed in the combustion chamber (RP1, RP2, RP3 and RP4), two further probes in the hot-nozzle (RPA and RPB), and six microphones in the near field of the engine (M1 to M6).

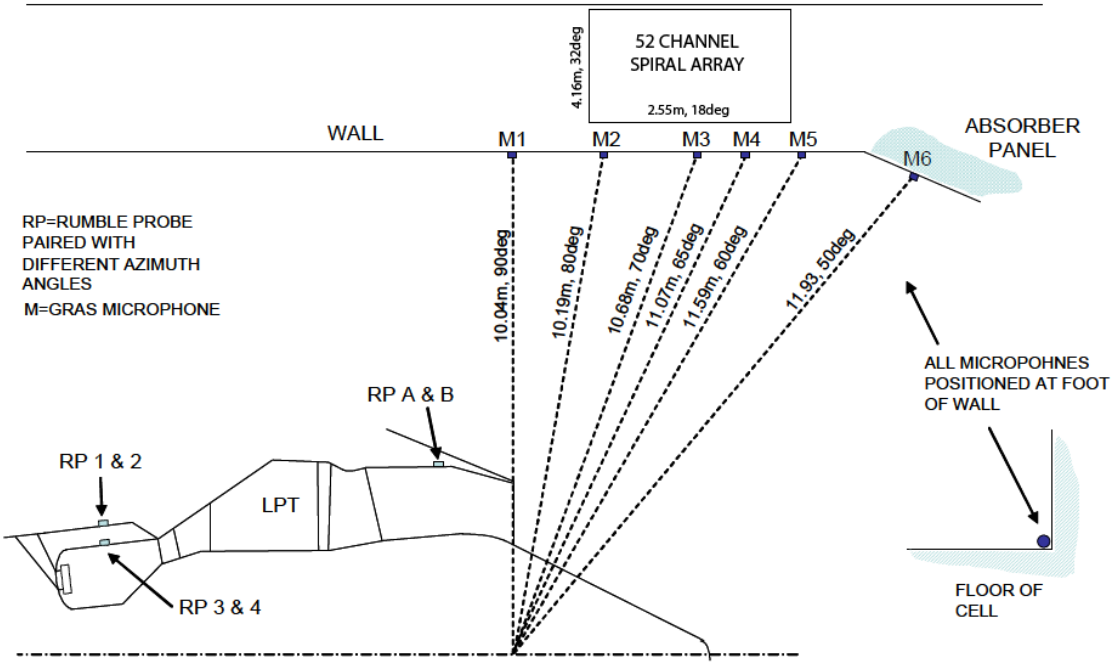

FIGURE 7.2: ANTLE instrumentation layout updated from [13]. The spiral array is placed in the wall at 7.2 m from the axis of the engine

A spiral array of microphones designed by ISVR (the data of the spiral array was also acquired by the ISVR) was situated in the wall at 7.2 m parallel to the axis of the engine, with its centre at the same height as the engine axis and at an axial position of 2.1 m downstream of the hot nozzle exit. The array consisted of 52 Bruel & Kjaer Type 4189 microphones situated in a spiral pattern truncated due to limitations of the wall covering an area of 2.55 x 4.16 m. This allowed an axial aperture of 18 degrees (from 82 to 64 degrees) and a vertical aperture of 32 degrees (from -10 to 22 degrees).

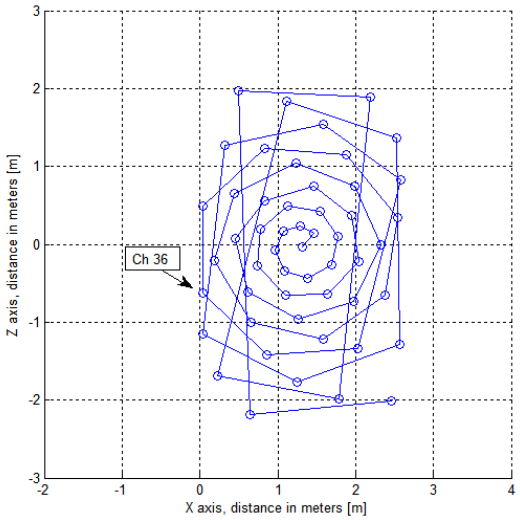

FIGURE 7.3: Detail of the geometry of the spiral array used in the ANTLE engine test, where (0,0) is the center of the hot nozzle

7.2 Data appraisal

The ANTLE set of data was supplied to the author to compare any new results with those from Harper-Bourne. Data from the spiral array and the rest of the sensors have been analysed separately in previous studies, since this would be the first time they could be analysed together, they needed to be synchronized and appraised again. Three data sets are available which corresponded with low, mid, and high speed power settings of the engine. The main results shown in this chapter are calculated using the low power setting because combustion noise is more dominant for low speeds such as in the approach manoeuvre, nevertheless, the results for the other power settings are presented in the Appendix.

7.2.1 Time domain appraisal

A representation of the acquired data in the time domain is a fast way to check if any transducers are faulty. Statistics such as the kurtosis level help to corroborate this [13].

Data are cropped to 30 s length, and re-sampled to 24 kHz to keep consistency with the rest of the data analysis carried out in this thesis. Generally, all the data sets from different acquisition systems are at different sampling rates (as it was the case in the Rolls-Royce BR700 campaign explained in next chapter). A sampling rate of 24 kHz provides a wide enough frequency range for the study of combustion noise.

Any spurious offset trends and very low-frequencies are removed from the time signals in order to avoid possible distortions in the post-processing of probability density, correlation, and spectral quantities [68].FBO in

The first 10 seconds of the time signals from three rumble probes are shown in Figure 7.4 for a low power setting, labelled 3_11. It can be seen that the means have been removed and that the signal RPA is faulty. The others, however, do not present any visible disturbances. The fault with RPA is corroborated with the statistics of the signals: the excess kurtosis value (obtained by subtracting 3 from the kurtosis value) for RPA is in the order of 1 while the excess kurtosis values for the other signals are in the expect order of 0.01. Similar inspection of the signals from the other microphones and probes reveals that they appear to be working correctly.

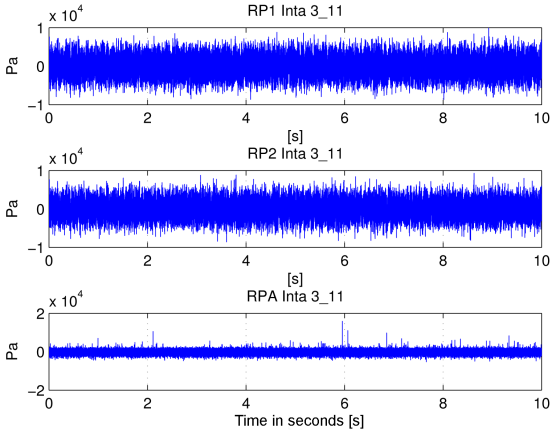

FIGURE 7.4: Replicated INTA time domain probe signals INTA at a low power setting, labelled 3_11.

7.2.1.1 Cross Correlation Analysis

Cross correlations between the signals acquired by the probes RPB, RP1, RP2, and one external microphone are shown in Figure 7.5. They were first calculated by following Equation 7.1 and Equation 7.2

$$C_{12} = \frac{1}{T}\int_0^T p_1(t) \cdot p(2)(t+\tau), \tag{7.1}$$

$$R_{12}(\tau) = \frac{C_{12}(\tau)}{\widetilde{p_1} \cdot \widetilde{p_2}}, \tag{7.2}$$

in order to reproduce the same process as Harper-Bourne, where $\widetilde{p}$ denotes the rms value. They can, however, be obtained in a faster way by calculating the inverse Fourier Transform of the signal cross spectra (using, for example, the MatLab function *xcorr*).

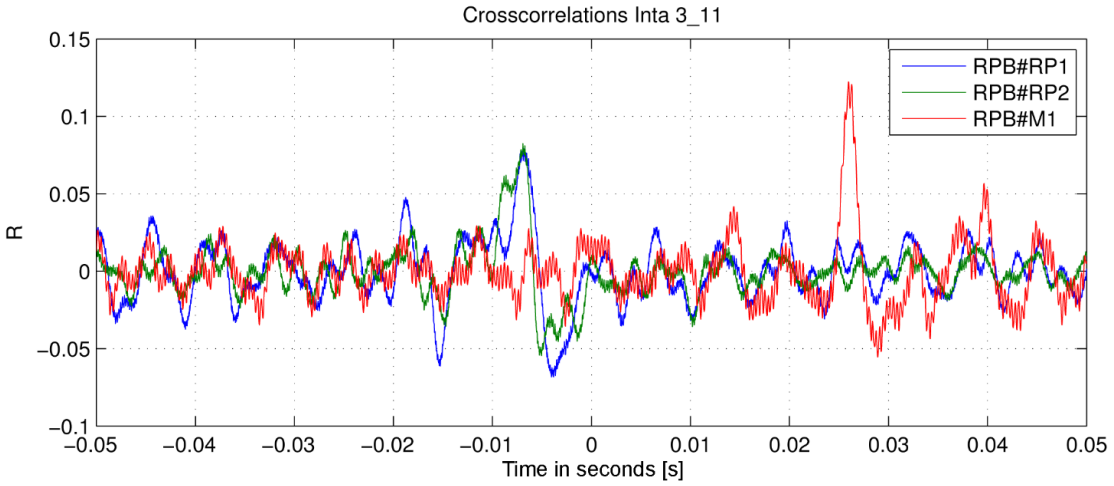

FIGURE 7.5: Cross correlation times between the probe in the nozzle (RPB) and the probes in the combustion chamber (RP1 and RP2) and in the external field (M1), at a low power setting

The parameter C_{12}, in Equation 7.1, is calculated by summing the signals $p_1(t)$ and a constantly displaced $p_2(t+\tau)$ [1]. A certain number of zeros is added to the beginning and end of the signal to fill the gap of the displacement. Signal samples of 30 seconds are used, and the factor R is applied to obtain a signal between -1 and 1.

Relative time differences can be extracted from the cross correlations. From Figure 7.5, a delay of 26 ms between the signals from the RPB probe and the microphone can be seen. The peak value of the relative level is about 0.12 R. Although it is not a very high value, it is enough to extract the physical delay between these two sources. The delay between RPB with RP1 and RP2 is -7 ms for both cases because they are separated by the same distance. The fact that the delay is negative indicates that the propagation direction is from the nozzle upstream to the combustion chamber (from the position of RPB to the position of RP1 and RP2[2]).

[1] Convolution process

[2] The peak of the cross correlation between RP1 and RPB is at +7ms

7.2.2 Frequency domain appraisal

7.2.2.1 Spectral Analysis

The data is transformed into the frequency domain by applying the Power Spectral Density (PSD) estimate to the discrete-time signals using Welch's method. Hanning windowing of 6000 samples (which corresponds to 0.250 s) is used to obtain a resolution of 4 Hz, and 960 samples (which corresponds to 0.040 s) for a 25 Hz resolution. An overlap of 50% is used in both cases with the same number of FFT points as samples per window. First, calculations are performed with a resolution of 5 Hz to be compared with those from Harper-Bourne, who chose that resolution in order to identify the presence of interference from electrical mains supplies in the data. The main results, nevertheless, are calculated with a resolution of 4 Hz, that is a standard type in Rolls-Royce. In Figure 7.6, the PSDs are displayed from the data acquired by the probes in: the combustion chamber, in the nozzle, and at 90 degrees in the external field of the ANTLE engine, at a low power setting.

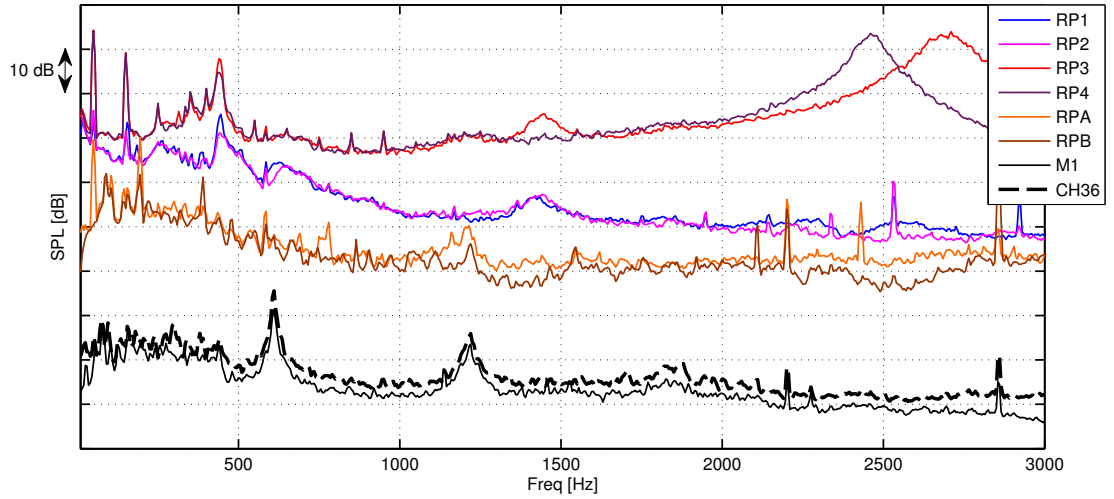

FIGURE 7.6: PSD spectra of the data acquired by the probes in the combustion chamber (RP1 and RP2: outer combustor; RP3 and RP4: inner combustor), in the nozzle (RPA and RPB), and at 90 degrees in the external field (M1: floor microphone, and CH36: microphone in the spiral array) of the ANTLE engine at low power settings.

Blade passing frequencies (BPF) and low pressure turbine tones (LPT) can be seen from the graphs of the near-field microphone spectra (shown in black). Broadband noise is seen between 100 Hz and 500 Hz, but it is not trivial to extract combustion noise information from the spectra of the external microphones.

The auto power spectra from the data acquired in the in-duct probes provide more information. RP1 and RP2 are the probes situated in the combustor outer casing and RP2 and RP3 are the probes placed in the igniter of combustion chamber, as shown in Figure 7.7. It can be seen from the graphs that the SPL in the igniter area is higher than in the outer case, as expected. A tone at 2.5 kHz appears in the response of the probes situated in the combustor. This tone is a resonance introduced by the tube in which the probes are installed (in the boroscope plane). The frequency of the tone equals to a quarter wavelength resonance.

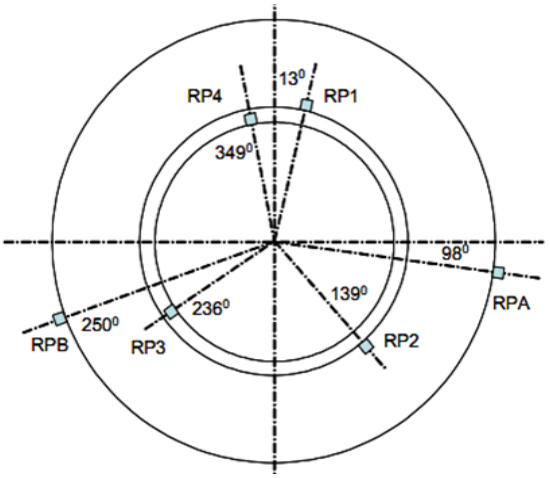

FIGURE 7.7: Location of the probes in the combustion chamber and the nozzle. The external circle represents the nozzle, and the internal circles represent the outer case and the interior of the combustion chamber.

RPA and RPB are the probes installed in the jet-pipe. The pressure levels at these points are lower than in the combustion chamber, as shown in Figure 7.6. The frequency response from the faulty probe, RPA, is slightly different to the response of RPB, especially at high frequencies, but no error is seen from the frequency domain.

7.2.2.2 Coherence Analysis

Coherence can be used as a first estimator to know how the data acquired inside and outside the engine is related.

The coherence between the data acquired at two different positions are calculated, using Equation 5.6 and are shown in Figure 7.8. Data from one transducer at each position is selected for the following analysis in order to be more reliable in the results. The various positions are shown in Table 7.1. They are each renamed for ease of reference in this chapter (as well as Chapter 8 and Appendix A). RP3 was chosen instead of RP4 because it is closer azimuthally to RPB. Less influence from the duct and the turbine

is also advantageous when studying the propagation between the combustion chamber and the nozzle. The name IGN represents the igniter, T30 is the technical name where the rumble probe is located in the combustion chamber instead of a temperature probe, NOZ1 refers to the nozzle, MIC90° refers to the floor microphone number 1 at 90°, and Spiral90° refers to the microphone of the spiral array at 90° which is the channel 36.

Position	**Probes Names**	**Selected variable**	**New Name**
Combustion Chamber Case	RP1, RP2	RP1	T30
Combustion Chamber Igniter	RP3, RP4	RP3	IGN
Nozzle	RPA, RPB	RPB	NOZ1
External field	M1 to M6	M1	MIC90°
Spiral Array	CH1 to CH52	CH36	Spiral90°

TABLE 7.1: Selection of variables and re-naming for reference

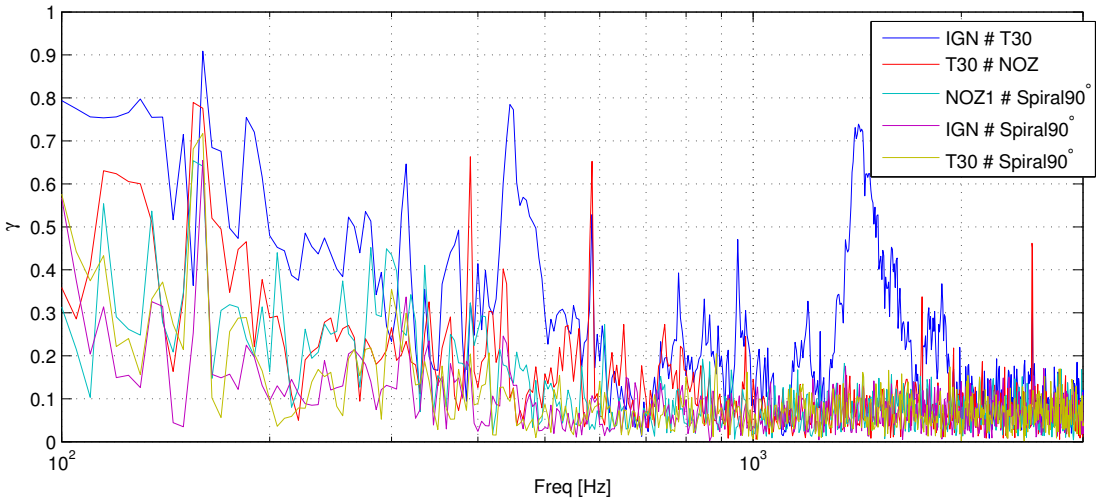

FIGURE 7.8: Coherence spectra between data acquired at different positions of the ANTLE engine at a low power setting

From Figure 7.8, it can be seen that the maximum levels of coherence for all the studied data is below 500 Hz. The coherence decays from the combustion chamber to the nozzle and from the nozzle to the external field. The coherence between the furthest sources such as the igniter and the external microphone is the lowest in the range of interest.

7.2.3 Source image

The source image of the ANTLE engine at a low engine power setting is shown in Figure 7.9. The area scanned ranges from 6 meters upstream to 6 meters downstream from the end of the nozzle, with a spatial resolution of 20 cm.

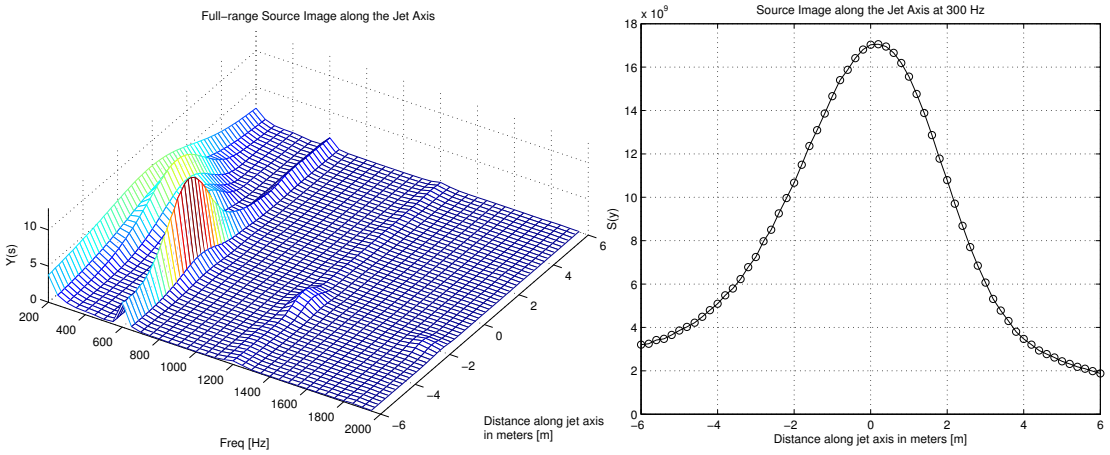

FIGURE 7.9: Full-range 3D source image along the jet axis (left) and detailed result of the source image at 300 Hz (right) for a low engine power setting

Two main sources can be located from the full-range source image. Firstly, the 600 Hz BPF tone is located between one and two meters upstream of the end of the nozzle, which corresponds with the end of the bypass of the engine. Moreover, its harmonics are noticeable around 1200 Hz and 1800 Hz. Secondly, a nozzle based tone at 300 Hz can be considered combustion noise. A detailed source image at 300 Hz is shown in the right graph of Figure 7.9. The maximum pressure is seen at 20 cm downstream of the nozzle due to the influence of the flow and it shows the best place to focus the external array in order to extract the 3S-Array estimator.

The same source image is presented with a two dimension axis in Figure 7.10. The hot and cold NBS (nozzle based sources) are well separated even at a low power setting because the bypass noise seems to be limited to tone noise from the fan (BPF at 600 Hz), with no appreciable broadband noise. The bypass nozzle is 1.4 m upstream of the core nozzle.

The 2D plot offers a detailed view of the source image in the space but the amplitude information is not that clear as with the 3D plot, which provides a fast overview to compare the amplitude of the different sources but lacks in the spatial information. Both representations are recommended for a full understanding of the source images.

The key point extracted from Figures 7.9 and 7.10 is that they show that the bypass fan broadband is very low compared to the core/NBS at least down to about 300 Hz. The array aperture limit is about 250 Hz.

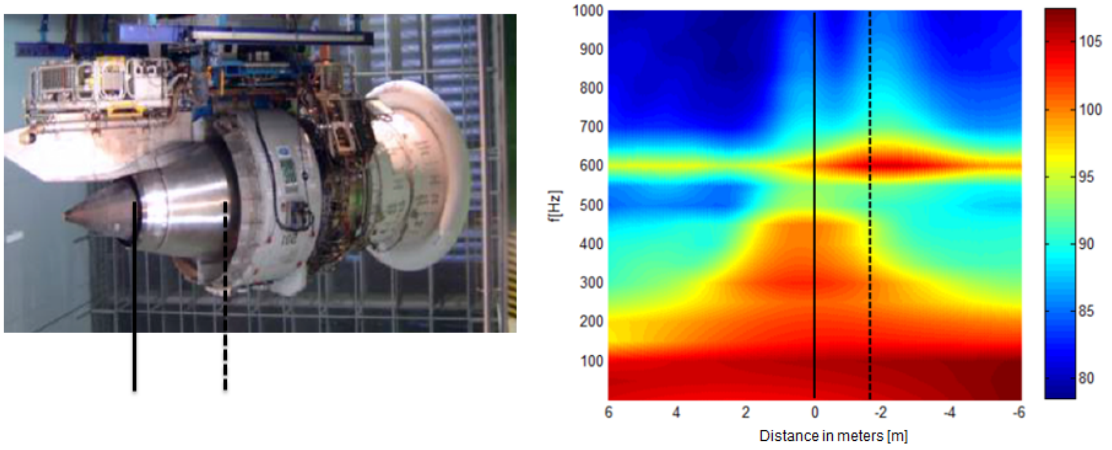

FIGURE 7.10: Full-range 2D source image along the jet axis of the ANTLE engine for a low power setting. The solid line marks the position of the hot nozzle while the dashed line marks the position of the cold nozzle.

7.3 Combustion noise estimation

7.3.1 Two Signals Technique: COP

The Coherence Output Power (COP) spectra was used by Harper-Bourne to estimate the amount of combustion noise that reaches the external field. In Figure 7.11, the COP spectra between the data acquired at the nozzle and at the 6 floor microphones are shown in the same way as Harper-Bourne, by using Equation 2.1.

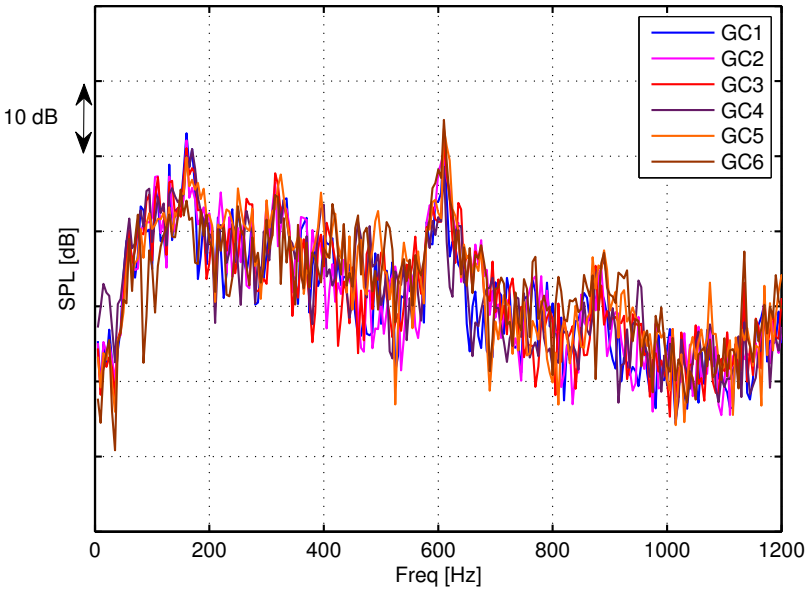

FIGURE 7.11: COP-replicated combustion noise spectra of ANTLE engine at a low power setting with 5Hz resolution

They are calculated using the cross spectra between the signals from the nozzle probes and microphones 1 to 6, and using the auto power spectra of the signals from the microphones. They are labelled "GCn", where n is the number of the external microphone.

In addition, the combustion noise spectra are represented in third octave bands versus the SPL of the external microphone at 90°, in Figure 7.12, and at 60°, in Figure 7.13. The black lines are the auto power spectra of the signals acquired by the external microphones and the coloured lines are the COP-replicated spectra. The COP spectra using data acquired from the probe in the combustion chamber is plotted with a blue line, meanwhile the COP spectra using data from the probe in the nozzle is plotted in red. Harper-Bourne assumed that direct combustion noise is acquired by the probes installed in the combustion chamber and a combination of direct and indirect combustion noise is acquired in the nozzle.

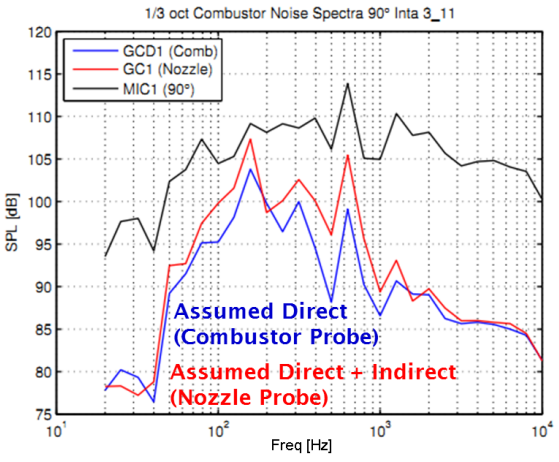

FIGURE 7.12: ANTLE 1/3rd octave Combustor Noise at 90 deg for comparison with Harper-Bourne

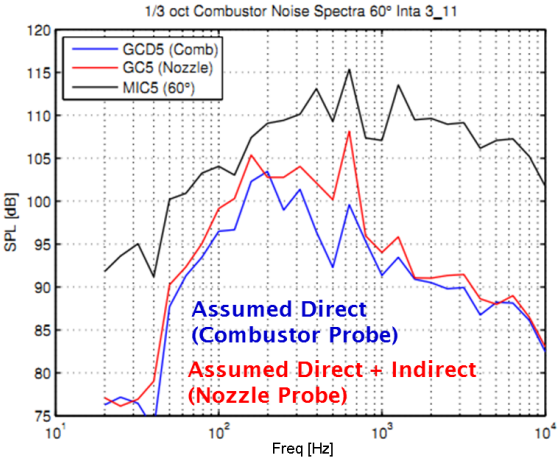

FIGURE 7.13: ANTLE 1/3rd octave Combustor Noise at 60 deg for comparison with Harper-Bourne

Harper-Bourne concluded that direct combustion noise dominates from 0 to 200 Hz, because both COP spectra are similar in that range of frequencies, but that indirect combustion noise dominates between 200 and 500, Hz because the COP from the nozzle dominates over the COP from the combustion chamber.

There are two issues with these conclusions. Firstly, it is not correct to assume that the probes in the combustion chamber are acquiring only direct combustion noise because indirect combustion noise can propagate upstream towards the igniter. Secondly, and more important, is the fact that the COP spectra from the combustion chamber and the nozzle are differently biased because they are different kind of sensors and also because

they acquire different unwanted noises, therefore, the COP spectra comparison between them is not reliable[3].

Analysis with a three signal technique is needed to avoid this bias error.

7.3.2 Three Signals Techniques: 3-S and 3S-Array

To apply the 3S-Array technique (using Equation 5.27), three coherence spectra are required, examples of which are shown in Figure 7.14. The coherence magnitude between the signal acquired in the outer casing of the combustion chamber and the FBO signal is plotted in blue, the nozzle internal signal to FBO in green, and the combustion chamber to nozzle in red. The coherence values are well above the "noise floor" at 0.1, except for frequencies above 600 Hz. The values exceed 0.7 at the lower frequencies.

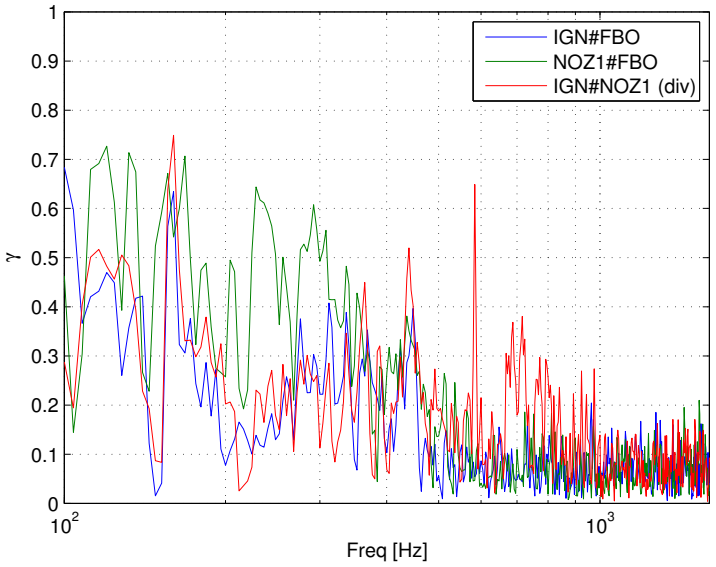

FIGURE 7.14: Coherence used for the calculation of the 3S-Array spectrum for the ANTLE engine at low engine power setting with data from in-duct sensors and a external spiral array of 52 microphones.

Results at this low engine power from the three techniques (3S-array, 3-S, and COP) are compared in Figures 7.15, 7.16, 7.17, and 7.18, along with the FBO spectrum and that of one external microphone at 90°.

The spectra of the 3S-Array is shown in Figure 7.15 in comparison with that from the FBO and from one external microphone. The 3S-Array spectrum (in yellow) uses one sensor in the combustion chamber, another in the nozzle, and the whole external array of

[3]The bias error affects the COP spectra as shown in Chapter 5, then it is not reliable to compare two COP spectra which are differently biased

microphones as the third signal. The spectra of the external microphone (in black) is the far-field overall response, used here as the main indicator of the overall noise measured in the far-field of the jet engine. The spectra of the FBO (in purple) is the response of a Nozzle Based Source, that is, the signal coming from the focused point at the nozzle that propagates to the far-field.

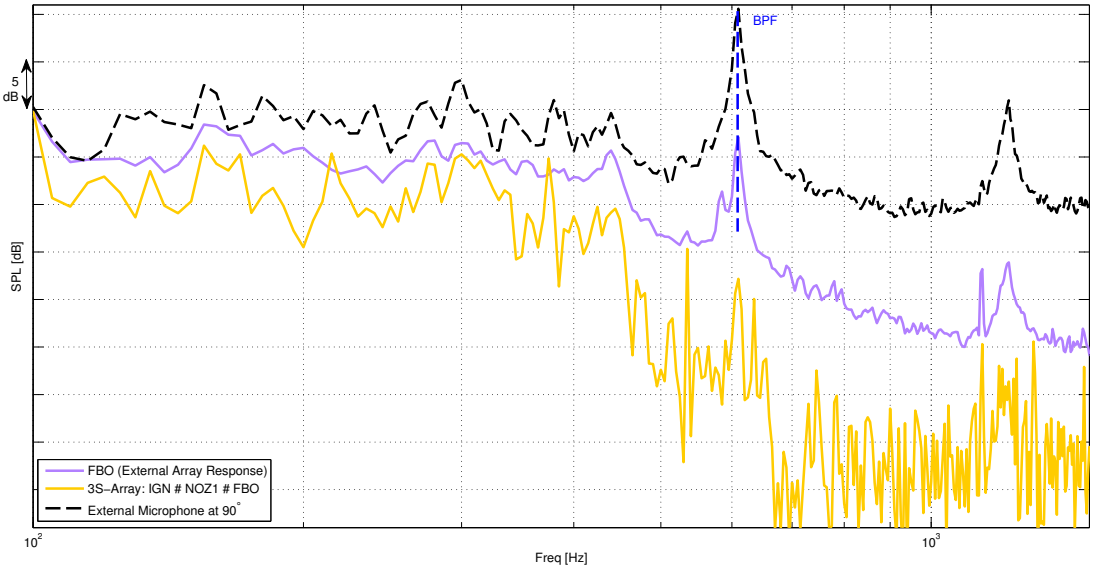

FIGURE 7.15: Comparison of combustion noise estimators. 3S-Array (in yellow), the far-field overall response from the spectra of an external microphone at 90 degrees (in black), and the spectra of the FBO (in purple).

The FBO spectrum (in purple) shows how much of the signal that reaches the far field (in black) is coming from the nozzle. It is on average about 3 dB below that of the external reference microphone, suggesting that the FBO is successfully rejecting reflections but that there are no other significant sources at this engine power.

The 3S-Array spectrum (in yellow) shows how much of the signal from the nozzle (the FBO spectrum in purple) is actually coming from the combustion chamber. This means that if the 3S-Array spectrum is close to the FBO's then the nozzle based source that propagates to the external field is composed by signal from the combustion chamber. From Figure 7.15 it can be seen that the 3S-Array spectrum is generally below that of the FBO, as expected, except at frequencies such as 150 Hz and 300 Hz, where the combustion noise is dominant, as seen in the source image in Figure 7.9.

The contribution of the combustion noise decreases for frequencies over 450 Hz, as seen from the largest separation between the FBO and 3S-Array spectra at that range. The 3S-Array rejects the BPF tone thanks of the focusing in the hot nozzle, avoiding the noise coming from the cold bypass of the jet engine where most of the noise from the fan

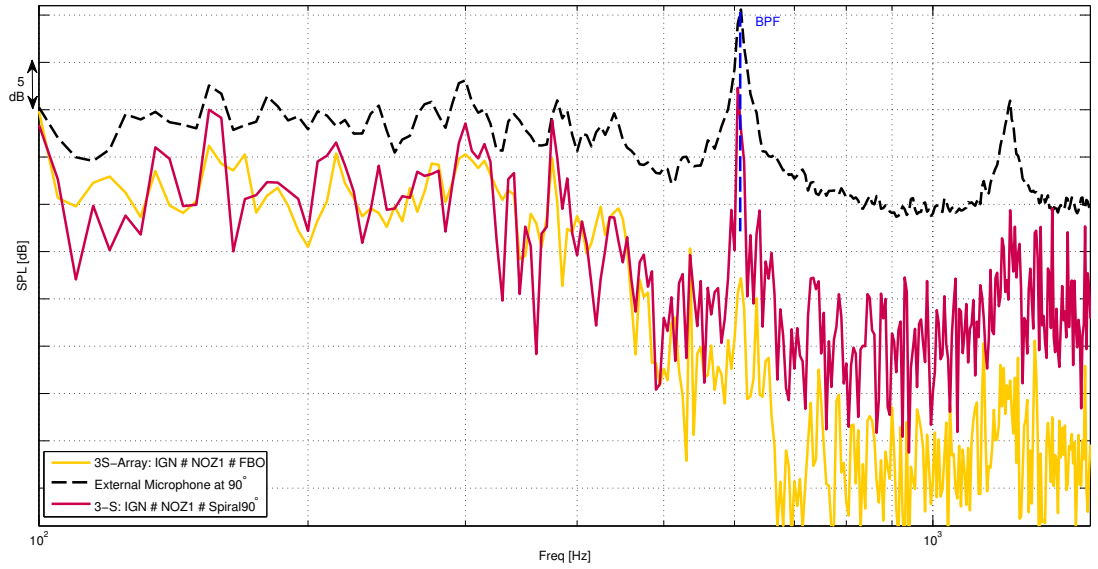

FIGURE 7.16: Comparison of combustion noise estimators. 3S-Array (in yellow), the far-field overall response (in black) from the spectra of an external microphone at 90 degrees, and the spectra of the 3-S using the same microphone as the third data point (in red).

goes. However, some of the tonal content of the BPF can be noticed in the FBO and the 3S-Array spectra, this is because some of the cold air from the intake that passes through the fan is used at the combustion process.

In Figure 7.16 the 3-S technique is compared with the 3S-Array for the same data-set. The 3-S spectrum (in red) uses two in-duct sensors (one in the combustion chamber and another in the nozzle) and one external microphone at 90 degrees (channel 36 from the spiral array). On the other hand, the 3S-Array spectrum (in yellow) uses the same two in-duct sensors as in the 3-S technique but the FBO from the whole array as the third signal.

There does not appear to be any systematic differences between the 3-S at that angle and 3S-Array techniques, which is perhaps expected given the comments above on the FBO spectrum, but the 3S-Array standard deviation is smaller than that of the 3-S, as proven with the simulations. Moreover, it seems that the 3-S starts to overestimate for high levels of contaminating noise, e.g. above 700 Hz. This can be seen in Figure 7.15 from the difference between the spectra of the FBO and the external microphone. This behaviour is also shown in the simulations in Section 6.1.3 for levels over 10 dB of SNR, but lower levels of mean deviation are expected.

It is clearly seen from Figure 7.16 that the 3-S technique is not rejecting the BPF tone as the 3S-Array does. This is a main prove of the benefits of the focusing beamforming

in the 3S-Array technique instead of using one single microphone in the far-field.

The spectra of the COP is shown in Figure 7.17 in comparison with that from the microphone at the external field. The COP using the signals from the combustion chamber and the external microphone is shown in green meanwhile the COP using the same external microphone but the probe at the nozzle is represented in blue.

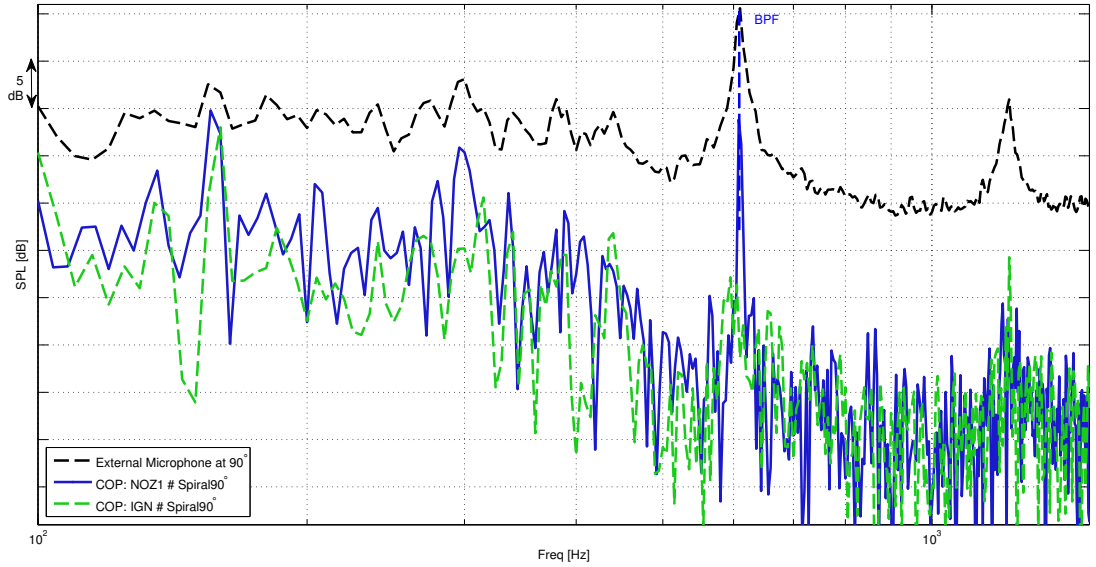

FIGURE 7.17: Comparison of combustion noise estimators. The spectra of the external microphone (in black) is the far-field overall response. The COP that uses one in-duct sensor in the igniter and the same external microphone (in green), and the COP using the sensor in the nozzle and the same external microphone (in blue).

From Figure 7.17 it can be seen that the difference between the spectra of both COP and the external microphone is larger than with the 3-signal techniques because of the underestimation of the 2-signal technique, as it is explained in Section 5.3, and proved with simulations in Section 6.1.3. Also, it can be noticed that the BPF tone is picked-up by the COP using the internal sensor at the nozzle and not when using the probe at the combustion chamber.

Another proof of the underestimation of the COP technique can be seen in Figure 7.18, where the 3S-Array spectrum is significantly above that given by the COP technique.

7.3.2.1 Estimators using an external microphone at a different angle

The 3S-Array and the 3-S do not represent the same estimator because the FBO used for the 3S-Array represents an averaged directivity while the 3-S uses a response from a single microphone in the external field, which only gives a single directivity point.

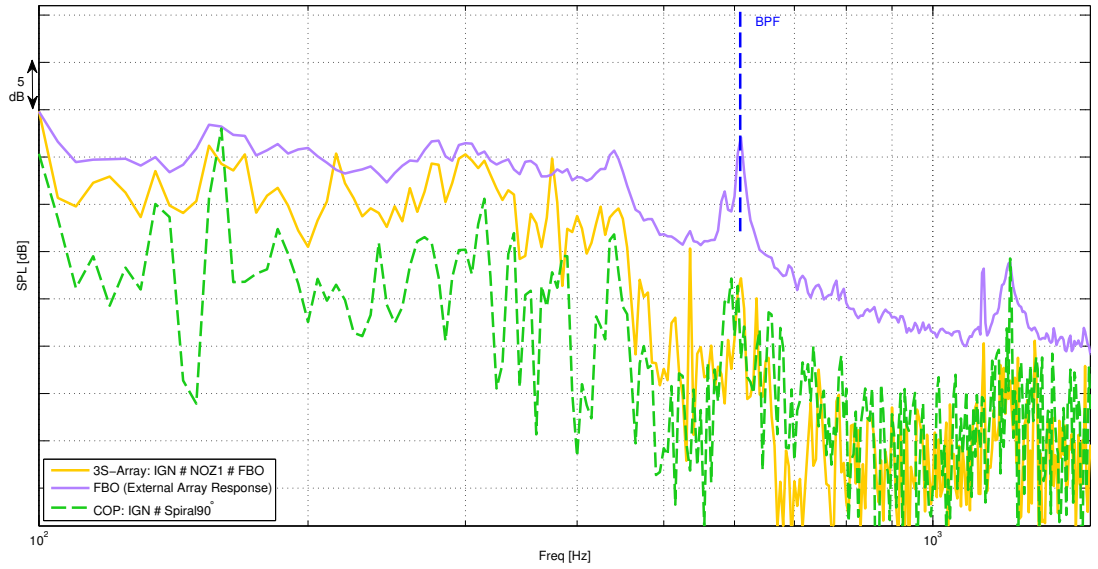

FIGURE 7.18: Comparison of combustion noise estimators. The spectra of the FBO (in purple), the COP that uses the sensor in the igniter (in green), and the 3S-Array (in yellow).

The same analysis is presented in Figure 7.19 using channel 1 of the spiral array (the external microphone placed at 108 degrees from the end of the nozzle) in order to check any difference in directivity.

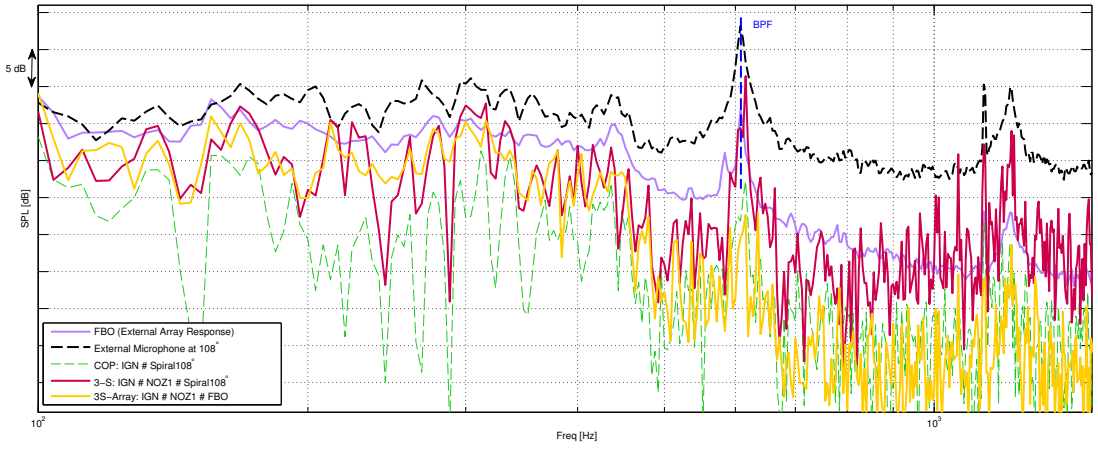

FIGURE 7.19: Comparison of combustion noise estimators. Spectra of the 3S-Array (in yellow), 3-S using the external microphone from the array at 108 degrees (in red), COP using the sensor in the igniter and the same external microphone (in green), the external microphone (in black, and the FBO (in purple).

The COP and 3-S results using the external microphone at 108 degrees are slightly different from those using the 90 degrees, which have less pronounced valleys. Again, the 3S-Array estimator has fewer spectral fluctuations than the 3-S thanks to the FBO and the use of the array instead of one single microphone, reducing the effects introduced by

the room. The author considers that the 3-S results at 90 and 108 degrees are descriptive enough, although an averaged 3-S at several angles would be interesting as future work.

7.3.2.2 The other two 3S-Array estimators: Guu and Gvv

The spectra of the other two uncontaminated signals defined in the system layout of Figure 5.4 are the original combustion noise signal $u(t)$ at the combustion chamber and its propagated version at the nozzle $v(t)$. They can be obtained (theoretically) by following Equation 5.27, as done for the 3S-Array in the external field, which is the actual $w(t)$. The estimators G_{uu} and G_{vv} are called here 3S-Array in the combustion chamber or in the nozzle respectively.

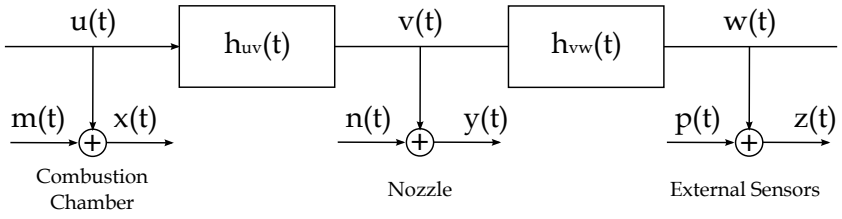

FIGURE 7.20: Representation of the propagation of combustion noise with 3 measurement points. Schematic diagram for coherence-techniques measurements

It is very important to note that although 3S-Array can yield a reliable estimate of G_{ww} because the calibration for the external microphones is accurately known, the spectra of G_{uu} and G_{vv} cannot be relied upon as they are dependent on the (generally unknown) calibration of the probes which its self is very dependent upon probe position. However, the coherence between the probe and external signals, upon which the estimate of G_{ww} depends, is largely independent of that calibration.

The estimators of the non contaminated signals $u(t)$ and $v(t)$ are plotted in Figure 7.21 together with the spectra of the contaminated signals $x(t)$ and $y(t)$, and the FBO and the 3S-Array estimator G_{ww}.

From Figure 7.21, looking first at the blue and green lines, the difference between the solid and dashed lines is the noise contaminating the combustion signal in the combustion chamber (the blue lines) and its propagated version in the nozzle (the green lines). Again, the effects of the room are observed by comparing the spectra of a single microphone in the external field (black-dashed line) with the FBO (purple line).

A wide tone is also standing out in the 3S-Array at the combustion chamber close to 550 Hz. That and other variations like higher order tones, or the dip just over 200 Hz are not obvious from the estimator at the nozzle and the external field respectively,

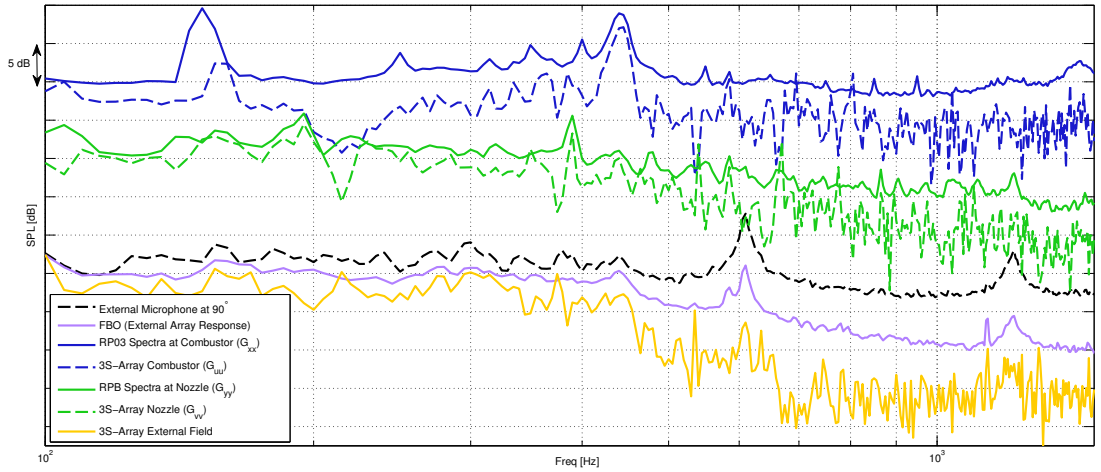

FIGURE 7.21: The blue-solid line (G_{xx}) is the spectra of the contaminated signal $x(t)$ as measured from the rumble probe RP3 in the combustion chamber, meanwhile the blue-dashed line (G_{uu}) is the estimated spectra of the uncontaminated signal $u(t)$. The green-solid line (G_{yy}) is the spectra of the contaminated signal $y(t)$ as measured from the rumble probe RPB at the nozzle, meanwhile the green-dashed line (G_{vv}) is the estimated spectra of the uncontaminated signal $v(t)$. The black, purple, and yellow lines represent the same as in the previous graphs. The black-dashed line (G_{zz}) is the spectra of the contaminated signal $z(t)$ in the external field from a microphone at 90 degrees, the yellow line (G_{ww}) is the spectra of the uncontaminated combustion noise signal propagated to the external field $w(t)$, and the purple line is the spectra of the beamformed array of microphones, FBO

which suggest that they do not propagate downstream to the nozzle and to the external field. Another working probe in the nozzle would bring more information for a better understanding of this.

7.3.2.3 Location of the probes in the combustion chamber

A study of the location of the probes in the combustion chamber is carried out by calculating the 3S-Array in the combustion chamber, G_{uu}. For this, data acquired from the probes RP1, RP2, RP3, and RP4, which are situated in different positions in the combustion chamber (as shown in Figure 7.7), are used.

The four combustion noise estimators G_{uu} are represented in Figure 7.22 using data from the four rumble probes in the combustion chamber, from the RPB probe at the nozzle, and from the FBO at the external field. Again, the spectra of the G_{uu} estimators are dependent on the unknown calibration of the probes, which are very dependent of their position, because even if the probes are calibrated prior to their installation, the exact position in their mounting is unknown.

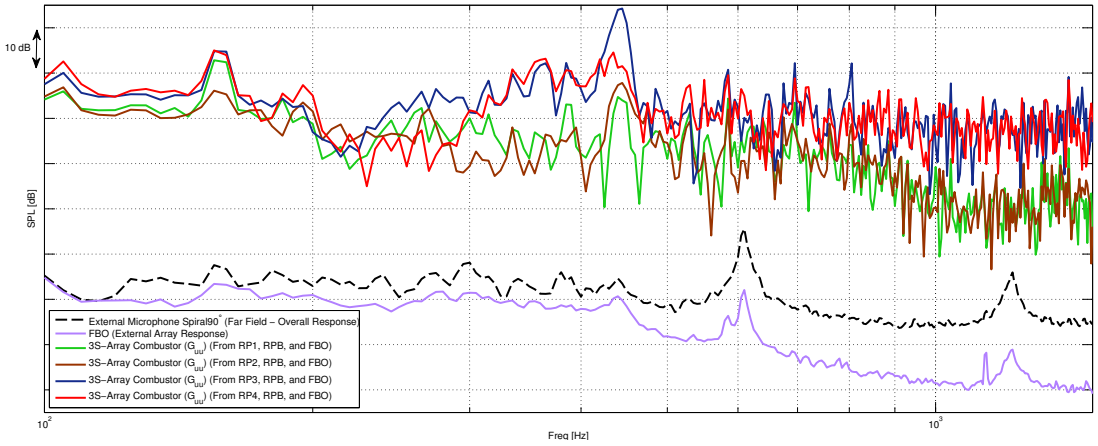

FIGURE 7.22: Comparison of the 3S-Array combustion noise estimator at the combustion chamber G_{uu} by using different probes installed in different azimuth angles in the igniter (RP3 and RP4, blue and red), and in the case at the combustion chamber (RP1 and RP2, green and brown)

There is an agreement between the estimators using data from the probes in the combustor case, RP1 and RP2 (green and brown lines), and between the estimators using data from the probes in the igniter, RP3 and RP4 (dark blue and red lines), which makes sense. This is especially true for mid and high frequencies, where we can expect the combustion noise to be statistically axisymmetric. Both pairs agree well below 200 Hz due to plane wave propagation before the first cut-on mode, as previously explained in Chapter 4.

The FBO response is obviously the same because it is the response of the array in the external field and does not depend on the in-duct probes, but the 3S-Array in the external field is not shown here because it varies depending on the specific G_{uu} chosen. A G_{uu} using RP3 was chosen for the previous results shown in this chapter because RP3 is the closest probe to RPB in the azimuth plane, providing the highest levels of coherence between those probes as it was previously shown.

7.4 Summary

Data from the large 3/4 cowl ANTLE engine, previously analysed by Harper-Bourne, is re-analysed by applying a three signal coherence technique instead of the two signal COP. Data from the external array is synchronised and analysed together with in-duct data for the first time. The spectral levels obtained using the 3S-Array technique are higher than those from the COP and below that of the FBO, as expected. The underestimation

of the COP is clearly shown with the comparison between the three signal coherence techniques 3S-Array and 3-S.

Data from the external array is used to calculate the image source of the engine along its axis and two main noise sources are located: one at 600 Hz from the bypass duct which corresponds with the BPF of the fan, and another from the nozzle at 300 Hz. Results of the 3S-Array estimator show that most of the information around 300 Hz is coming from the combustion chamber and, thus, that the nozzle-based source is principally formed by combustion noise.

The effects of using a focused beamformer to reject the external noise is proven by comparing the spectrum of the FBO versus that from an external microphone. The spectrum of the FBO focused at the nozzle rejects most of the unwanted noise that is not coming from the nozzle. This benefits the 3S-Array results, which clearly reject, for example, the BPF coming from the bypass duct. Moreover, the spectra of the 3S-Array is cleaner than that from the 3-S because it rejects the external noise and effects of the room, that the 3-S technique cannot reject with one single microphone.

The FBO provides a measure of the strength of the nozzle-based source but this can be contaminated by other sources such as fan and turbine noise. A comparison with source breakdowns techniques will help to confirm whether the FBO is rejecting reflections and other sources. This is done in Chapter 8 with data from a Rolls-Royce BR700 series engine.

Two additional 3S-Array estimators are calculated at the combustion chamber and the nozzle, but further research into this is needed as a comparison might help to understand possible differences between direct and indirect combustion noise.

Chapter 8

Application of 3S-Array: BR700 engine

8.1 Test set-up, engine, and instrumentation

An indoor noise test was carried out with a Rolls-Royce BR700 type engine, in October 2011, at the test bed ADAM, in the Rolls-Royce facilities of Dahlewitz, Germany, shown in Figure 8.1.

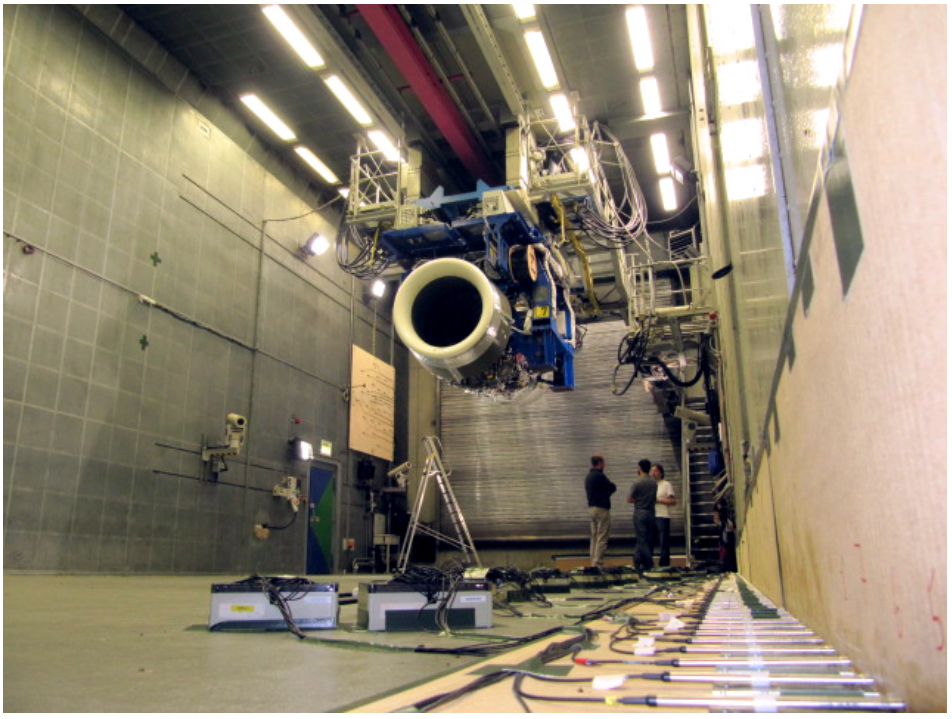

FIGURE 8.1: Indoor noise test of a Rolls-Royce BR700 type engine in Dahlewitz.

The test was partly funded by the German national R&T project "MASSIF-EffekT" and the Ministry of Commerce and Technology. Its main objectives were to study the generation and radiation characteristics of turbine and combustion noise, and to develop and validate indoor noise measurement techniques from ISVR and DLR. It was a replica version of the test conducted in the outdoor facility of Rolls-Royce's Stennis Bed 59 (former Bed 1) in July 2011 with exactly the same engine. The engine conditions were the same in both tests, except for the IDG (Integrated Drive Generator) of the engine, which was with a different build standard at Dahlewitz. An extra noise test was carried out to check that the use of the IDG did not affect the acoustic near field data.

The instrumentation of the rig is shown in Figure 8.2.

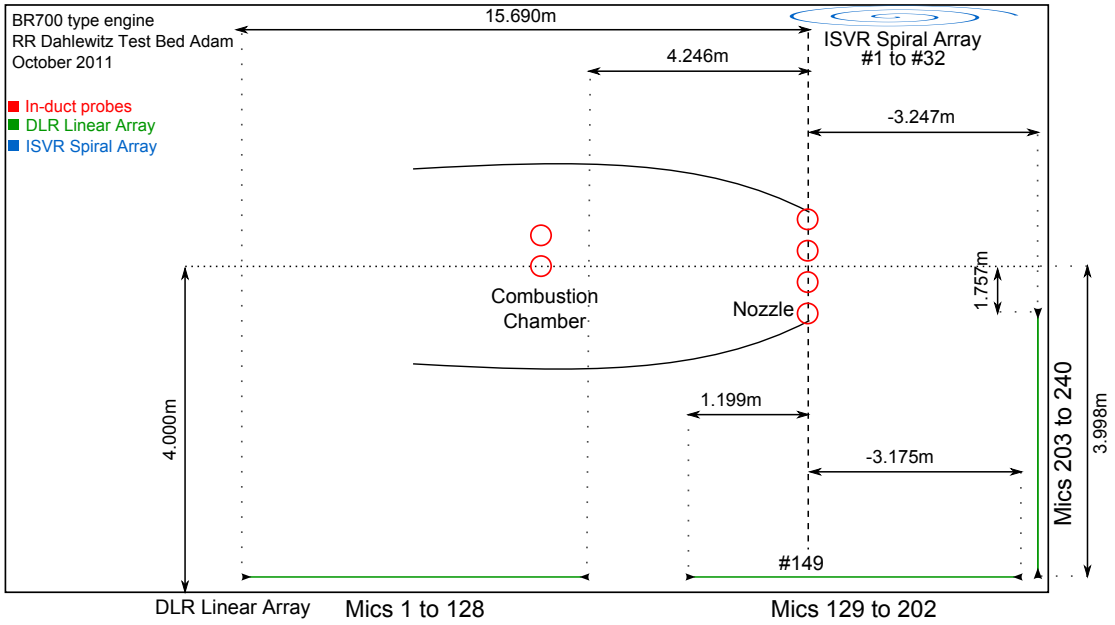

FIGURE 8.2: Layout of the noise measurement set-up of the Rolls-Royce BR700 type engine at Dahlewitz, RR Germany in 2011.

Two rumble probes were installed in the combustion chamber, four surface-mounted transducers at the end of the nozzle, and two different arrays of microphones in the external field of the engine.

8.1.1 In-duct sensors

The location of the in-duct sensors installed in the BR700 type engine are shown in Figure 8.3. The probes in the combustion chamber were placed in a similar location to the ANTLE engine tests: one in the igniter and another in the case of the combustion chamber (replacing the temperature probe in the T30 position).

FIGURE 8.3: In-duct sensors utilised for the noise test: two rumble probes in the combustion chamber and four surface-mounted transducers at the end of the nozzle.

Four surface-mounted sensors were glued at the end of the nozzle with a separation of 90°, see Figure 8.4. Data acquired from these sensors was not usable for high power settings, as will be explained in Section 8.2.

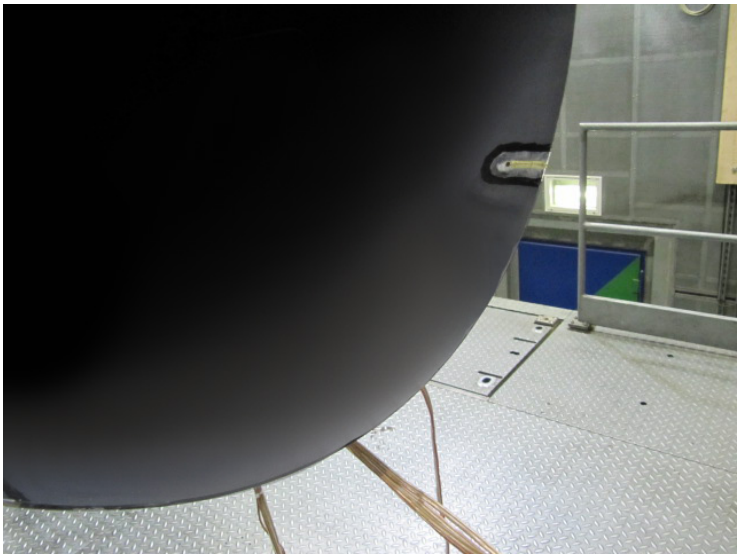

FIGURE 8.4: Detail of the installation of one of the four surface-mounted probes at the end of the nozzle.

8.1.2 Arrays in the external field

A linear array of 240 microphones was deployed by DLR in the test bed at the same distance to the engine as in the outdoor test at Stennis. The main differences between the tests are that (1) the array had to be cropped in Dahlewitz due to the control room staircase, and (2), the end of the array had to be installed on the rear wall due to space constraints. Further information concerning the linear array can be seen in Figure 8.2 and Figure 8.5.

FIGURE 8.5: Linear array deployed by DLR. A total of 240 microphones were installed pointing to the wall on the surface of a board. The array is interrupted by the control room staircase.

A spiral array of 32 microphones was deployed by ISVR in a side wall of the test bed downstream of the end of the nozzle. Microphone number 1 was located at the center of the array and it was placed at the same height as the centre of the engine. Microphone number 28 was located to the left in the spiral and was also used as a guide to align the array with the end of the nozzle, as shown in Figure 8.6 and Figure 8.7.

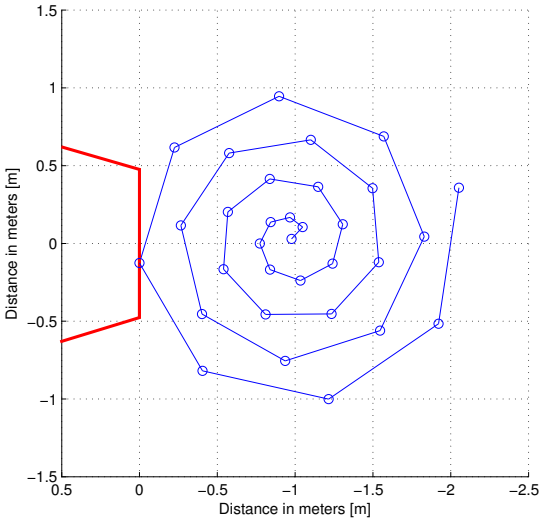

FIGURE 8.6: Geometry of the spiral array deployed in t the BR700 type engine at Dahlewitz in reference with the end of the nozzle (in red)

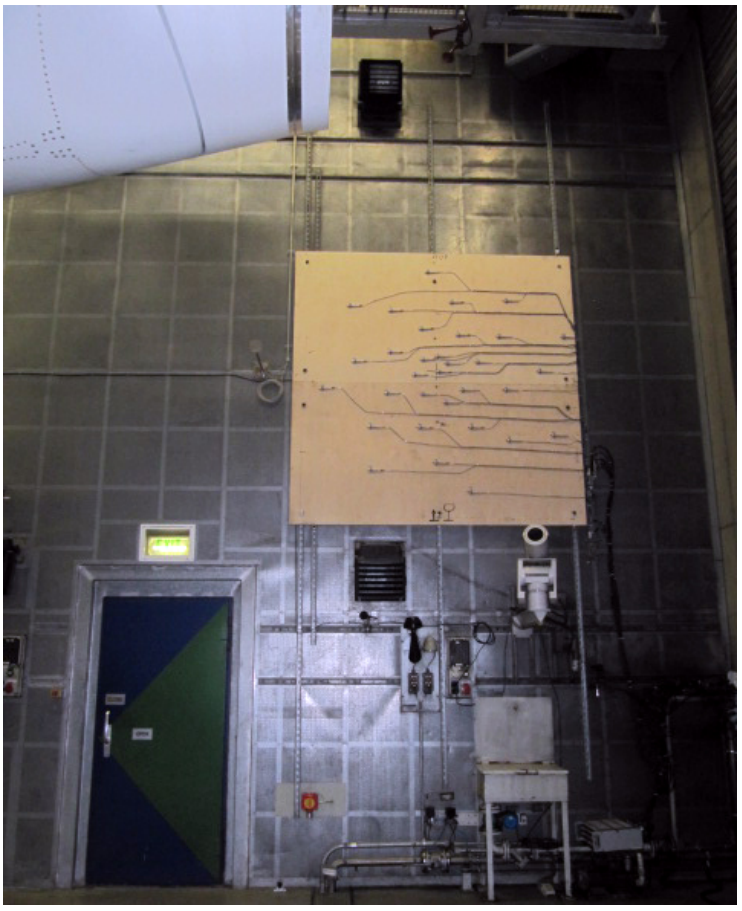

FIGURE 8.7: Spiral array designed and installed by ISVR at Dahlewitz, Rolls-Royce Germany, 2011.

8.2 Data appraisal

Each of the arrays used different acquisition systems. The data from the in-duct sensors were acquired with the PAK recording system from Rolls-Royce Deutschland, the data from the spiral array was acquired by ISVR with a SONY recorder, and the data from the DLR linear array was acquired with their own system from DLR. An IRIG-B synchronisation signal was sent to the ISVR system and to the DLR system. Moreover, the sampling rates were different for the three systems.

In order to combat this, all the data was post-processed by Chris Knighton from Rolls-Royce UK. Each of the signals were synchronised, resampled to 24000 Hz, and cropped into 26-second samples to facilitate the further post-processing. For future tests it is recommended to acquire all signals with the same acquisition system.

Several noise curves (data acquisition per engine set-up) were run during the indoor test, including backup repeats. Different set-ups and power settings were carried out

to replicate the outdoor test in Stennis, but, here, only one of those noise curves, the standard baseline configuration, is analysed.

Once the engine was stabilised, signals were recorded for two minutes at each test point. The test points were set from the low idle to the maximum power settings in small increments. The results in this chapter focus on one low power setting. The remain data are shown in Appendix C.

The names of the variables have been reassigned by the author for clarity, see Table 8.1.

Position	**Probe Name**	**New Variable Name**
Combustion Chamber Igniter	B2339A1	IGN
Combustion Chamber Case	B2340A1	T30
Nozzle	B3684A1 to B3684D1	NOZ1 to NOZ4
Linear Array	CH01 to CH240	DLR XX°
Spiral Array	CHANNEL1 to CHANNEL32	Spiral XX°

TABLE 8.1: Renaming of the BR700 test variables (following the same notation as in the ANTLE experiment).

8.2.1 Time domain appraisal

A representation in the time domain of one second of the acquired data is shown in Figure 8.8. It can be seen that the NOZ2 and NOZ3 signals are clearly corrupted.

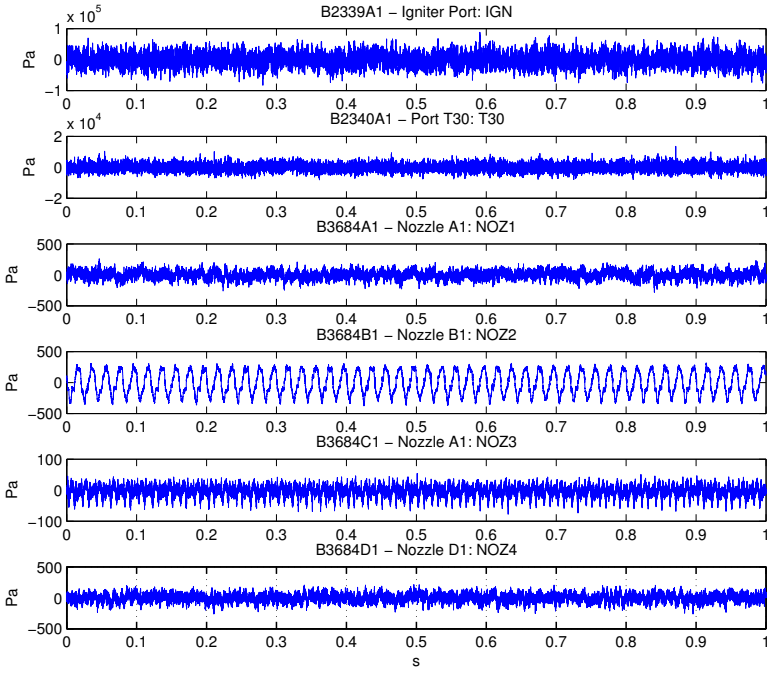

FIGURE 8.8: Time signals in seconds [s] from BR700

The kurtosis statistics, shown in Table 8.2, further indicate that the signals from NOZ2 and NOZ3 are corrupted (due to faulty sensors). Levels of excess kurtosis (kurtosis -3) far from zero indicate a variation from the normal distribution, which indicates that the signals are corrupt.

Signal	**Excess Kurtosis**
IGN	0.012675704
T30	-0.056922846
NOZ1	-0.028742472
NOZ2	-1.32785773
NOZ3	0.158856347
NOZ4	0.096422933

TABLE 8.2: Kurtosis statistics from BR700 test probes

8.2.2 Frequency domain appraisal

The time signals were transformed into the frequency domain by applying the Welch's Power Spectral Density estimate, as previously done with the ANTLE data. In Figure 8.9, the PSD of the data acquired by the probes in the combustion chamber, in the nozzle, and at ±90 degrees in the external field of the engine from both arrays, are displayed at the High Idle test condition power setting.

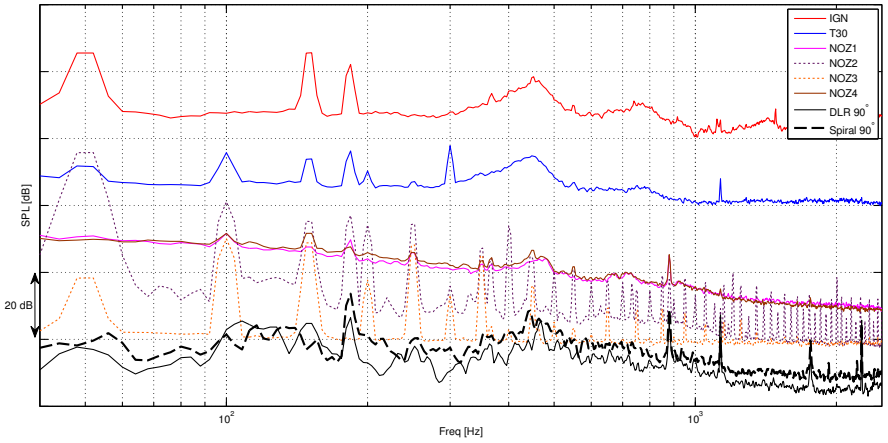

FIGURE 8.9: Spectra of the data acquired by the probes in the combustion chamber (IGN and T30), in the nozzle (NOZ1 to NOZ4), and at ±90 degrees in the external field (spiral and linear arrays) of the BR700 type engine at the High Idle power setting.

At the low end frequencies, the influence of the electric mains can be seen in the spectra acquired by the probes in the combustion chamber. An in-house tone subtraction script was applied to the data to reduce this influence but the tones still remained due to

their spectral width. A tone located at 180 Hz is not related with the mains and was acquired by all sensors (although is quieter at the nozzle). The BPF tone at 880 Hz can be found in the nozzle and in the external field, and another tone is located around 1100 Hz. Source image analysis will explain this later. Furthermore, from the graph it can be concluded that sensors NOZ2 and NOZ3 are faulty. The main spectral characteristic from the spectra of the probes in the combustion chamber is the hump at 450 Hz, which is also noticeable in the nozzle and the external sensors. A second hump at 770 Hz can be seen from both the IGN and T30 spectra but not in the nozzle or the external field.

The flat NOZ1 and NOZ4 spectra suggests that the tonal data is masked by the broadband noise. It is necessary to analyse other power settings to check this.

Spectral characteristics that can be seen in the combustion chamber and in the external field should be noticed in the nozzle spectra too. The tone at 180 Hz, for example, and the hump above 400 Hz are only seen from the nozzle spectra at the lowest power settings, see Figure 8.10. The spectra at the nozzle becomes more flat for higher power settings, which suggests that the acquired signal is masked by background or self-induced noise from the sensor.

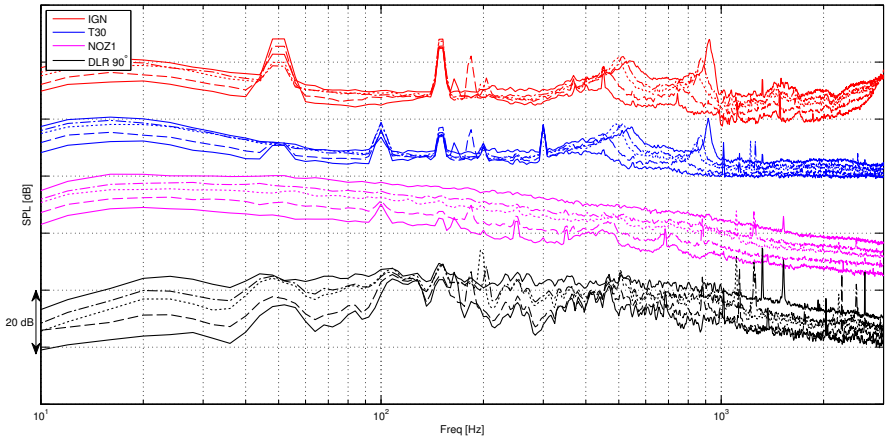

FIGURE 8.10: Spectral data acquired by the probes in the combustion chamber (IGN and T30), in the nozzle (NOZ1), and at 90 degrees in the external field (from the linear array) of the BR700 type engine at different power settings: Low Idle (solid), High Idle (dash), Low Speed (dot), Low-Mid Speed (dash-dot), Mid Speed (upper solid).

8.2.2.1 Coherence Analysis

A study of the coherence between the data from the working probes at the nozzle (NOZ1 and NOZ4) has been carried out. It was concluded that the surface sensors at the nozzle only acquired reliable data at the low power settings. Moreover, a lack of coherence

between the data from the spiral array and from the other sensors was found. This indicates a possible problem with the synchronisation of the data from the spiral array. Both cases are explained here.

The coherence between data from the two working sensors at the nozzle (NOZ1 and NOZ4), and between NOZ1 and DLR90° are shown in Figure 8.11 (left and right graphs respectively) for different power settings. For display clarity, results are presented in the frequency range of interest where the combustion noise hump is located, between 400 and 750 Hz. The levels of coherence are expected to be high at both situations because of their proximity (for NOZ1 and NOZ4), and the direct propagation (for NOZ1 and DLR90°). But values over 0.2 (considered as the minimum acceptable by the author as explained in Section 5.3) are only found at Low-Mid power setting or lower.

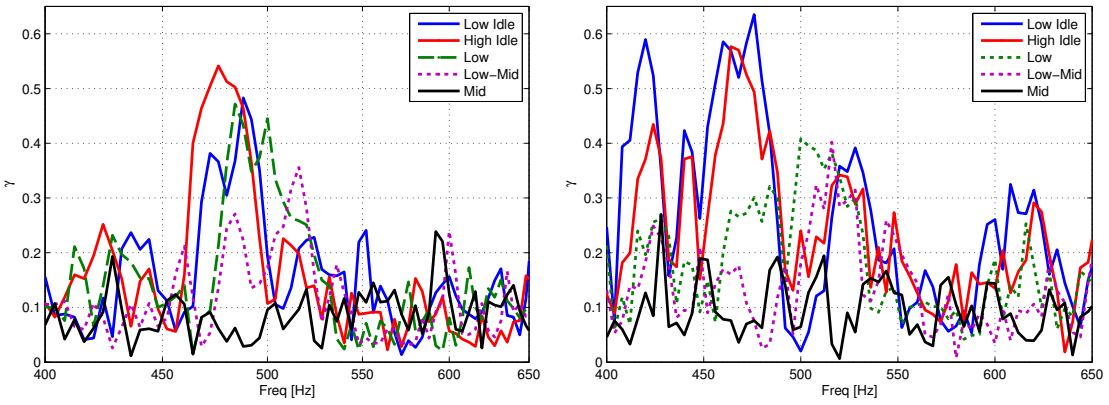

FIGURE 8.11: Coherence between the data from the pair NOZ1-NOZ4 (left), and from NOZ1-DLR90° (right), at different power settings of the Rolls-Royce BR700 type engine.

Note that the average coherence between the data from the nozzle sensors at a mid power setting is roughly 0.1; the same as the coherence between two random signals. This indicates that the surface sensors at the nozzle are acquiring random noise for mid or higher power settings. In the rest of this chapter, therefore, only the first three power settings, "Low Idle", "High Idle" and "Low" will be analysed.

The coherence between the data from the pairs SPIRAL90°-IGN, SPIRAL90°-NOZ1, and SPIRAL90°-DLR90° (exactly opposite one to each other) is shown in the top graph of Figure 8.12. In the bottom plot, the same coherence calculations are plotted but instead using data from the microphone at 90 degrees to the nozzle from the external linear array. A direct comparison between the data from both external arrays and the rest of the sensors.

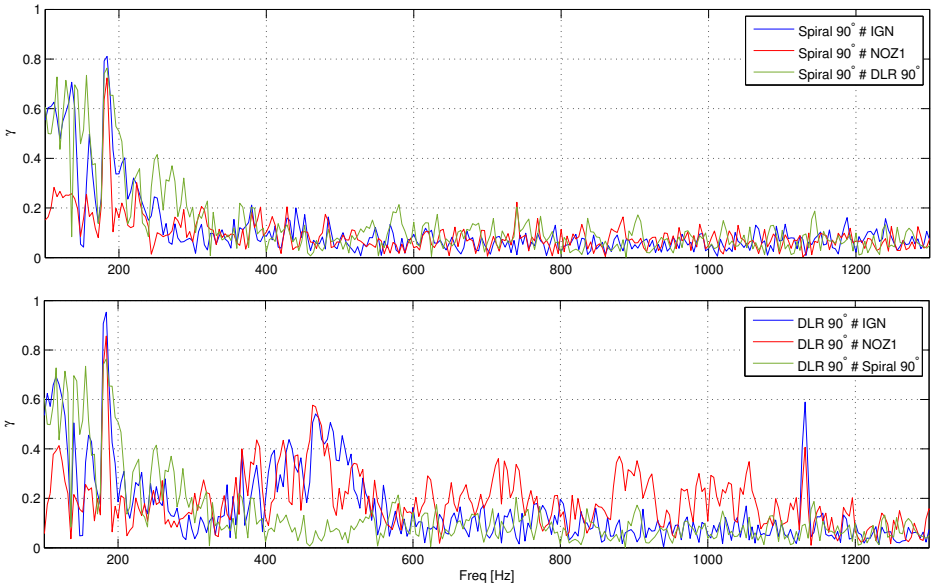

FIGURE 8.12: Comparison of the coherence between data from the pairs SPIRAL90°-IGN, SPIRAL90°-NOZ1, and SPIRAL90°-DLR90° (graph at the top); and using data from the pairs DLR90°-IGN, DLR90°-NOZ1, and DLR90°-SPIRAL90° (graph at the bottom). The data from the arrays are corrected to 4 m, and all the signals are synchronised in the time domain with the data from the nozzle.

It can be seen that there is no coherence between the data from the spiral array and the other sensors at frequencies above 250 Hz. The coherence level between the data from the nozzle sensor and both external microphones, which was expected to be similar, is also not showing any coherence over 0.1 in the range where the combustion noise hump should appear (at 450 Hz) as can be seen when the data from the linear array is used (see red line in Figure 8.12). The coherence using data from different microphones of the spiral array and probes was also analysed (not shown here) and the same lack of coherence was observed. It can be concluded from Figure 8.12, therefore, that the data acquired by the spiral array is not coherent with the other arrays. The coherence results from the spiral array below 250 Hz may also be biased due to lack of resolution of the array at low frequencies (because of its size) as shown with its PSFs.

The data acquired using the spiral array is still of good quality since the coherence between all the microphones behaves as expected. This is also proved with the source images, shown in the next section, which make sense. It is clear that spiral array data is just not well synchronised with the linear array and the in-duct probes. As previously mentioned, the three sets of data were recorded with different acquisition systems but using a common IRIG-B synchronisation linking the test bed to the ISVR system, and to the DLR system using a BNC "T" connector. Since the DLR linear array is well synchronised, it is strange that the ISVR system is not.

Further research into this topic is needed in order to use the data from the spiral array in combination with the in-duct data. In the rest of this chapter, the 3S-Array results for the Rolls-Royce BR700 type engine will be given using data only from the linear array. Nevertheless, a re-synchronisation of the signals is recommended.

8.2.3 Source image

The source image of the BR700 type engine at a high idle power setting was calculated using both external arrays of microphones. The result using the spiral array is shown in Figure 8.13, while that from the linear array is in Figure 8.14. The area scanned in both cases ranges from 3 metres upstream to 3 metres downstream from the end of the nozzle, with a spatial resolution of 10 cm. Only the rear part of the linear array (microphones #129 to #202) was used to avoid the gap in the control room staircase.

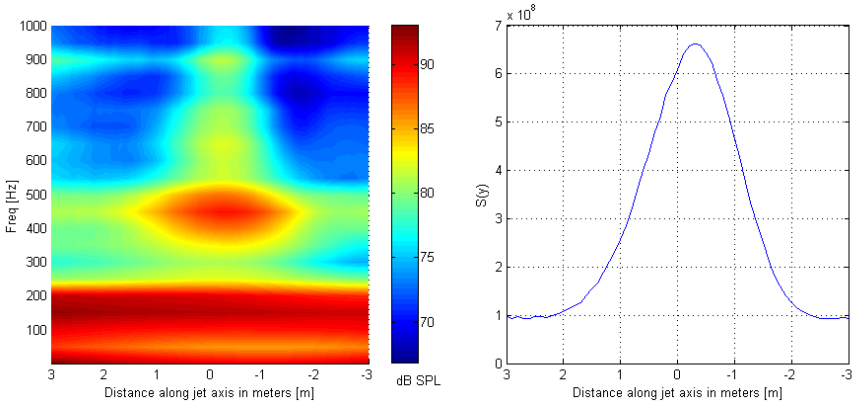

FIGURE 8.13: Source image of the Rolls-Royce BR700 engine at a High Idle setting using the spiral array of microphones in the external field (Left). 'Slice' through the left hand plot at 450 Hz (Right)

This engine has a common nozzle, which means that the hot air from the core and the cold air from the intake exit together from the same nozzle. A nozzle based tone at 450 Hz can be considered combustion noise, while the bypass noise seems to be limited to the BPF tone from the fan at 900 Hz.

A detailed source image at 450 Hz is shown in the right hand plots of Figures 8.13 and 8.14. The maximum pressure is seen at 20 cm downstream of the nozzle due to the influence of the flow and it shows the best place to focus the external array in order to extract the 3S-Array estimator.

A second main source is located at 180 Hz, which can just be seen by the linear array (the linear array axial aperture is larger than the spiral array and so it has a better low frequency resolution). Also, reflections from the wall at the end of the test bed will

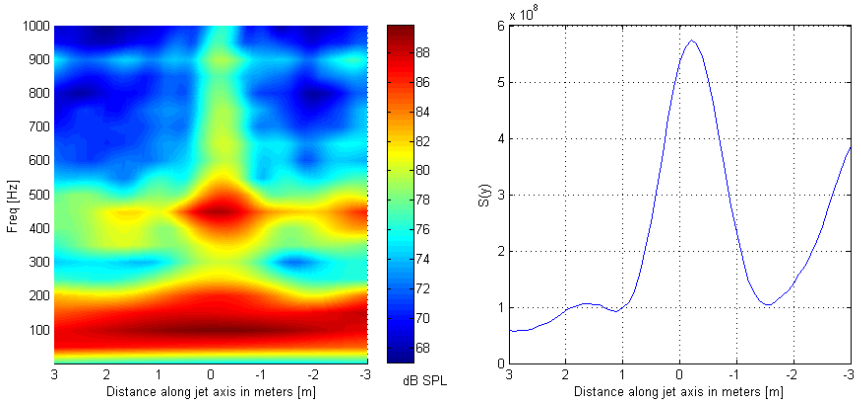

FIGURE 8.14: Source image of the Rolls-Royce BR700 engine at a High Idle setting using the linear array of microphones in the external field (Left). 'Slice' through the left hand plot at 450 Hz (Right)

affect the results from the linear array but not from the spiral array, which is further from the wall.

The response of the arrays and other proposed geometries are shown in Appendix B and extended results for other power settings are shown in Appendix C.

The coherences between two close microphones (1 and 2) and to separated microphones (1 and 28) are shown in Figure 8.15

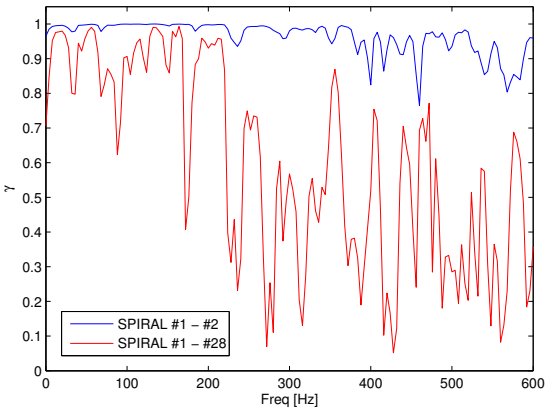

FIGURE 8.15: Coherences between Microphones 1 and 2, and 1 and 28 of the Spiral Array at a low power setting

8.3 Combustion noise estimation

The following 3S-Array results have been calculated using data acquired on a Rolls-Royce BR700 type engine at Dahlewitz, Rolls-Royce Germany in 2011. The results are compared with source spectra obtained from the same engine on a free-field outdoor

test bed at Stennis, using the AFINDS [46] source breakdown technique. These source breakdowns have been found to agree with certification data at a radius of 150 feet and, therefore, provide a good benchmark. Results are presented for the High Idle power setting.

The coherence spectra required to calculate the 3S-Array spectrum (using Equation 5.27) are shown in Figure 8.16. A comparison with data from the spiral array is also shown in the right hand plot of Figure 8.16, which shows that the data from the spiral array is clearly wrong at frequencies over 250 Hz.

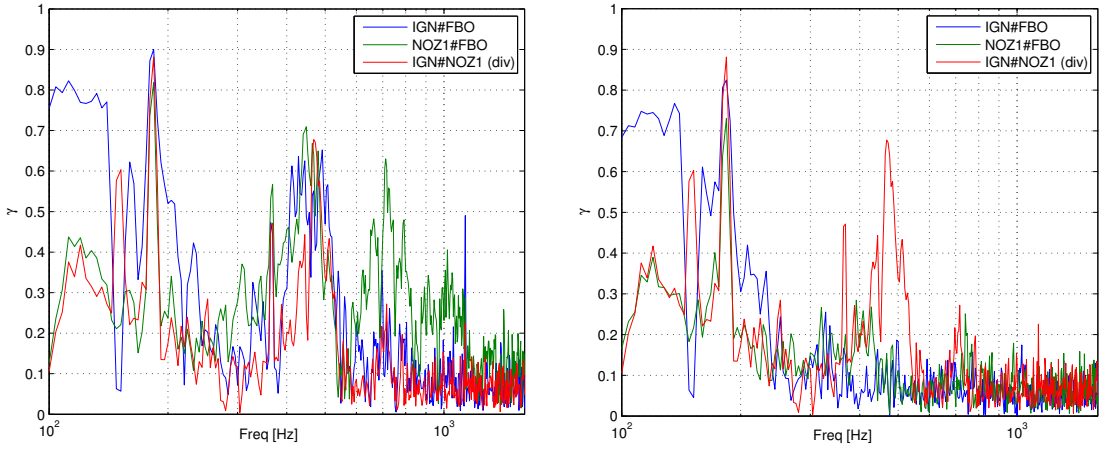

FIGURE 8.16: Coherences used for the calculation of the 3S-Array spectrum for the BR700 type engine at the High Idle power setting with data: from in-duct sensors and an external linear sub-array (left); from in-duct sensors and the external spiral array (right).

It can be seen from Figure 8.16 that the maximum values of coherence are located below 200 Hz with a broad spectral "hump" at around 450 Hz. The coherence spectrum levels are for the most part comfortably above the "noise floor" of 0.1 except at frequencies above 800 Hz. This means that the 3S-Array spectrum estimates are not subject to a significant error.

The 3S-Array spectrum using data from the DLR external linear array is presented in Figure 8.17.

It is compared with the averaged AFINDS core noise source (in red) obtained from the data of the Stennis outdoor test with the same engine at the same power setting [47].

The agreement in Figure 8.17 between the indoor measured FBO and the outdoor AFINDS core spectra is reasonably good suggesting that the FBO is effectively rejecting reflections and other noise sources inside the test cell at Dahlewitz. The 3S-Array spectrum is generally below these two spectra except at frequencies around 450 Hz, where

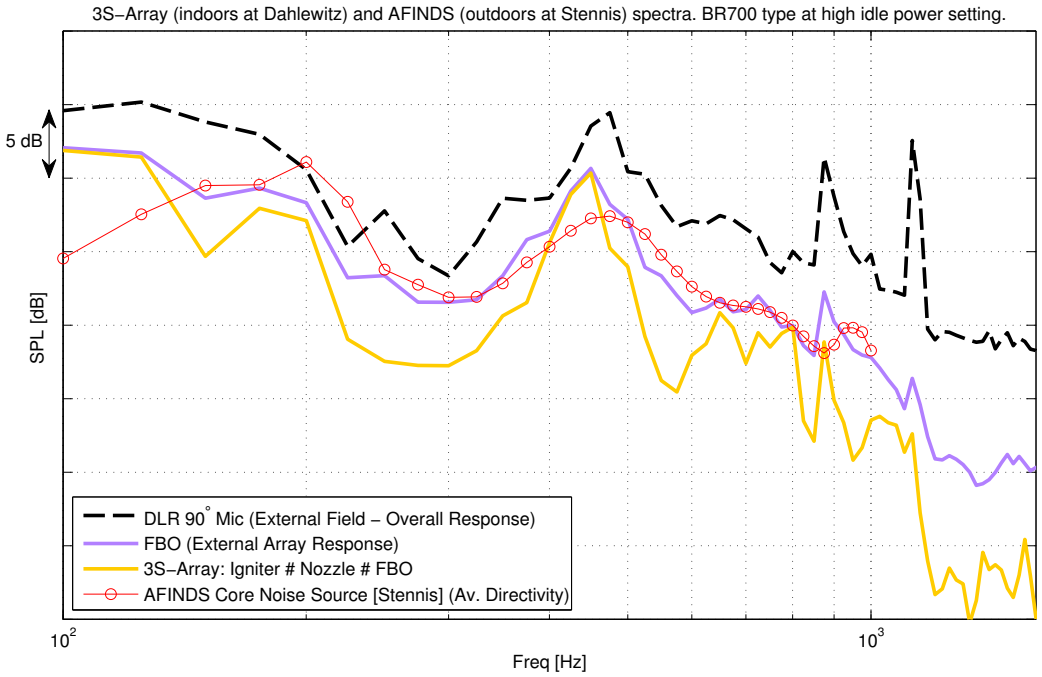

FIGURE 8.17: 3S-Array combustion noise spectrum using BR700 engine data at Dahlewitz from a DLR linear sub-array and in-duct sensors; engine at a High Idle power setting. Comparison with AFINDS core spectrum from DLR linear array at Stennis averaged over the aperture of the linear sub-array. Levels corrected to 4m.

the combustion noise is dominant. At other frequencies, the 3S-Array levels are significantly lower but provide a more reliable estimate of the true combustion noise than the nozzle-based source levels measured by the FBO or AFINDS methods.

Extended results at other power settings are shown in Appendix C.

8.3.1 The other two 3S-Array estimators: Guu and Gvv

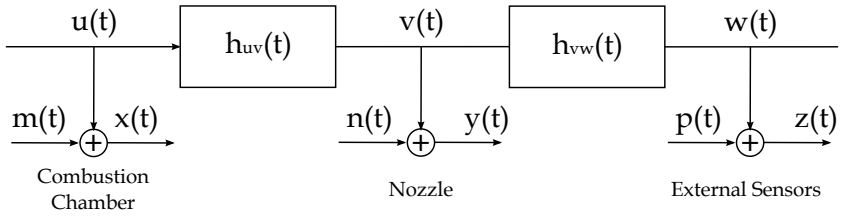

FIGURE 8.18: Representation of the propagation of combustion noise with 3 measurement points. Schematic diagram for coherence-techniques measurements

The spectra of the other two uncontaminated signals from the 3S-Array system $u(t)$ and $v(t)$ (defined in Figure 5.4), are plotted in Figure 8.19 together with the spectra of the contaminated signals, $x(t)$ and $y(t)$, the FBO, and the 3S-Array estimator G_{ww}.

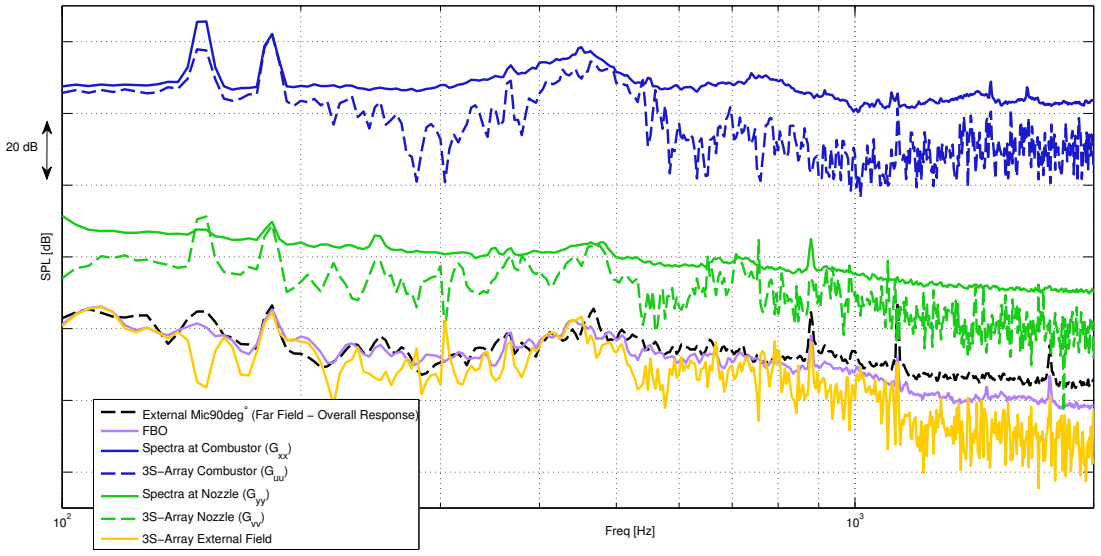

FIGURE 8.19: The blue-solid line (G_{xx}) is the spectra of the contaminated signal $x(t)$ as measured from the rumble probe IGN in the combustion chamber; the blue-dashed line (G_{uu}) is the estimated spectra of the uncontaminated signal $u(t)$. The green-solid line (G_{yy}) is the spectra of the contaminated signal $y(t)$ as measured from the probe NOZ1 at the nozzle; the green-dashed line (G_{vv}) is the estimated spectra of the uncontaminated signal $v(t)$. The black-dashed line (G_{zz}) is the spectra of the contaminated signal $z(t)$ in the external field from DLR90°, the yellow line (G_{ww}) is the spectra of the uncontaminated combustion noise signal propagated to the external field $w(t)$, and the purple line is the spectra of the beamformed array of microphones, FBO

From Figure 8.19, it can be concluded that the uncontaminated signal in the combustion chamber dominates (at 180 and 450 Hz) the main sources of combustion noise extracted by the 3S-Array in the external field (as seen in Figure 8.17). From the nozzle estimator, the uncontaminated signal also predominates at 180 Hz and 450 Hz, but the hump for the second one is not as wide as in the combustion chamber. However, from the 3S-Array estimator in Figure 8.17, the uncontaminated signal at the nozzle dominates at 700 Hz too.

In summary, the main combustion noise sources obtained from the 3S-Array at the High Idle power setting are located at 180 Hz (tonal), 450 Hz (hump), and 700 Hz (narrow hump). The two former seem to be produced at the combustion chamber and propagated to the external field. The third one has a maximum coherence between the nozzle and the external field, which indicates that it was amplified at the nozzle.

The reverberation and acoustic characteristics of the test bed are analysed in [108]. The reverberation time for frequencies higher than 300 Hz is below 0.5 s, and it rises for lower frequencies up to 0.85 s at 100 Hz. The reverberant radius (which "defines the distance from a source where the pressure level of the direct sound and the diffuse

noise field are equal") is below 4 m in the entire frequency range. This means that the microphones installed in the wall at 4 m are in the diffuse field, and beamforming or cross correlation of the acquired signals is necessary to measure the direct source. The beamforming processing effectively extends the critical distance in the focusing direction only, reducing the pick-up of reverberation.

8.4 Summary

In this chapter, the 3S-Array technique is applied to a new set of data acquired from a Rolls-Rolls BR700 type engine at Dahlewitz, in the German Rolls-Royce facility. Data was acquired in the combustion chamber and the nozzle of the engine and also in the external field by using a spiral and a linear array of microphones. A full appraisal of the data is carried out and two main issues were found. Firstly, regarding the probes at the nozzle of the engine, which were surface-mounted, it is clear that two of the four probes were not working and that the other two probes acquired reliable data only at low power settings of the engine. Secondly, the data from the external spiral array of microphones, is found not to be coherent with that from other arrays (i.e. the in-duct sensors or the external linear array of microphones over). A problem with the synchronisation of the data between the spiral array and the others would explain this issue.

Data from both external arrays have been used to calculate the image source of the engine along its axis and two main noise sources were located: one at 180 Hz and another at 450 Hz. These are nozzle based tones and can be considered as combustion noise. The BPF tone from the fan through the bypass is located at 900 Hz for the studied speed (High Idle).

The 3S-Array combustion noise estimator is then calculated using data from the probes in the combustion chamber, the nozzle, and a portion of the external linear array of microphones (deployed by DLR). Results from the 3S-Array estimator show that most of the information around 180 Hz, and especially at 450 Hz, was coming from the combustion chamber. Thus, it is possible to say the nozzle-based source at those frequencies was principally formed by combustion noise.

The FBO result for this indoor test fits with the nozzle-based source extracted with AFINDS from data of the same engine acquired outdoors at the Rolls-Royce facility in Stennis, at the same power setting.

Finally, the other two 3S-Array estimators at the combustion chamber and the nozzle are calculated. Further research into this, however, is needed to understand possible differences between direct and indirect combustion noise.

Chapter 9

Summary of Key Results

The work presented in this thesis is motivated by the need to predict combustion noise in modern turbofan engines to reduce community noise. Investigations into the study of the combustion noise generated by a turbofan are introduced, from which it is clear the need to develop novel processing techniques to separate combustion noise from other jet engine sources. An extended literature review is presented including references to existing combustion noise studies and the definition of direct and indirect combustion noise concepts.

Two main techniques are classified in terms of the number of sensors used. A two-signal technique uses data acquired in two positions either in the combustion chamber and the external field, or in the nozzle and the external field. The processing applied in this case is known as Coherence Output Power (COP) spectrum. A three-signal technique, called here "3-S", uses data acquired in the combustion chamber, the nozzle, and the external field. The main difference between the COP and the 3-S techniques is the validity of their assumptions. The former is sensitive to unwanted sources, which can contaminate the required combustion noise signal. Many tests of full-scale aircraft engines are also carried out indoors in order to reduce costs. This introduces room-environmental noise into the external field measurement, such as reflections and reverberation, which degrade both the COP and 3-S estimators.

Larger delays are estimated when data is filtered below 100 Hz from the study of the cross correlations between the data acquired in different points of the in-duct of the ANTLE engine. The aim of that study is to try to locate and differentiate direct and indirect combustion noise, following the processing suggested by Miles in [19]. Nevertheless, the delays and differences are not so conclusive to set any statement about that. Moreover, it was found that the filtering technique proposed by Miles was not so conclusive probably

due to the difference in the experiments. Finally, it seems that direct and indirect combustion noise might be situated in the same frequency range, and to keep trying to separate them need more research, which would have deviated the main aim of this thesis.

The advantage of using the cross-spectral phase data is also demonstrated. An estimated delay of 1 ms is found to be added to the propagation between the combustion chamber and the nozzle, meanwhile no delay is added between the nozzle and external microphones (at least it was not found using the cross correlation techniques). The modal behaviour of the combustion chamber is also related to the study of the phase of the cross spectra.

A physical approximation of the modal behaviour of an annular duct is introduced and explained. Moreover, the first cut-on modes for the annular combustion chamber of the ANTLE engine are estimated and cross-compared with the behaviour of the phase of the cross spectra, calculated from the measured data. It was concluded that a plane wave alone is propagating along the outer case of the combustion chamber up to 200 Hz.

The theoretical foundations of the novel combustion noise extraction method "3S-Array" are presented in comparison with the COP and 3-S techniques. The 3S-Array enhances the benefit of using the 3-S processing technique by including an array of microphones in the external field of the engine, then, unwanted sources in the external field can be rejected by calculating the Focused Beamformed Output (FBO) of the signals acquired by the microphones in the external array, focused on the end of the nozzle of the engine. A summary of the relevant signal processing definitions needed to understand the different techniques, and the process to calculate the focused beamformed signal in the time domain are also given.

The proposed 3S-Array method is validated and characterized by studying and evaluating different simulated scenarios. Computer simulations were carried out in order to evaluate the differences between the COP, the 3-S, and the 3S-Array coherence techniques, and to asses the benefits of the FBO of the external array in the 3S-Array method. The FBO depends directly of the ability of the array to locate and discriminate a source and its response is represented by its Point Spread Function (PSF). The responses of the utilised arrays are analysed in addition to those from other proposed arrays with different geometries. External noise signals are also simulated in order to validate the benefit of using the 3S-Array versus COP and 3-S techniques.

Data from the large 3/4 cowl ANTLE engine, previously analysed by Harper-Bourne, is re-analysed by applying the three signal coherence techniques instead of the two signal

COP. Data from the external array was synchronised and analysed together with in-duct data for the first time. The spectral levels obtained using the 3S-Array technique are higher than those from the COP and below that of the FBO, as expected. The underestimation of the COP is clearly shown with the comparison between the three signal coherence techniques 3S-Array and 3-S. In addition, data from the external array is used to calculate the image source of the engine along its axis and two main noise sources are located: one at 600 Hz from the bypass duct which corresponds with the BPF of the fan, and another from the nozzle at 300 Hz. Results of the 3S-Array estimator show that most of the information around 300 Hz was coming from the combustion chamber and, thus, that the nozzle-based source was principally formed by combustion noise.

The effects of using a focused beamformer to reject the external noise is proven by comparing the spectrum of the FBO versus that from an external microphone using data from the ANTLE engine campaign. The spectrum of the FBO focused at the nozzle rejects most of the unwanted noise that is not coming from the nozzle. This benefits the 3S-Array results, which clearly reject, for example, the BPF coming from the bypass duct. Moreover, the spectra of the 3S-Array was cleaner than that from the 3-S because it rejects the external noise and effects of the room, that the 3-S technique cannot reject with one single microphone. Two additional 3S-Array estimators are calculated at the combustion chamber and the nozzle, but further research into this is needed as a comparison might help to understand possible differences between direct and indirect combustion noise.

Finally, the 3S-Array technique is applied to a new set of data acquired from a Rolls-Rolls BR700 type engine at Dahlewitz, in the German Rolls-Royce facility. Data was acquired in the combustion chamber, the nozzle, and the external field of the engine by using an spiral and a linear array of microphones. A full appraisal of the data is carried out and two main issues are found. Firstly, regarding the probes at the nozzle of the engine, which were surface-mounted, it was clear that two of the four probes were not working and that the other two probes acquired reliable data only at low power settings of the engine. Secondly, the data from the external spiral array of microphones was found not to be coherent with that from other arrays (i.e. the in-duct sensors or the external linear array of microphones). A problem with the synchronisation of the data between the spiral array and the others would explain this issue. Data from both external arrays are used to calculate the image source of the engine along its axis and two main noise sources are located: one at 180 Hz and another at 450 Hz. These are

nozzle based tones and can be considered as combustion noise. The BPF tone from the fan through the bypass was located at 900 Hz for the studied speed (High Idle).

The 3S-Array combustion noise estimator is then calculated using data from the probes in the combustion chamber, the nozzle, and a portion of the external linear array of microphones (deployed by DLR). Results from the 3S-Array estimator showed that most of the information around 180 Hz, and especially at 450 Hz, was coming from the combustion chamber. Thus, it is possible to say the nozzle-based source at those frequencies was principally formed by combustion noise.

The FBO result for this indoor test agrees with the nozzle-based source results extracted using AFINDS [46] from data of the same engine acquired outdoors at the Rolls-Royce facility in Stennis, at the same power setting, which proved the FBO as a reliable process to extract nozzle based source indoors.

Chapter 10

Conclusions and Recommendations

10.1 Main conclusions

The main conclusions of this thesis may be summarised as follows:

1. The initial objectives of this work have been largely achieved, that is, to develop and evaluate an improved technique for extracting an estimate of the radiated engine combustion spectrum using pressure signals measured inside and outside the engine, with the engine located in a test cell.

2. The improved technique is an enhanced version of the three signal coherence technique used previously (3-S) with the first signal measured near the combustion chamber, the second near the nozzle exit and the third in the external radiated field. The enhancement is that the external single microphone signal is replaced by a composite signal formed by beamforming the signals from an array of microphones (FBO). The rationale is that this provides a method for not only rejecting reflections from within the test cell but also other sources of engine noise such as jet noise.

3. The FBO signal on its own provides a measure of the strength of the nozzle based source but this can be contaminated by other sources such as fan and turbine noise. However, to confirm that the FBO is rejecting reflections and other sources, FBO spectra from a BR700 type engine have been shown to agree well with nozzle-based source spectra derived (AFINDS) from a linear array test at an outdoor site on the same engine.

4. The 3S-Array has been compared with the previously used COP and 3-S techniques using data from a large 3/4 cowl engine (ANTLE) and a medium long cowl engine (BR700 type), measured in a test cell. The new 3S-Array spectrum levels are in general higher than those of the COP technique and lower than those of the FBO, as expected.

5. Based on this preliminary evaluation, the 3S-Array technique is recommended for combustion noise spectrum estimation but it is crucially important to assess the quality of the coherence data that provides the basis for computing the spectrum with this technique.

The way combustion noise is generated is not fully understood. There is controversy between researchers when they try to characterise different types of combustion noise depending on how it is produced.

Different techniques for extracting and analysing combustion noise are explained and compared. They are based in single experiments over different engines and different testing conditions. It is not possible to cross-compare the data from the different techniques presented in the literature, but the presented processing techniques were applied to the same acquired data for comparison.

The major difficulty in the study of combustion noise is that it is very complicated and expensive to carry out a set of measurements and all of them are very specific. Moreover, the geometry and design of the combustion chambers, and the exact information about the measurement set-up is most of the time confidential information which is very difficult for a researcher outside the engine manufacturer's organisation to obtain.

It can be concluded that a comprehension of the current techniques used in combustion noise analysis has been achieved. That is fundamental as a starting point for any future work and design of new processing techniques for combustion noise extraction. However, further research is needed to clarify how exactly direct and indirect combustion noise is generated and propagated.

10.2 Recommendations for future work

10.2.1 Suggested Improved Spiral Array

An improved array with a better ability to discriminate unwanted sources at low frequencies is suggested. Figure 10.1 shows the PSF of a double-sized spiral array located

in the same scenario as the previous array, which keeps the vertical and horizontal resolution to discriminate unwanted sources. It has a better response at low frequencies on account of a lower high frequency resolution, which it is not a problem because it is out of the range of interest for combustion noise. A full set of its PSF for different frequencies can be found in Appendix B.

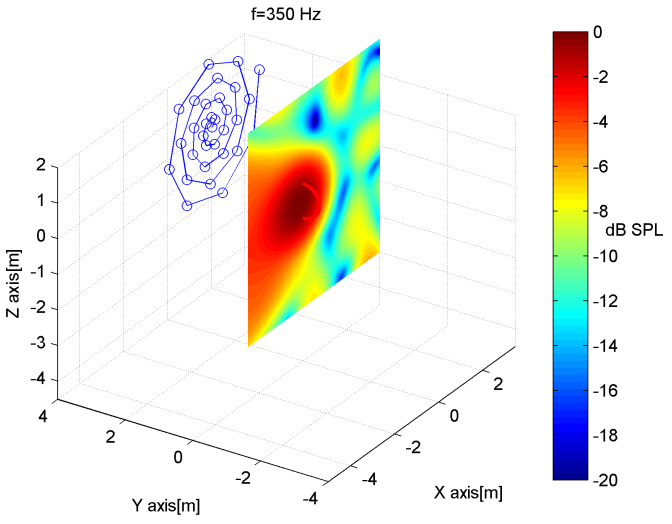

FIGURE 10.1: Point spread function for a double-sized spiral array focussed on the nozzle at 350Hz

In addition, other shapes and geometries are considered, which are shown in Appendix B. The PSF of an array made from a combination of two spiral arrays are shown in Figure B.3. It can be seen from the figure that there is a lack of vertical resolution due to the horizontally spread shape of the array. Moreover, a set of PSF for a double-width spiral array are shown in Figure B.4, where the vertical resolution seems to be not enough in order to locate the point source at low frequencies.

Finally, the Point Spread Functions of the rear part of the DLR Linear Array in the BR700 type measurement campaign are represented in Figure B.5. This is the extreme case where there is only horizontally resolution.

Summarising, the horizontally-shaped arrays are better for differentiating sources along the jet-axis, which makes them a good option for outdoors measurements especially if they are grounded, then floor and walls reflections are not a problem. But vertical resolution is needed in indoors measurements in order to avoid unwanted sources produced by reflections which will contaminate the acquired data. This makes spiral arrays the best choice for indoor use.

10.2.2 Suggestions for future data acquisition and processing

During a measurement campaign it is highly recommended to synchronise all the recording systems or to have at least one system which records all the data from the different acquisition systems. That was the main lesson learnt from the Rolls-Royce Trent 1000 engine data acquisition (described in the Appendix A), where some valuable data was not recorded because of a lack of synchronisation between the acquisition systems.

The installation of the spiral array over a rigid surface is recommended for future tests in rooms like the test-bed 55 at Rolls-Royce UK (where the spiral array is usually installed in the hand rail of the scaffold) in order to be able to calculate the FBO and then obtain the source images and the 3S-Array spectra.

The two additional 3S-Array estimators from the combustion chamber and the nozzle need to be further investigated to understand possible differences between direct and indirect combustion noise.

Source location techniques could be useful for the extraction of combustion noise. Principal components analysis, singular value decomposition, independent component analysis, dependent component analysis, non-negative matrix factorization, low-complexity coding and decoding, stationary subspace analysis and common spatial pattern are a few examples.

10.2.2.1 ICA and BSS

It is possible to extract independent sources from observed data that are a mixture of unknown sources by using a signal processing technique called Independent Component Analysis (ICA).

Nowadays, Blind Source Separation (BSS) by ICA has obtained substantial attention due to its potential signal-processing applications such as image processing, speech enhancement systems, telecommunications, medical signal processing and also source separation.

ICA has supplanted in many applications other decomposition methods such as Singular Value Decomposition (SVD). ICA is one of the most used BSS techniques for extracting hidden factors that lie behind groups of random variables, signals, or measurements, and it is based on a process for extracting individual signals from mixtures [109].

10.2.2.2 Tone removal techniques

Unwanted tones can affect the cross correlation calculations, and then, the coherence results. Assuming combustion noise as broadband noise for certain frequency ranges, it can be isolated subtracting the tones which appear in the measured spectrum. Some tones could be acquired by the probes due to rumble or just because they are louder than the noise measured close to where the probes are installed in the combustion chamber. Power line or mains interference may introduce in the acquired signals a tonal component tuned at 50 Hz and its harmonics. The mains interference can be noticed in the data acquired from the ANTLE engine experiment by the probes situated in the combustion chamber.

Three possible power line interference removal techniques are presented in [110]. It is suggested that the tone produced by the mains can be removed or reduced by the use of *Notch Filtering*, a *Regression-Subtraction* technique, or a *Spectrum Interpolation* technique. Linear and recursive digital notch filters would remove the tonal component. Its harmonics could be removed too with a comb filter[1]. Those different processing techniques have benefits and consequences. The application of notch filters produces a non linear phase response and distortion in the signal. Moreover the comb filtering would introduce spectral alteration. On the other hand, the regression-subtraction technique (time-correlated power line noise subtraction) works by subtracting a tone with the exact same phase and amplitude to the original signal, but the amplitude and phase of the tone should be estimated from a silent period. However, the spectrum interpolation technique seems to be the most appropriate one for the type of signals acquired in jet engine noise measurements. The magnitude of the desired signal without tonal components can be estimated interpolating the spectrum before and after the tone.

In this thesis, a tone removal technique based on the regression-subtraction technique was applied to the acquired data to reduce the influence of spurious tonal components. The reduction of the unwanted tones was achieved, however, they still remained in the spectra due to their spectral width. Further investigation on tonal removal techniques is recommended.

[1] multiple notch filter

Appendix A

Applications of 3S-Array: T1000 Engine

A.1 Test set-up

An indoor noise test was carried out with a Rolls-Royce T1000 engine, in August 2011, at the test bed 55, in the Rolls-Royce facilities of Derby, UK, as shown in Figure A.1.

The instrumentation and the acquisition systems of the rig are shown in Figure A.2.

FIGURE A.1: Floor Microphones Setup in the Test Bed

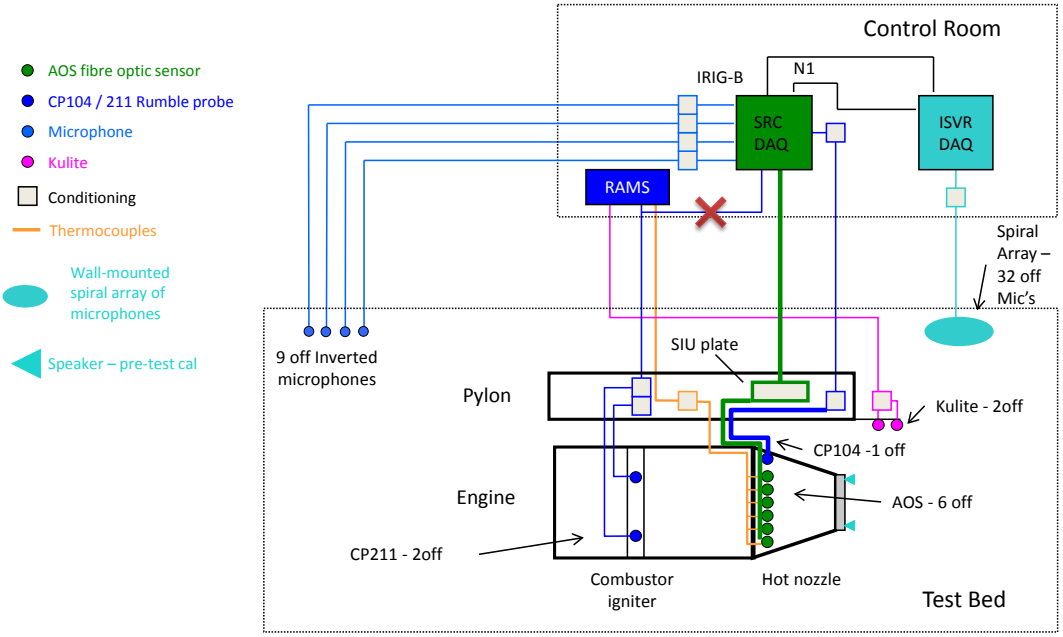

FIGURE A.2: T1000 9/4A Schematic Layout

Two piezoelectric pressure transducers were installed in the combustion chamber, six optic sensors and a piezoelectric pressure transducer in the hot nozzle, and two Kulite transducers at the end of the pylon. In the external field, an spiral array of 32 microphones was installed by ISVR in the hand rail of the scaffold that gives access to the control room of the test bed, and nine microphones were positioned on the floor of the test bed as seen from Figures A.1 and A.3.

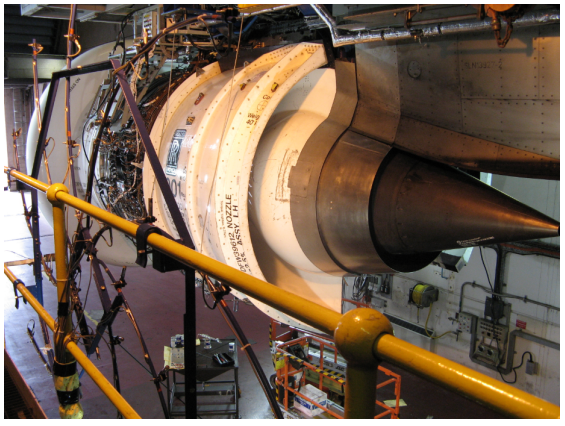

FIGURE A.3: Spiral array in the hand rail of the scaffold pointing to the end of the nozzle

The data from the spiral array was acquired by ISVR with a Sony tape-recording system, the 9 external microphones and sensors at the nozzle were acquired by Scitek, and the Kulites and the probes in the combustor by the RAMS system of the test-bed. An IRIG-B synchronisation signal and N1 motor signal were shared between the ISVR's and Scitek's systems from the test-bed. The RAMS and Scitek systems should be linked (but they were not) as it will be explained in the next section.

Different set-ups and power settings were carried out, and the test points were set from the low idle to the maximum power settings in small increments.

A.2 Data appraisal

Data was recorded by ISVR and Scitek for one minute at each test point when the engine was stabilised. But data appraisal revealed that the RAMS system was acquiring data only during the ramp conditions instead that with the engine stabilised due to a misunderstanding from the engine operators of the test-bed when reading the instructions of the test point. Then, the data from the sensors at the combustion chamber were not acquired at the same time with that from the nozzle and the external sensors as needed for the 3-S processing.

However, after an intensive work of synchronisation of all the data sets, some small portions of data were found with all the signals acquired when the engine was stabilised. In this Appendix, one section of 10 seconds of data at low speed is used.

The issue would be solved if the link between rams and DAQ were performed, but it was not. This reinforces the idea of recording all the data in the same acquisition system to avoid the same kind of problem in future tests.

A.2.1 Time domain appraisal

Time domain signals were extracted from the Sony Tapes as it is explained in Appendix D. Trend was removed from the time signals.

Figure A.4 shows the response of the RAMS in the Time Domain. Calculated kurtosis level of the signal acquired by the probe "Comb 2"' (Z0301E1) in the combustion chamber shows that it may be faulty, as it can be proved from its time domain representation. It has a kurtosis level of 6.4 meanwhile the rest of combustor probes have a kurtosis level around 0.1.

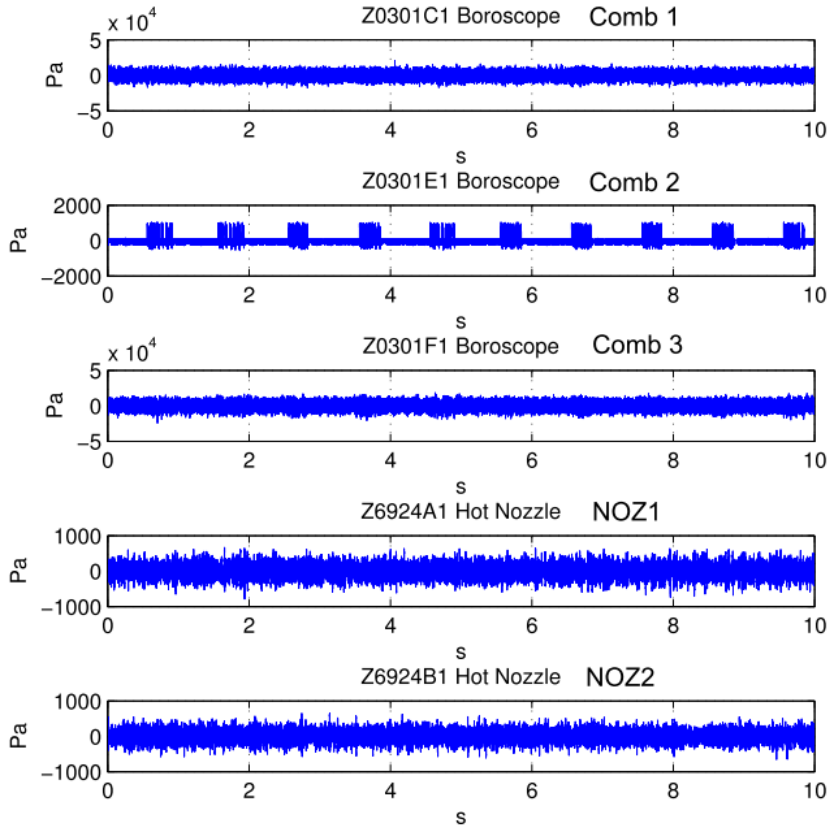

FIGURE A.4: Signals aqcuired from RAMS in the time domain

The graphs show that the trend was removed from the time signals, and the signals look good in terms of shape and amplitude between them. No more information can be extracted from the rest of the time domain responses a priori.

A.2.2 Frequency domain appraisal

A.2.2.1 Spectral Analysis

The data is transformed into the frequency domain by applying the Power Spectral Density (PSD) estimate to the discrete-time signals using Welch's method in a same way as in the previous chapters. The main difference here is that the number of averages is increased because of the shorter length of the acquisitions.

In Figure A.5, the PSD of the data acquired by the probes in the combustion chamber, in the nozzle, and in the external field of the engine are displayed at a low power setting.

At 50 Hz, the influence of the electric mains can be seen in the spectra acquired by the probes in the combustion chamber. The main spectral characteristic from the spectra

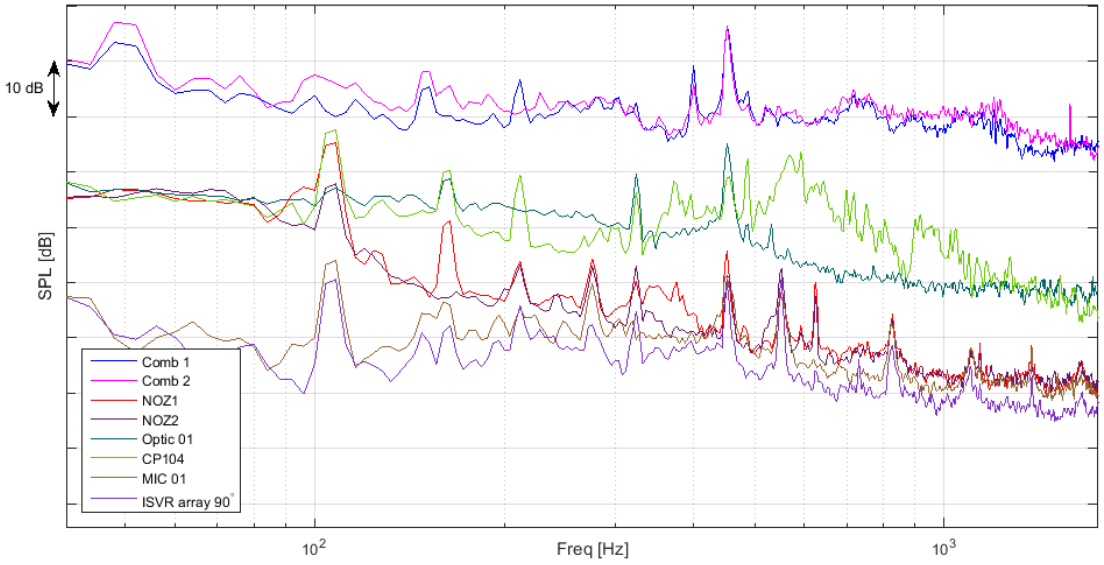

FIGURE A.5: Spectra of the data acquired by the probes in the combustion chamber (Comb 1 and Comb 2), in the hot nozzle (CP104 and Optic 1), in the pylon (NOZ1 and NOZ2), and in the external field (spiral array, and microphone 01 in the floor) of the T1000 engine at a low power setting.

of the probes in the combustion chamber is the tone at 450 Hz, which is also noticeable in the nozzle and the external sensors.

The BPF tone at 550 Hz can be found in the nozzle and in the external field. A hump over 500 Hz can be seen in the spectra from the CP104 sensor. All the spectra from the nozzle and external sensors have a tone close 100 Hz which appears to be harmonically related with the mains.

A.2.2.2 Coherence Analysis

From Figure A.6, it can be seen that the maximum levels of coherence for all the studied data are below 500 Hz. The coherence decays from the combustion chamber to the nozzle and from the nozzle to the external field. The coherence between the furthest sources such as the igniter and the external microphone is the lowest in the range of interest.

The maximum levels of coherence are found at 100 and 450 Hz, but only the second one is combustion noise related.

The FBO cannot be calculated because of the disposal of the array. The spiral array could only be installed in the hand rail of the scaffold, which is more than 1 m away from the wall of the test-bed. This separation between the array and a rigid surface makes no possible the beamforming calculation. Then, neither the FBO or the source

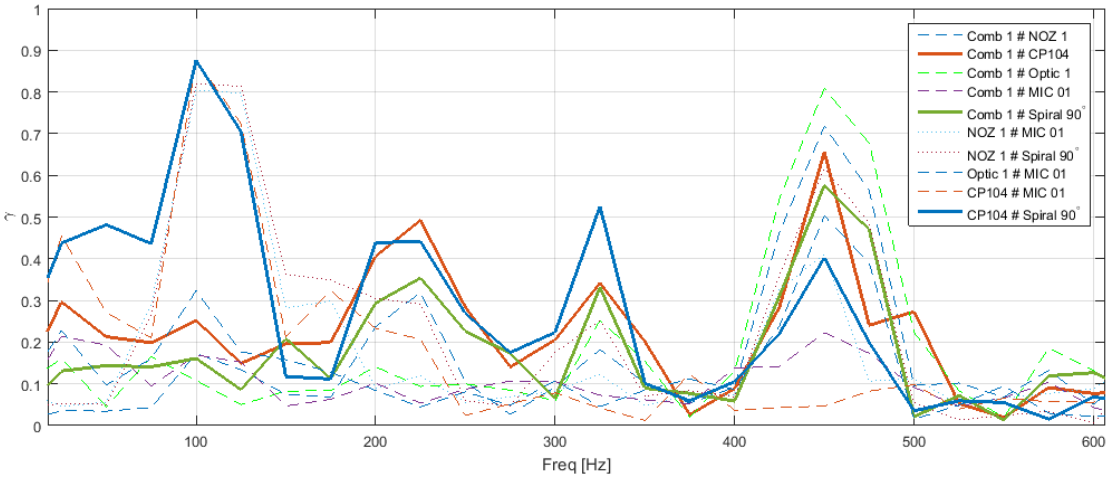

FIGURE A.6: Coherence spectra between data acquired at different positions of the T1000 engine at a low power setting

image spectra could be calculated for this set of data. It is recommended to install the array over a rigid board in future tests in this test-bed, or either over the floor (although that will interfere with the technicians work and could be risky for the microphones due to the fluids that might drop from the engine to the floor).

A.3 Combustion noise estimation

The spectra of the COP and 3-S calculations are shown in Figure A.7, using the coherences shown in Figure A.6 in the previous section. Results at this low engine power from the COP and 3-S techniques are compared. Different 3-S spectra are calculated using different sensors at the second and third position. The COP spectrum uses one in-duct sensor and the one external microphone signal.

The 3-S spectra levels are significantly above that given by the COP technique (which are biased as seen also with the previous sets of data of the other engines).

The 3-S uses a response from a single microphone in the external field, and then, it depends of the angle, giving only a spectra from a single directivity point of view, a response averaged in directivity of the 3-S spectra using different angles is suggested as future work. However, the 3-S spectra using a microphone from the spiral array at 90 degrees is less affected by the BPF tone at 550 Hz than that using the external MIC 01 in the floor (placed close to the central axis of the engine).

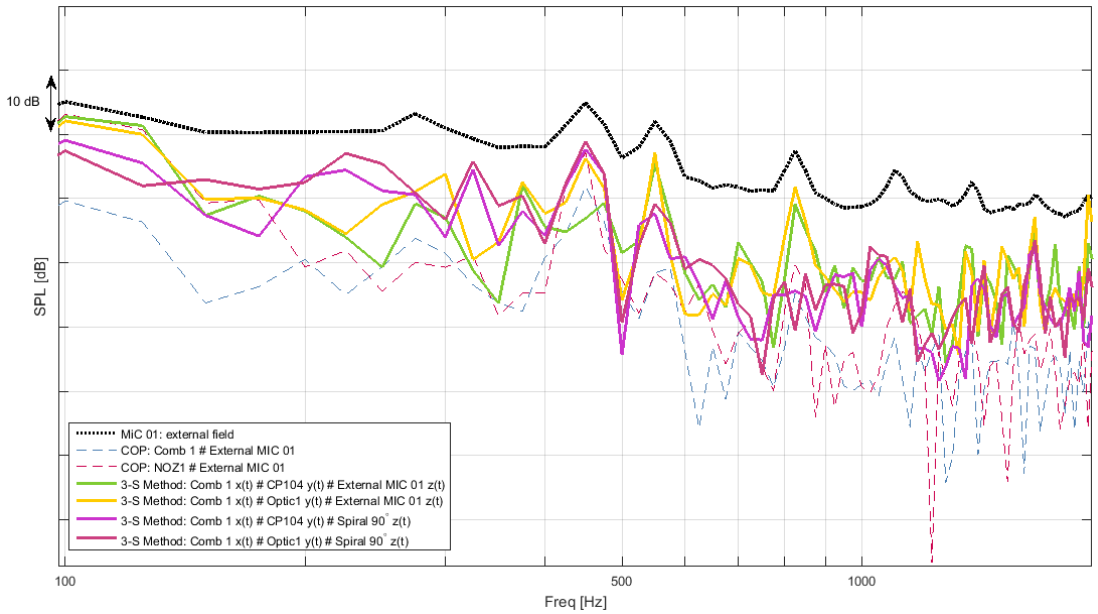

FIGURE A.7: COP and 3-S combustion noise spectrum using T1000 engine data acquired at different positions at a low power setting

Not significant differences are found in the second position between using the optic sensor or the CP104 at the pylon, unless when using MIC 01 as external sensor because their spectra are not coherent as shown in Figure A.6.

The FBO will produce clearer results (with smaller standard deviation) because of the reduction of the noise in the external field, then, it is recommended to set up the spiral array over a rigid surface in the next tests.

A.4 Spiral Array Installation

Distances between the spiral array of microphones and the engine can be seen from Figure A.8.

The distances between the microphones and the floor and rear wall of the test bed are shown in Table A.1; meanwhile the distance y (distance from all the microphones to their front wall) is 8.657 m for all of them.

A.5 Summary

In this Appendix, the 3-S coherence techniques are applied to a new set of data acquired from a Rolls-Rolls T1000 engine at Derby, UK. Data was acquired in the combustion

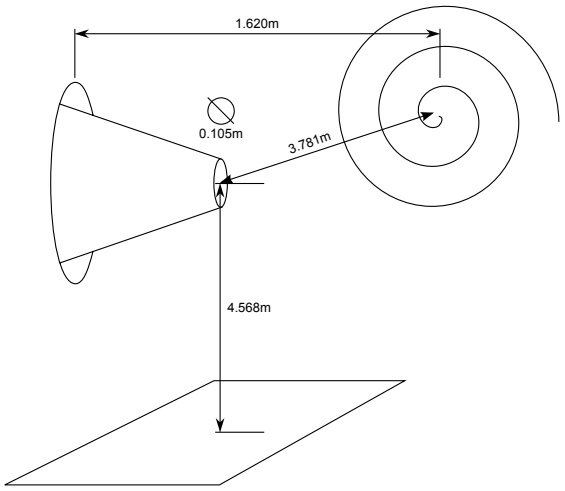

FIGURE A.8: Position of the Spiral Array with the Nozzle

chamber and the nozzle of the engine and also in the external field by using a spiral array and floor microphones. This Appendix focuses on one event of one test point, which was the only one where data were recorded for all systems at the same time when the engine was stabilised.

The FBO cannot be calculated from this set of data because of the place where the array was installed in the test-bed (the design of the experiment was prior to the idea of using a beamforming technique) but COP and 3-S spectra were presented.

The main lesson learnt from this experiment was the importance to synchronise all the recording systems or to have at least one system that records all the data. Moreover, the installation of the spiral array over a rigid surface is recommended for the future tests in this test-bed in order to be able to calculate the FBO and then obtain the source images and the 3S-Array spectra.

Microphone #	**Dist. front wall(m)**	**Dist. rear wall(m)**
1	8.962	4.920
2	9.160	4.988
3	9.102	5.154
4	8.815	5.178
5	8.713	4.986
6	8.704	4.731
7	8.955	4.554
8	9.281	4.666
9	9.475	4.978
10	9.282	5.342
11	8.863	5.482
12	8.462	5.242
13	8.373	4.761
14	8.666	4.330
15	9.380	4.268
16	9.705	4.663
17	9.710	5.306
18	9.187	5.774
19	8.466	5.723
20	8.024	5.144
21	8.179	4.364
22	8.846	3.922
23	9.663	4.132
24	10.119	4.901
25	9.789	5.776
26	8.916	6.148
27	7.983	5.761
28	7.677	4.805
29	8.183	4.805
30	9.231	3.577
31	10.185	4.168
32	10.380	5.346

TABLE A.1: Spiral Array Microphone Positions

Appendix B

Array Response: Point Spread Functions

The Point Spread Functions (PSF) of the ISVR Spiral Array and the DLR Linear Array are represented in the following Figures. The geometries used are the ones of the measurement campaign at test bed Adam in RRD, at Dahlewitz. Moreover, new proposed designs for the Spiral Array are added.

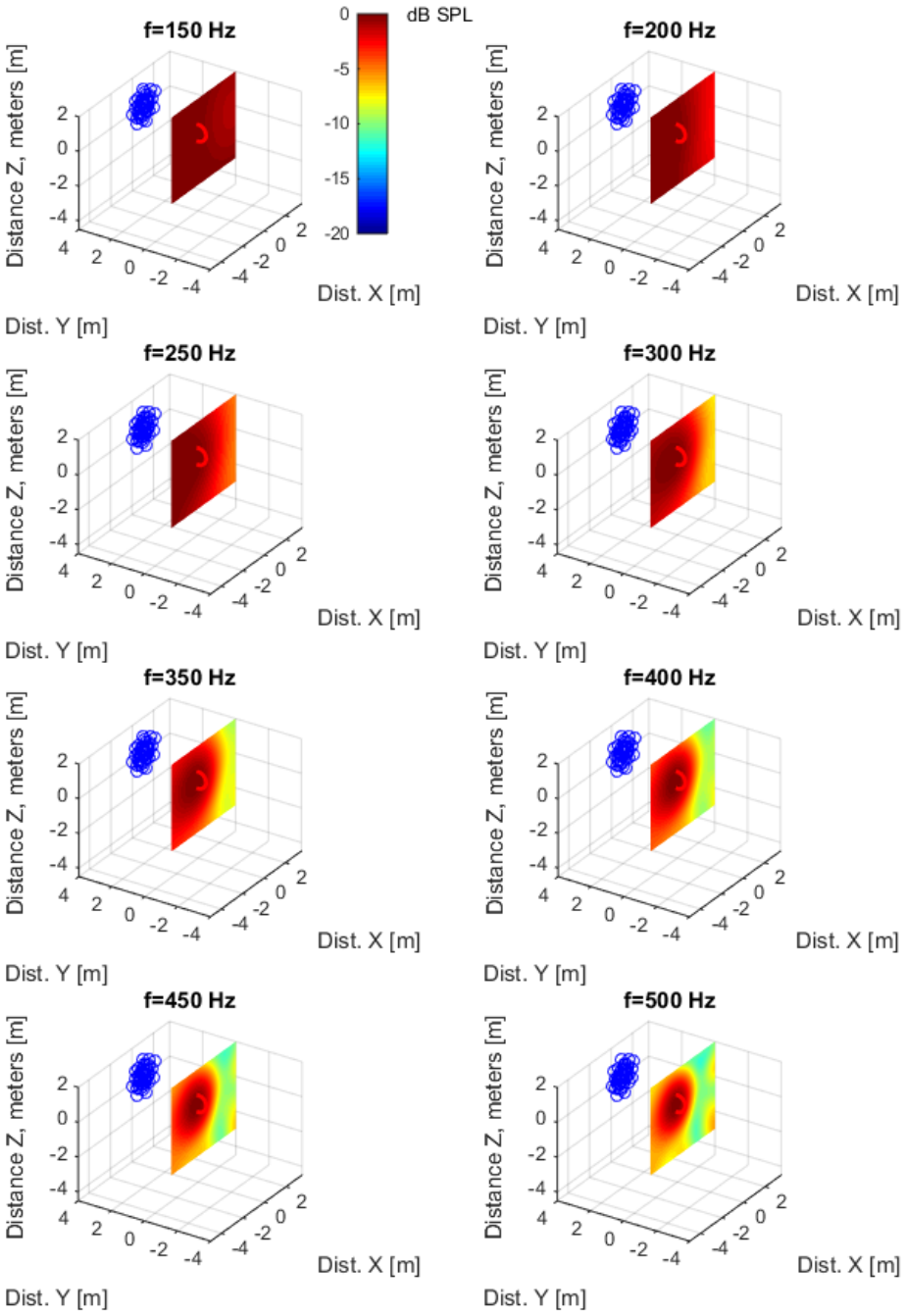

FIGURE B.1: Point Spread Function of the 32 Microphone ISVR Spiral Array in the BR700 campaign, Dahlewitz, RRD, 2011.

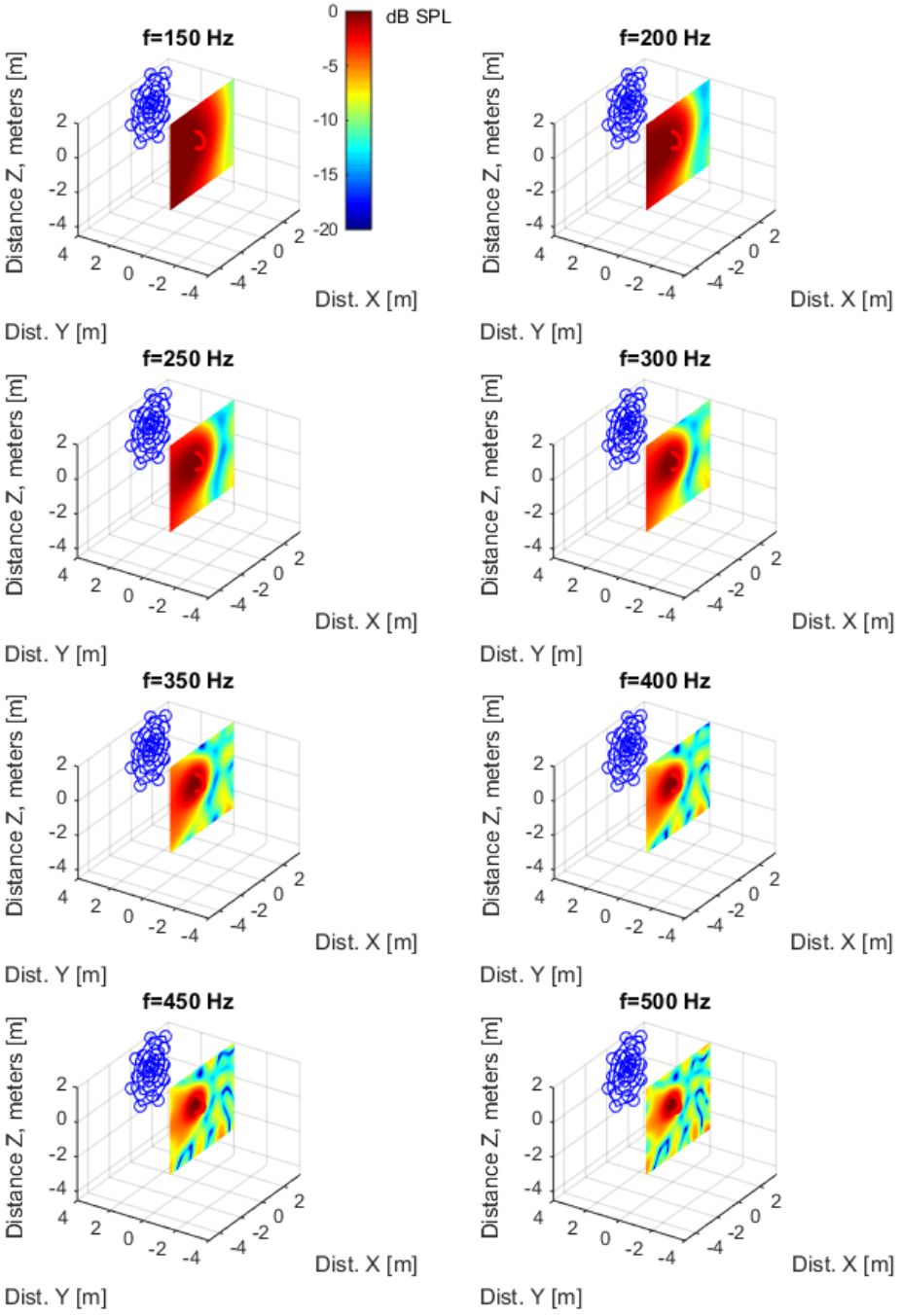

FIGURE B.2: Point Spread Function of a proposed double sized 32 Microphone ISVR Spiral Array

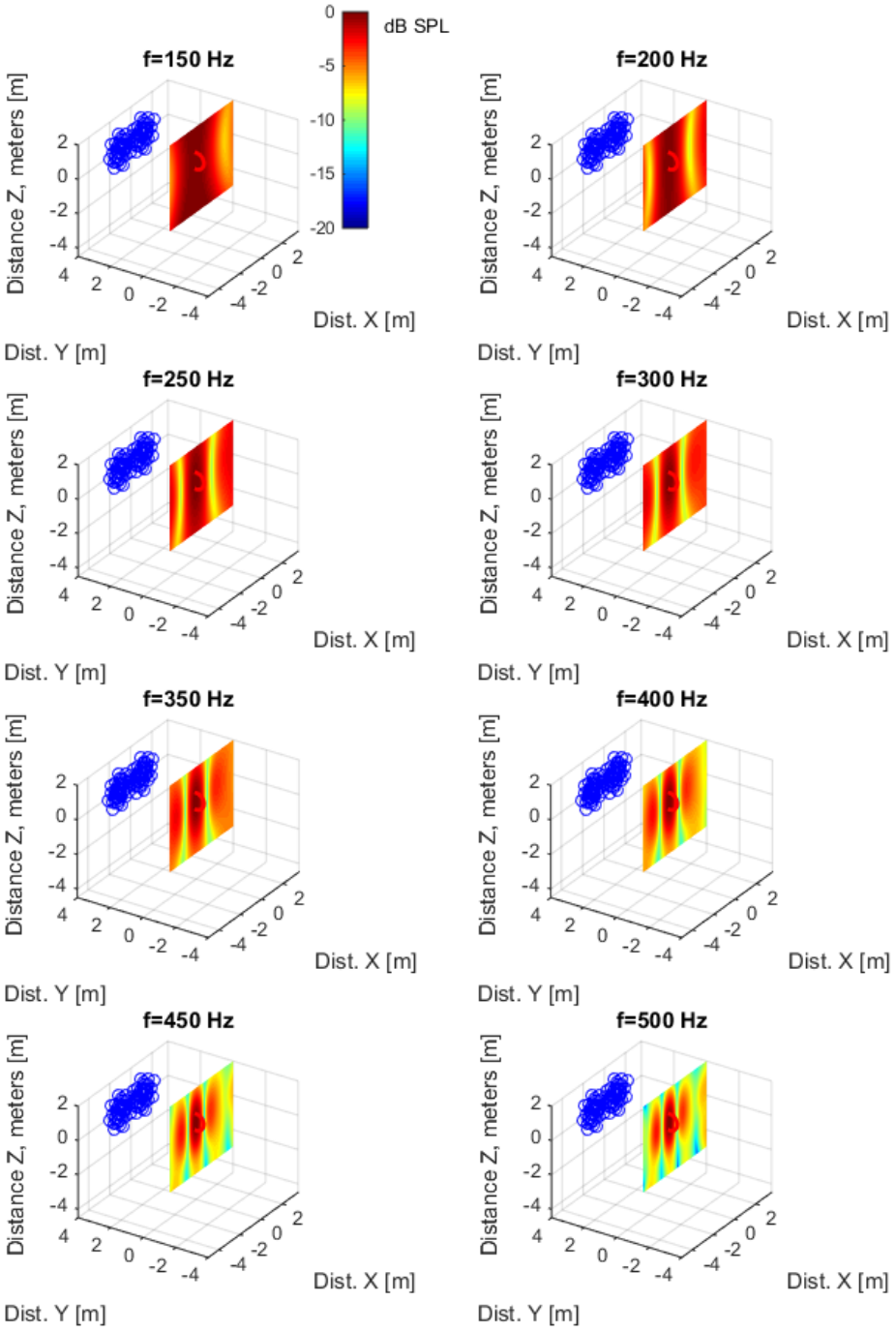

FIGURE B.3: Point Spread Function of a proposed two 32 Microphone ISVR Spiral Arrays

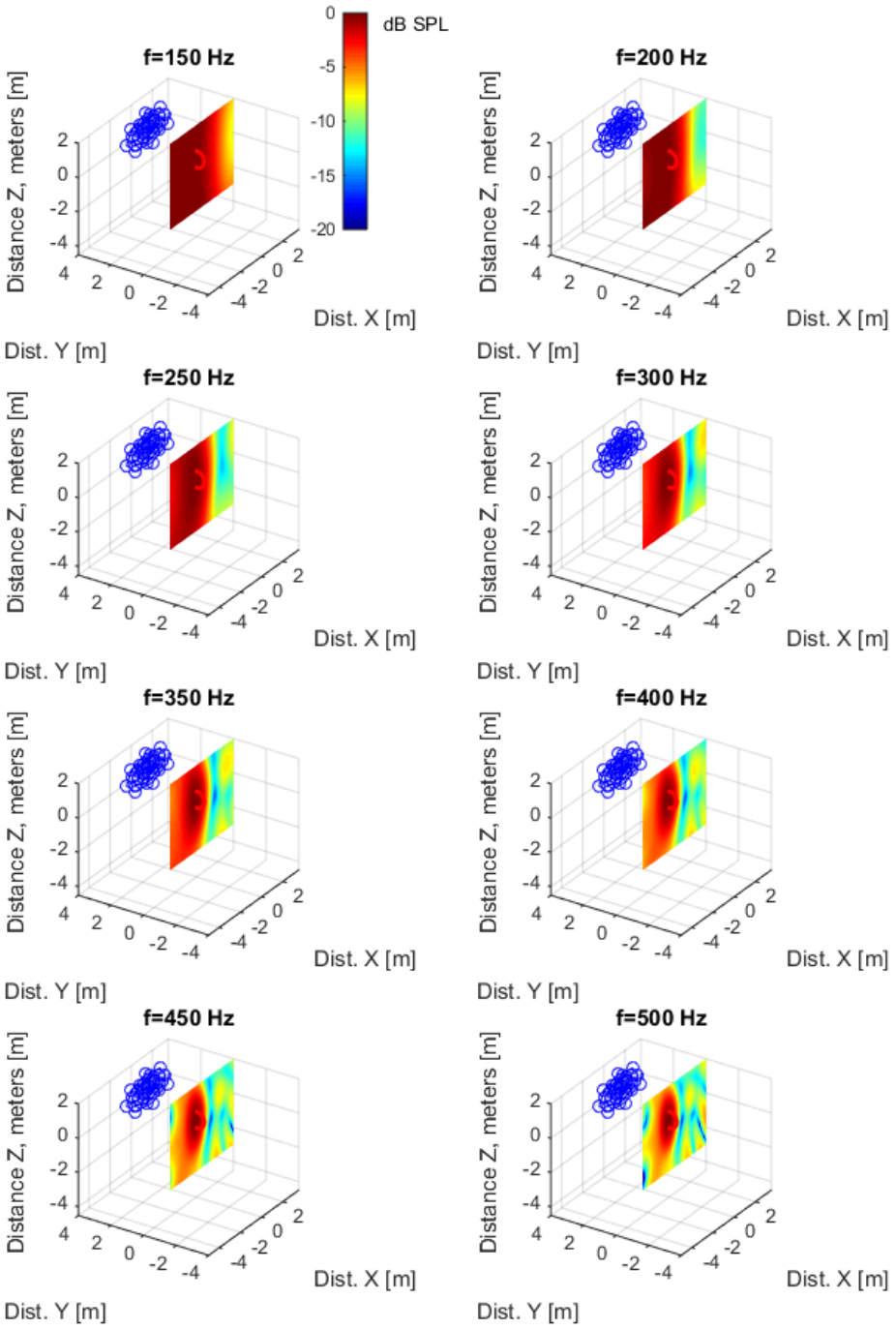

FIGURE B.4: Point Spread Function of a proposed axially extended 32 Microphone ISVR Spiral Array

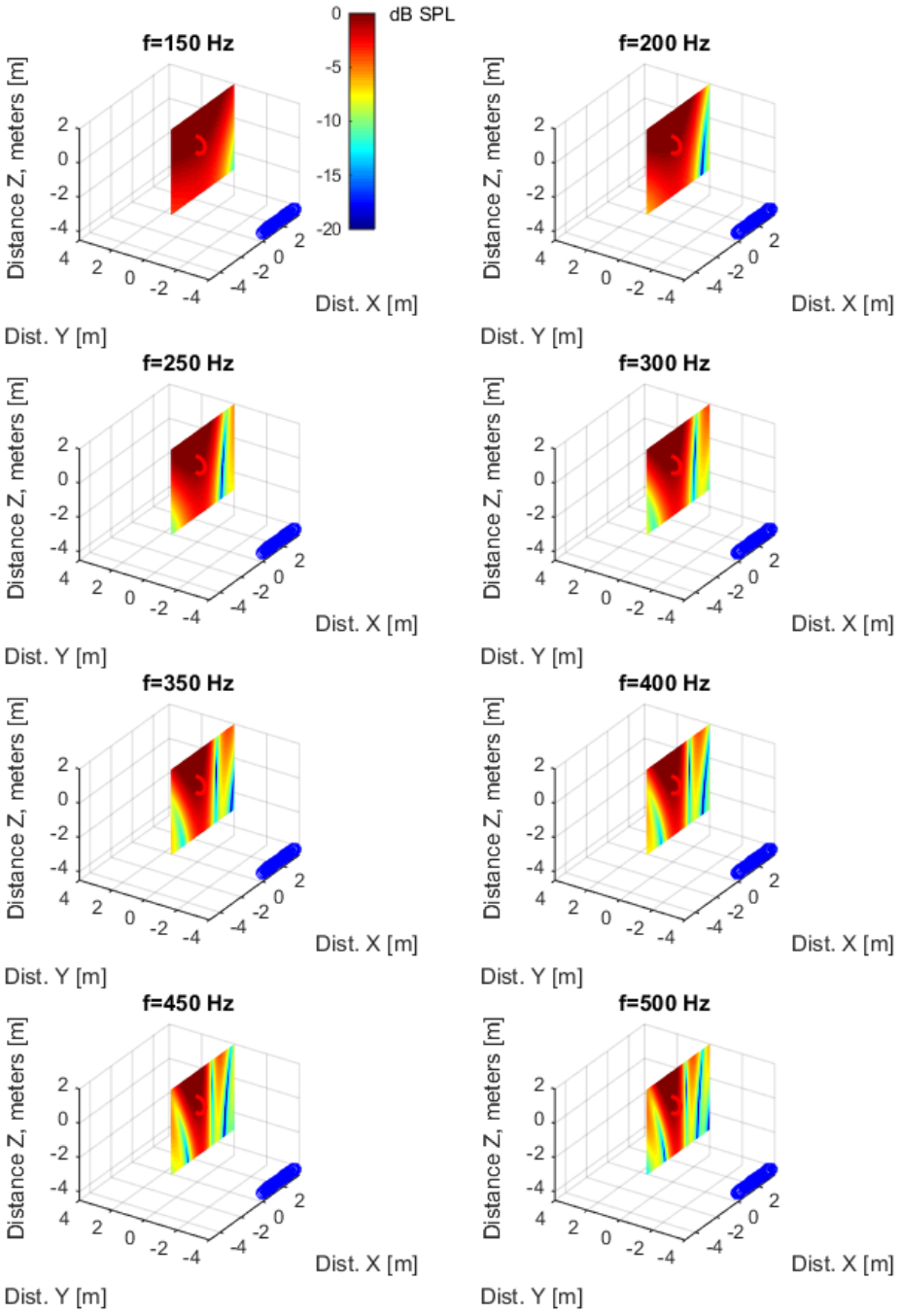

FIGURE B.5: Point Spread Function of the rear part of the DLR Linear Array in the BR700 measurement campaign, Dahlewitz, RRD, 2011.

Appendix C

Extended Results

Extension of the results presented in this thesis.

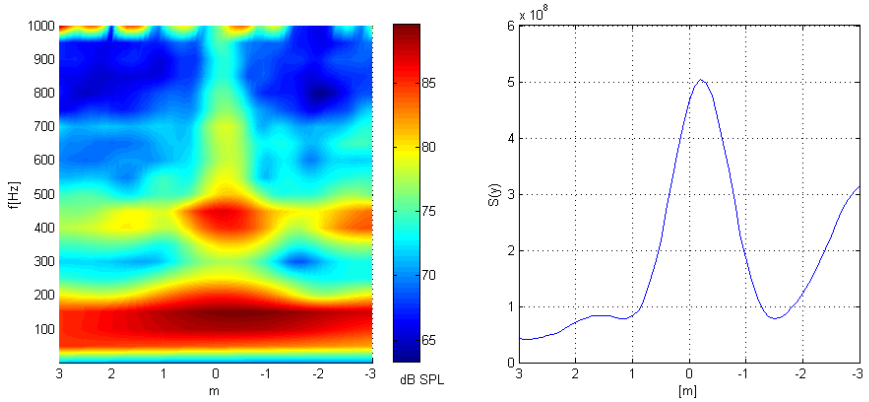

FIGURE C.1: Source image of the Rolls-Royce BR700 engine at a low idle setting using the linear array of microphone in the external field.

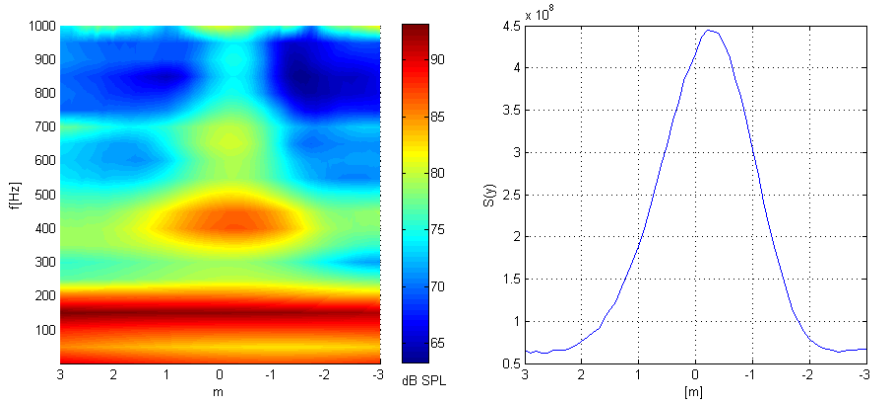

FIGURE C.2: Source image of the Rolls-Royce BR700 engine at a low idle setting using the spiral array of microphone in the external field.

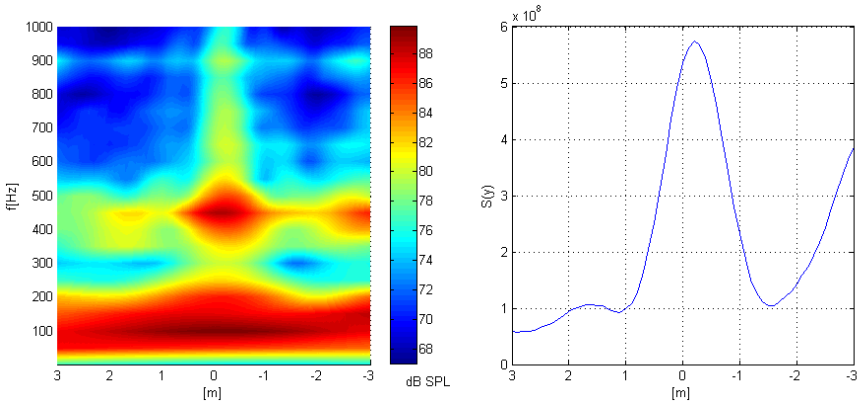

FIGURE C.3: Source image of the Rolls-Royce BR700 engine at a high idle setting using the linear array of microphone in the external field.

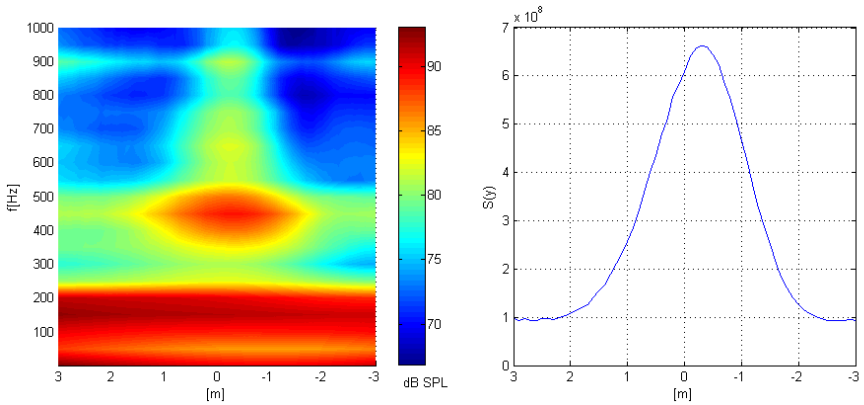

FIGURE C.4: Source image of the Rolls-Royce BR700 engine at a high idle setting using the spiral array of microphone in the external field.

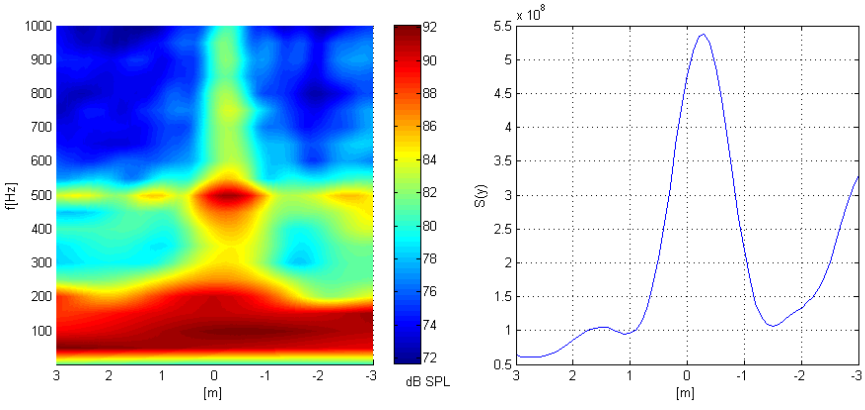

FIGURE C.5: Source image of the Rolls-Royce BR700 engine at a low power setting using the linear array of microphone in the external field.

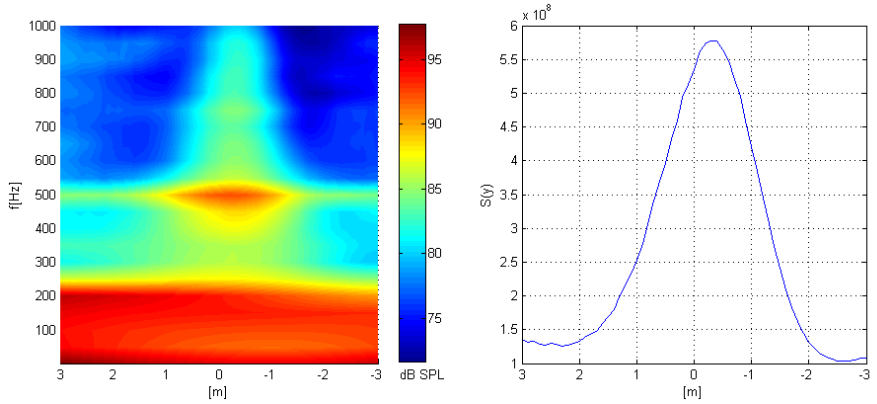

FIGURE C.6: Source image of the Rolls-Royce BR700 engine at a low power setting using the spiral array of microphone in the external field.

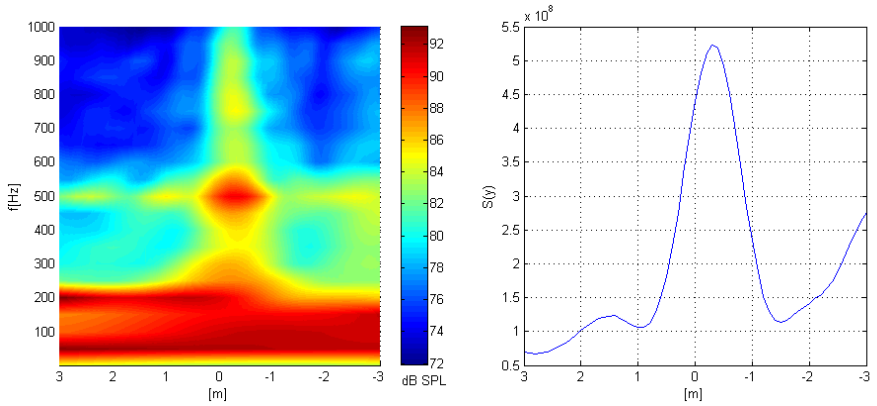

FIGURE C.7: Source image of the Rolls-Royce BR700 engine at a low-mid power setting using the linear array of microphone in the external field.

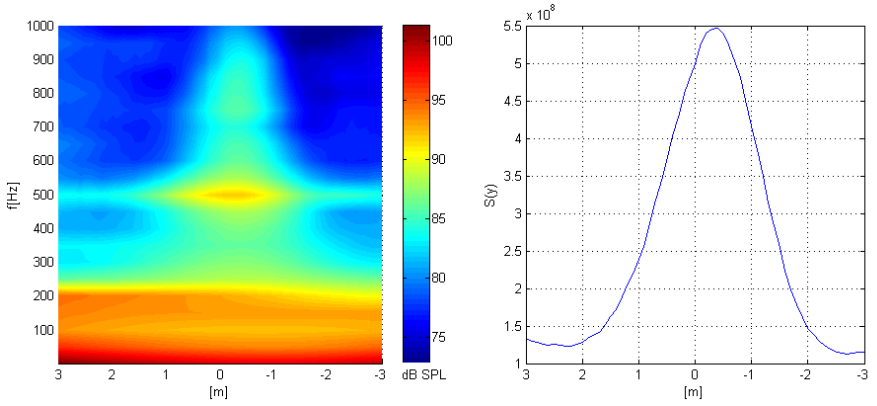

FIGURE C.8: Source image of the Rolls-Royce BR700 engine at a low-mid power setting using the spiral array of microphone in the external field.

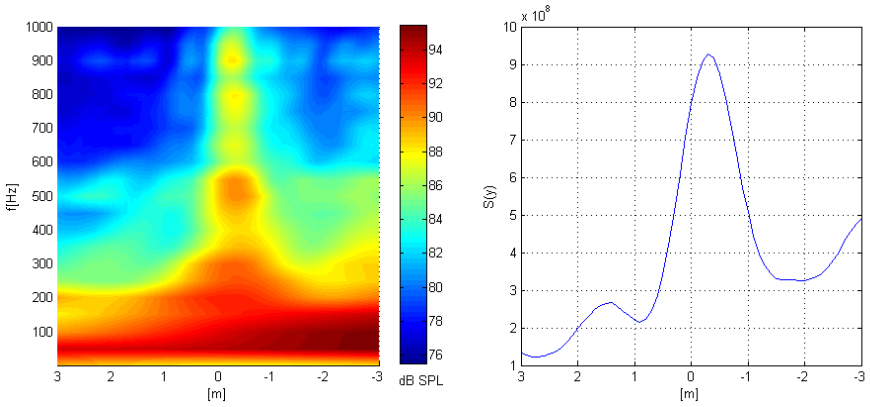

FIGURE C.9: Source image of the Rolls-Royce BR700 engine at a mid power setting using the linear array of microphone in the external field.

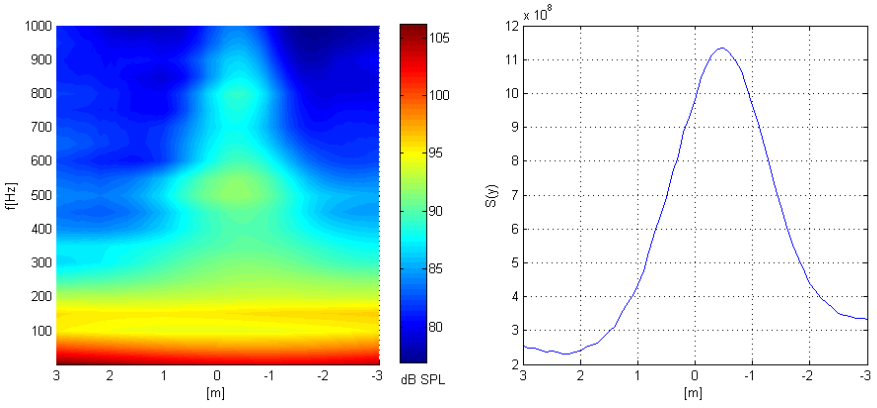

FIGURE C.10: Source image of the Rolls-Royce BR700 engine at a mid power setting using the spiral array of microphone in the external field.

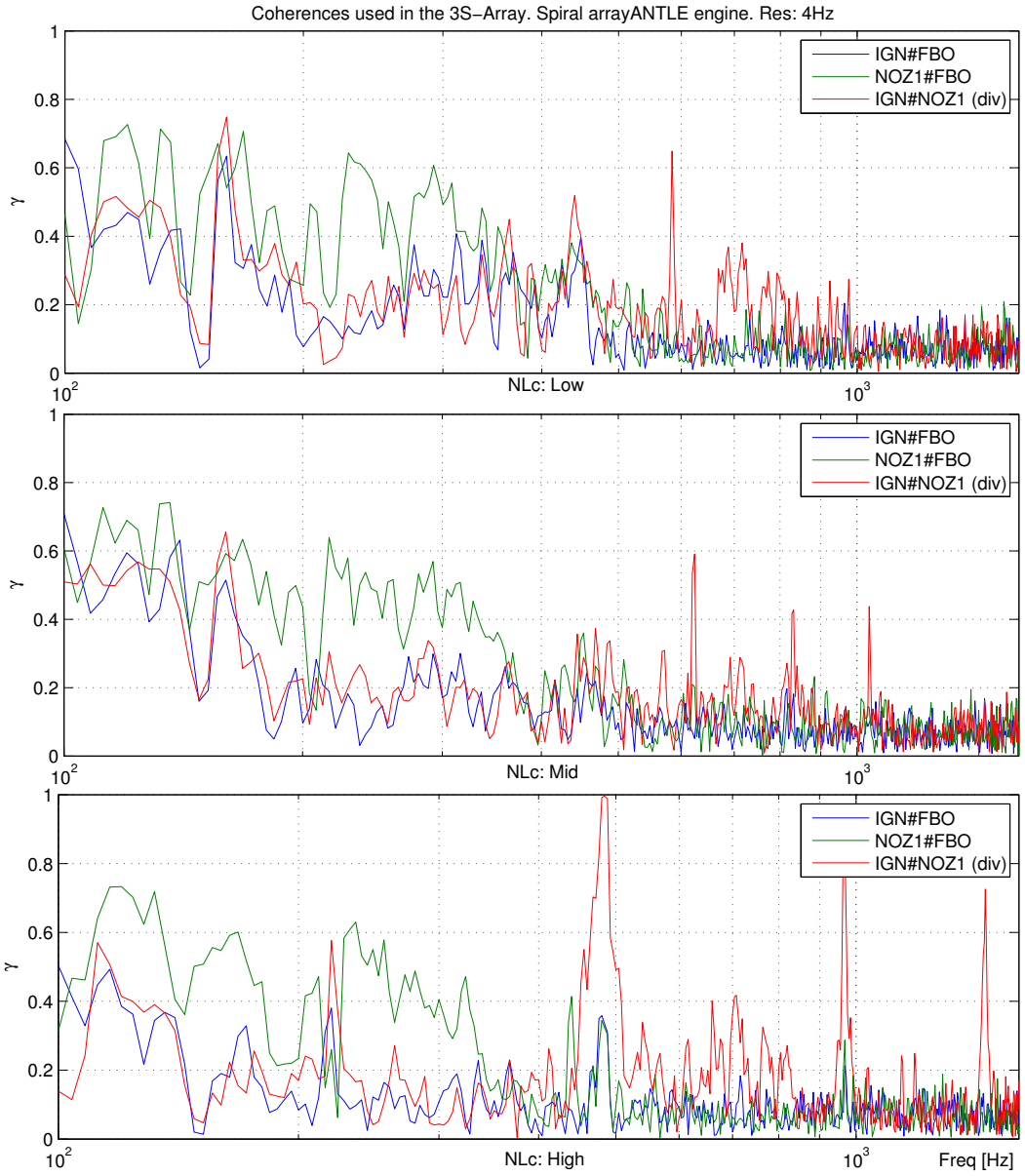

FIGURE C.11: Coherences utilised in the calculation of the new 3S-Array estimator. ANTLE engine. NLc: Low (top), NLc: Mid (middle), and NLc: High (bottom)

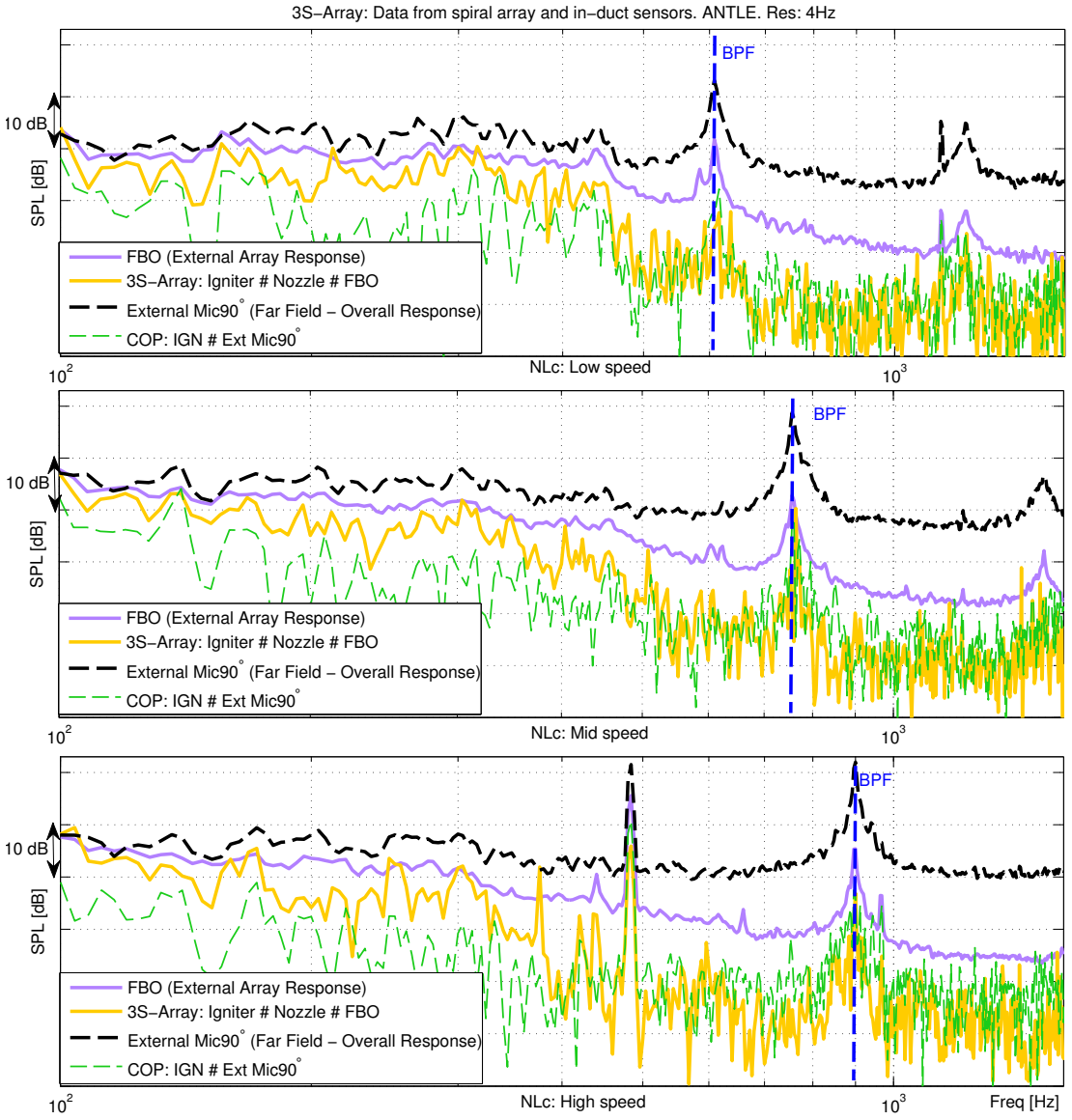

FIGURE C.12: New Combustion Noise estimator 3S-Array, using data from a spiral array in the external field and in-duct sensors. ANTLE engine. NLc: Low (top), NLc: Mid (middle), and NLc: High (bottom)

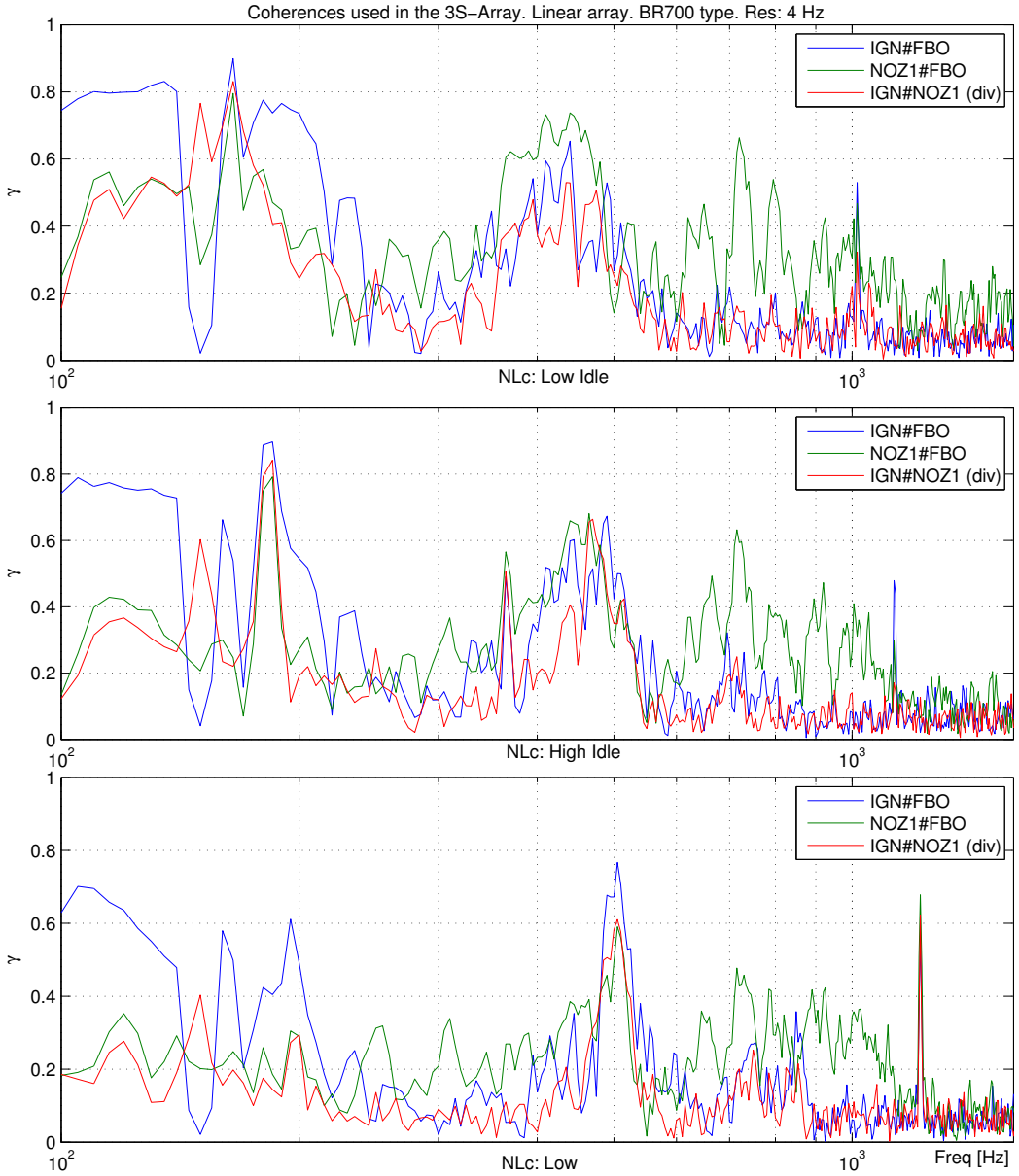

FIGURE C.13: Coherences utilised in the calculation of the new 3S-Array estimator. BR700 type engine. Low Idle (top), High Idle (middle), and NLc: 40% (bottom)

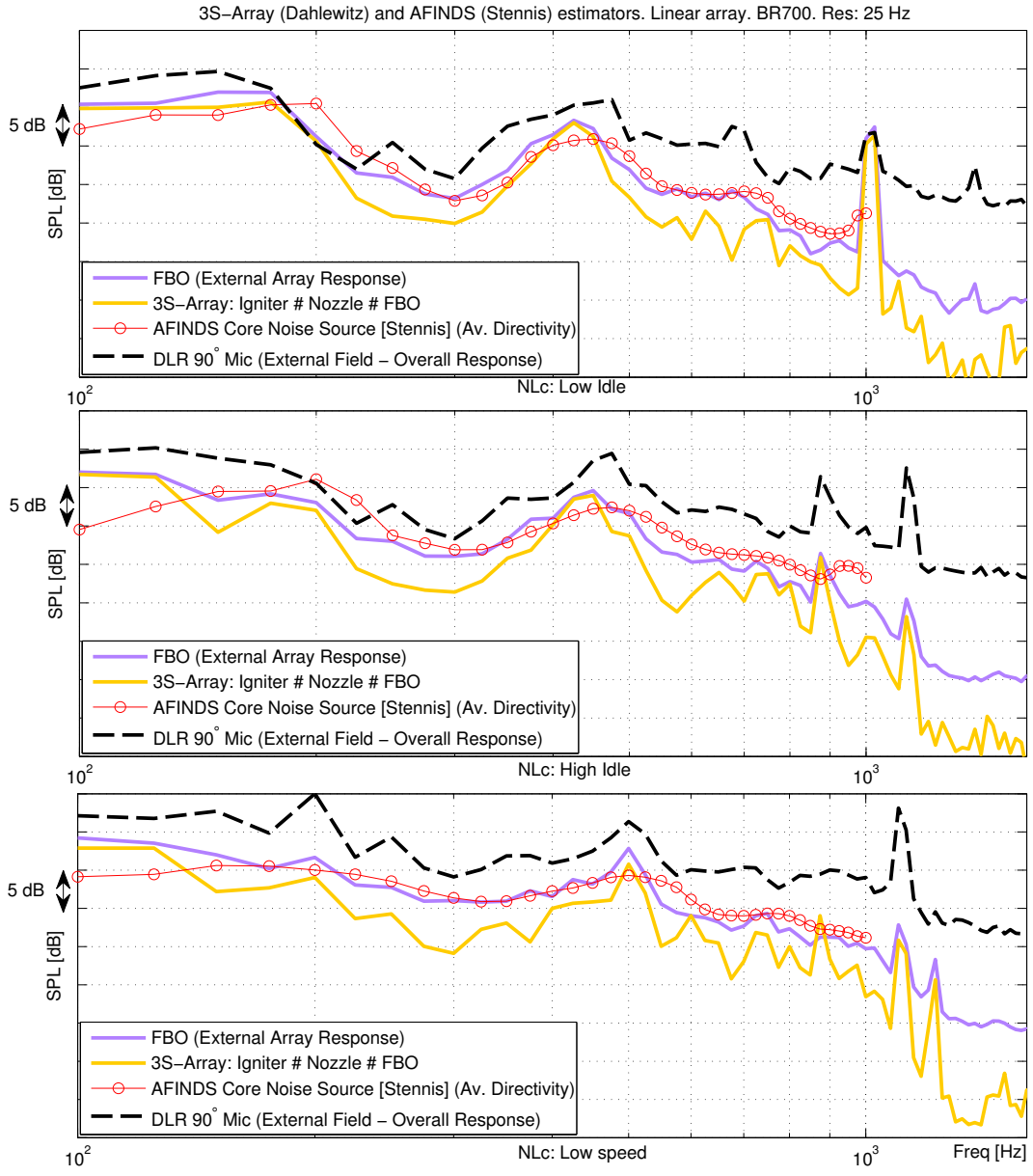

FIGURE C.14: New Combustion Noise estimator: 3S-Array, using data from a linear array in the external field and in-duct sensors. BR700 type engine. Low Idle (top), High Idle (middle), and NLc: Low-Mid (bottom). In comparison with AFINDS Core Noise Source using outdoors data recorded in Stennis with the same engine. AFINDS results were averaged to the same directivity of the aperture of the linear array used for the 3S-Array calculations. Results are corrected to 4m.

Appendix D

LMS CADA-X and Test-Lab first steps user guide

Data has to be extracted before any calculation is done. This is a short user guide of CADA-X program from LMS. It is very easy to forget how to use this Sofwtare if you do not use it every day. The aim of this guide is to remember the not common user of LMS how to work with data.

D.1 Extracting data from Sony AIT tapes

Data recorded during measurement campaigns should be extracted from Digital Tapes into Hard Disk Drive in order to be post-processed. This extraction has been done transferring the data using the software LMS CADA-X (the process will be similar using the new version "Test-Lab").

The most important windows meanwhile you are working with this software are "Time data processing monitor" and "Block table" (useful for looking results). They can be opened from the tab "File" once the program has been started.

You can access to your time domain data, that is, the recordings, through the menu "Options/Trace list".

A special dedicated interface should be launched inside X-CADA to work with. It can be done from the menu "Applications/RR Production/Recorder Interface".

Three files should be generated with this interface before any data extraction.

These three files are:

- TOC (Table Of Contents - *.toc)
- Channel List File (*.chl)
- Transfer List (*.trl)

The first step to get any information from the tapes is to connect them with your computer. That has to be done after selecting your data acquisition system by "Applications/Recorders/SIR1000" (in this case).

D.1.1 The TOC file

The steps to create the TOC file are:

- Insert the tape into the Tape Reader
- Connect the reader to the system by "File/Connect/OK"
- Make click on "Create TOC"
- Save the TOC file by "File/Save TOC" with name "tapeXXX" (where XXX is the number of the tape) and press "OK".
- Finally, the tape can be ejected by making click on "File/Eject"

This process should be repeated for as many tapes as you want to analyse. It is recommended to create one folder in where to extract and generate all the files of each tape.

D.1.2 Channel List file

This file has to content the sensitivity obtained from the calibration of the transducers.

A flat default Channel List File can be created at the first time in order to extract the calibration data and then, the correct Channel List File can be created with the calculated sensitivities.

The steps for calculating the sensitivity of each channel are:

- Select the calibration signals and transfer them
- Select the signal from one single channel
- View the data in the time domain and select a correct piece of signal avoiding clicks and undesired noise
- Apply a 1/3 octave band analyser
- Take the value at the 1kHz band of the analysed "Global Analysed Process" from the Block Process window
- Store the value in the system by clicking "Store"
- Write down the value down in an excel document

The sensitivity can be calculated in an excel style sheet as it is shown in Table D.1.

	A	B	C	D	E	F	G
Units	dB (Volts)	dB (Volts)	Volts (rms)	dB SPL	dB	p (rms)	Pa/V
Value	x	120 + A	$10^{(B/20)} * 10^{-6}$	x	D - B	$10^{(D/20)} * 20e - 6$	F/C

TABLE D.1: Sensitivities Calculation Excel File

Where column A is the measured Value at $1kHz$, B the reference ($10V$), D the calibrated pistophone value, E the correction Factor in dB, F the corrected PPN value, and G the PPN calibration.

D.1.3 The Transfer List file

This file will apply information to the extracted data during the transferring. Basically, it contents the name of each event and the reference to the Channel List File, where the calibration values and units are. These values will be directly applied to the extracted data during the transferring process.

Dedicated Transfer List Files of the measurement should be created, but again, one Transfer List File should be created per tape. The steps to create the Transfer List File are:

- Open the Recording Interface ("Applications/RR Production/Recorder Interface") or type "history" in the command line for opening it with a shortcut (i.e. ">>! 1", ">> S!",)

- Connect to the drive with the tape in “File/Connect/OK”
- Create TOC file as previous steps
- Highlight all the events with left click and press “Add to transfer list”
- Save the Transfer List by “File/Save Transfer List” At the beginning, it is recommended to save the file as “Default.tapeXXX.trl”. This file has to be modified in an external editor (i.e. “TexPad.exe”). All the names of the events should be renamed to their correct value from “eventXXX” to “event001”, “event002”, etc. and save the file as “tapeXXX.trl” depending on the number of the tapes you are working with.

D.1.4 Data Transfer

- Close the recorder interface if it is open
- Create a new project in the correct folder or load it if it was already created
- Open the recorder interface and connect to the drive
- Load the correct “.toc” and “.trl” files.
- Select the events to transfer
- Click on “Transfer Data”

The read data will appear in the Transfer List window after the transferring. They should be saved as events using the “Save as” menu.

D.2 Data Analysis

All the events acquired with the transferring from the tapes can be displayed, modified, and edited widely.

Events can be opened in the “Trace List” window previously to their edition.

The program offers a big number of possible processes. They can be applied in ’real time’ or programmed with the Streamline processing application (“Applications/RR production/BP Streamline processing”).

An input, a process, and an output should be introduced in the Streamline processing application. Inputs and outputs can be defined as traces or block data. The path where the data are can be selected by using the button "Search path", and xxx using "search for attributes matching" menu. Options will be saved by clicking "File/Exit", but they will not be saved if "Quit" option is done.

A number of processes can be defined in the streamline and they can be processed all together or individually.

"Tacho to rpm" is an example of a process which can be carried out in order to obtain the rpm signal from the N1 signal obtained from the LP. Common options for "Tacho to rpm" are shown in Table D.2.

Trace Analysis	Tacho to RPM
Pulses per rev	60 (for T1000)
Cross level	$2.5V$
Lower tolerance	$0.1V$
Upper tolerance	$0.1V$
Target sampling	$1Hz$

TABLE D.2: Tacho to rpm options

Note that the processes can be implemented in the trace analysis through the application menu. The output of the process should be defined with right click and "new/TDF". All the outputs should be selected and they can be replaced or renamed by the user.

The process to be done should be highlighted and then launched by clicking "execute". Results will be checked from the Trace List window. They can be displayed by highlighting the correspondent events and selecting "Trace/Strip chart display" from the menu.

D.3 Data Edition

Data can be edited all together as a single process or individually. Markers can be added to the events and then special edition tools can be lunched from the Streamline processing to apply a process to the data selected with the markers. Individually edition processes can be applied to the events or the selected part of them using the menu "Edit". Common tools as "copy", "paste", "cut", "replace", "insert in the cursor position", "replace from the cursor position", etc. are available.

Appendix E

Phase Study Results

E.1 N1 = 35%

Combustion Chamber Results

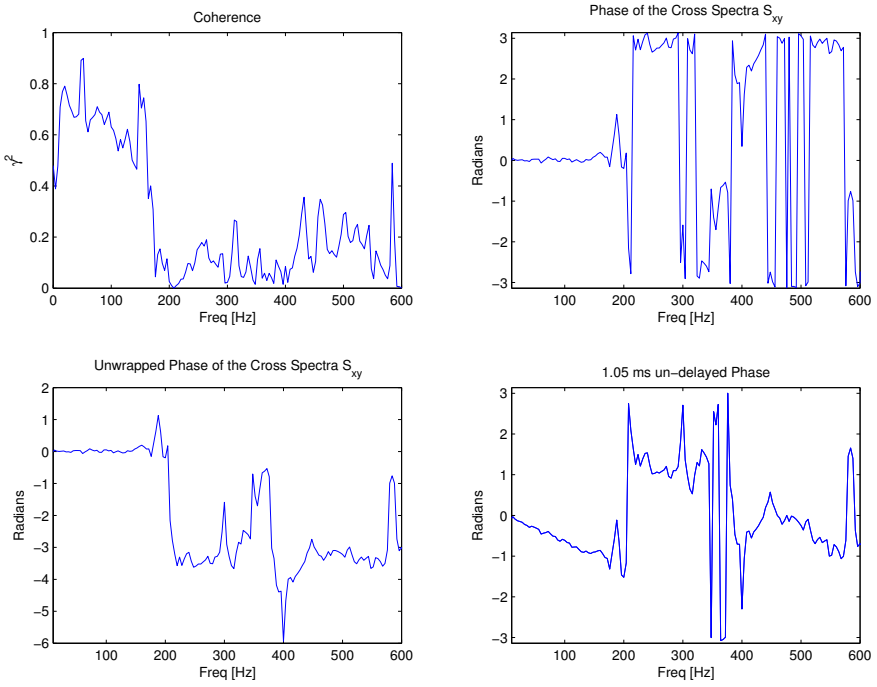

FIGURE E.1: Phase Study between RP1 and RP2 for N1=35%

Nozzle Results

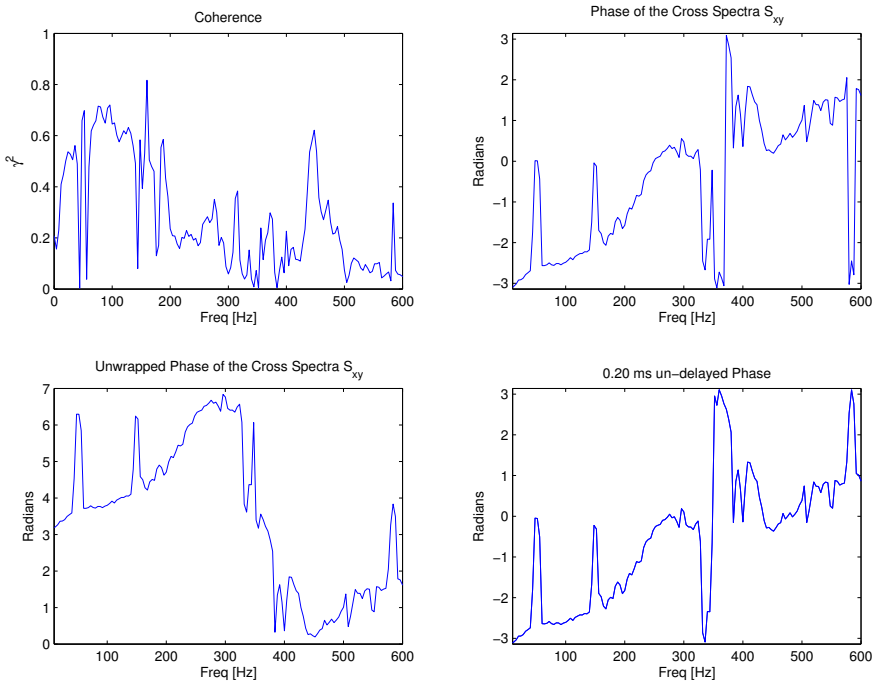

FIGURE E.2: Phase Study between RP1 and RP3 for N1=35%

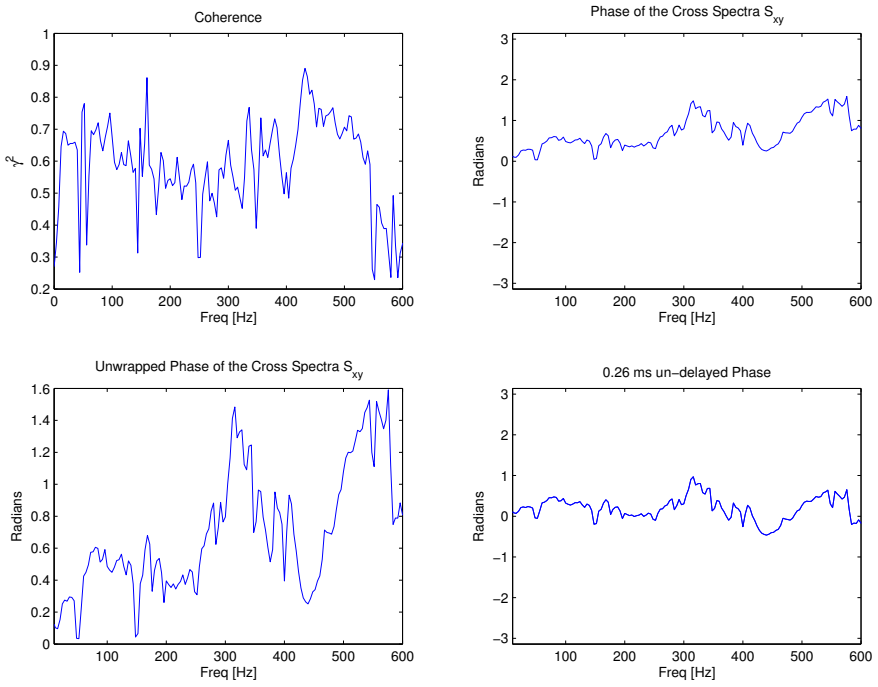

FIGURE E.3: Phase Study between RP1 and RP4 for N1=35%

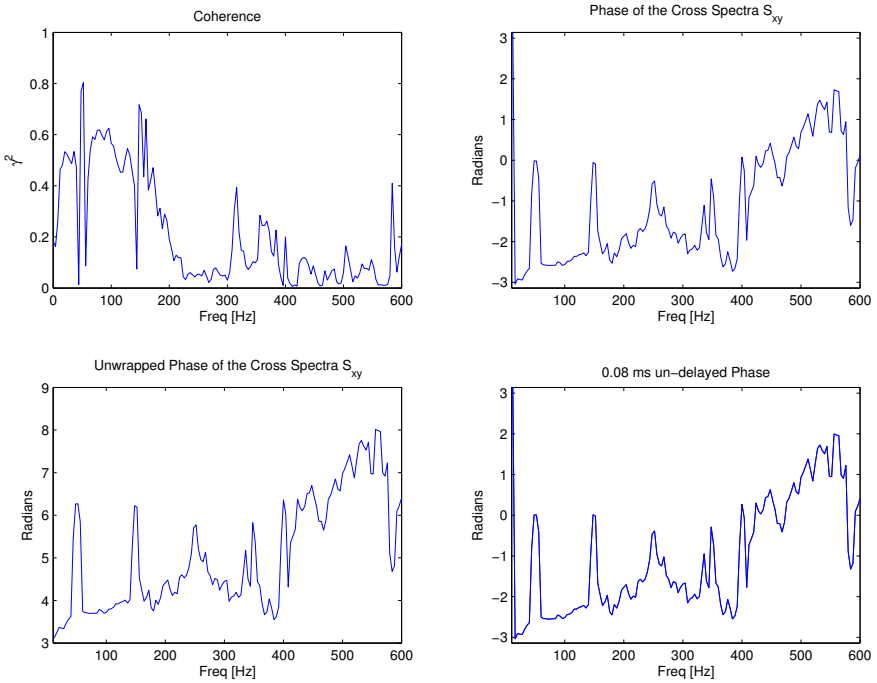

FIGURE E.4: Phase Study between RP2 and RP3 for N1=35%

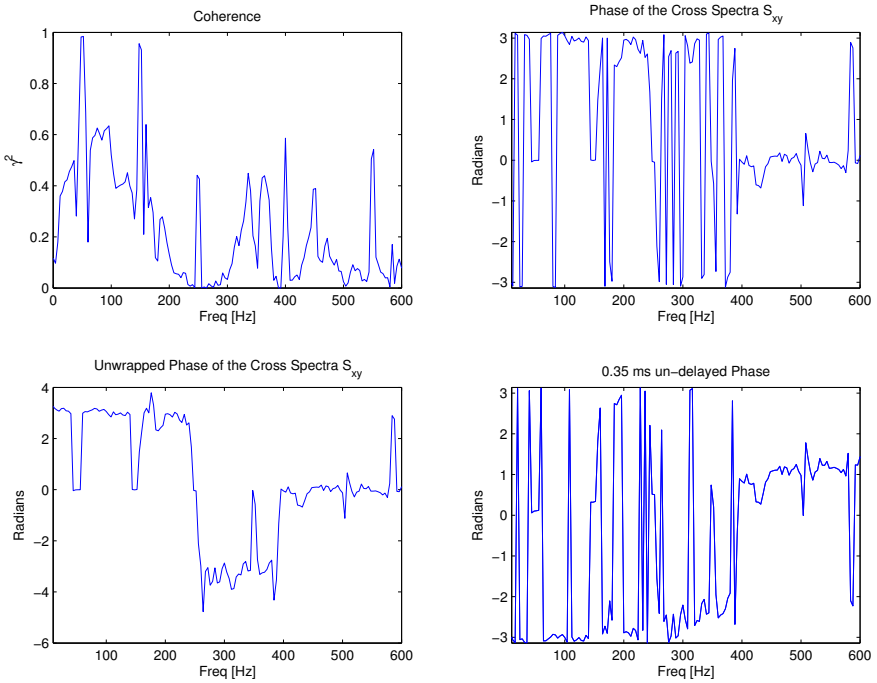

FIGURE E.5: Phase Study between RP3 and RP4 for N1=35%

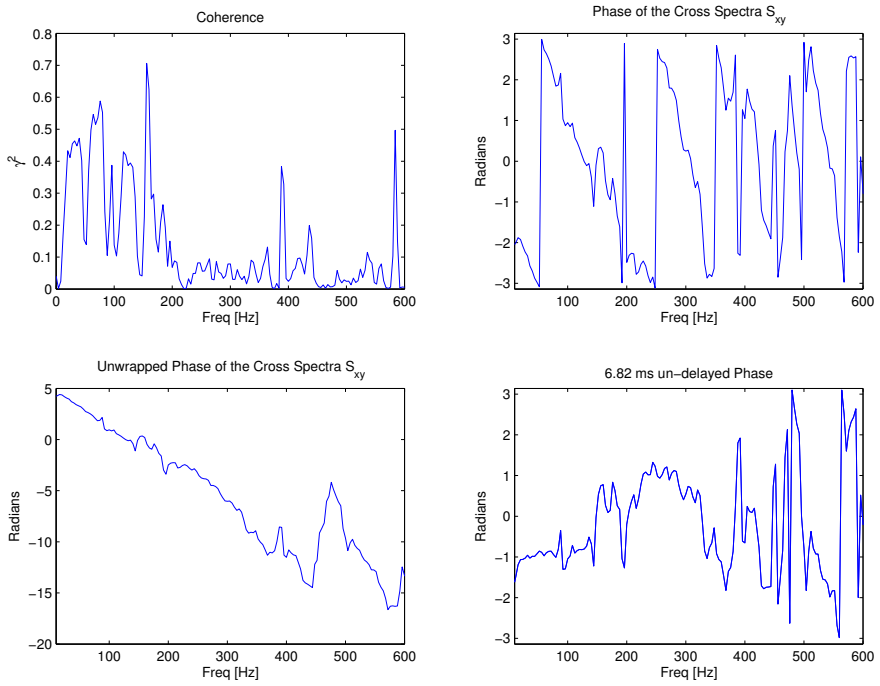

FIGURE E.6: Phase Study between RP1 and RPB for N1=35%

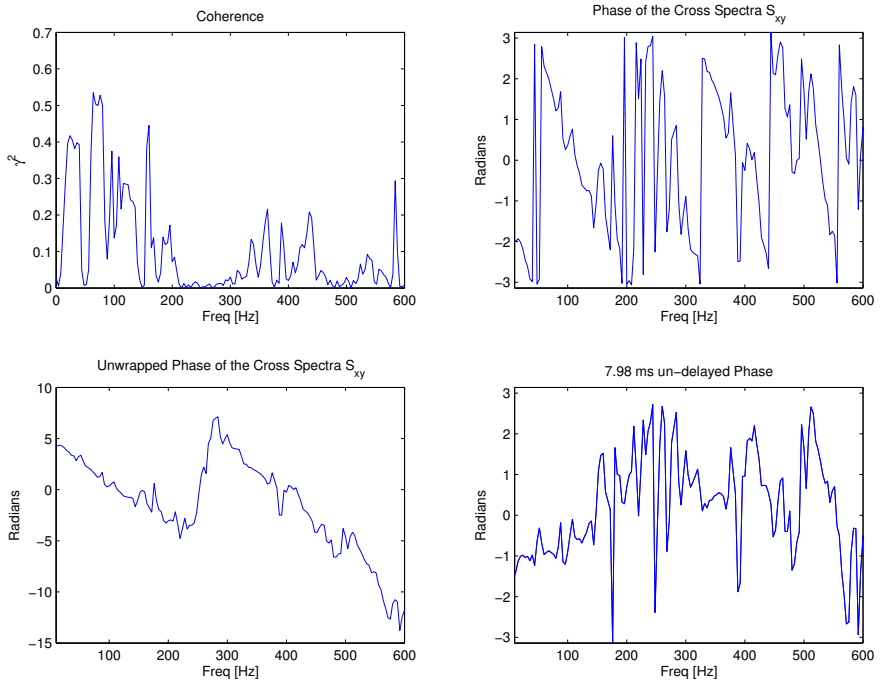

FIGURE E.7: Phase Study between RP4 and RPB for N1=35%

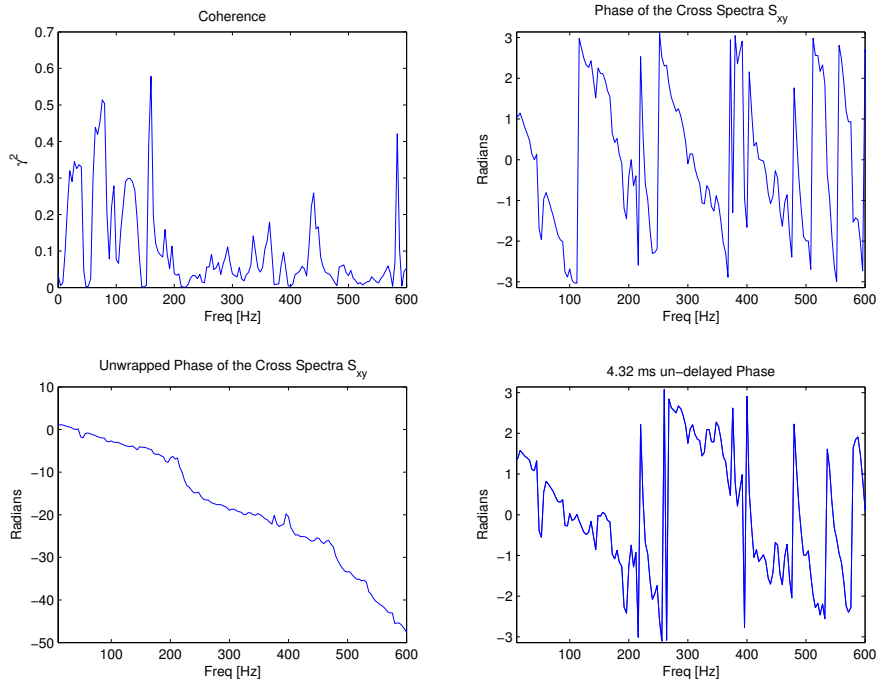

FIGURE E.8: Phase Study between RP3 and RPB for N1=35%

Microphone Results

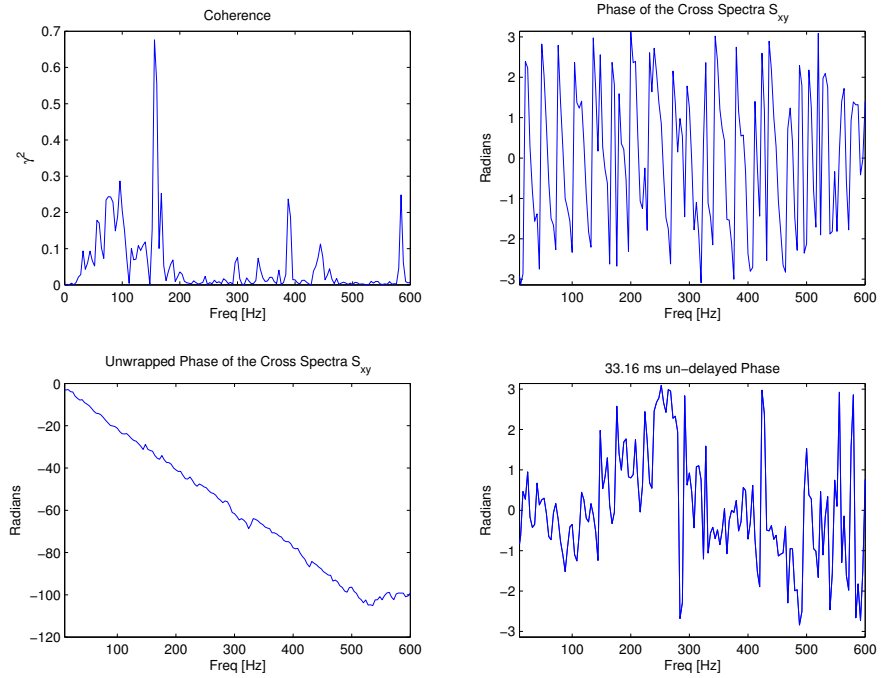

FIGURE E.9: Phase Study between RP1 and MIC1 for N1=35%

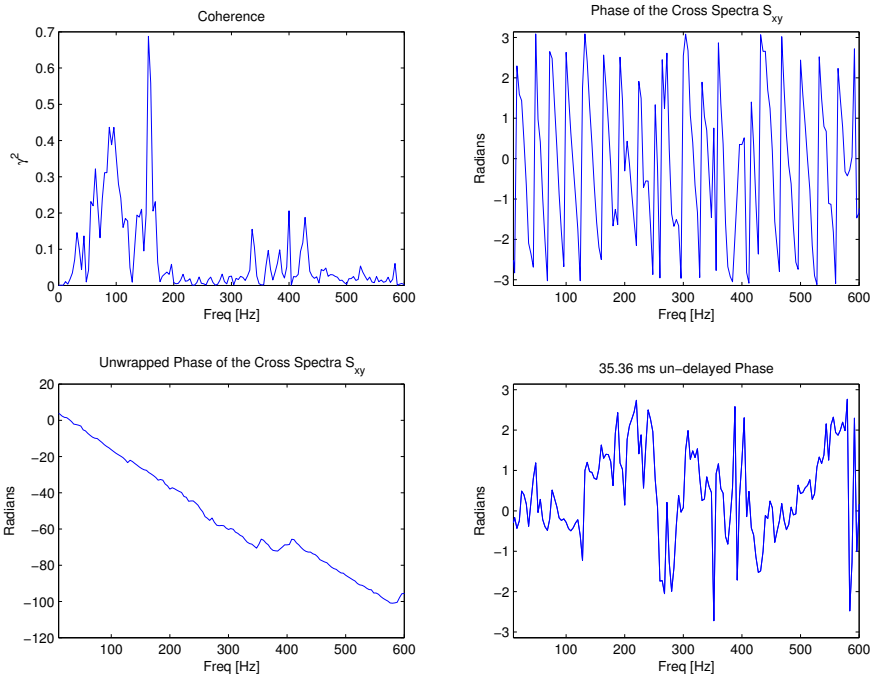

FIGURE E.10: Phase Study between RP1 and MIC5 for N1=35%

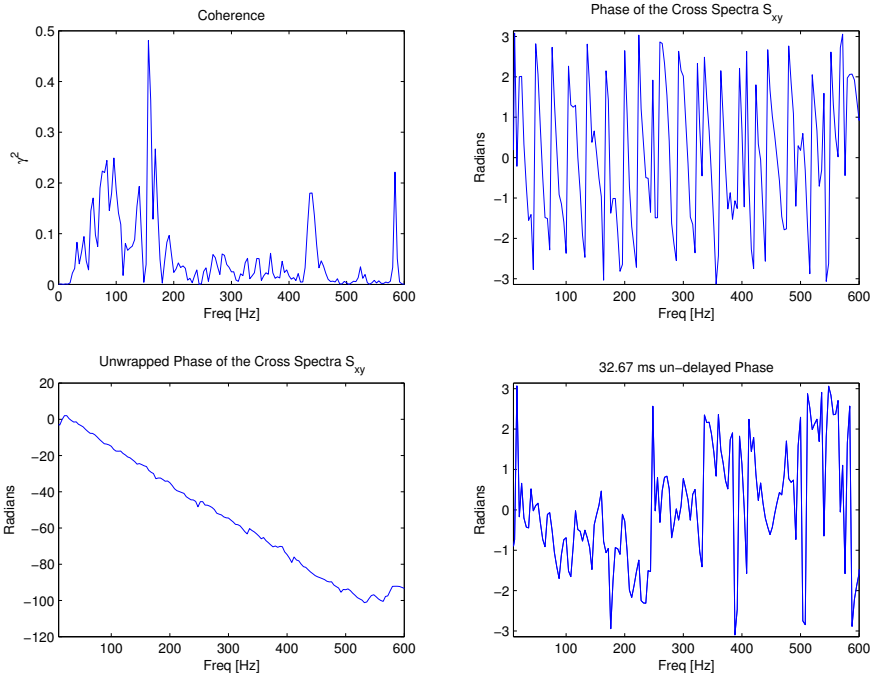

FIGURE E.11: Phase Study between RP2 and MIC1 for N1=35%

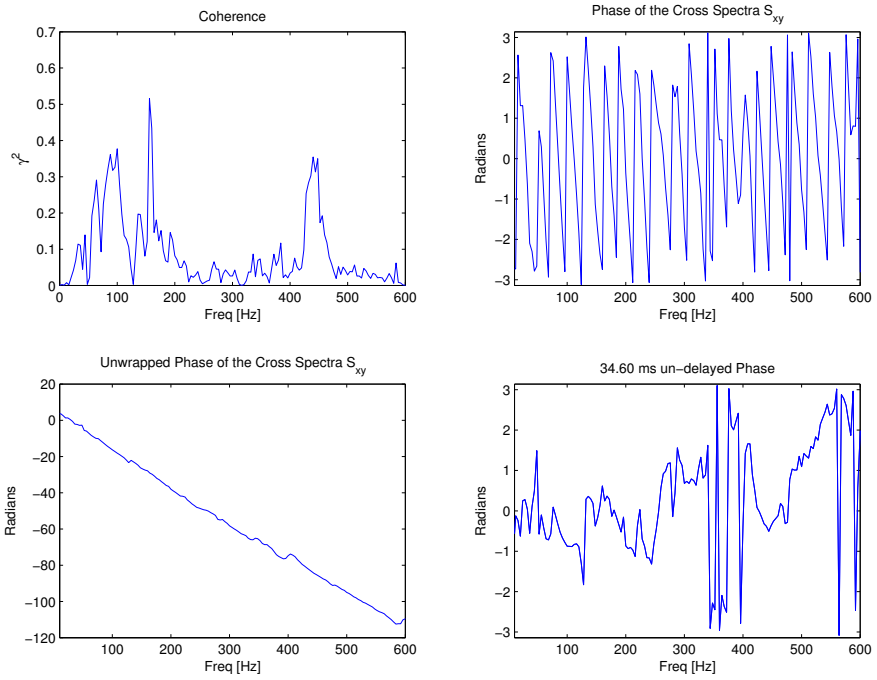

FIGURE E.12: Phase Study between RP2 and MIC5 for N1=35%

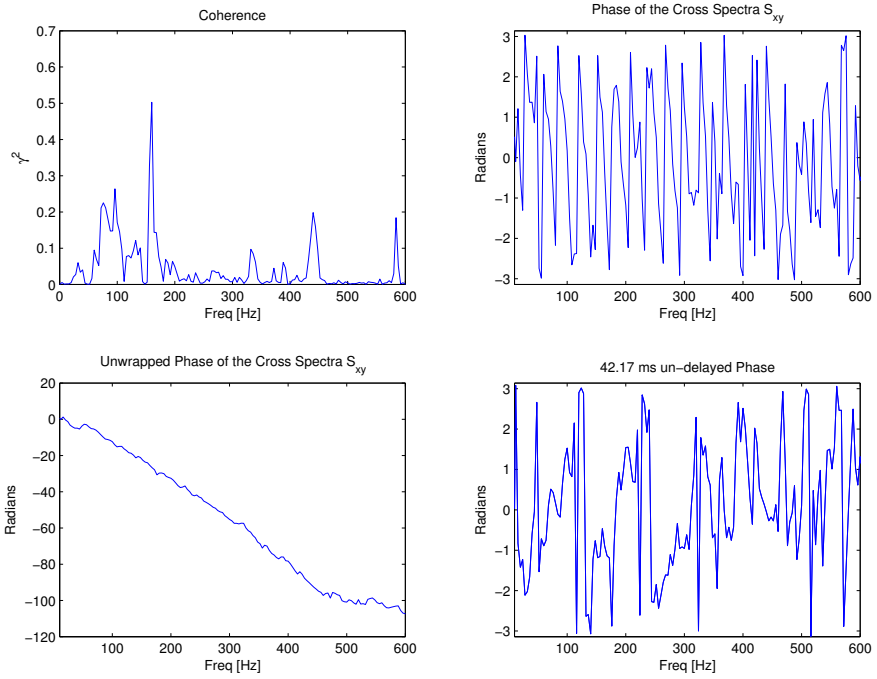

FIGURE E.13: Phase Study between RP3 and MIC1 for N1=35%

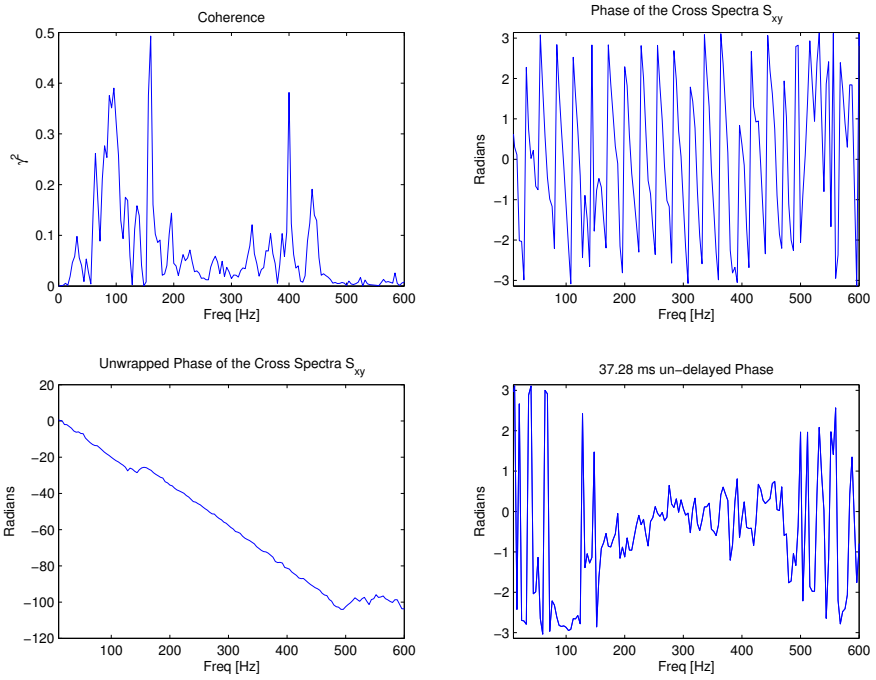

FIGURE E.14: Phase Study between RP3 and MIC5 for N1=35%

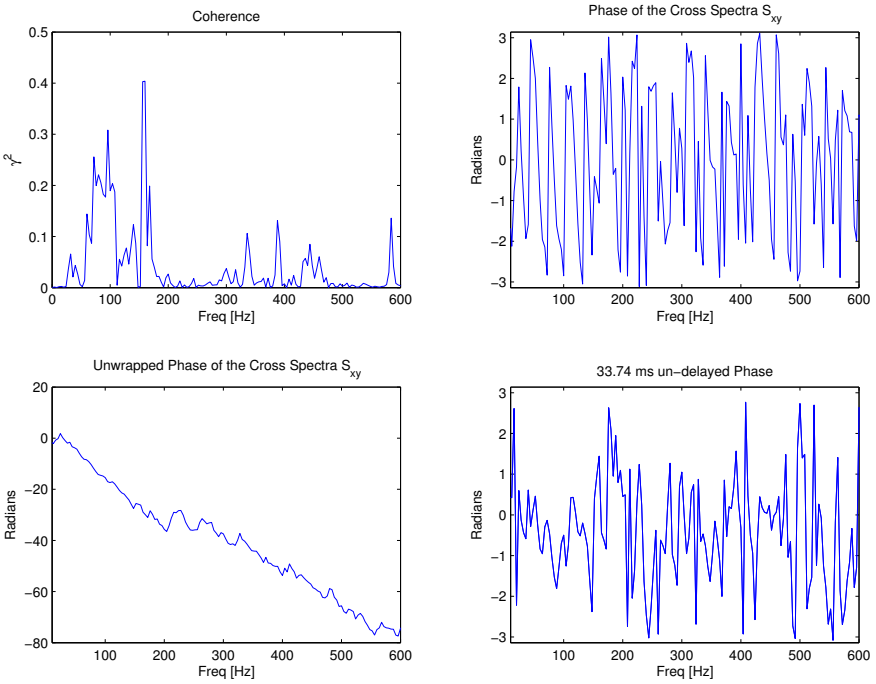

FIGURE E.15: Phase Study between RP4 and MIC1 for N1=35%

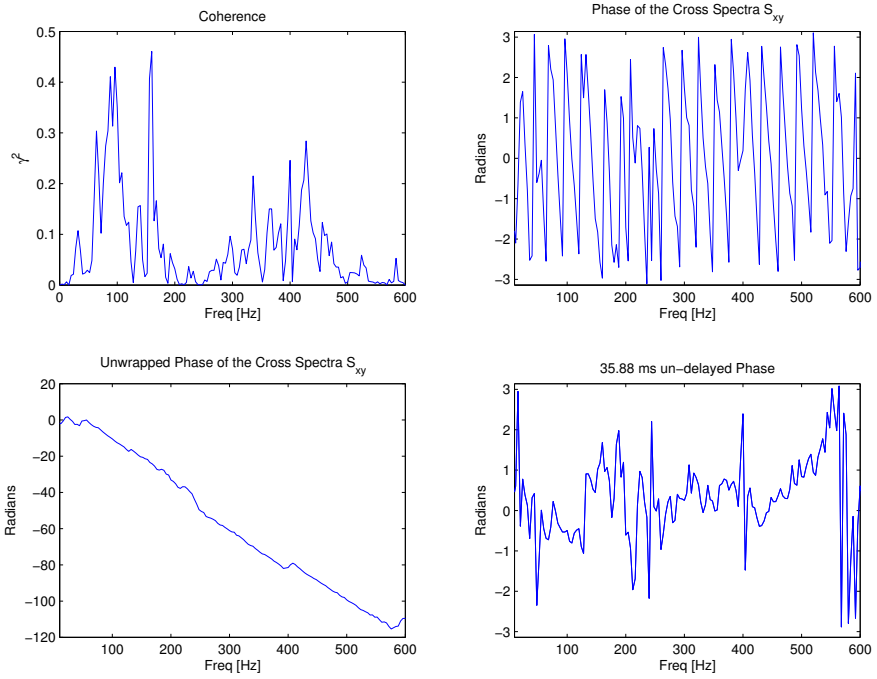

FIGURE E.16: Phase Study between RP4 and MIC5 for N1=35%

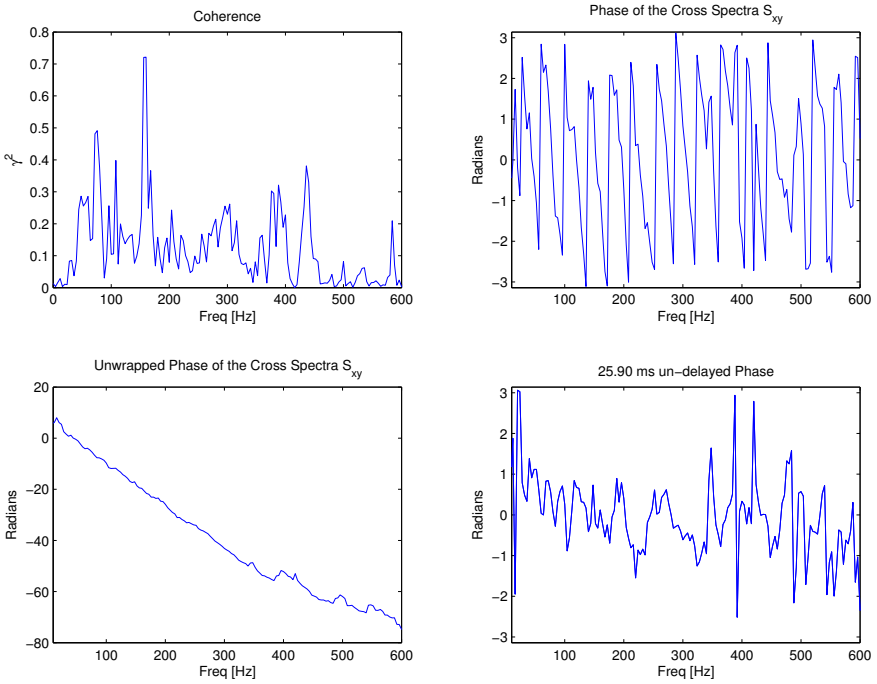

FIGURE E.17: Phase Study between RPB and MIC1 for N1=35%

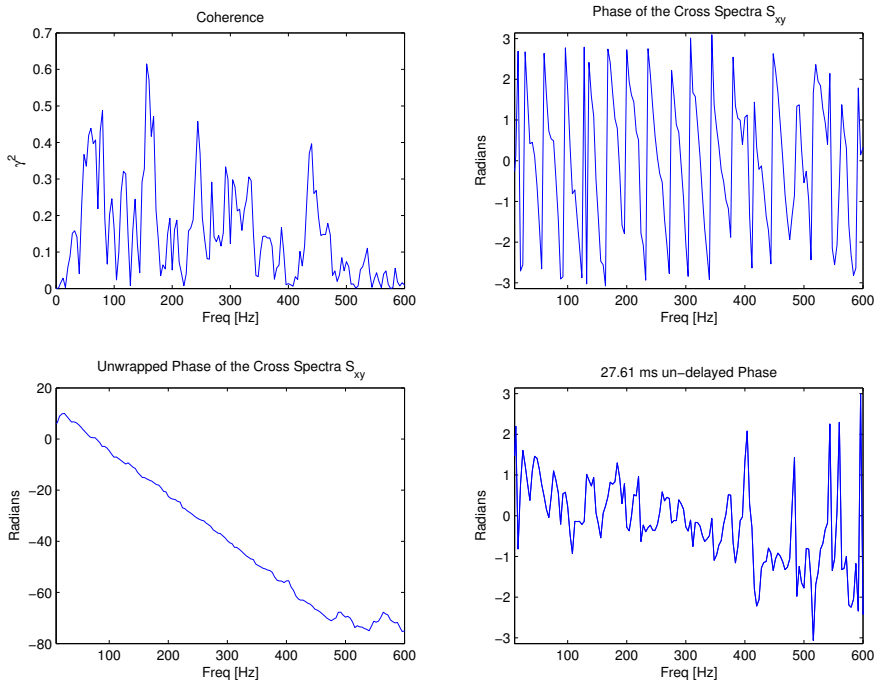

FIGURE E.18: Phase Study between RPB and MIC5 for N1=35%

E.2 N1 = 44%

E.2.1 Comobustion Chamber Results

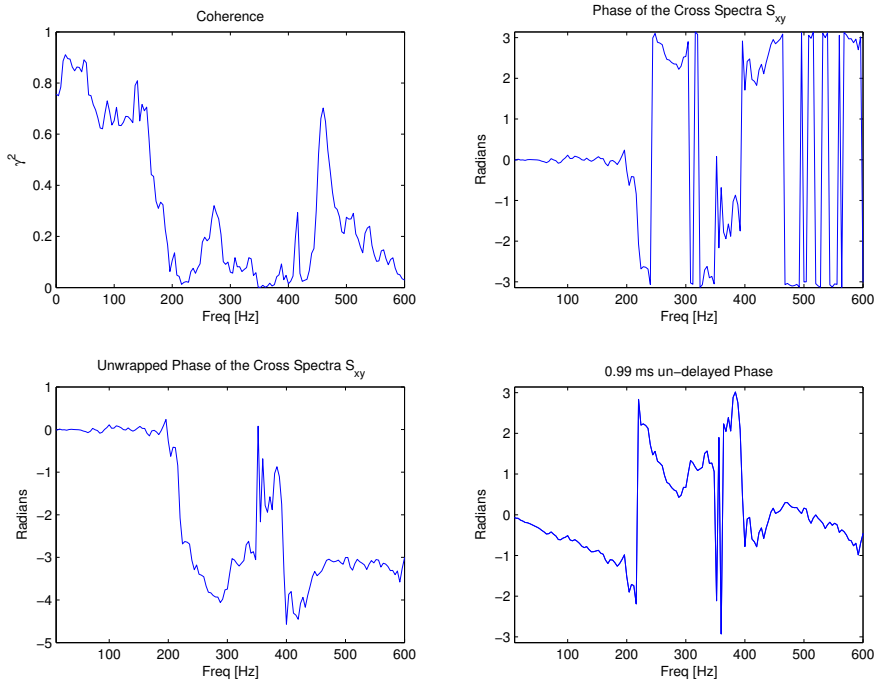

FIGURE E.19: Phase Study between RP1 and RP2 for N1=44%

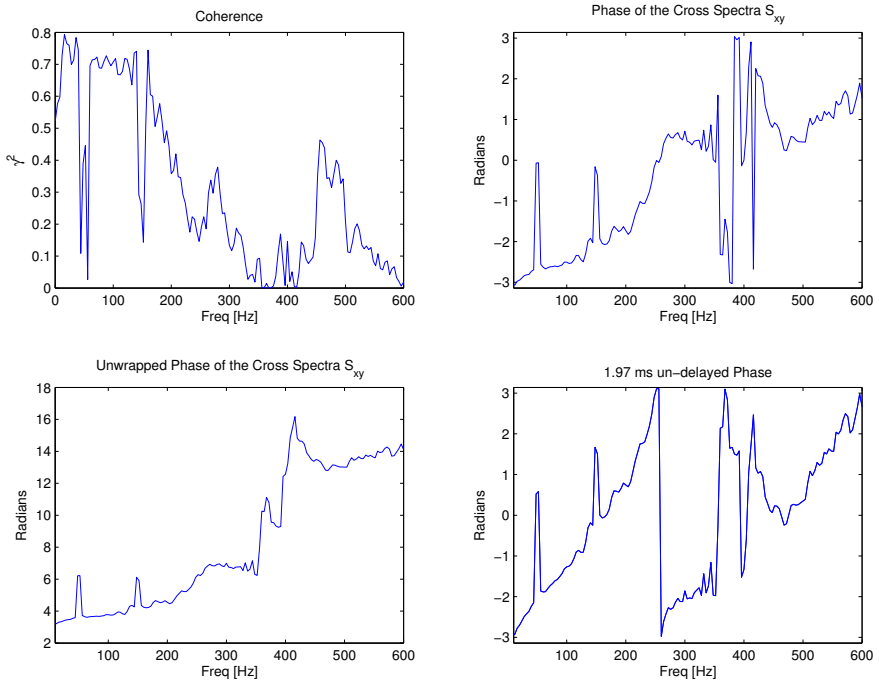

FIGURE E.20: Phase Study between RP1 and RP3 for N1=44%

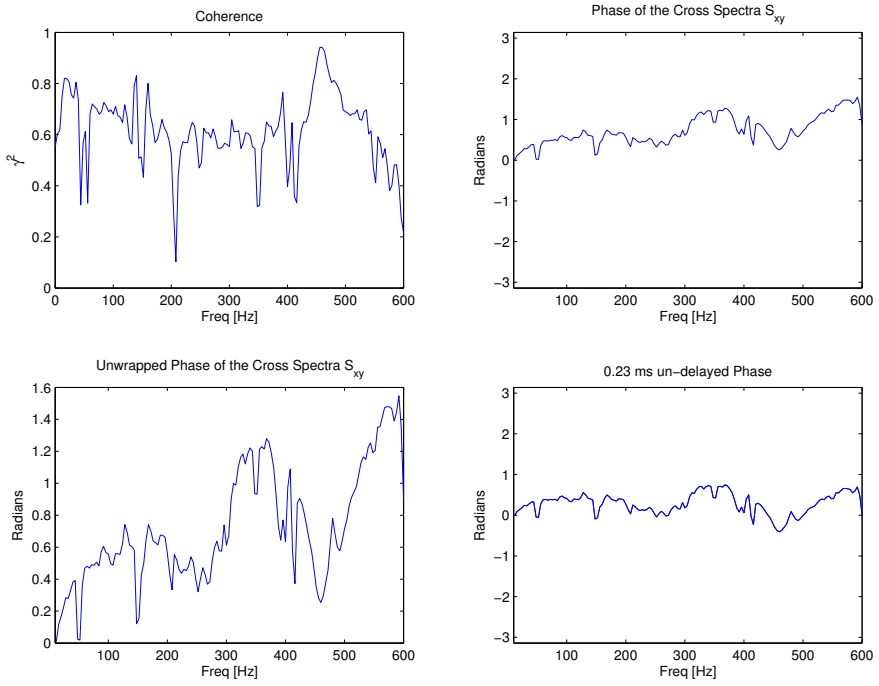

FIGURE E.21: Phase Study between RP1 and RP4 for N1=44%

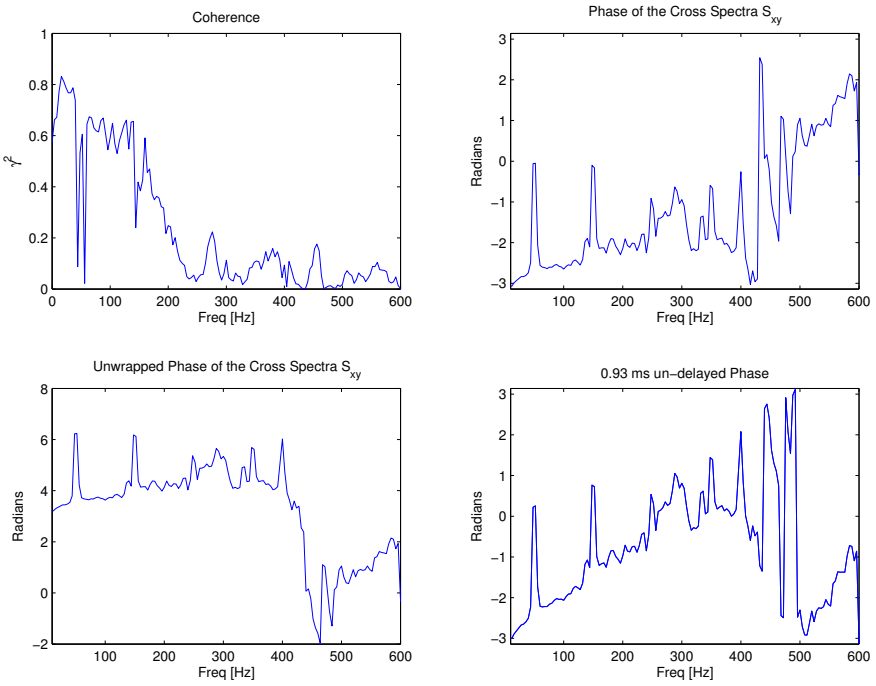

FIGURE E.22: Phase Study between RP2 and RP3 for N1=44%

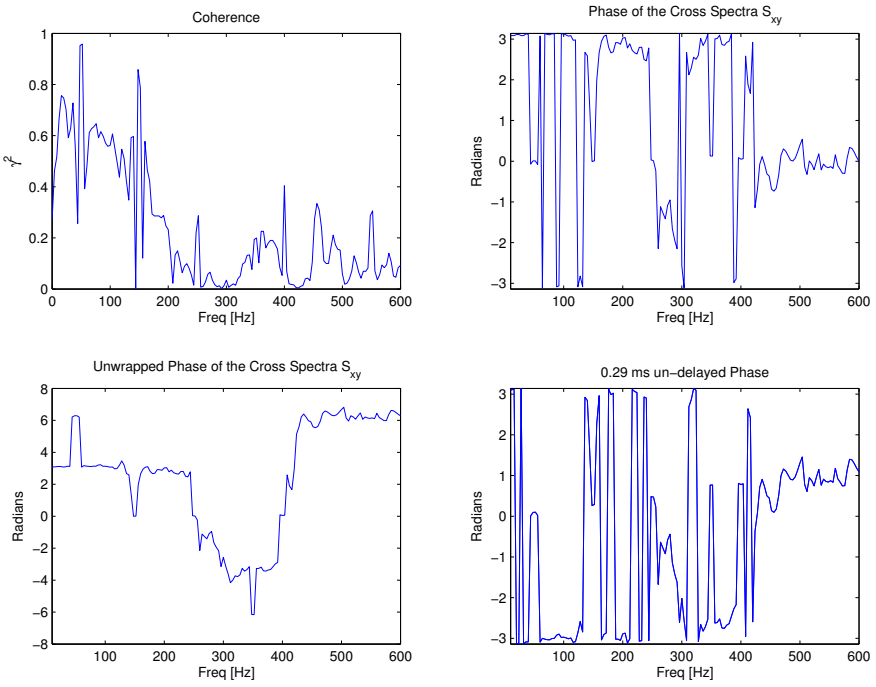

FIGURE E.23: Phase Study between RP3 and RP4 for N1=44%

Nozzle Results

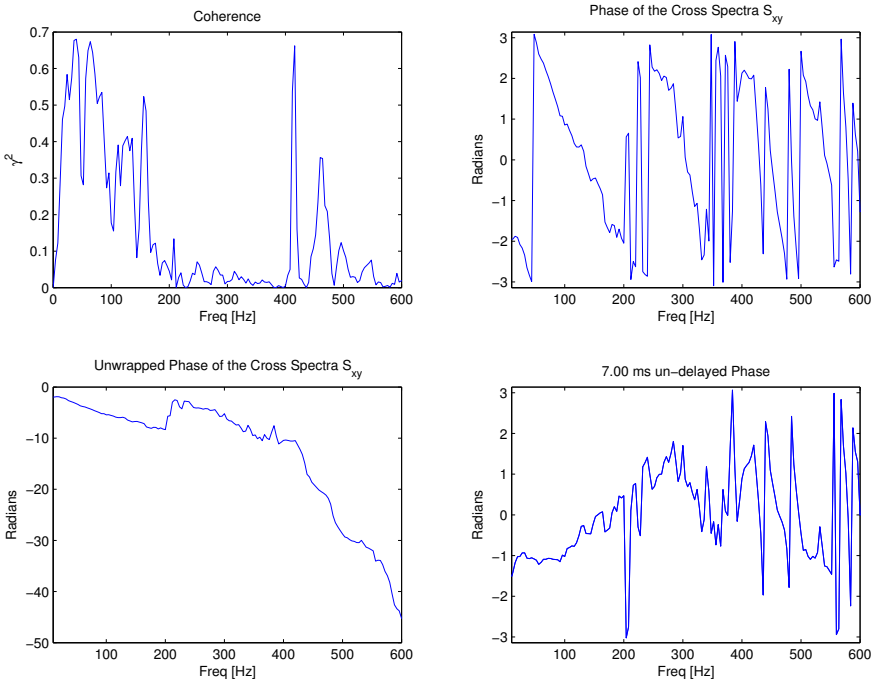

FIGURE E.24: Phase Study between RP1 and RPB for N1=44%

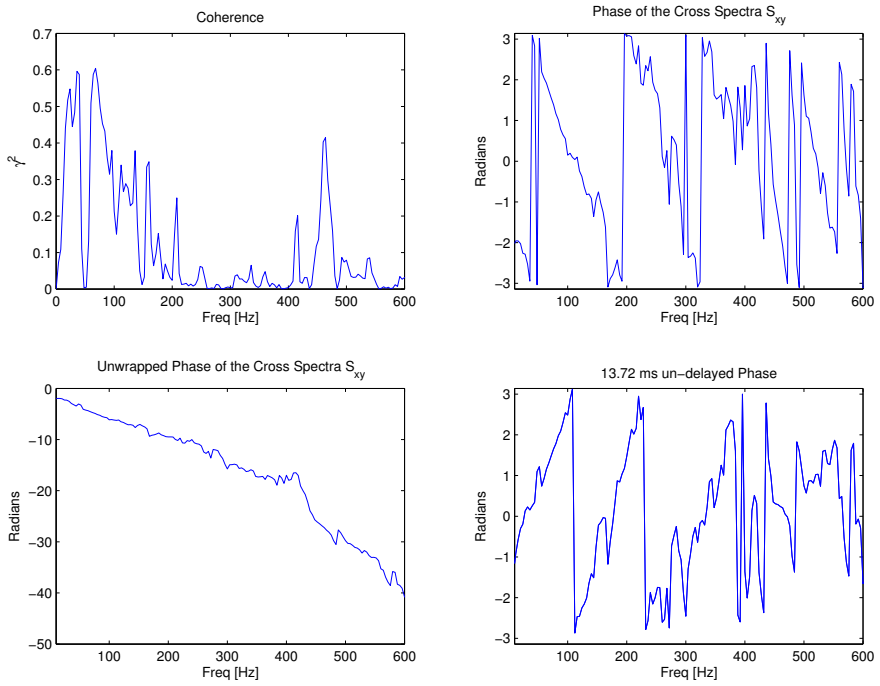

FIGURE E.25: Phase Study between RP4 and RPB for N1=44%

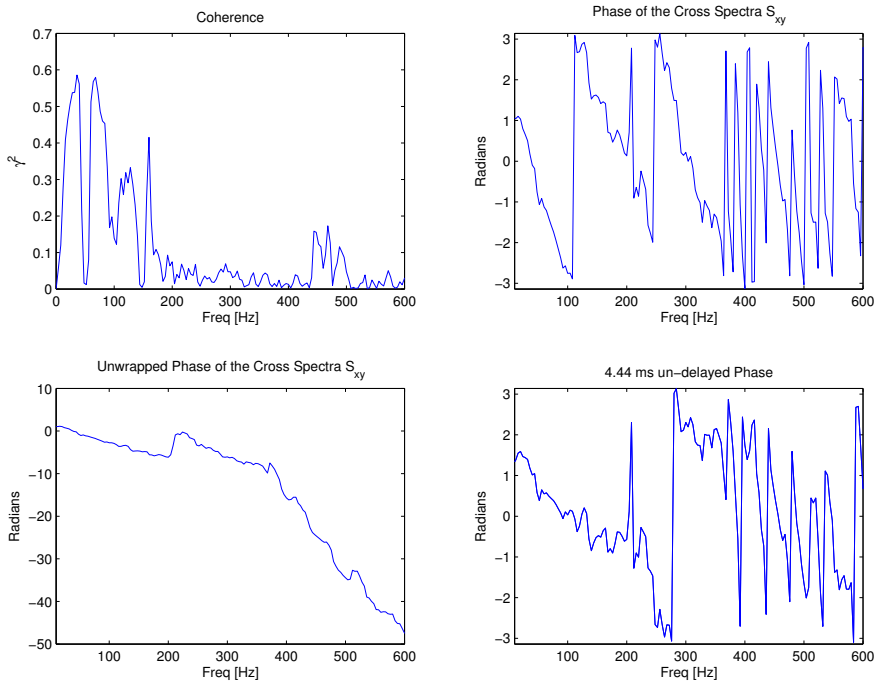

FIGURE E.26: Phase Study between RP3 and RPB for N1=44%

Microphone Results

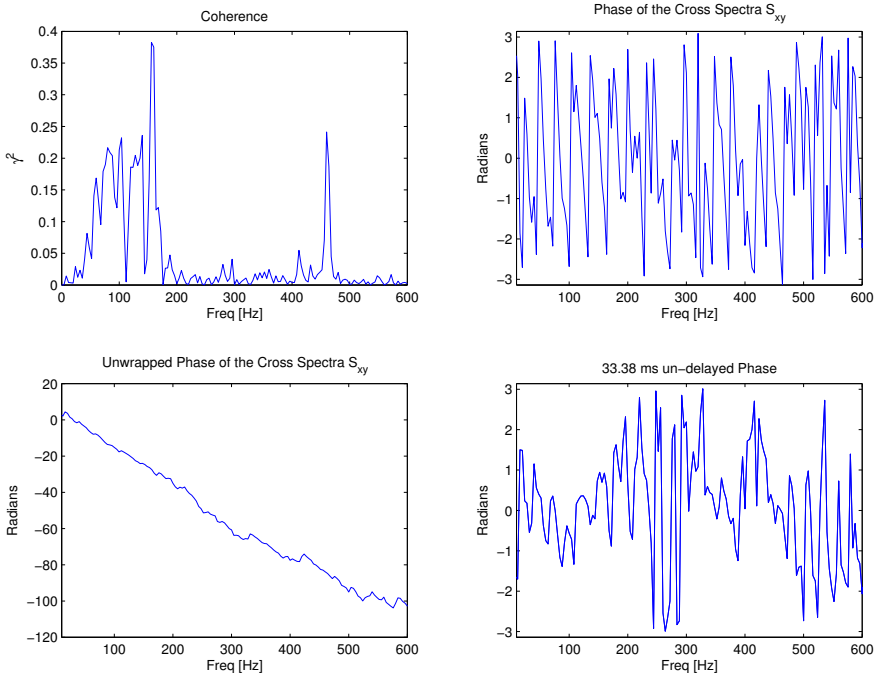

FIGURE E.27: Phase Study between RP1 and MIC1 for N1=44%

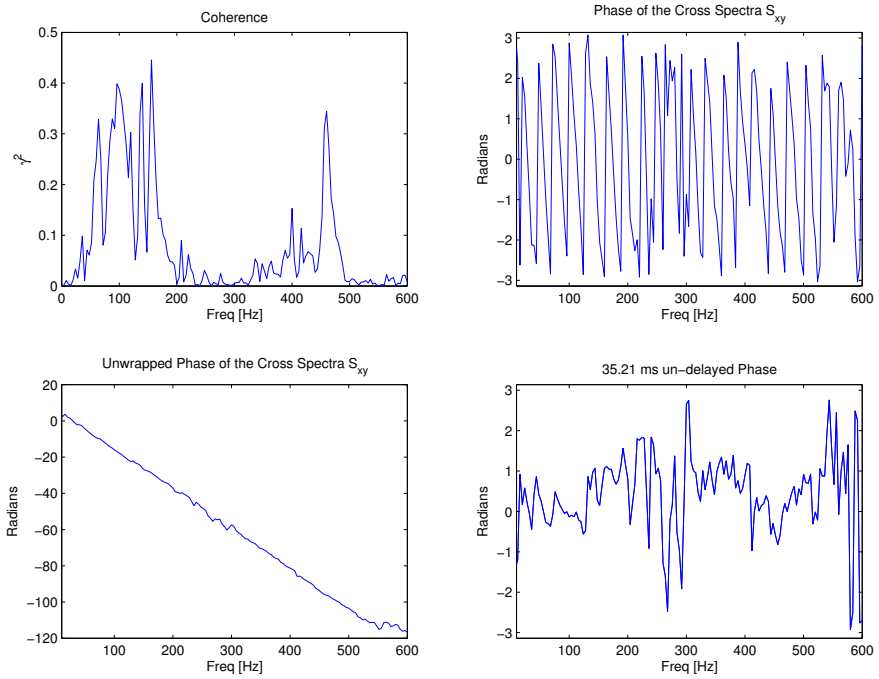

FIGURE E.28: Phase Study between RP1 and MIC5 for N1=44%

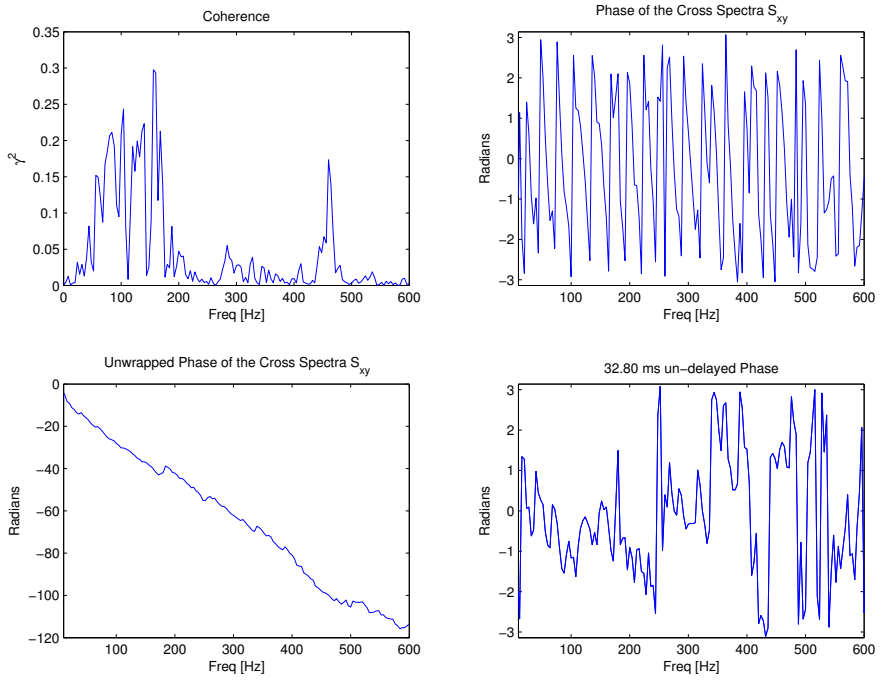

FIGURE E.29: Phase Study between RP2 and MIC1 for N1=44%

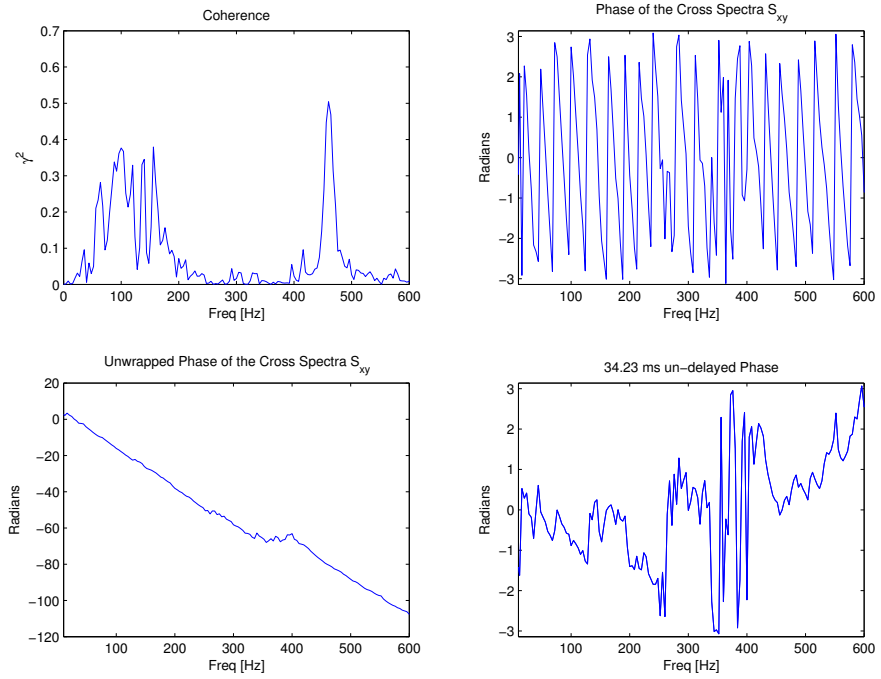

FIGURE E.30: Phase Study between RP2 and MIC5 for N1=44%

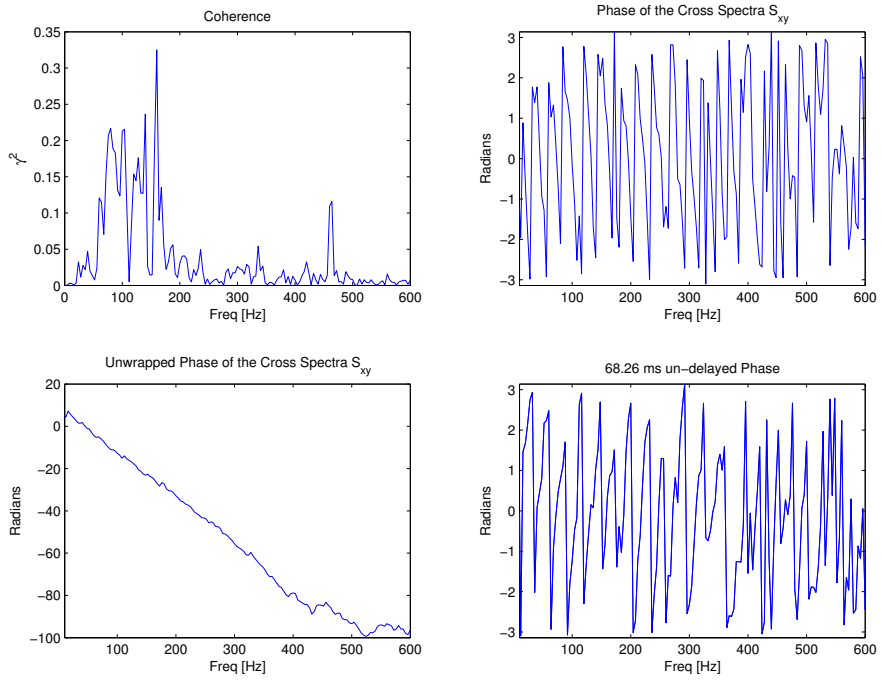

FIGURE E.31: Phase Study between RP3 and MIC1 for N1=44%

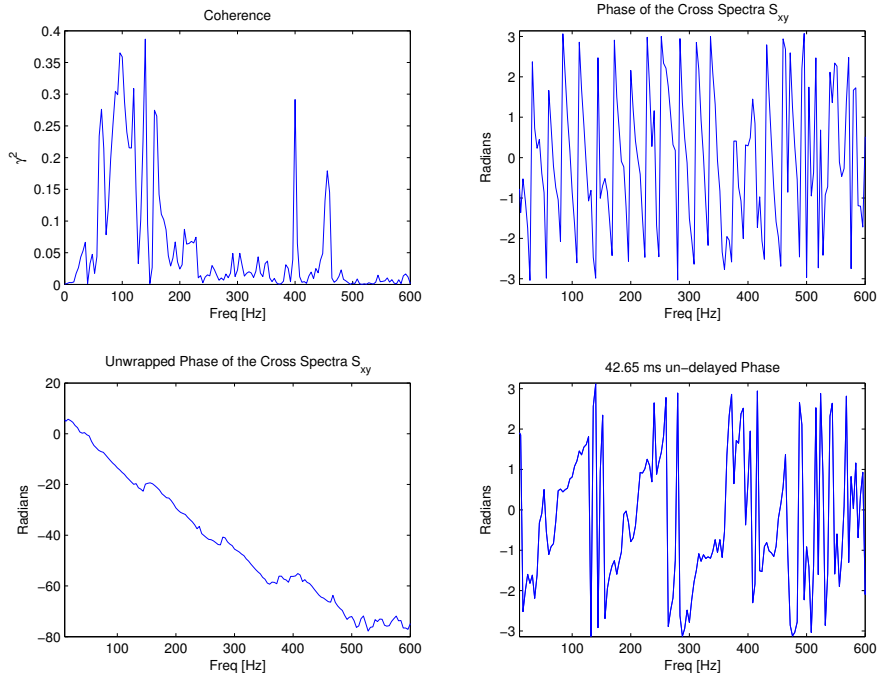

FIGURE E.32: Phase Study between RP3 and MIC5 for N1=44%

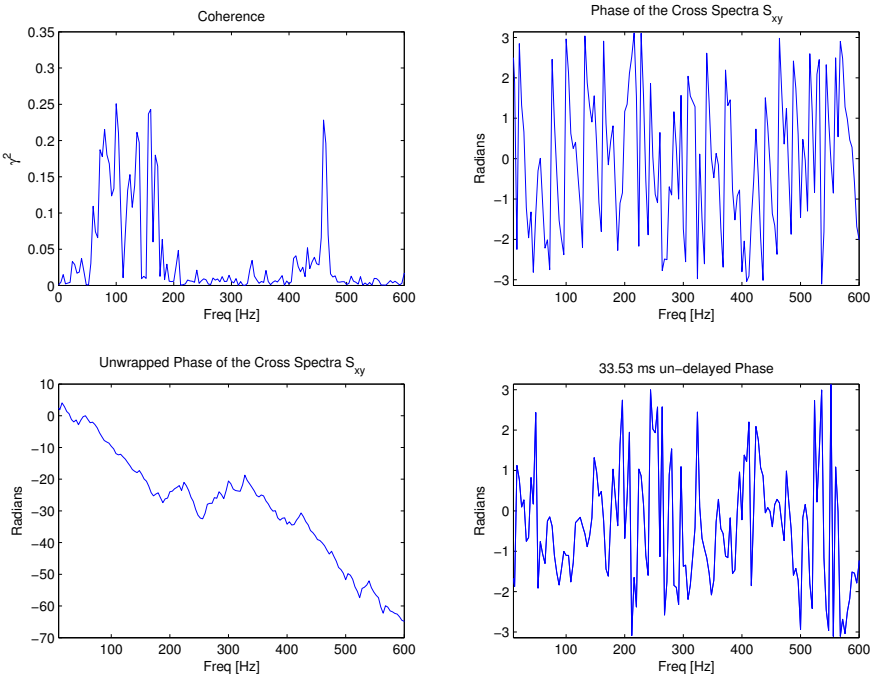

FIGURE E.33: Phase Study between RP4 and MIC1 for N1=44%

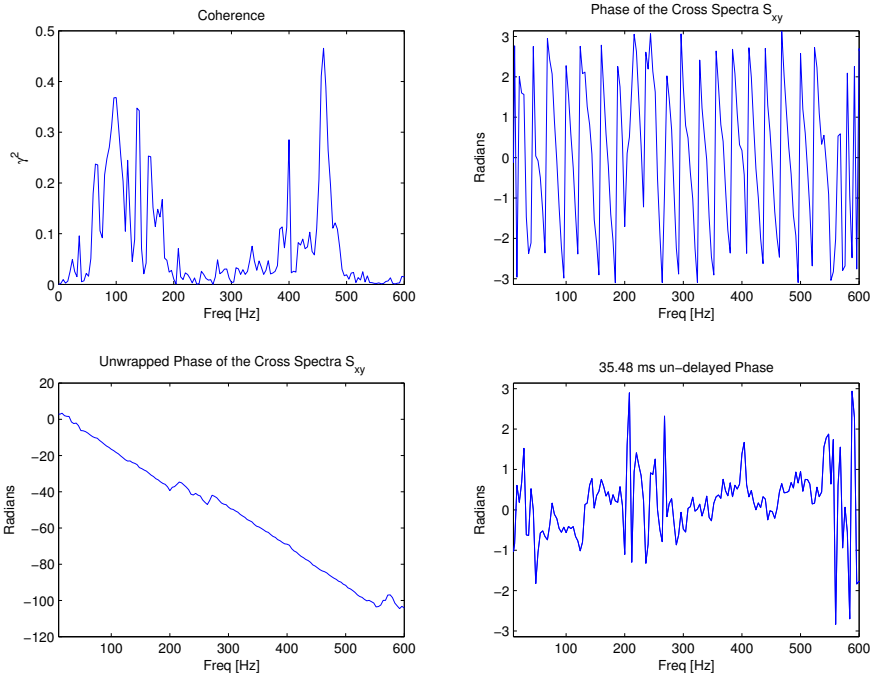

FIGURE E.34: Phase Study between RP4 and MIC5 for N1=44%

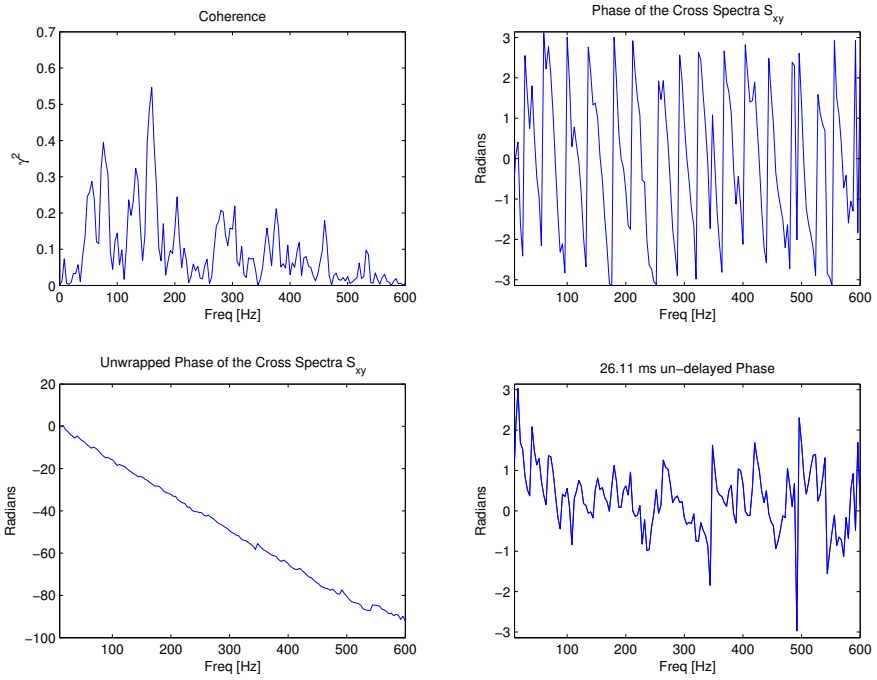

FIGURE E.35: Phase Study between RPB and MIC1 for N1=44%

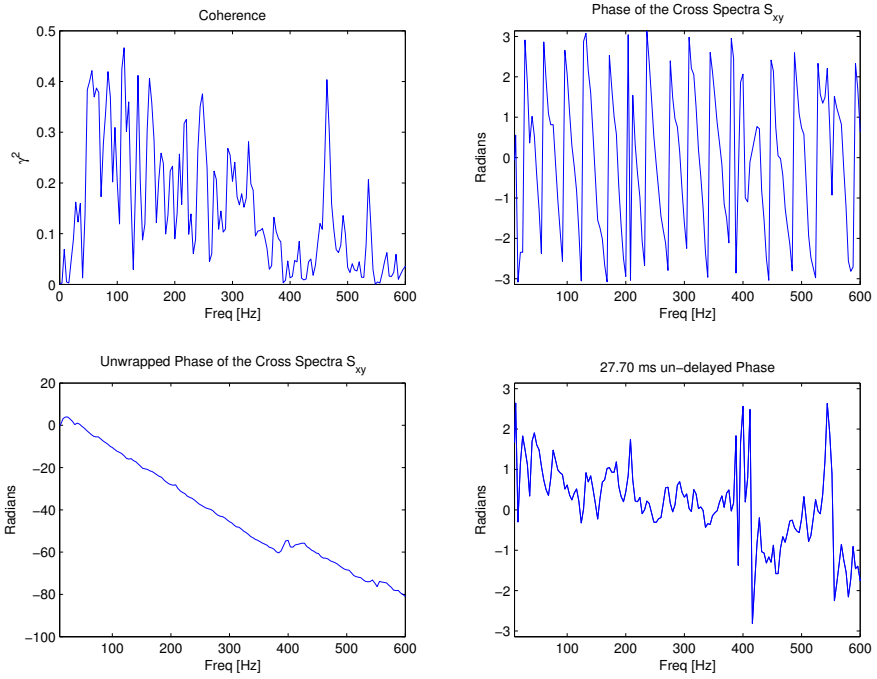

FIGURE E.36: Phase Study between RPB and MIC5 for N1=44%

E.3 N1 = 61%

Combustion Chamber Results

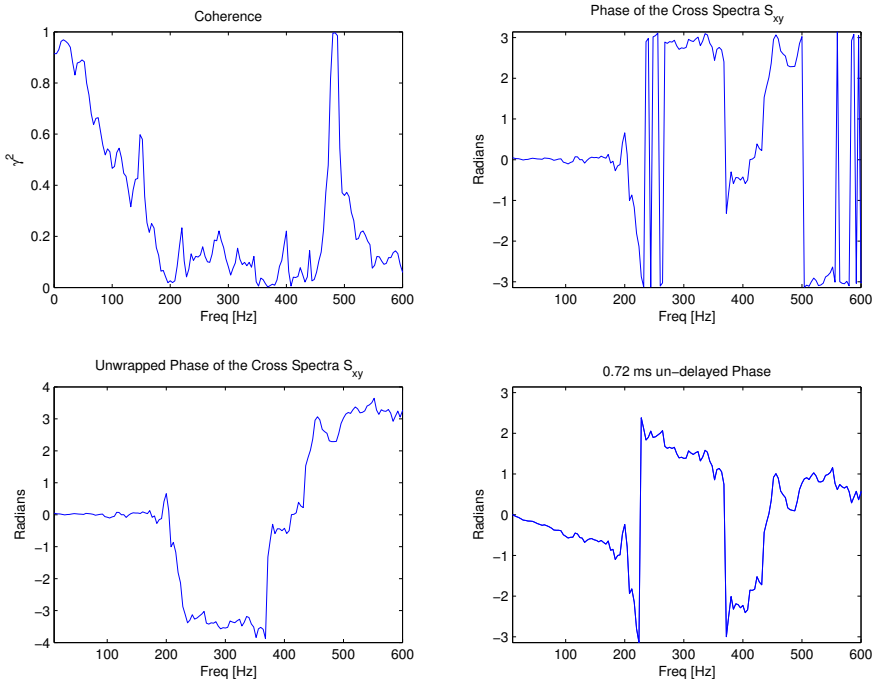

FIGURE E.37: Phase Study between RP1 and RP2 for N1=61%

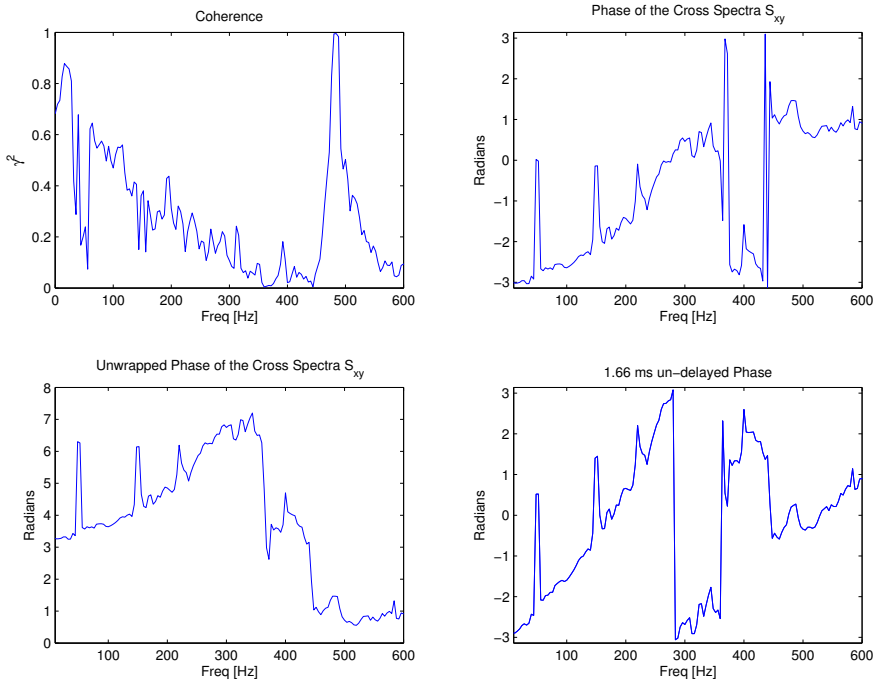

FIGURE E.38: Phase Study between RP1 and RP3 for N1=61%

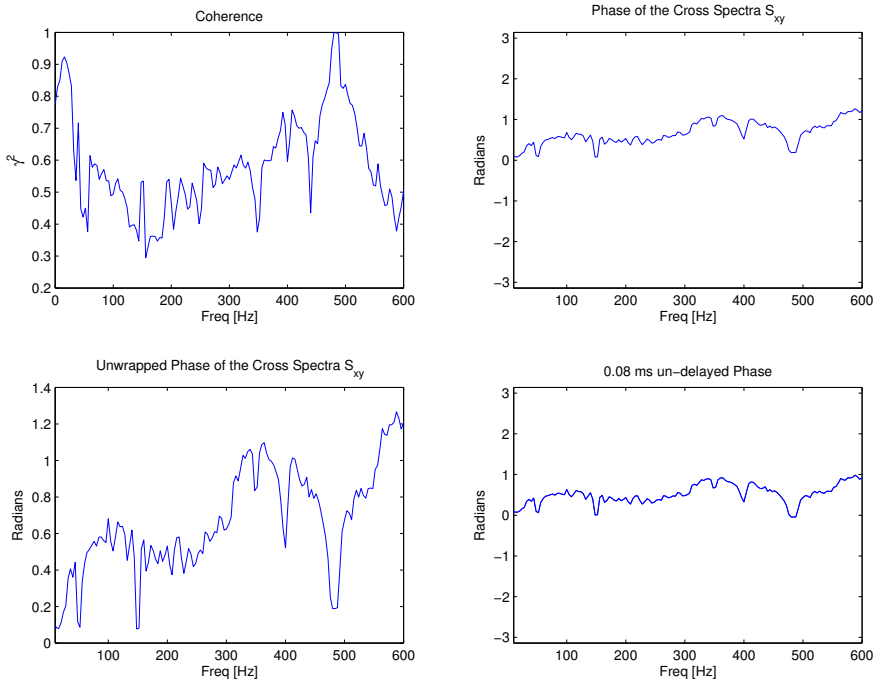

FIGURE E.39: Phase Study between RP1 and RP4 for N1=61%

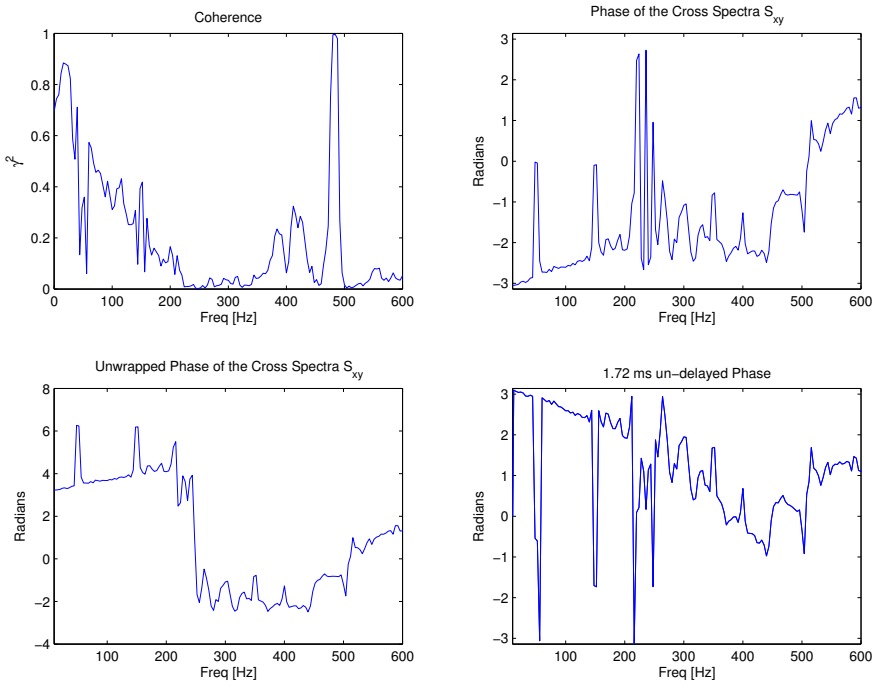

FIGURE E.40: Phase Study between RP2 and RP3 for N1=61%

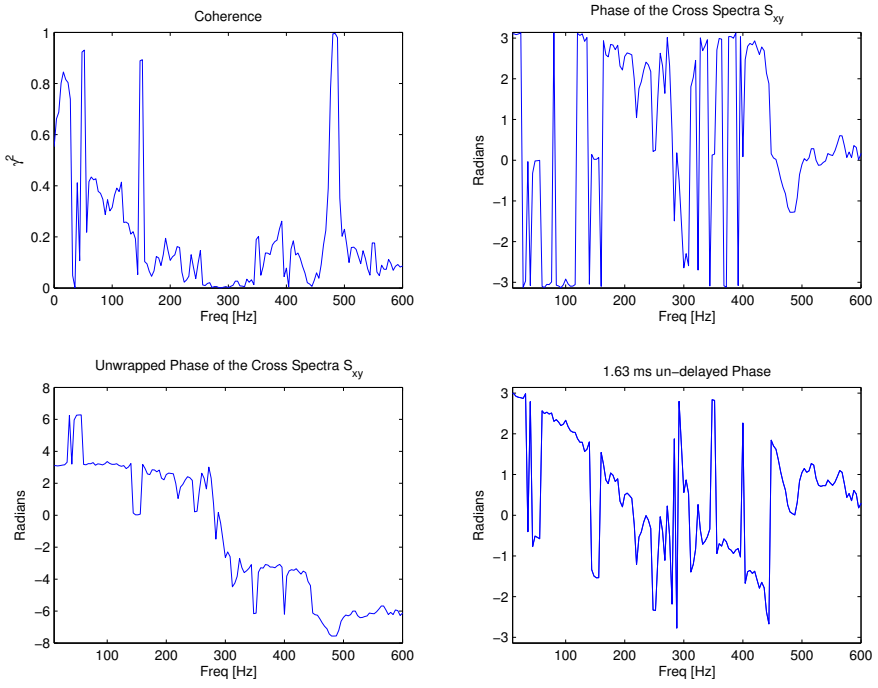

FIGURE E.41: Phase Study between RP3 and RP4 for N1=61%

Nozzle Results

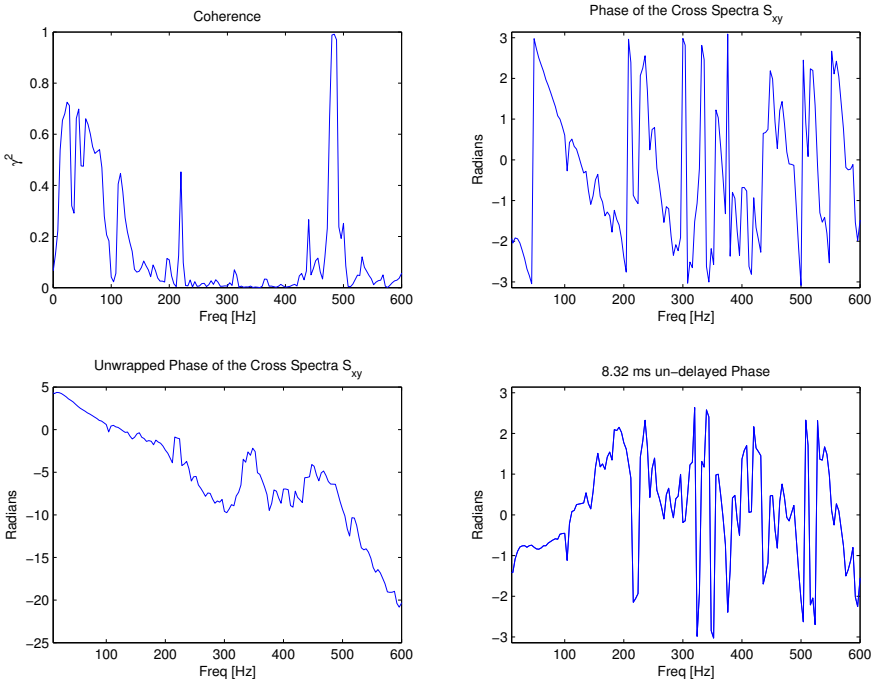

FIGURE E.42: Phase Study between RP1 and RPB for N1=61%

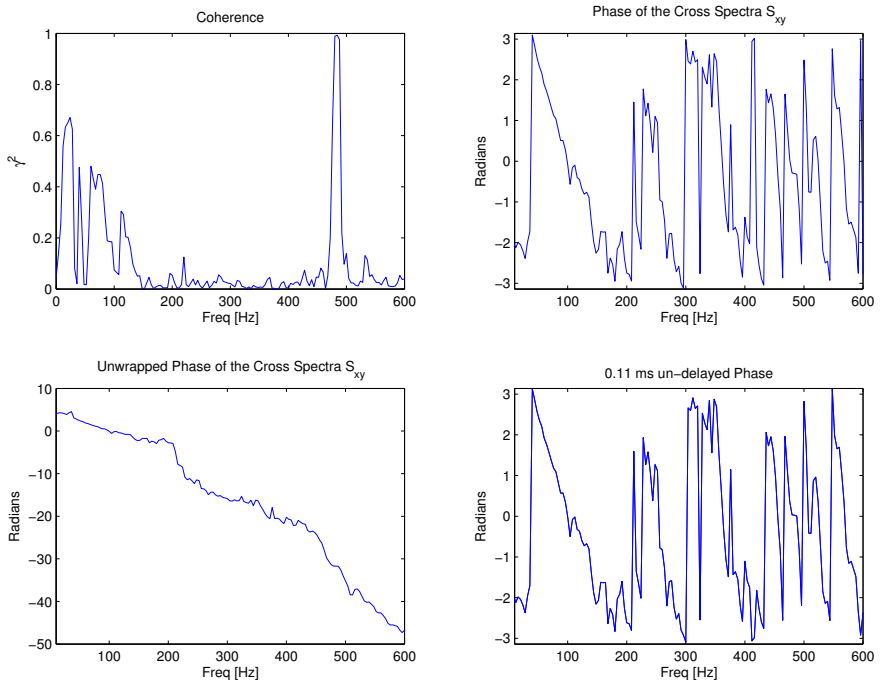

FIGURE E.43: Phase Study between RP4 and RPB for N1=61%

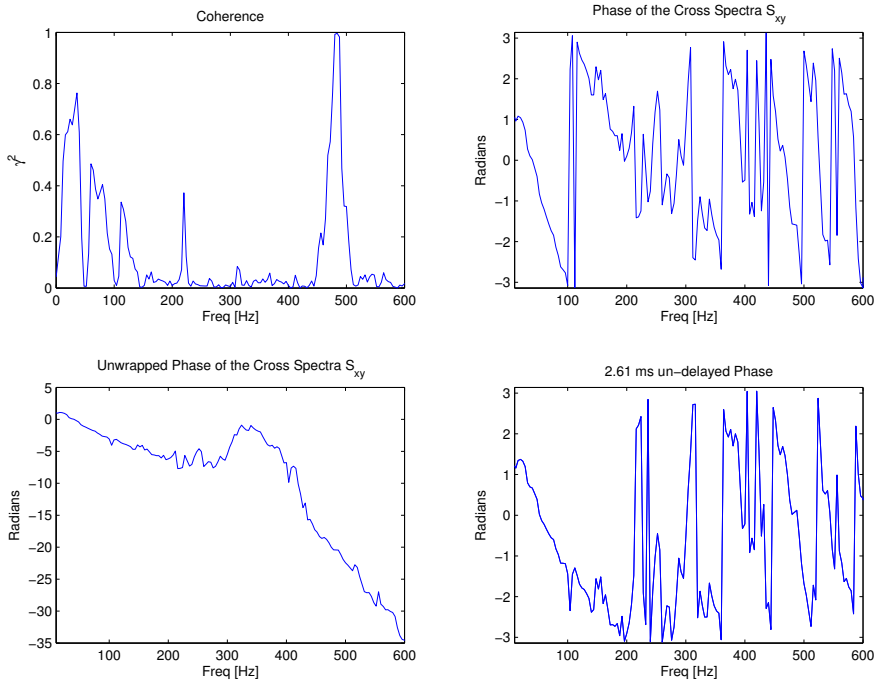

FIGURE E.44: Phase Study between RP3 and RPB for N1=61%

Microphone Results

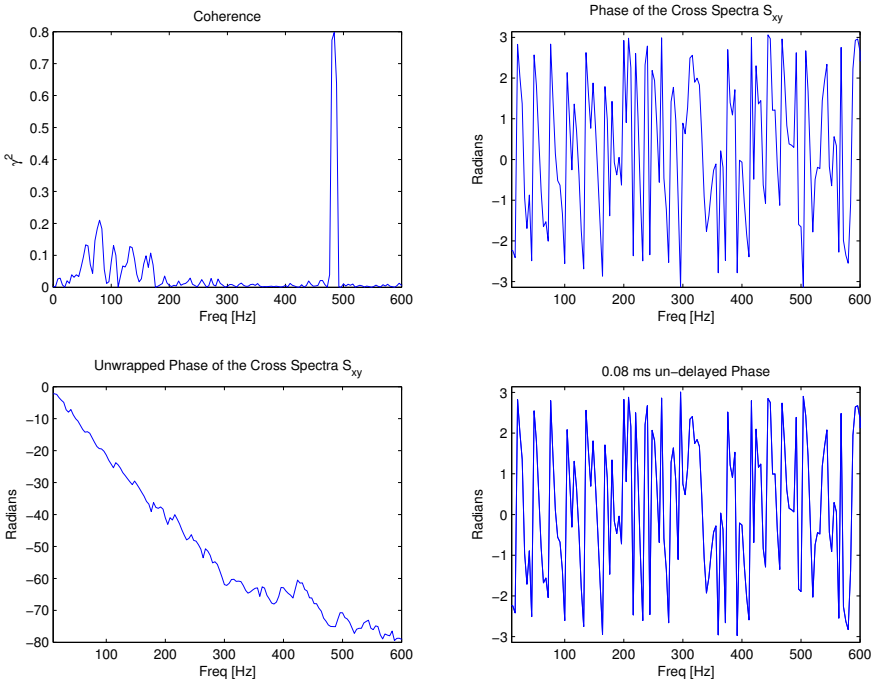

FIGURE E.45: Phase Study between RP1 and MIC1 for N1=61%

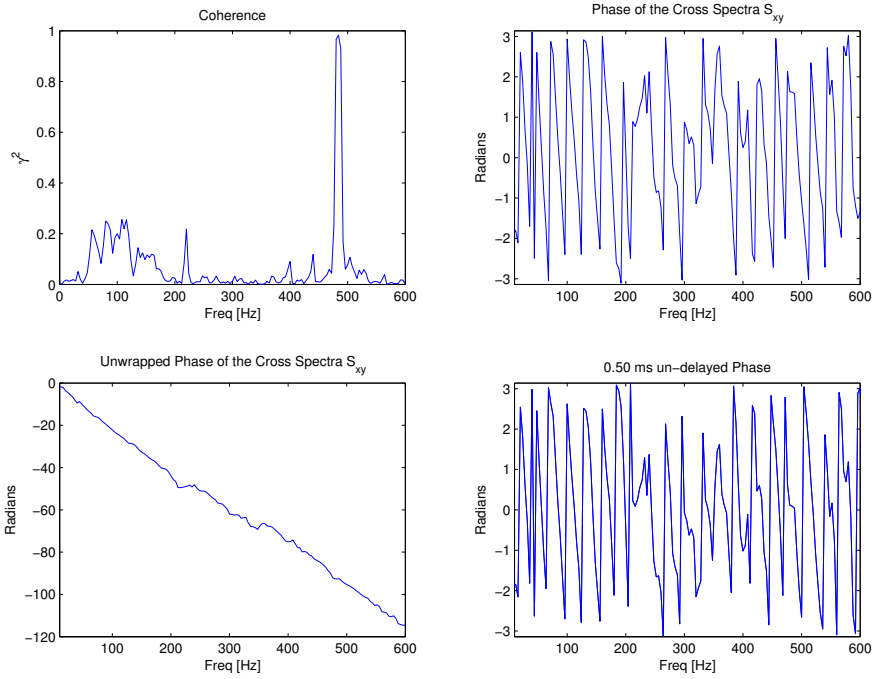

FIGURE E.46: Phase Study between RP1 and MIC5 for N1=61%

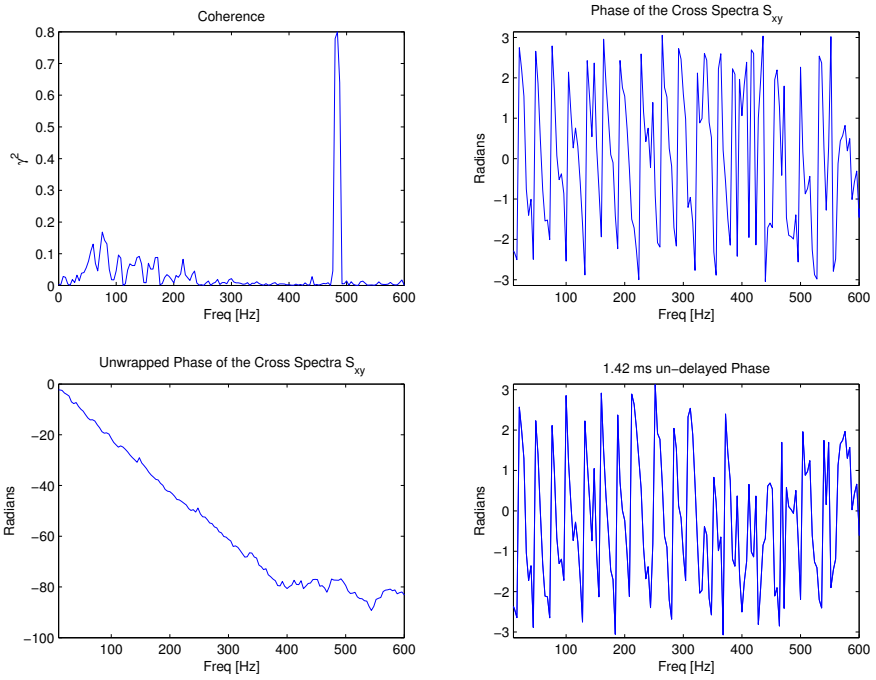

FIGURE E.47: Phase Study between RP2 and MIC1 for N1=61%

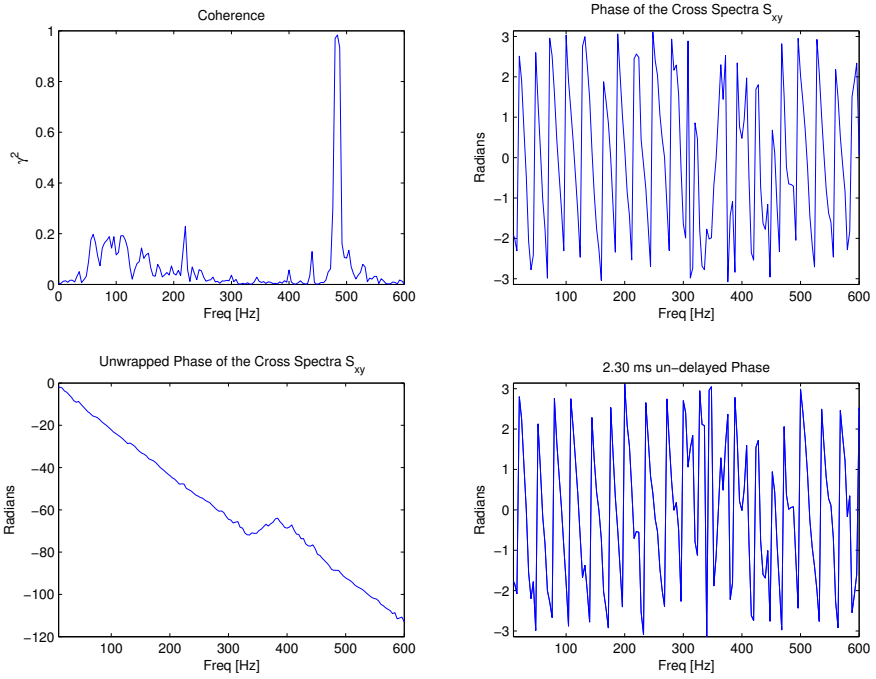

FIGURE E.48: Phase Study between RP2 and MIC5 for N1=61%

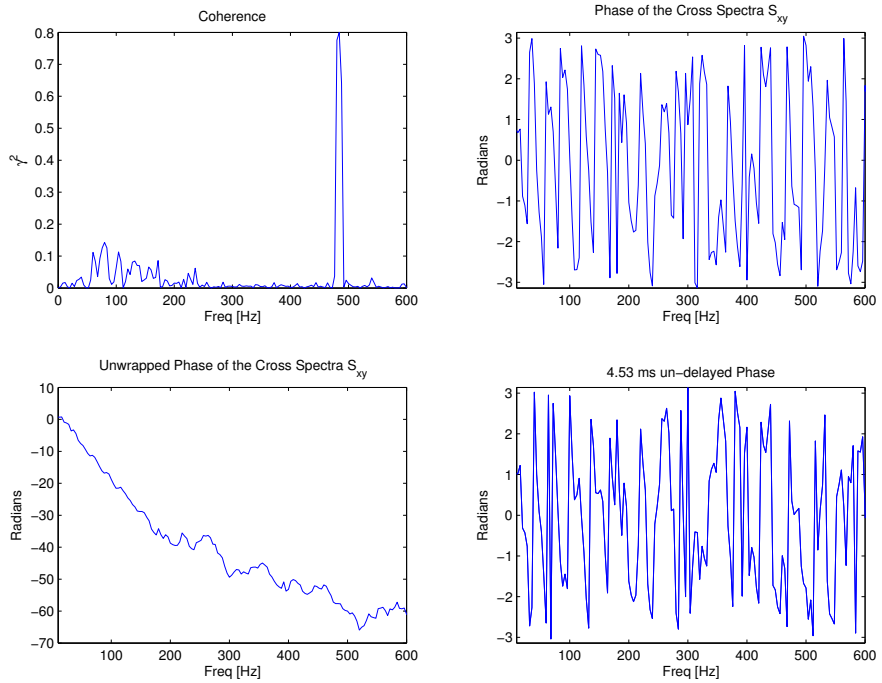

FIGURE E.49: Phase Study between RP3 and MIC1 for N1=61%

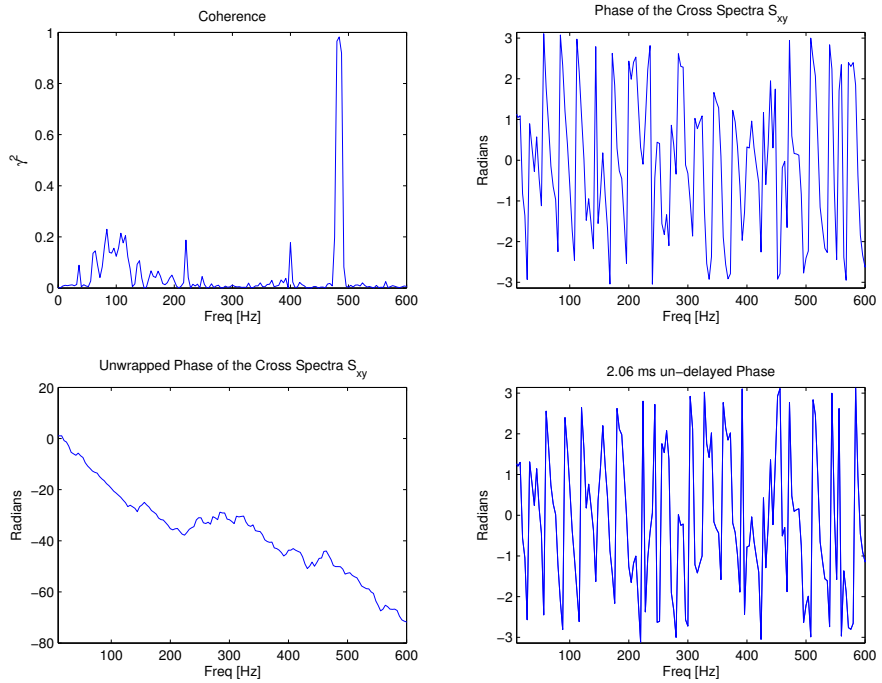

FIGURE E.50: Phase Study between RP3 and MIC5 for N1=61%

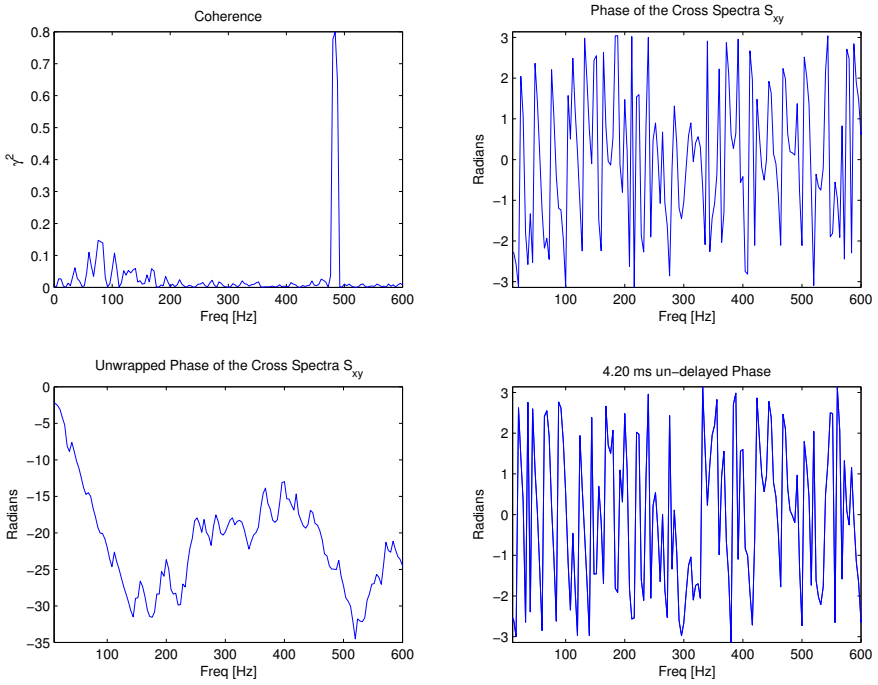

FIGURE E.51: Phase Study between RP4 and MIC1 for N1=61%

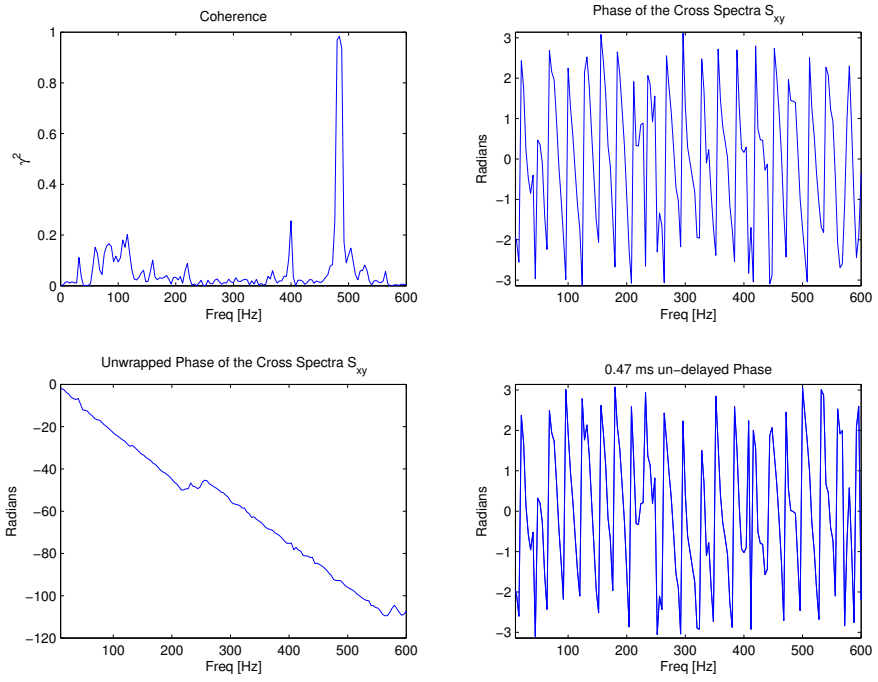

FIGURE E.52: Phase Study between RP4 and MIC5 for N1=61%

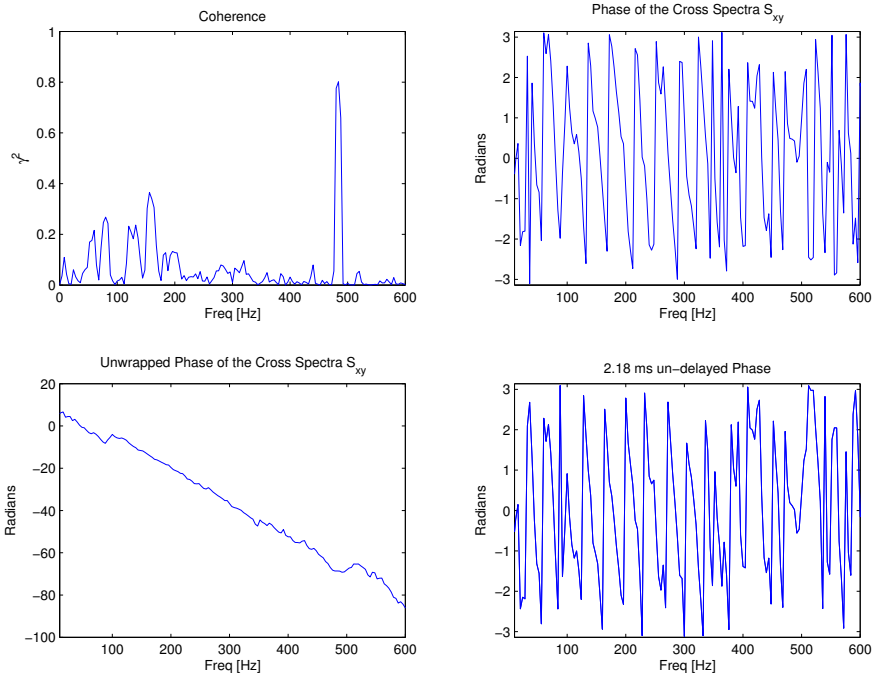

FIGURE E.53: Phase Study between RPB and MIC1 for N1=61%

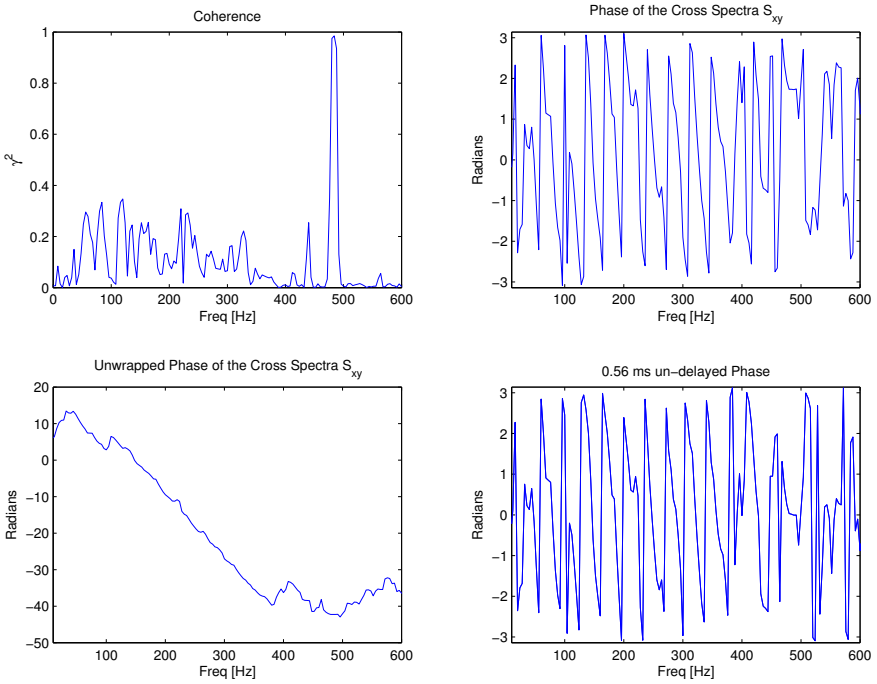

FIGURE E.54: Phase Study between RPB and MIC5 for N1=61%

Bibliography

[1] M. J. T. Smith, *Aircraft Noise*. Cambridge University Press, 1989.

[2] Rolls-Royce, *The Jet Engine*. Rolls-Royce PLC, 2005.

[3] A. M. Karchmer, "Turbofan engine core noise source diagnostics," in *NOISE-CON 87*, 1987.

[4] E. A. Krejsa, "New technique for the direct measurement of core noise from aircraft engines," in *Technical Report AIAA Paper 1981-1587 (NASA TM-82634), 17th AIAA/SAE/ASME Joint Propulsion Conference*, (Colorado Springs, Colorado), 1981.

[5] A. M. Karchmer, "Measurement of far-field combustion noise from a turbofan engine using coherence functions," in *AIAA 77-1277*, 1977.

[6] D. Dunn-Rankin, *Lean Combustion*. Academic Press, 2008.

[7] I. Segalman, R. G. McKinney, G. J. Sturgess, and L. M. Huang, "Reduction of NOx by fuel-staging in gas turbine engines - a commitment to the future," *AGARD CP-536*, pp. 29/1–17, 1993.

[8] A. H. Lefebvre, *Gas Turbine Combustion*. Taylor and Francis, 1999.

[9] H. C. Mongia, "TAPS - a 4th generation propulsion combustor technology for low emissions," in *AIAA Paper 2003-2657*, 2003.

[10] P. Gliebe, R. Mani, H. Shin, B. Mitchell, G. Ashford, S. Salamah, and S. Cornell, "Aeroacoustic prediction codes," in *NASA/CR-2000-210244* (NASA, ed.), 2000.

[11] M. Ihme and H. Pitsch, "On the generation of direct combustion noise in turbulent non-premixed flames," *International Journal*, vol. 11, no. 1, pp. 25–78, 2012.

[12] ACARE2020, "European aeronautics: A vision for 2020," 2001. (http://www.acare4europe.org accessed February 20, 2013).

[13] M. Harper-Bourne, A. Moore, and H. A. Siller, "A study of large aero-engine combustor noise," in *AIAA paper 2008-2942*, May 2008.

[14] J. H. Miles, "Aligned and unaligned coherence: A new diagnostic tool," in *AIAA-2006-0010*, 2006.

[15] J. H. Miles, "Spectral separation of the turbofan engine coherent combustion noise component," in *AIAA paper 2008-50*, May 2008.

[16] J. H. Miles, "Core noise diagnostics of turbofan engine noise using correlation and coherence functions," in *AIAA-2009-1237*, 2009.

[17] J. H. Miles, "Time delay analysis of turbofan engine direct and indirect combustion noise sources," in *AARC Turbine Noise Workshop*, 2008.

[18] L. S. Hultgren and J. H. Miles, "Noise-source separation using internal and far-field sensors for a full-scale turbofan engine," in *AIAA 2009-3220*, 2009.

[19] J. H. Miles, "Separating direct and indirect turbofan engine combustion noise while estimating post-combustion (post-flame) residence time using the correlation function," in *AIAA-2010-0019*, 2010.

[20] P. Rodríguez García and K. R. Holland, "Exploring and developing processing techniques for the extraction of aircraft combustion noise," in *20th International Congress in Sound and Vibration*, 2013.

[21] P. Rodríguez García, K. R. Holland, and B. K. Tester, "Extraction of turbofan combustion noise spectra using a combined coherence-beamforming technique," in *AIAA-2014-3286 Atlanta, GA.*, 2014.

[22] Advisory Group for Aeronautical Research and Development, *Combustion Researches and Reviews, 1955*. Butterworths Scientific Publications, 1955.

[23] Advisory Group for Aeronautical Research and Development, *Combustion Researches and Reviews, 1957*. Butterworths Scientific Publications, 1957.

[24] G. Cummings, "Stationary flames at pressures above one atmosphere," *Combustion Researches and Review 1957*, 1957.

[25] B. Karlovitz, *Selected Combustion Problems*. Butterworths Scientific Publications, 1954.

[26] K. K. Kuo and R. Acharya, *Fundamentals of Turbulent and Multiphase Combustion*. John Wiley & Sons, Inc., 2012.

[27] N. R. L. Maccallum, "Flame-spreading characteristics in combustion," *Combustion Researches and Rreview 1957*, 1957.

[28] Williams and Wilkins, 1953.

[29] D. B. Spalding, "The combustion of liquid fuels," in *Fourth Symposium (International) on Combustion*, vol. 4, p. 847864, 1953.

[30] E. E. O'Brien, *Turbulent Reacting Flows*, ch. The Probability Density Function (pdf) Approach to Reacting Turbulent Flows, pp. 185–218. Springer, p. a. libby and f. a. williams ed., 1980.

[31] S. B. Pope, "Pdf methods for turbulent reacting flows," *Progress in Energy and Combustion Science*, vol. 11, no. 2, pp. 119–192, 1985.

[32] S. B. Pope, "An improved turbulent mixing model," *Combustion Science and Technology*, vol. 28, no. 3-4, pp. 131–145, 1982.

[33] F. A. Williams, "A review of some theoretical considerations of turbulent flame structure," *Analytical and Numerical Methods for Investigation of Flow Fields with Chemical Reactions, Especially Related to Combustion*, 1975.

[34] F. A. Williams, *Combustion Theory*. Benjamin/Cummings, 1985.

[35] N. Peters, "Laminar diffusion flamelet models in non-premixed turbulent combustion," in *Progress in Energy and Combustion Science*, vol. 10 (3), pp. 319–339, 1984.

[36] W. C. Strahle, "A review of combustion generated noise," in *AIAA 73-1023*, pp. 229–248, 1973.

[37] M. Reshotko, "Core noise mmeasurement on a yf-102 turbofan engine," in *AIAA Paper 77-21, Los Angeles, CA.*, 1977.

[38] M. J. Fisher, M. Harper-Bourne, and S. A. L. Clegg, "Jet engine noise source location: The polar correlation technique," *Journal of Sound and Vibration*, vol. 51, pp. 23–54, 1977.

[39] B. J. Tester and M. J. Fisher, "Engine source breakdown; theory, simulation and results," in *AIAA 81-2040, Palo Alto, CA.*, 1981.

[40] D. Johnson and D. Dudgeon, *Array signal processing: concepts and techniques*. P T R Prentice-Hall, 1993.

[41] S. Glegg, "Jet noise source location using an acoustic mirror," Master's thesis, Univerisity of Southampton, 1975.

[42] J. Billingsley and R. Kinns, "The acoustic telescope," *Journal of Sound and Vibration*, 1976.

[43] P. M. W. Pack and P. J. R. Strange, "Recente developments in source location," in *AIAA 87-2685*, 1987.

[44] M. Mosher, "Phased arrays for aeroacoustic testing: theoretical development," in *AIAA 96-1713*, 1996.

[45] M. J. Fisher, *Source Location*. Rolls-Royce UTC in Gas Turbine Noise, Institue of Sound and Vibration Research (ISVR), University of Southampton, Southampton, SO17 1BJ, UK.

[46] B. J. Tester, T. Ricoup, and G. Gabard, "Extracting engine noise source levels from phased arrays with improved internal source models and evaluation against simulated and measured data," in *AIAA-2012-2272*, 18th AIAA/CEAS Aeroacoustics Conference, 2012.

[47] B. J. Tester, "Engine noise source breakdowns from an improved inverse method (AFINDS) of processing phased array measurements," in *AIAA-2014-3067, Atlanta, GA.*, (Atlanta GA), 20th AIAA/CEAS Aeroacoustics Conference, 2014.

[48] S. P. Parthasarathy, R. F. Cuffel, and P. F. Massier, "Separation of core noise and jet noise," *AIAA Journal*, vol. 18, no. 3, pp. 256–261, 1980.

[49] S. Funke, H. A. Siller, and W. Hage, "Microphone-array measurements of a Rolls-Royce BR700 series aeroengine in an indoor test-bed and comparison with free-field data," in *AIAA-2014-3070, Atlanta, GA.*, (Atlanta GA), 20th AIAA/CEAS Aeroacoustics Conference, 2014.

[50] K. R. Holland, "Antle engine noise test: Source location in-cell data appraisal report. european project deliverable, silencer (d2.2-4.5-01)," tech. rep., ISVR UK, 2006.

[51] R. Dougherty, "Extension of DAMAS and benefits and limitations of deconvolution in beamforming," in *11th AIAA/CEAS Aeroacoustics Conference*, vol. 3, pp. 2036–2048, 2005.

[52] T. F. Brooks and W. M. Humphreys, "A deconvolution approach for the mapping of acoustic sources (DAMAS) determined from phased microphone arrays," *Journal of Sound and Vibration*, vol. 294(4), pp. 586–879, 2006.

[53] C. Lawson and R. Hanson, *Solving Least Squares Problems*. Society for Industrial and Applied Mathematics, 1974.

[54] D. F. Comesana, *Scan-based sound visualisation mmethod using sound pressure and particle velocity*. PhD thesis, University of Southampton, 2014.

[55] I. Rakotoarisa, J. Fisher, D. Marx, V. Valeau, C. Prax, and L. Brizzi, "Detection of Non-Stationary Aeroacoustic Sources by Time-Domain Imaging Methods," in *AIAA-2014-2916*, 2014.

[56] Z. Prime, A. Mimani, D. Moreau, and C. Doolan, "An Experimental Comparison of Beamforming, Time-reversal and Near-field Acoustic holography for Aeroacoustic Source Localisation," in *AIAA-2014-2917*, 2014.

[57] R. Dougherty, "Functional Beamforming for Aeroacoustic Source Distributions," in *AIAA-2014-3066*, 2014.

[58] R. Ramachandran and G. Raman, "On Using Functional Beamforming To Resolve Noise Sources On A Large Wind Turbine," in *AIAA-2014-2914*, 2014.

[59] H. A. Siller, F. Arnold, and U. Michel, "Investigation of aero-engine core-noise using a phased microphone array," in *7th AIAA/CEAS Aeroacoustics Conference and Exhibit, Maastricht, Netherlands, May 28-30, 2001, Collection of Technical Papers. Vol. 2 (A01-30800 07-71)*, 2001.

[60] E. A. Krejsa, "Application of 3-signal coherence to core noise transmission," in *Technical Report AIAA Paper 1983-0759 (NASA TM-83333), 8th AIAA Aeroacoustics Conference*, (Atlanta, Georgia), 1983.

[61] E. A. Krejsa, "Combustion noise from gas turbine aircraft engines measurement of far-field levels," in *NOISE-CON 87*, 1987.

[62] J. Y. Chung, M. J. Crocker, and J. F. Hamiton, "Measurement of frequency response and the multiple coherence function of the noise-generation system of a diesel engine," *Journal of the Acoustical Society of America*, vol. 58, no. 3, pp. 636–642, 1975.

[63] J. Y. Chung, "Rejection of flow noise using a coherence function method," *Journal of the Acoustical Society of America*, vol. 62, p. 338, 1977.

[64] D. C. Matthews and A. A. Perachio, "Progress in Core Engine and Turbine Noise Technology," in *AIAA 74-648*, 1974.

[65] E. A. Burdsall, F. P. Brochu, and V. M. Scaramella, "Results of Acoustic Testing of the JT8D-109 Refran Engines," tech. rep., NASA CR-134875, 1975.

[66] A. M. Karchmer and M. Reshotko, "Core noise source diagnostics on a turbofan engine using correlation and coherence techniques," tech. rep., NASA TM-X73535, 1976.

[67] J. S. Bendat and A. G. Piersol, *Measurement and Analysis of Random Data.* John Wiley & Sons Ltd, 1966.

[68] J. S. Bendat and A. G. Piersol, *Random Data: Analysis and Measurement Procedures.* Wiley-Interscience, 1986.

[69] J. S. Bendat and A. G. Piersol, *Engineering applications of correlation and spectral analysis.* Wiley-Interscience, 1993.

[70] D. Percival and A. Walden, *Spectral Analysis for Physical Applications.* Cambridge University Press, 1993.

[71] A. M. Karchmer, "Identification and measurement of combustion noise from a turbofan engine using correlation and coherence techniques," tech. rep., NASA TM-73747, 1978.

[72] L. S. Hultgren, "Full-scale turbofan-engine turbine-transfer function determination using three internal sensors," in *AIAA-2011-2912*, 2011.

[73] J. M. Mendoza, D. K. Nance, and K. K. Ahuja, "Source separation from multiple microphone measurements in the far field of a full scale aero engine," in *AIAA-2008-2809*, 2008.

[74] J. S. Hsu and K. K. Ahuja, "A coherence-based technique to separate ejector internal mixing noise from farfield measurements," in *AIAA 1998-2296, Toulousse*, 1998.

[75] T. Minami and K. K. Ahuja, "Five-microphone method for separating two different correlated noise sources from far-field measurements contaminated by extraneous noise," in *AIAA 2003-3261*, 2003.

[76] G. J. Bennett and J. A. Fitzpatrick, "A comparison of coherence based acoustic source identification techniques," in *12th International Congress on Sound and Vibration, Lisbon, Portugal*, 2005.

[77] I. Davis and G. J. Bennett, "Novel noise-source-identification technique combining acoustic modal analysis and a coherence-based noise-source-identification method," *AIAA Journal. 53 (2015) 30883101. doi:10.2514/1.J053907*, 2015.

[78] B. Pardowitz, U. Tapken, K. Knobloch, F. Bake, E. Bouty, I. Davis, and G. J. Bennett, "Core noise - identification of broadband noise sources of a turbo-shaft engine," in *AIAA 2014-3321*, 2014.

[79] I. Davis and G. J. Bennett, "Experimental investigations of coherence based noise source identification techniques for turbomachinery applications - classic and novel techniques," in *(AIAA-2011-2830), in: 17th AIAA/CEAS Aeroacoustics Conference (32nd AIAA Aeroacoustics Conference), Portland, Oregon, USA*, 2011.

[80] G. J. Bennett, *Noise source identification for ducted fans.* PhD thesis, Trinity College Dublin, Dublin, 2006.

[81] P. D. Yardley, *Measurement of Noise and Turbulence Generated by Rotating Machinery.* PhD thesis, University of Southampton, England, U.K., 2074.

[82] M. Abom, "Modal decomposition in ducts based on transfer function measurements between microphone pairs," *Journal of Sound and Vibration Vol. 135, No. 1, pp. 95-114*, 1989.

[83] I. Davis and G. J. Bennett, "Sum and difference scattering of tonal noise in turbomachinery," in *AIAA 2013-2149*, 2013.

[84] I. Davis and G. J. Bennett, "Spatial noise source identification of tonal noise in turbomachinery using the coherence function on a modal basis," in *AIAA 2001-2825, 17th AIAA/CEAS (32nd AIAA Aeroacoustics Conference), Portland, Oregon*, 2011.

[85] D. Blacodon and S. Lewy, "Source localization of turboshaft engine broadband noise using a three-sensor coherence method," *Journal of Sound and Vibration. 338 (2015) 250262. doi:10.1016/j.jsv.2014.10.019*, 2014.

[86] L. S. Hultgren, "A comparison of combustor-noise models," in *AIAA-2012-2087, NASA/TM-2012-217671*, 2012.

[87] M. Muthukrishnan, W. C. Strahle, and D. H. Neale, "Separation of hydrodynamic entropy, and combustion noise in a gas turbine combustion noise component," *AIAA Journal*, vol. 16(4), pp. 320–327, 1978.

[88] P. M. Morse and K. U. Ingard, *Theoretical Acoustics.* Princetown University Press, 1986.

[89] J. E. F. Williams and M. S. Howe, "The generation of sound by density inhomogeneities in low mach number nozzle flows," *Journal of Fluid Mechanics*, vol. 70(3), pp. 605–622, 1975.

[90] F. E. Marble and S. M. Candel, "Acoustic disturbance from gas non-uniformities convected through a nozzle," *Journal of Sound and Vibration*, vol. 55(2), pp. 225–243, 1977.

[91] M. Leyko, F. Nicoud, and T. Poinsot, "Comparison of direct and indirect combustion noise mechanisms in a model combustor," tech. rep., SNECMA, 2012.

[92] F. Bake, N. Kings, and I. Röhle, "Fundamental mechanism of entropy noise in aero-engines: Experimental investigation," *J. Eng. Gas Turbines Power 130(1), 011202*, 2008.

[93] B. Mühlbauer, A. Widenhorn, M. Liu, B. Noll, and M. Aigner, "Fundamental mechanism of entropy noise in aero-engines: Numerical simulation," in *Proceedings of the ASME Turbo Expo , 2, pp. 115-124, American Society of Mechanical Engineers*, 2007.

[94] F. Bake, C. Richter, B. Mühlbauer, N. Kings, I. Röhle, F. Thiele, and B. Noll, "The entropy wave generator (ewg): A reference case on entropy noise," *Journal of Sound and Vibration, Volume 326, Issues 3-5, Pages 574-598*, 2009.

[95] I. Duran, S. Moreau, F. Nicaud, T. Livebardon, E. Bouty, and T. Poinsot, "Combustion noise in modern Aero-Engines," *AerospaceLab*, 2014.

[96] J. M. Tyler and T. G. Sofrin, "Axial flow compressor noise studies," *Aeronautic Meeting*, 1961.

[97] C. L. Morfey, "Rotating pressure patterns in ducts: their generation and transmission," *J. Sound Vib.*, vol. 1, pp. 60–87, 1964.

[98] E. Richards and D. Mead, *Noise and Acoustic Fatigue in Aeronautics*. John Wiley & Sons Ltd, 1968.

[99] P. M. Morse, *Vibration and Sound*. McGraw-Hill Book Company Inc., 1948.

[100] F. Jacobsen, "Propagation of sound waves in ducts," tech. rep., Technical University of Denmark, 2011.

[101] "Fundamentals of gas turbine engines." CAST Safety Plan technical notes.

[102] K. Shin and J. Hammond, *Fundamentals of Signal Processing for Sound and Vibration Engineers*. Wiley, 2008.

[103] I. A. McCowan, *Robust Speech Recognition using Microphone Arrays*. PhD thesis, Queensland University of Technology, Australia, 2001.

[104] R. Lundberg, M. Leijon, L. Strm, and O. Isaksson, "Development of structural components for antle and clean, the european technology validator engines," in *ISABE-2005-1276*, 2005.

[105] N. Peacock, "Antle an integration of european & national research programmes," tech. rep., Rolls-Royce plc, 2006.

[106] G. J. Bennett and J. A. Fitzpatrick, "Data appraisal report: Combustor noise lpt propagation assessment report," tech. rep., TCD, 2006.

[107] G. J. Bennett and J. A. Fitzpatrick, "Noise-source identification for ducted fan systems," *AIAA Journal. 46 (2008) 16631674. doi:10.2514/1.33522*, 2008.

[108] P. Bohning, H. Siller, K. Holland, F. Arnold, A. Kempton, and U. Michel, "Novel methods for acoustic indoor measurements and applications in aero-engine test cells," in *Berlin Beamforming Conference BeBec-2006-04*, 2006.

[109] G. R. Naik, ed., *Independent Component Analysis for Audio and Biosignal Application*. InTech, 2012.

[110] D. T. Mewett, H. Nazeran, and K. J. Reynolds, "Removing power line noise from recorded EMG," in *2001 procedings of the 23rd Annual EMBS International Conference*, 2001.